THE UNIVERSITY OF MICHIGAN

INDUSTRY PROGRAM OF THE COLLEGE OF ENGINEERING

HIGH SPEED PHOTOGRAPHIC STUDIES OF ULTRASONICALLY-INDUCED CAVITATION AND DETAILED EXAMINATION OF DAMAGE TO SELECTED MATERIALS

Hilding G. Olson

A dissertation submitted in partial fulfillment
of the requirements for the degree of
Doctor of Philosophy in the
University of Michigan
Department of Nuclear Engineering
1966

IP-746

Doctoral Committee:

Professor Frederick G. Hammitt, Chairman
Professor Lloyd E. Brownell
Professor William Kerr
Professor Clarence A. Siebert

ACKNOWLEDGMENTS

The guidance and assistance given the author by Professor Frederick G. Hammitt and the other members of the doctoral committee are gratefully appreciated.

The financial support of the National Science Foundation is acknowledged.

Thanks are due to Dr. M. John Robinson for his advice and to Mr. Ramon Garcia for the use of his ultrasonic transducer system.

The staffs of the Instrument and Electronic Shops of the Phoenix Memorial Laboratory were most helpful. A special thanks to Mr. Paul Herman who designed and constructed the high intensity photographic light source.

The author also wishes to thank the research assistants of the Phoenix Memorial Laboratory and of the Nuclear Engineering Department who did a large part of the metallographic work.

A special thanks to my wife, Evalynn, for her encouragement.

TABLE OF CONTENTS

LIST OF TABLES

LIST OF FIGURES

Figure Page

Figure Page

Figure Page

Figure Page

Figure

Page

Figure Page

Figure Page

NOMENCLATURE

cm	Centimeter
bar	.987 Atmospheres
ν	Resonance frequency
R_r	Resonance radius, i. e., mean radius of resonating bubble
γ	Ratio of the specific heats of the gas content of the bubble
ρ	Density of water
p	Ambient equilibrium pressure of the water
σ	Surface tension
$\sim$	Approximate
X	Enlargement multiple
mg	Milligram
cps	Cycles per second
fps	Frames per second
μ	Micro
mil	.001 inch
C. W.	Cold worked
psi	Pounds per square inch
MDPR	Mean depth of penetration rate
L. Ht. Trt.	Light Heat Treat

CHAPTER I

INTRODUCTION

A. Motivation for the Investigation

For any process or system involving liquid flow where a two-phase condition is a possibility (such as most liquid cooled or moderated nuclear power reactors), the phenomenon of cavitation with respect to the fluid-handling components which make up the system, must be considered from both the damage and performance viewpoints. This is especially true in the nuclear space and nuclear field in general due to long-life requirements and difficulties of maintenance. Most of the presently available experimental data on cavitation have been gathered from experiments using water, although the data is still fragmentary even for this common fluid. However, very little data exists at all for most other fluids, and almost none for liquid metals due to the considerable difficulties involved in working with these fluids.

That we now associate occurrences such as rain drop erosion of supersonic aircraft and some types of bearing pitting with processes that are basically analagous to cavitation damage, shows the importance of an investigation into

the basic damaging mechanisms of the collapsing cavitation bubble and also the desirability of arriving at a relatively simple, inexpensive, and quick method for testing and rating proposed materials for systems where cavitation-type damage might be expected. The present work is a basic study of the behavior of cavitation bubbles in an experimental facility which was designed and used in the past primarily for high-temperature liquid metals. For the present study, however, water has been the test fluid.

B. Previous Experimental Work

Vibratory testing devices for acceleration of cavitation damage have been used by Wheeler,[1] Kerr,[2] Rheingans,[3] Plesset and Ellis,[4] Thiruvengadam and Preisser,[5] Kerr and Leith,[6] Garcia et al[7,8,9] in this laboratory, and many others. The latter study used a piezoelectric ultrasonic transducer (as opposed to magnetostriction facility used by most of the others) in both water and liquid metals. A direct comparison of these vibratory tests results, considering a wide range of physical characteristics for the test specimens, with data taken from flowing system tests with a venturi by Robinson,[10] shows strikingly similar rankings for resistance to cavitation damage, but the rate of damage using the vibratory method was approximately 10^3 higher than that of the venturi.

A comprehensive computer study is still in process to seek out the physical property or properties of the many

materials tested to justify the ranking that was experimentally obtained. No single property or multiple correlation in terms of the conventional mechanical and/or fluid properties has been found which will apply with precision to both venturi and vibratory data or even to all the data peculiar to either system. This lack of any really precise or even general relationship between the mechanical and fluid properties and the cavitation damage rates may be a result of the combination of the following factors:

a) Cavitation loading is highly transient, but mechanical properties of the material are measured in a semi-static method.

b) Corrosion and other chemical activity is involved in varying degrees for various conditions.

c) The actual damage mechanism may vary from fatigue type to single blow fracturing, with the applicable combination being dependent upon flow conditions, fluid properties, mechanical properties, etc.

d) Different materials fail in entirely different methods, i. e., compare ceramics as contrasted with highly ductile metals, etc.

Robinson,[10] using a cavitating venturi, showed in a high speed photographic study that there were 10^4 to 10^5 bubbles observed adjacent to the exposed specimen surfaces for every pit that was later detected on these surfaces. A similar result was previously given by Plesset[11] who reported approximately 10^4 bubbles per pit for a vibratory facility.

Robinson[10] and Robinson and Hammitt[12,13] compared depth to diameter ratios of the individual pits to data obtained from impact tests by Engel[14] and also compared profiles of cavitation pits to profiles of high velocity impact pits from an experiment by DeCorso[15] and a very close comparison was evident. Evidence was found in Robinson's work,[10] and further reported by Robinson and Hammitt,[12,13] that cavitation damage is probably caused by the asymmetrical collapse of bubbles which evolve into a micro-jet which impacts the surface. It is assumed that this micro-jet impingement damages the material surface as had been previously suggested by Kornfeld and Surorov[16] and later emphasized by the work of Naudé and Ellis.[17] The micro-jet theory is opposed to the classical theory originated by Rayleigh[18] in his early analysis of the spherical collapse of a bubble in an ideal fluid, whereby it was postulated that a shock wave resulting from the collapse caused the damage.

Harrison,[19] Ivany,[20] Ivany and Hammitt,[21] and Ivany, Hammitt and Mitchell[22] have shown, with high speed photographic techniques, the non-spherical, toroidal, collapse of large cavitation bubbles in a venturi diffuser where the pressure gradient was large, thus causing the non-symmetry. Naudé and Ellis's[17] theoretical and experimental investigations of the effect of perturbations on the collapse of hemispherical, spark-generated bubbles adjacent to a surface gave strong impetus to the theory that the resultant micro-jet from this

collapse caused the observed damage. Shutler and Mesler[23] further pursued this experimental approach and presented many high quality and interesting short exposure photographs of the collapse of individual, spark-induced bubbles, but concluded that the damage was caused by shock waves from the rebounding (i.e., expanding after reaching its minimum volume) torus and not by the central jet, which they also observed.

Benjamin and Ellis[24] photographically showed the non-symmetrical, toroidal collapse and rebound of bubbles formed from an electrolytically formed gas nucleus at reduced pressure and collapsed by the arresting of the fall of the containing vessel. Thus the bubble grew in a spherically-symmetric, gravity-free environment. Quite similar work is reported by Florschuetz and Chao.[25]

Meanwhile numerical calculations using real fluid properties by Ivany and Hammitt[21] and Hickling and Plesset[26] showed that the shock pressures generated by symmetrically collapsing bubbles were not sufficient to cause the observed damage, whereas the shock pressures from a symmetrically rebounding bubble would suffice. However, a symmetrical collapse or rebound close enough to the surface to cause damage does not seem likely, and any departure from symmetry would probably reduce the shock pressure. On theoretical grounds, the collapse center is believed to move toward the adjacent material surface during the collapse sequence. Whether this movement, if it occurs, is of any significance is not known.

Schmid,[27] experimenting with single cavitation bubbles, photographed the collapse and subsequent rebounds of the bubbles and noted their grossly distorted shapes as well as the circular shock wave that was emitted after the bubble implosion and before the rebound. The shock wave was apparently sufficiently strong so that its density gradient could be seen photographically without Schlieren techniques.

Willard,[28] Ellis,[29,30] Leith and Thomson,[31] Rosenberg and Eknadiosyants,[32] Numachi,[33] Plesset and Devine,[34] and Saneyoshi and Okushima,[35] have photographed ultrasonically-induced cavitation bubble clouds.

Jackson and Nyborg[36,37] and Jackson[38] have presented experimental evidence of the existence of vortices around the corners of a vibrating horn (as shown in Fig. 56, Chapter IV, Section G), which could act to raise the pressure at the outer periphery of the horn, thus suppressing cavitation in the outer annular portion of the specimen face. Most exposed specimens show this undamaged annulus. They considered both an ultrasonic horn in water far from all boundaries and also the case with the horn adjacent to the bottom boundary. In both of their experiments the horn was held in a vertical position.

The fact that a spectrum of bubble sizes exists for a cavitation flowing system and that this may be related to the pit spectrum of the damaged materials was recently considered by Hammitt.[39] Robinson[10] and Robinson and Hammitt[12,13]

have then experimentally measured such bubble and pit spectra for various materials in both water and mercury.

Knapp[40] suggested that the pitting rate would be a possible measure for a relative rating of resistance of materials to cavitation damage. This concept suffers, however, from many limitations and difficulties.

It has been established by work in this laboratory[10,13,39] that cavitation damage in many cases is initiated by single bubble collapses which produce single craters. These are randomly dispersed over the surface, having little regard as to grain boundaries, etc. Eventually most of the exposed surface is damaged by the craters so that gross fatigue failures then occur. Of course, it is also possible in some cases that blows of sufficient intensity to cause a crater do not occur in one event, but the cumulative effect is sufficient to cause eventual fatigue failure. In the case where the collapse of a single bubble can cause a crater type pit from which material is removed, no "incubation time period" exists before material removel starts, and no pre-conditioning of the material is required before damage is obtained. Extensive tests involving damage rates as a function of exposure time or accumulated damage have been done in this laboratory on flowing[10,13,39] and vibrating systems.[7,8,9] However, prior to the present study only tests of one hour or longer incremental durations had been made. Kerr and Leith[6] studied minimum times of 5 minutes and Plesset and Devine[34] reported no detectable weight loss (by precision balance) for times as low as one minute.

Noltingk and Neppiras[41,42] derived the equations to describe the behavior of a gas filled bubble in a liquid that was subjected to alternating pressure from an acoustic field. Their extensive numerical work and theoretical conclusions led to the thought that, ideally, a cavitation bubble grows and collapses in less than one acoustic cycle provided that the bubble nuclei are in a size range that is greater than a certain critical radius and less than a resonant radius. At the resonant radius, the bubble was expected to go through complex oscillations with a slow increase in radius, but no collapse of these resonant bubbles was predicted. Rebound of collapsing bubbles was not discussed. Willard[28] experimentally observed the rebound and the oscillation of unstable bubbles but not their final collapse.

C. The Present Investigation

There have been efforts in the past[43] to make the vibratory system the accepted standard for cavitation specimen testing, and the possibility of the adoption of this system as the standard is currently under study by the American Society for Testing Materials. The cost for vibratory tests is considerably less than for a venturi or other flowing system because of lower initial costs for the test equipment and also the fact that the higher damage rates allow reduced running time. The vibratory type test has been considered an ideal standard by some investigators, but since the flow,

geometry and many physical parameters of the vibratory system differ so greatly from any flowing system, it is of paramount importance that all aspects of the vibratory damaging process and the resultant damage be thoroughly examined so that testing and rating of specimens will be meaningful.

It is the purpose of this study to explore the many facets of the vibratory cavitation problem in water and to present a comparison, when possible, to the vast amount of data and evidence accumulated from venturi and previous vibratory experiments.

Specimens have been fabricated for study from eight materials that differ markedly in mechanical properties. It is hoped that the rate of pit generation, weight loss, and the character of the individual pits will help in delineating the parameter or parameters by which materials may be more adequately rated for cavitation resistance.

It is apparent that the population and characteristics of the cavitation bubble field itself can have an important bearing on the damage rate. A comprehensive understanding of the dynamics of the bubble field and how it varies for various fluids, specimen materials, surface condition, gas content of water, etc. is highly important in the overall effort to establish a uniform rating system.

Further effort will be made in an attempt to explain the damaging mechanism of the collapsing bubble.

It is hoped that the assembling of the information from this investigation will be of assistance to those interested in the basic problem of the cavitation bubble field around a vibrating specimen, and to those who are considering the vibrating system as an accelerated test means for cavitation specimens.

CHAPTER II

ULTRASONICALLY-INDUCED CAVITATION BUBBLE FIELDS-THEORY

The ultrasonic transducer provides high frequency mechanical vibrations at the end of the horn, Fig. 1, which generate an acoustic field in a fluid into which the horn is submerged. This can result in cavitation at the horn tip on the face that is normal to the direction of vibration. Cavitation here is defined as the generation of and collapse of individual bubbles in an aggregate herein called the cavitation bubble field, the field occurring on and near the surface of the specimen. The generation and collapse is caused by the acoustically-induced, time-varying pressure in the liquid that is adjacent to the specimen. The bubbles presumably originate from some form of gas "nuclei." The acoustically induced rarefaction or negative pressure wave causes these nuclei to expand until the acoustic compressional or positive pressure wave arrests their growth and then presumably causes them to collapse before the start of the next negative pressure part of the cycle.

Noltingk and Neppiras[41] showed theoretically and in detail how a bubble grows during the negative pressure portion

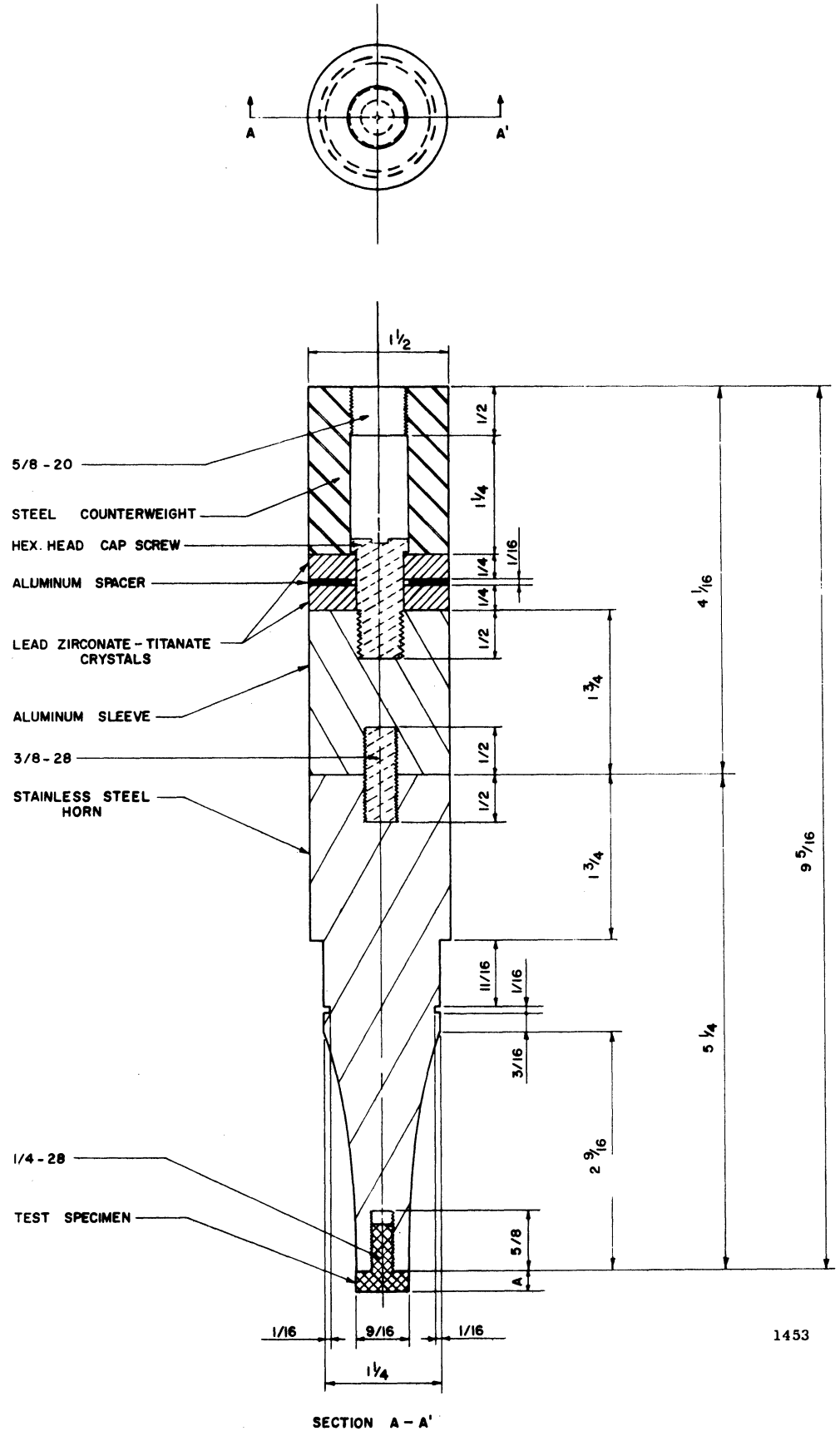

Fig. 1.--Exponential horn and ultrasonic transducer assembly.

of the acoustic cycle and, subject to various limitations, collapses in a part of the positive pressure portion of the cycle. They developed equations for the acoustically-induced motion of gas filled bubbles, assuming that the liquid was incompressible, neglecting the pressure of the vapor in the bubble, considering the mass of gas to be constant in the bubble over its life cycle, and also that the applied acoustic wave is exactly sinusoidal. They then solved the equations numerically, and were able to predict the growth and collapse patterns for the bubbles under various acoustic conditions. Collapse time was found to be a small fraction of the acoustic period.

There is a size range of a bubble nucleus that will permit growth and collapse of the bubble in one acoustic cycle, completing the cavitation event as defined acoustically. Flynn[44] defines this bubble as the transient type.

Noltingk and Neppiras[42] extended their theoretical work to study extremely small nuclei, and found that for nuclei in a certain radius range cavitation will not occur for a given applied negative pressure because surface tension forces prevent the bubble from growing sufficiently to a size from which it can collapse in a single acoustic cycle. However, for nuclei of a larger radius, where the bubble can grow sufficiently in size under the influence of the applied acoustic field, cavitation is possible.

While cavitation is a dynamic process, some knowledge of the process can be gained from study of equilibrium conditions. For example, it can be shown quite simply[44] that the critical radius in water for equilibrium conditions at 68°F is 9.5×10^{-5} cm for a negative pressure of 1 bar (1 bar = .987 atmospheres) and 1.9×10^{-5} cm for -5 bars,[44]* i.e., if the liquid pressure is reduced below this value and maintained at the reduced value, the bubble will grow without limit. On the other hand, if the liquid pressure is raised above the "critical" value, and maintained at this higher level, the bubble should collapse completely.

If the bubble nucleus is of proper size for the applied acoustic frequency, it will resonate with that frequency, pulsating under the action of the acoustic field in a series of complex oscillations. It will not then collapse as a transient cavity in one cycle.

The fundamental frequency for such a resonance condition according to Minnaert[45] is, assuming small amplitudes and adiabatic compression,

$$\nu = \frac{1}{2\pi R_r}\sqrt{\frac{3\gamma}{\rho}\left(P + \frac{2\sigma}{R_r}\right)} \qquad (1)$$

where the bubble motion is approximately simple harmonic, and

---

*These values from Flynn[44] consider a bubble filled with gas at the saturation partial pressure as well as saturated vapor.

ν = resonance frequency

R_r = resonance radius, i.e., mean radius of resonating bubble

γ = ratio of the specific heats of the gas content of the bubble

ρ = density of the water

P = ambient equilibrium pressure of the water

σ = surface tension of the water

Neglecting the surface tension term, this is approximately

$$\nu = \frac{1}{2\pi R_r}\sqrt{\frac{3\gamma P}{\rho}} \tag{2}$$

For P=1 atmosphere

$$R_r(\text{in cm}) \cong \frac{.32\times 10^3}{\nu} \tag{3}$$

Noltingk and Neppiras[41,42] calculated that a resonating bubble would go through complex oscillations with a slow increase in radius, but no collapse of such bubbles was predicted.

Thus for a given size bubble there is a resonance frequency and conversely for a given acoustic frequency there is a certain size bubble which will resonate.

Flynn[44] points out that resonant bubbles will oscillate under the action of the acoustic pressure with an amplitude that increases with time. If the radius is increased sufficiently through perturbations, rectified diffusion, etc. such that the inward liquid inertia due to spherical contraction of the bubble becomes sufficient to overcome the gas pressure buildup inside the bubble at a rate fast enough to allow completion of the collapse before the start of the

next negative acoustic pressure cycle, collapse of such a bubble is possible.

Besides the transfer of energy at the resonance frequency, there exists additional transfer mechanisms if the applied frequency of the acoustic system differs from the resonance frequency.[44] The actions of these two frequencies and harmonics of both could induce instabilities that would cause the radius to reach sufficient size for a cavitation collapse.

There exists also for a given acoustic frequency and ambient pressure a range in size of bubble nuclei that will permit cavitation with "transient" bubbles, i.e., growth and collapse in one acoustic cycle, with the lower limit of bubble radius that minimum threshold radius from which "nuclei" may be raised by the acoustic field to a cavitation condition, and the upper limit the resonance radius for the acoustic frequency. At a radius less than the above minimum radius, the changes in the bubble radius under the applied acoustic field are very small; but nevertheless, the bubble would grow and shrink in phase with the field. There would be no "cavitation," i.e., violent collapse, however. If the nuclei radii were equal to or very slightly greater than that for resonance, then the bubbles would not complete a cavitation collapse in one acoustic cycle. However, again they would grow and shrink somewhat, pulsating in phase with the acoustic field, with an increasing amplitude until collapse would become possible.

The possible radius range for transient-type cavitation at a given acoustic pressure is narrowed as the frequency increases, with the limiting frequency being reached when the maximum radius which will allow collapse in one acoustic cycle is lowered to coincide with that of the minimum nuclei radius from which cavitation can be generated by the given acoustic field.

Figure 2 is constructed for a fixed frequency and ambient pressure and also considers that $R_{nucleus}$ is less than the resonance radius for the applied frequency. If $R_{nucleus}$ was equal to or greater than the resonance radius, then the bubble would not grow and collapse as a transient bubble, but would undergo complex oscillations about $R_{nucleus}$ in phase with the acoustic field or its subharmonics. Curve no. 1 shows an ideal transient collapse which is completed in one acoustic cycle, the maximum Relative Radius being a function of the acoustic pressure. Curve no. 2 shows the condition where the acoustic negative pressure is insufficient to expand the nucleus to a radius where its collapse energy is sufficient to overcome the gas pressure buildup in the bubble. The bubble will pulsate in the acoustic field as a stable bubble, but will not increase in radius as a resonant bubble would. Curve no. 3 shows conditions where an increase in the acoustic pressure has occurred such that the bubble has been raised to such a large radius that its collapse time is too long to allow its complete collapse before

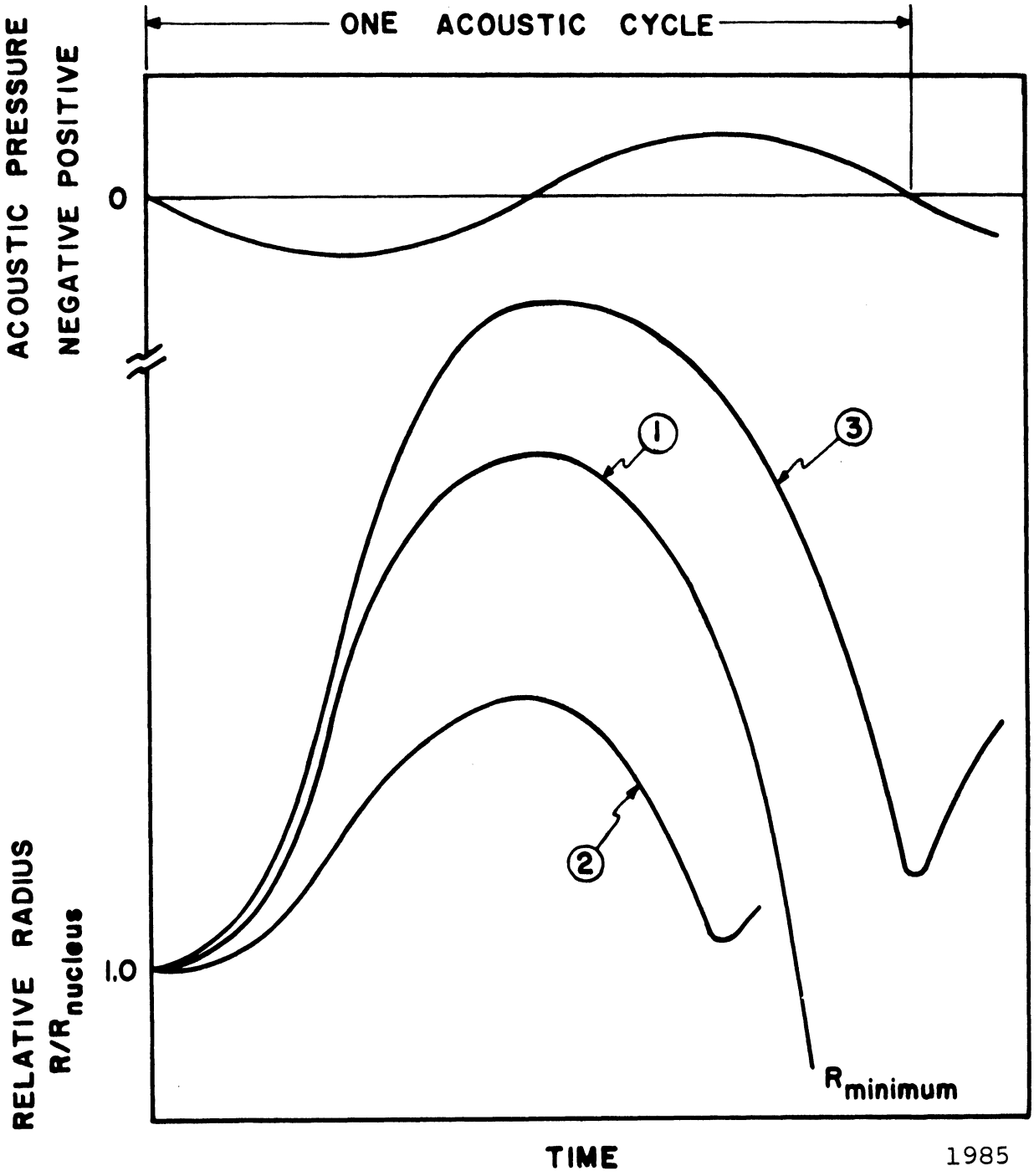

① IDEAL TRANSIENT TYPE COLLAPSE, BUBBLE CAN DISINTEGRATE OR REBOUND AT $R_{minimum}$ (SHAPE SUGGESTED BY FLYNN[44]).

② COLLAPSE SPEED INSUFFICIENT FOR COLLAPSE IN ONE CYCLE.

③ TIME REQUIRED FOR COLLAPSE IS TOO GREAT FOR COLLAPSE IN ONE CYCLE.

Fig. 2.--Theoretical relative radius vs time of an acoustic cavitation cycle.

the start of the next negative pressure part of the cycle. This bubble will also pulsate in the acoustic field, as a stable bubble, but again will not do so with an increasing radius as a resonant bubble would. There are perturbations in acoustic conditions that could occur and result in collapse velocities that would permit cavitation type collapse of either of the two stable bubbles that were previously discussed. Note that the bubble vibrations and the acoustic field are not necessarily in phase,[44] although they are shown in phase in Fig. 2 for simplicity.

The condition of a maximum acoustic pressure for successful cavitation in one cycle as typified by curve no. 3 has been verified experimentally by Sirotyuk.[46]

For typical cavitation frequencies and acoustic pressures, the condition of the water will determine the static equilibrium radius of the bubbles; but the applied acoustic field must be of sufficient pressure to raise these gas bubbles to the status of cavitation bubbles. Flynn[44] reports that freshly drawn tap water that has been standing for several hours contains nuclei that average about 0.0005 cm in radius. Strasberg[47] and others have concluded that microscopic undissolved air cavities are the most likely form of gas nuclei. A bubble that contains some gas is a necessary condition for cavitation under the relatively moderate acoustic pressure for which it is observed. This gas is then available after a bubble collapses to a nucleus for subsequent bubble growth.

Such gas nuclei exist in microscopic or submicroscopic cracks, in solid, unwetted impurities, or on the vessel wall. In acute-angle, non-wetted cracks, gas could exist with the pressure of the trapped gas being less than the partial gas pressure in the liquid because of the effect of surface tension at the interface between the gas and the liquid. Fox and Herzfeld[48] suggested alternatively that the nuclei could be gas bubbles that existed in equilibrium within some form of organic shell.

Bernd[49] interpreted his tests to have experimentally demonstrated the existence of organic surface films about gas nuclei. These films could greatly affect the tensile strength of the water.

Sette and Wanderlingh[50] experimentally verified that an important mechanism in the maintenance of a stable nuclei population was, at least in their experiment, the action of cosmic rays on the liquid.

Harvey[51] et al and later Knapp[52] showed by exposing water to extreme pressure and then failing to get cavitation without unusually high negative pressures, that some form of gas nuclei was responsible for the existence of cavitation as it ordinarily occurs.

When a bubble collapses under the action of positive pressure, the collapse starts slowly, but, in the final stages, the imploding walls attain a very high velocity. A collapsing bubble containing gas and/or vapor collapses to some minimum radius where the pressure buildup of the contents

(or centrifugal actions of the torus in an asymmetric toroidal collapse) has balanced the collapse force and liquid inertia, providing the bubble does not disintegrate during the collapse process because of surface instabilities. The minimum radius that is reached for either type of collapse is dependent upon the magnitude of the collapse forces and the amount and make-up of the contents in the bubble. After the arresting process has been completed, the bubble can then, conceivably, either shatter into a few or many smaller bubbles, or rebound as one large bubble. During rebound, the bubble or bubbles could disintegrate through some form of instabilities or expand in one or more acoustic cycles to a radius where a cavitation collapse is again possible.

When the buildup in pressure near the bubble wall (in the gas or adjacent liquid) starts to arrest the bubble collapse, compressional waves will be emitted which conceivably may form a shock wave (i.e., a very sharp pressure and density discontinuity) that would proceed radially outward from the bubble at approximately sonic velocity. Hickling and Plesset[26] and Ivany[20] found that the rebounding bubble generated a sufficient pressure in the liquid to provide the observed cavitation pitting within a distance equal to the original bubble radius that existed when the collapse sequence began. However, this was not the case during bubble collapse. Ivany's numerical results for rebound, based on 1/r attenuation which is in approximate agreement with exact numerical

results,[26] showed that the maximum pressure during rebound for a typical bubble in water was approximately 10^3 atmospheres at a distance equal to the original radius. Both of these investigations assumed that the bubble remained spherically symmetrical during collapse and rebound.

An acoustic cavitation bubble field consists of transient bubbles that grow and collapse in one acoustic cycle, resonant and stable bubbles that exist for more than one cycle, and bubbles that have rebounded from a cavitation collapse and could be in any of the foregoing classes. The rebounding bubbles often grow immensely during one or two cycles after the rebound. This apparent rapid growth could be aided by the coalescence of smaller bubbles generated by the collapse or rebound forces. The rebounding bubbles most often appear to rebound to radii greater than the mean resonance radius for the applied frequency. Willard[28] mentions a phase of the cavitation cycle where a large bubble vibrated with immensely increasing amplitude. No final collapse was noted.

That a nucleus under the influence of acoustic pressure can grow by a net gain of gas by a "rectified diffusion" process has been shown by Hsieh and Plesset.[53] When the bubble is in the positive part of the acoustic pressure cycle and the gas in the bubble is compressed above the ambient liquid pressure, the concentration of the dissolved gas in the liquid surrounding the bubble is less than the saturation value for this higher pressure so that there will

be a net outflow of gas from the bubble to the liquid. Conversely, during the part of the cycle when the gas pressure in the bubble is less than the surrounding liquid pressure, gas flows into the bubble from the liquid. Because of the larger surface area in this latter condition there will be a net flow of gas into the bubble. However, a bubble requires many acoustic cycles for any appreciable increase in radius by this mechanism. This is illustrated by a numerical example.[52] If the mean ambient pressure is one atmosphere and the difference between the maximum and the average pressure of the gas in the bubble is 0.25 atmospheres, then it would take $1.1X10^6$ seconds for a bubble of radius 0.1 cm to double in size. Even if the 0.25 atmosphere differential was increased 100-fold, it would still take $\sim$ 20,000 cycles for a bubble to double in size by this mechanism. Thus in the terms of high speed photographic observations in the present study, rectified diffusion effects are negligible. However, this may be an important mechanism in raising nuclei initially below the cavitation threshold to a size where they become cavitating bubbles.

The actual damaging mechanism from a collapsing bubble has been the subject of considerable conjecture and still is not entirely understood. An interesting recent study by Sirotyuk[46] from a viewpoint not previously explored has shown that for a fixed acoustic frequency both the cavitation damage as measured by weight loss and the cavitation intensity as

measured by the intensity of luminescence increase together as the maximum radii of the bubbles are increased by increasing the acoustic pressure.

Using the time for complete collapse of a spherical bubble, as determined by Rayleigh,[18] Sirotyuk[46] found that the maximum cavitation damage occurred when the Rayleigh collapse time for the maximum size bubble which could collapse within a cycle was equal to half of the period of the acoustic cycle. The damage declined for higher acoustic pressures where the collapse time of the larger maximum bubble so generated exceeded a half acoustic period.

The larger the ratio of the maximimum bubble radius before collapse to the radius of the original nucleus, the more violent the collapse as shown by Rayleigh's[18] original analysis for an ideal fluid. Numerical calculations,[20,26] assuming real fluid properties, emphasize the extremely rapid buildup in pressure as the collapse proceeds towards zero volume. Thus the further the collapse proceeds, the more violent the pressure pulse or micro-jet velocity resulting from the toroidal collapse.

Noltingk and Neppiras[41,42] and Flynn[44] have shown that for a given acoustic pressure and a given frequency, those nuclei that are just larger than the threshold radius will have the highest ratio of expansion, defined as the maximum radius to the radius of the nucleus. Therefore, the smallest possible nuclei above the threshold radius are the

most damaging. The damaging potential is greatest when these nuclei are raised to the maximum possible radius to which bubbles can be expanded and yet still be collapsed within one acoustic cycle.

CHAPTER III

THE SPECIMENS, EQUIPMENT, AND PROCEDURES

A. The Vibratory System

The ultrasonic trandsucer system used in this laboratory was developed, constructed, and originally used by Garcia.[7,8,9] Fig. 1 shows the design of the exponential horn and the ultrasonic transducer assembly. The normal position of the horn for cavitation damage studies is vertical with the specimen attached to the bottom as shown. For convenient photography, the horn can be tilted to various angles from the vertical.

The remaining parts of the system include an audio-oscillator, a power amplifier, an oscilloscope, a frequency counter, an accelerometer, and a container for the liquid that is to be cavitated. The signal supplied by the variable frequency audio-oscillator is amplified and applied to the piezoelectric crystals. The standing waves that are generated are amplified by the exponential shape of the horn. The vibrations of the specimen end of the horn generates the acoustic field in the liquid. This results in the cavitation bubble field on the specimen surface.

B. The Specimens

The design of the two types of specimens used are shown in Fig. 3. A total of 8 specimens of different materials was used. It was important that the material used for the actual cavitation damage tests and that used for the measurement of mechanical properties of the material be the same. Hence, if a material was machinable, the entire specimen for damage testing and the test specimen for mechanical property testing were made from the same piece of bar stock. When machinability posed a problem, or the precise material desired was only available in sheet stock, discs from the material used for mechanical property tests were soldered to a brass adaptor.

With the exception of Plexiglas, where extremely low density made it unfeasible, all of the specimens were designed to weigh 9.4 ± .1 grams so as to achieve proper resonance with the horn.

A tight mechanical bond between the specimens and the ultrasonic horn is absolutely essential for suitable vibration of the specimen. A special wrench was fabricated to seat and remove the specimens without damaging them in any way.

The specimens were metallographically polished before exposure. One specimen was lightly abrased with emery cloth and was used to examine by photographic means the effects of minor surface roughness. Also, half the polished surface of one specimen was lightly abrased to test the effect of such a surface on the cavitation bubble field.

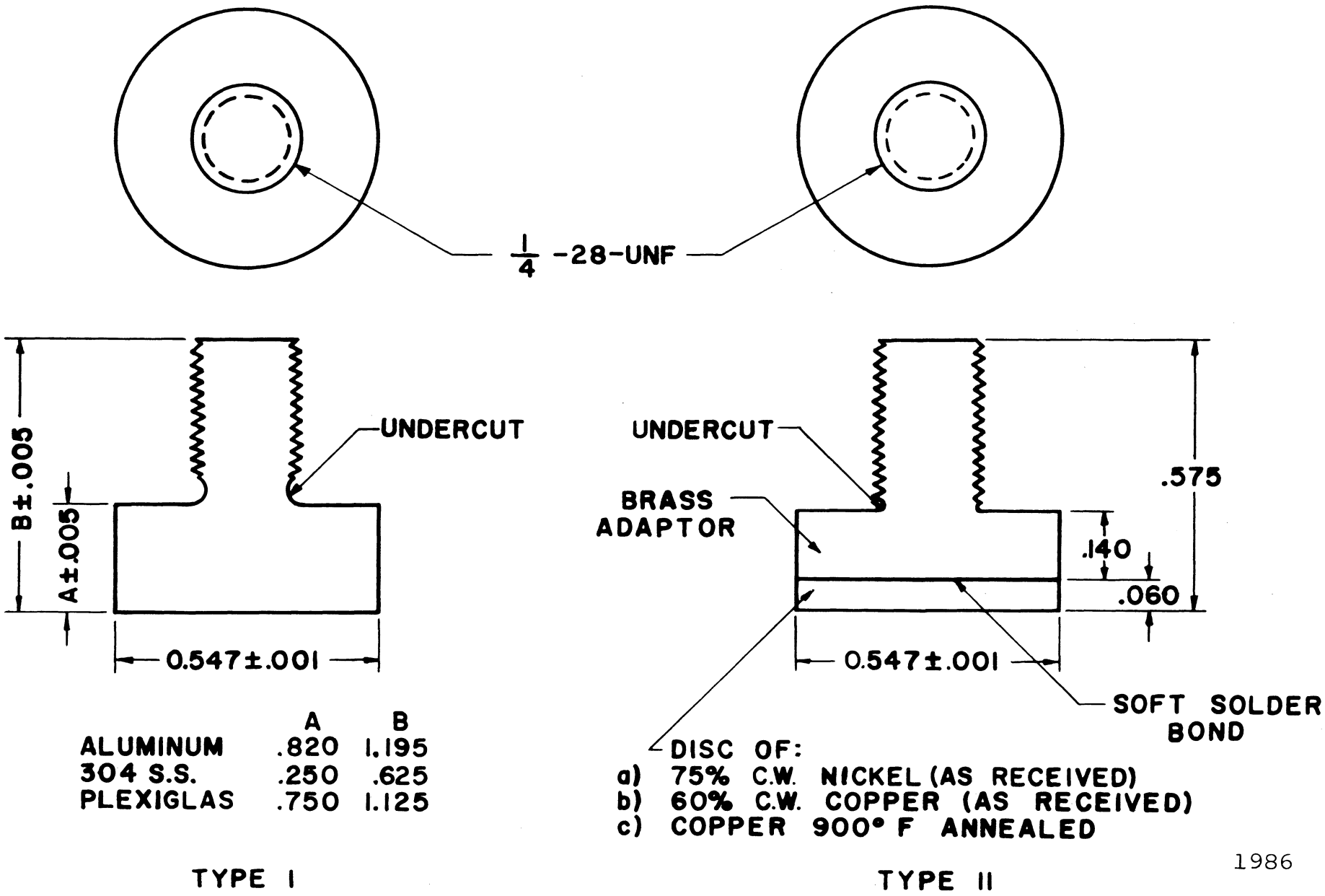

Fig. 3.--Details of specimens

C. Special Specimen Attachment

Fig. 4 shows the design of the specimen attachment used to expose thin foils to cavitation. Its overall weight was made the same as that of the standard specimen to assure horn resonance at the usual operating frequency.

The foil to be exposed was stretched over the stainless steel mandrel, and then was held securely in place by the cover which was screwed into position.

The slot in the mandrel permitted part of the foil to be unsupported so the damage resulting from cavitation exposure could be noted on both sides of the foils.

Using the special attachment, foils were exposed with an indicated amplitude of 0.5 mils which produced only a minor amount of cavitation. Exposure per foil was approximately 30 seconds.

D. Use of the Metallograph

A Bausch and Lomb metallograph with a Polaroid camera attachment was used for studies of the surfaces of the specimens before and after exposure to cavitation. The metallograph was also used to obtain photomicrographs that were used for pit counting of selected damaged areas, and also for photomicrographing of interesting individual pits.

A type 2024-T351 aluminum specimen was completely mapped at 53X before and after exposure using 78 individual photomicrographs for each mapping. The remaining seven

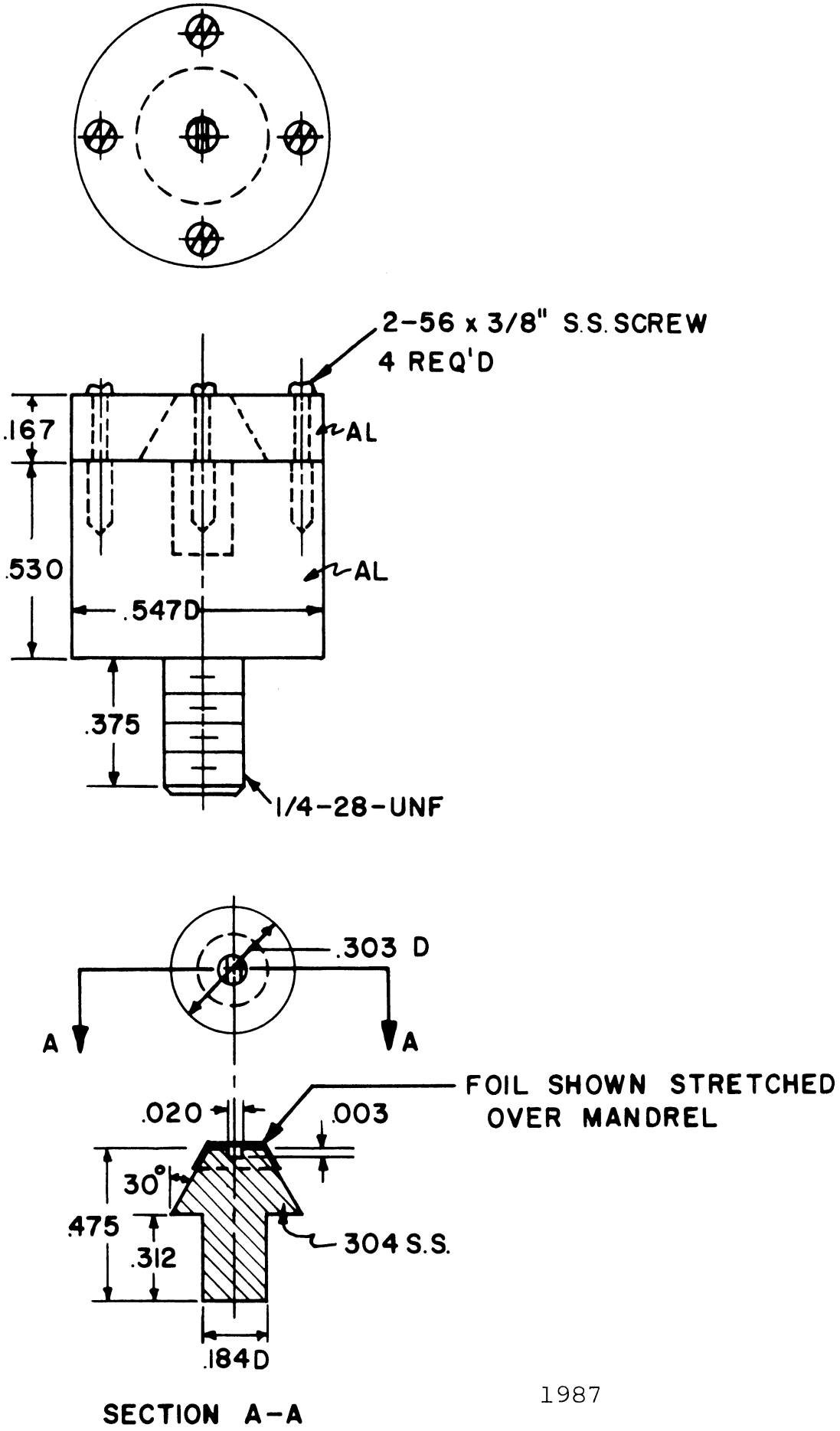

Fig. 4.--Special attachment for exposing thin foils to cavitation.

specimens were scribed with a chord near the diameter to assist in assembling of the individual photomicrographs. A symmetrical photomicrographic sweep was made around the scribe at 53X and 24 individual photomicrographs were assembled for each mapping.

E. Weighing

The individual specimens were weighed twice before and after exposure on a precision Mettler balance and the respective averages were used. The Mettler balance is accurate to 0.01 mg.

F. Counting of Pits

The counting and classification of the pits into various size ranges was done using a microscope following the standards previously developed for the venturi tests in this laboratory.[10]

G. Profiles of Pits

The profiles of the pits were traced with a Bendix Corporation Linear Proficorder using a horizontal sensitivity of 500:1 for all 8 specimens and a vertical sensitivity of 25,000:1 for all specimens but Plexiglas, where 10,000:1 was used.

A number of traces were run over the damaged specimens in areas where microscopic examination indicated lack of multiple pitting. The diamond tipped stylus which indicates

the profile, leaves a visible trace which is of great assistance when matching the traces with photomicrographs. This was possible for all specimens but Plexiglas.

A large number of traces were made to provide data for the depth to diameter ratio of well defined individual pits.

H. High Speed Photography

1. Equipment and Techniques

Because of the short duration of the acoustic cycle which ran from 50 to 160 μseconds, and because of the extremely short formation and collapse times of the cavitation bubbles, it is mandatory that high speed photography techniques be employed.

While it was desirable to have a camera with a capability of up to 1,000,000 frames per second with a sufficient total number of frames to record such short duration events as the expansion and collapse of a bubble, only cameras with considerably less framing speed were available. For illumination of the subject, extremely powerful light sources are required. Only conventional ones were available, which were used for experiments requiring relatively low intensity light sources. When a more intense light source was required, it was necessary that it be constructed, and this was indeed accomplished.

Two high speed cameras were used. A Wollensak Optical Co. Fastax Model WF 1, was used where a large field of view and a relatively long time coverage was important. A Beckman and Whitley Model 326 Dynafax was used where a high framing rate and low exposure time per individual frame were desired and a lesser number of exposed frames per run was tolerable.

In the Fastax the film travels continuously and the rotation of a prism is geared to the film motion. The camera has a rated top speed of 16,000 frames per second. However, the maximum speed actually obtainable was slightly under 13,000 frames per second, and this was near the end of the sequence, since the framing speed for this camera increases throughout its cycle. One hundred foot rolls of Kodak Plus X or Tri X reversal film were used for each run. Development was provided by a commerical processor. The light source used for all Fastax pictures, including both reflective and profile settings, was a Sylvania FF-33 Flood Flash Lamp with a 6 inch parabolic reflector.

The Beckman and Whitley Dynafax camera has a rotating film drum and a rotating octagonal mirror. It will expose a maximum of 224 frames at a maximum framing rate of 26,000 per second. By adjusting the diamond light stops a minimum exposure time per frame of 1 μ second at 26,000 frames per second can be obtained. At this framing rate, the time between corresponding points of successive frames is 38.5 μ seconds. Kemlite xenon electronic flash tubes were used for the light

sources. The camera used 35 mm Kodak Plus X or Tri X film. Development was done by the author using Kodak or Acufine developers.

Both cameras operated with the shutter open. Thus duration of the light blast controlled the number of frames for the Beckman and Whitley Dynafax Camera. For the Fastax the light blast was initiated by the camera controls and exposure was terminated by the run off of the film.

Fig. 5 shows a schematic of the arrangement for high speed photography. Light was not a problem for the profile shots with the Beckman and Whitley Dynafax camera even when it passed through a considerable length of water. Thus an ordinary commercial photographer's xenon electronic flash tube was used for early work. The light blast was of short duration so that only 40 of the available 224 frames were exposed at 26,000 frames per second.

When photographing the specimen surface where the light must be reflected from the specimen (because of light loss in both the glass and the water of the container), it was necessary to build a more powerful light source and also to use 1-1/2" of lens extensions so that the subject could be focused at a position that was closer to the camera, again reducing light loss.

A 1,000 joule light source was constructed for this study in the Electronic Shop of the Phoenix Memorial Laboratory of this University. It used a Kemlight xenon electronic

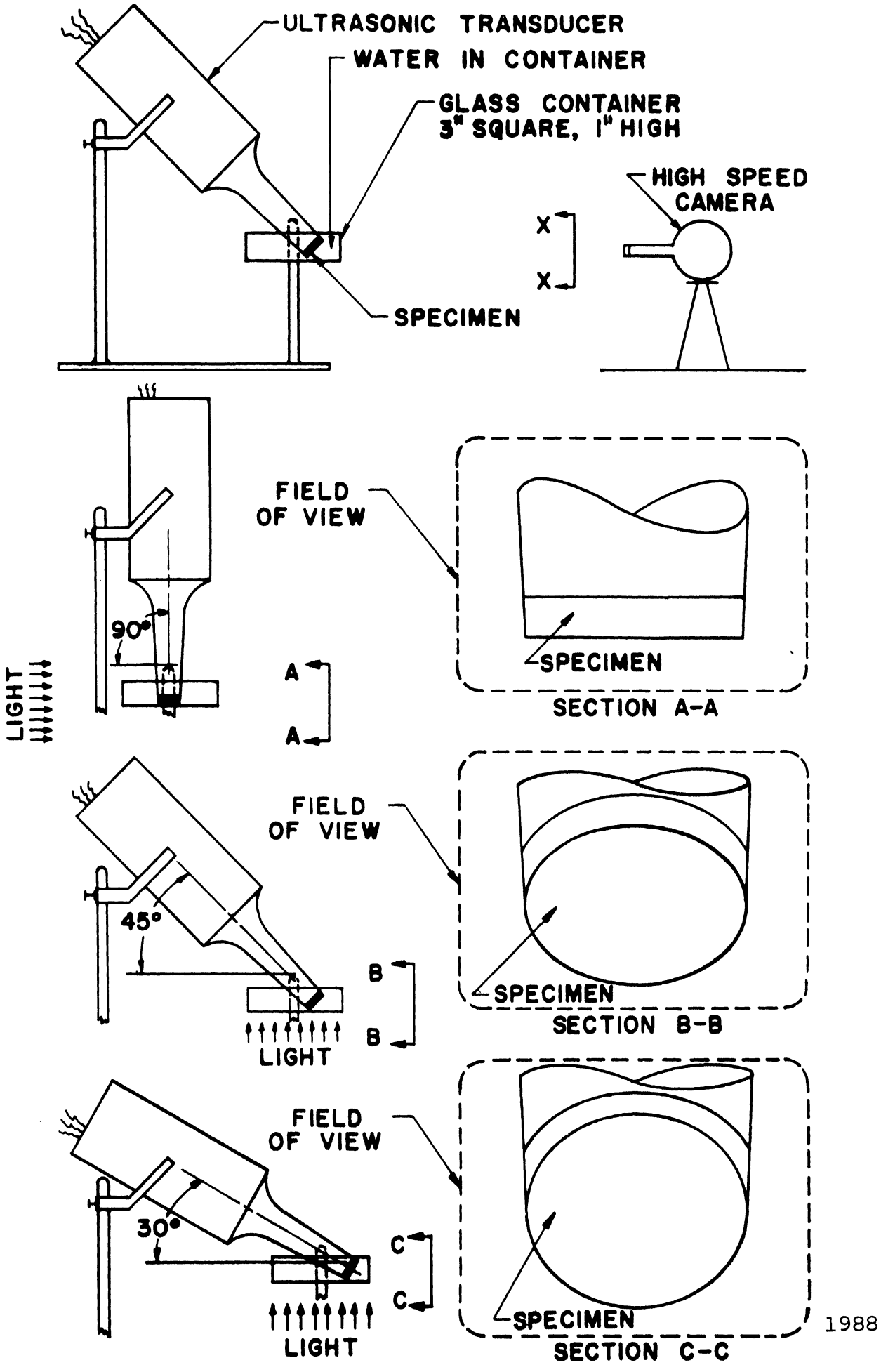

Fig. 5.--Schematic of camera arrangement for high speed photography of the cavitation bubble field on the specimens.

flash tube and was designed to give controlled bursts of light with rapid, variable-time shut-offs, the bursts being less than the camera exposure time for the particular framing speed. Capacitors were used to accumulate a charge, which was then discharged through an artificial delay line and terminated rapidly through an internal electronic flash tube.

Because of the lens extensions the modified optical system has an extremely small depth of field which made focusing quite difficult.

The negative from the Beckman and Whitley Dynafax camera was approximately one-half actual size. Up to 75X enlargements of the negative were made (see Figs. 34-A and B) before grain size limitations were reached. Kodak Polycontrast Rapid printing paper with Kodak printing solutions were used for the enlargements. Extensive use of filters was required in many cases because of poorly contrasted negatives.

2. Determination of Amplitude

The Beckman and Whitley Dynafax camera was used successfully to determine the total amplitude of the horn by photographic means. A profile photographic arrangement was used (Fig. 5). A fixed reference block was attached to the bottom of the water container. The over-all maximum and minimum distance as shown in Fig. 48 of Chapter IV, Section F, was used to determine the total amplitude. A large number of pictures were taken so that the extreme positions of the horn would be photographed in at least one of the frames.

A similar fixed reference block was used in an effort to fix the horn's vertical position with respect to bubble field conditions at various points of the acoustic cycle. However, very little success was attained in localizing the horn position because the horn motion is so small.

3. Photography of Bubble Fields

For studies involving the effect of variation in the gas content of the water, specimen surface roughness, horn amplitude, and frequency, the Fastax camera was more suitable with its larger number of frames to show gross changes in the cavitation bubble cloud. Because of lower lighting requirements with this camera, even sufficient reflective lighting was not difficult to obtain.

Using reflective lighting and the Beckman and Whitley Dynafax camera, the most difficult of the sequences were made. These were the 30° and 45° horn position sequences (Fig. 5) since the lighting was reflective and passed through water before and after reflection from the specimen surface. These horn positions were used to get sequential pictures of the cavitation bubble field to study its detailed characteristics for the various studies that are explained later.

For these studies a maximum camera speed of 26,000 frames per second was used with the horn frequency set at the following approximate levels: 6,200, 10,000, 18,500, and 20,000 cps. Each of these corresponded to a local maximum in the amplitude vs. frequency curve.

It was noted at the three higher frequencies (the 6,200 cps setting produced little cavitation) that the bubble field pattern was repetitive during the photographic sequence and reproducible during a subsequent sequence. Hence, these patterns were studied extensively.

The oscillator frequency and the camera framing rate were then matched as closely as possible at the major resonance point (approximately 20,200 cps for cold water tests). The actual resonant frequency is a function of the weight of the specimen (which was maintained as constant as possible) and possibly, the material itself to a minor extent. The tightness of the mechanically threaded bond between specimen and horn is also a definite factor. Using a Hewlett-Packard Dymec computing digital indicator, the oscillator frequency was indicated directly, but the camera gave one pulse from a magnetic pick up every 16 frames, so inclusion of this multiple in the computing digital indicator lessens the counting accuracy of the camera by a decade from that of the oscillator, since it records multiples of 10 frames. When matching horn frequency and camera framing rate, it was found that the oscillator frequency remained very constant so that the camera framing rate could be adjusted slowly to the point where a satisfactory match occurred. Then cavitation was initiated and the light source triggered.

By examining two 117 frame sequences from two different runs of the same specimen and experimental set-up, it was

found that the maximum bubble population existed in some of the frames of the sequence in all but one run where apparently the sequence was photographed when only the minimum bubble population of the acoustic cycle existed. Thus it was established that photographing even several milliseconds of a 5 to 15 second cavitation damage run would give a quite reasonable estimate of the total number and type of bubbles generated during the exposure. Several photographic sequences were made for each run for all 8 specimens which were tested, but not all were successful. Some sequences were lost because of technical difficulties in the high speed photographic process, mostly because it was difficult to predict reflectivity of the different specimen surfaces. Also some were so covered with bubbles, that accurate counting was difficult.

As previously mentioned the available cameras did not have sufficient framing rates to investigate the formation and collapse of a single bubble, but the minimum exposure time per frame of 1μ second on the Beckman and Whitley camera was sufficiently short to provide additional information about the bubble lifetime throughout the acoustic cycle, if the camera framing rate could be slightly advanced or slowed over the oscillator frequency. It was decided to increase the camera framing rate approximately 2% over the oscillator frequency. Then, assuming that the bubble pattern reproduced approximately for each cycle, the entire acoustical cycle could be explored and the bubble population distribution obtained.

4. Profile Photography

The Beckman and Whitley Dynafax camera was used to make sequential photographs of the cavitation bubble field and its individual bubbles using profile lighting where the horn was vertical and also when it was tilted approximately two degrees from the vertical with part of the specimen surface in view of the camera. In these positions it was also possible to gain some insight into the nature of the vortices near the edge of the specimens.

CHAPTER IV

EVALUATION OF DATA

A. Exposure of Foils

As previously discussed (Chapter III, Section C), thin foils were exposed to cavitation for very short periods. These were unsupported over a small central portion of the foil and supported by a mandril around the outer radius (Fig. 4). It was hoped that something might be learned of the basic mechanism of cavitation damage through studying the result of shock-wave or jet impact on such thin, unsupported members.

Comparing photomicrographs of the various foils before and after exposure to cavitation in water, it was noted that extensive damage had resulted. The total exposure time for each foil was approximately 30 seconds. Beyond this, the foils were quickly destroyed even with the extremely small intensity (i.e., small amplitude of horn and thus small acoustic pressure) of cavitation that was used for this particular experiment.

Examination of individual pits, as shown on the photomicrographs, shows interesting damage. Fig. 6 is of 1.5 mil gold and shows a wide spectrum of pit diameters with some

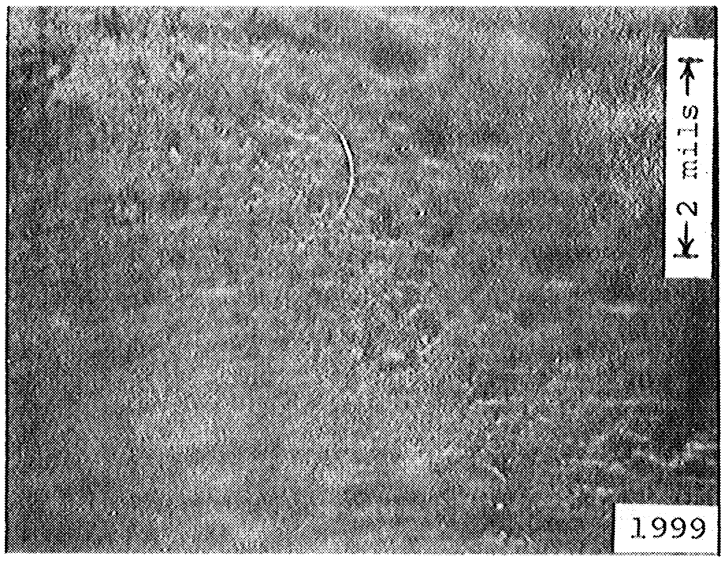

Fig. 6.--Photomicrograph of the exposed side of 1 1/2 mil gold foil (500X) after approximately 30 seconds of exposure to cavitation in water at an amplitude of 1/2 mil and with the oscillator at approximately 20,000 cps.

Fig. 7.--Photomicrograph of the exposed side of 1 1/2 mil gold foil (1800X) after approximately 30 seconds of exposure to cavitation in water at an amplitude of 1/2 mil and with the oscillator at approximately 20,000 cps.

as small as 0.02 mil. The round depression of the large pit in the center of the photograph is clearly evident. The symmetry of this pit clearly implies that it was formed by a single blow, either microjet or shock wave. Fig. 7, also of 1.5 mil gold, shows a pit that appears to be the result of two or more implosions (or rebounds), since it is not a symmetrical crater. It appears to be formed from two individual round craters. It is extremely difficult to focus the metallographic camera over the entire area covered by the foil photomicrographs because of the flexibility of the foil and the difficulty in holding and leveling it.

Fig. 8 shows two large pits on 1.5 mil gold that are characterized by a peculiar swirling appearance with the center part of the crater depressed. These are very unusual. A possible explanation for the shape is that the swirled appearance was caused by high pressures under the torus and the center depression by the micro-jet resulting from the toroidal collapse.

Fig. 9 shows the piercing and shattering that is characteristic of spallation-type damage which occurred on the unexposed side of the gold specimen in the area behind the pits shown in Fig. 8, but there is no exact match as to position. Despite this lack of position match, the presence of such spallation damage on the unexposed side of the foil strongly supports the hypothesis of a very transient and intense localized loading imposed either by impinging shock waves or micro-jets.

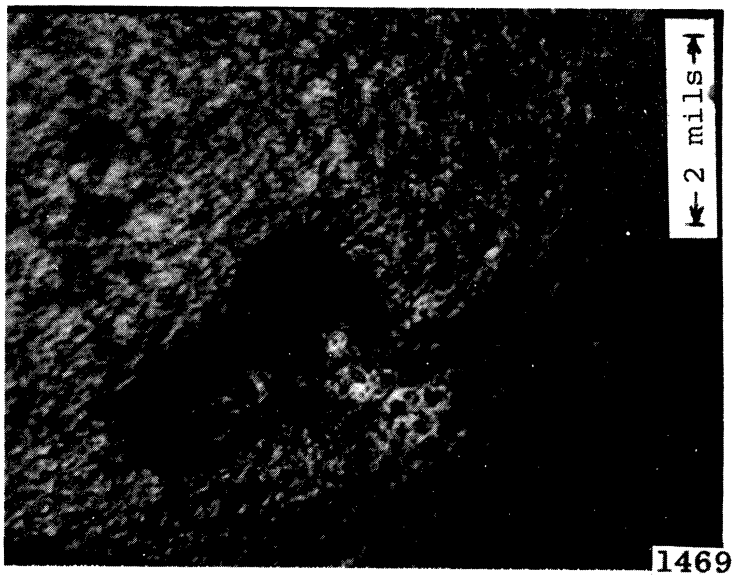

Fig. 8.--Photomicrograph of the exposed side of 1 1/2 mil gold foil (485X) after approximately 30 seconds of exposure to cavitation in water at an amplitude of 1/2 mil and with the oscillator at approximately 20,000 cps.

Fig. 9.--Photomicrograph of the unexposed side of 1 1/2 mil gold foil (250X) after approximately 30 seconds of exposure to cavitation in water at an amplitude of 1/2 mil and with the oscillator at approximately 20,000 cps.

Figs. 10 and 11, also of 1.5 mil gold, again show some form of multiple pitting which together form a relatively large pit. Fig. 12 shows general pitting on 1.5 mil gold at a lower magnification. Fig. 13 shows damage on 2 mil brass shim stock which is much harder than the gold. Each of the two connected large pits apparently shows the result of several blows, and are similar to those on gold. Fig. 14 is of 2 mil cadmium. Again the damage, especially the large pit, is similar to that on the gold and the brass. Fig. 15 shows a typical portion of 2 mil aluminum foil with a larger number of very small pits.

Examination of the gold foils shows that the majority of the pits are approximately 0.3 mils in diameter, with some as large as 1 mil and some as small as 0.02 mil. On the aluminum foil the diameters were as small as 0.01 mil.

One would expect that the average pit diameter would be small because the cavitation field that was applied contained mostly small bubbles which had been raised to a small relative radius (R max./R nucleus) because of the low applied amplitude. Thus the collapse energy of the bubbles would be relatively low. Fig. 25, Section B of this Chapter shows a typical cavitation bubble field with the minimum cavitation that can be detected by eye without the aid of a stroboscope. While this cavitation field was photographed at 26,000 frames per second with the oscillator set at 6,200 cps, and the foils were exposed with the oscillator at approximately 20,000

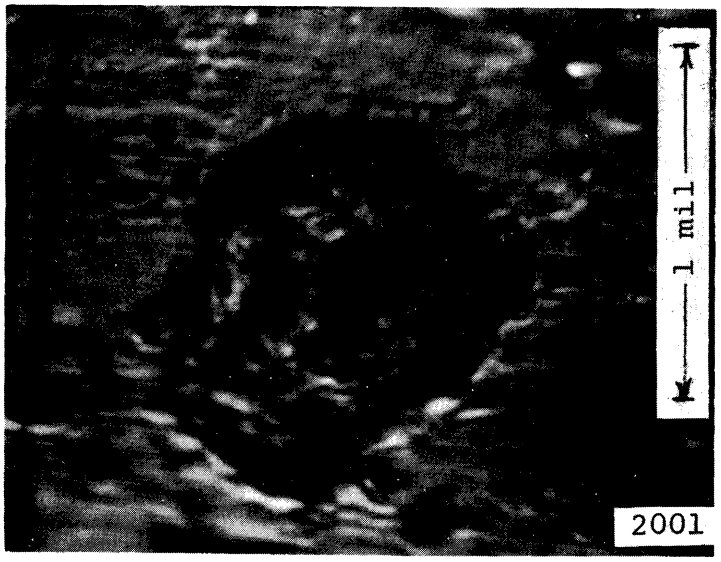

Fig. 10.--Photomicrograph of the exposed side of 1 1/2 mil gold foil (1800X) after approximately 30 seconds of exposure to cavitation in water at an amplitude of 1/2 mil and with the oscillator at approximately 20,000 cps.

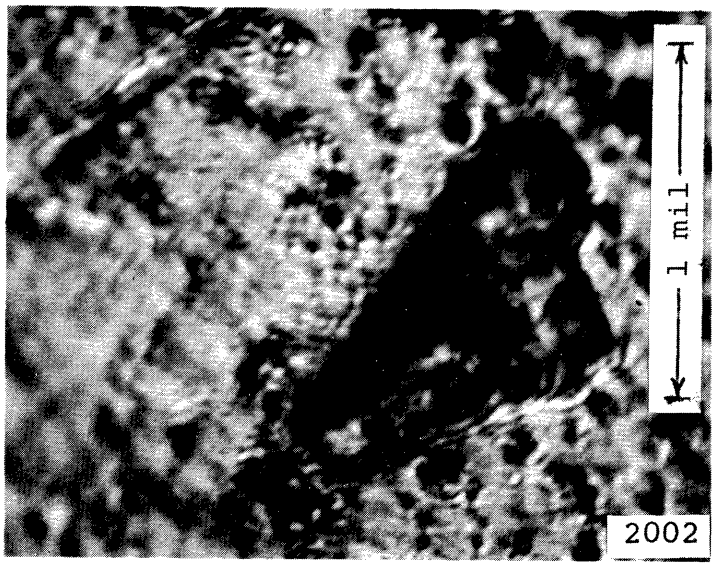

Fig. 11--Photomicrograph of the exposed side of 1 1/2 mil gold foil (1800X) after approximately 30 seconds of exposure to cavitation in water at an amplitude of 1/2 mil and with the oscillator at approximately 20,000 cps.

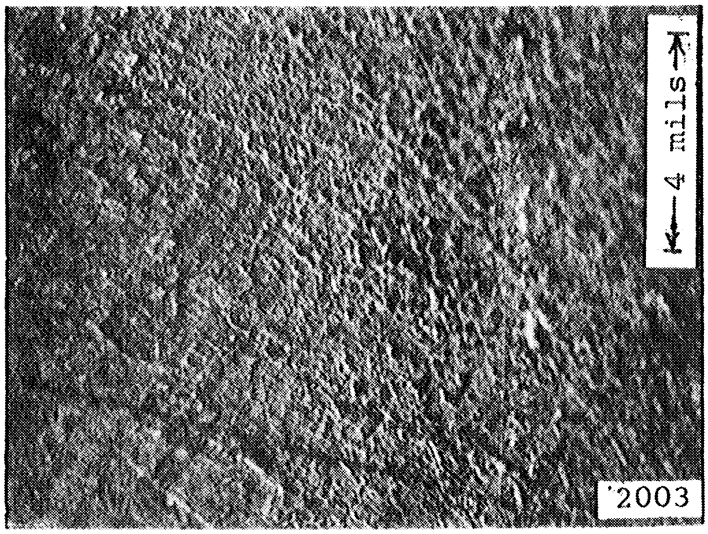

Fig. 12.--Photomicrograph of the exposed side of 1 1/2 mil gold foil (280X) after approximately 30 seconds of exposure to cavitation in water at an amplitude of 1/2 mil and with the oscillator at approximately 20,000 cps.

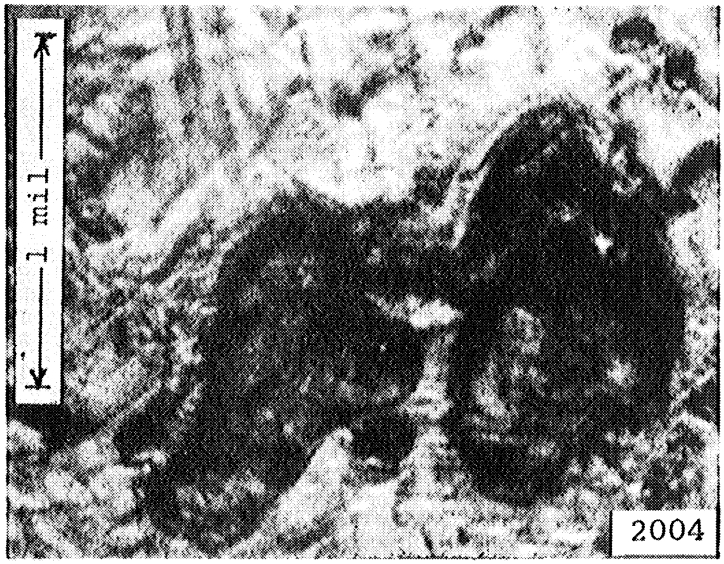

Fig. 13.--Photomicrograph of the exposed side of 2 mil brass shim stock (1800X) after approximately 30 seconds of exposure to cavitation in water at an amplitude of 1/2 mil and with the oscillator at approximately 20,000 cps.

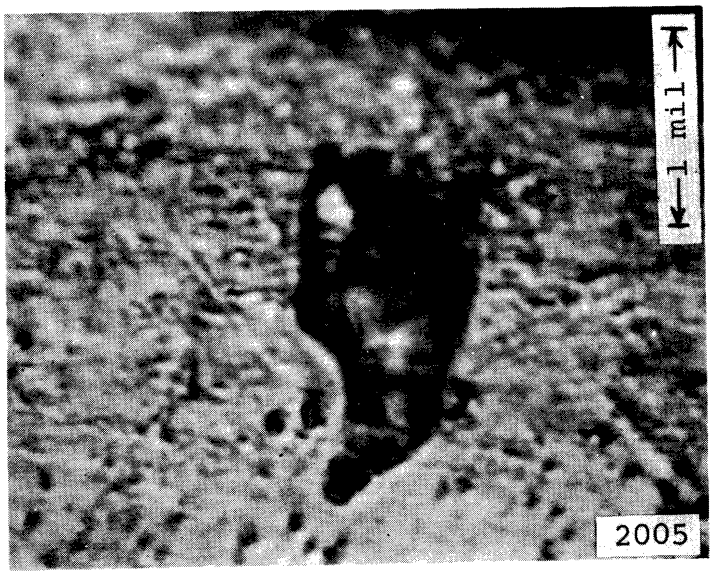

Fig. 14.--Photomicrograph of the exposed side of 2 mil cadmium foil (1000X) after approximately 30 seconds of exposure to cavitation in water at an amplitude of 1/2 mil and with the oscillator at approximately 20,000 cps.

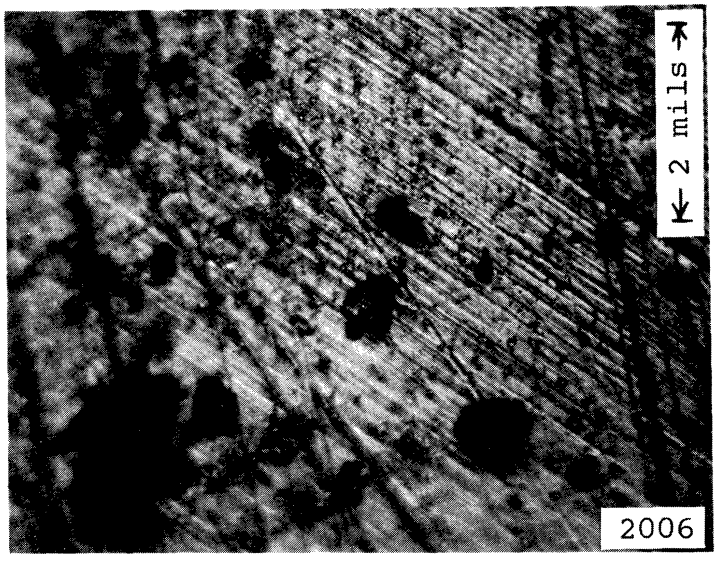

Fig. 15.--Photomicrograph of the exposed side of 2 mil aluminum foil (500X) after approximately 30 seconds of exposure to cavitation in water at an amplitude of 1/2 mil and with the oscillator at approximately 20,000 cps.

cps, the same type of limited cavitation was seen, perhaps because of the reduced rigidity of the foil and its consequent inability to transmit the full horn amplitude, and partly because of the low amplitude of approximately 1/2 mil. The unaided eye could only detect a few bubbles darting about the specimen surface; there was none of the violent hissing and snapping and visually observed full bubble clouds that are so evident at higher amplitudes. Since very soft foils were used, with the exception of brass where relatively few pits were noted, the softness is a factor with respect to the number of the pits. On very soft or malleable materials, apparently the number of bubbles in a cavitation field per number of pits produced is much lower than with harder, stronger materials. No pit count was made on the foils because the bubble cloud was not photographed and it doubtlessly was different from that observed with standard specimens because of the shape of the special attachment (Fig. 4).

It was hoped that the character of the pit damage would give some clue as to the damaging mechanism of the collapsing bubble. The round depressions as typified by the large pit shown in Fig. 6 appear almost as if the impressions were caused by the indenter of a hardness tester. Similar pits have also been observed in the venturi systems used in this laboratory. However, these pits could result from the pressure pulse occurring during bubble collapse or rebound, or from a micro-jet that evolves from a toroidal collapse.

The spallation damage shown in Fig. 9 is typical of that caused when a projectile or a jet impacts a thin material. However, either the impinging shock wave or the micro-jet could cause such damage.

B. Cavitation Conditions: Gas Content of Water; Surface; Amplitude; Water Level; and Oscillation Frequency.

A general study of how the cavitation bubble field would change as the air content of the water was changed was not within the scope of this study. However, there is some indication in the literature of the effects to be expected. Saneyoshi and Okushima[35] have studied and have recorded photographically the effect of using boiled water, air saturated water, and a mixture of both. Photographs of the overall profile of the cavitation cloud show that with boiled water there was relatively little cavitation cloud visible at the minimum population point of the acoustic cycle; more was visible for the mixture; and substantially more for the air saturated water. Ellis[30] noted by using extremely high speed photographic techniques that the bubbles of the cavitation field completely disappeared during one point of each cycle when degassed water was used.

An experiment with partially de-aerated water (approximately 1.60 volume percent) using an applied amplitude of 2 mils and a frequency slightly greater than 20,000 cps, was made to see how a minor variation in the gas content would affect the cavitation bubble field. Figs. 16 and 17 are

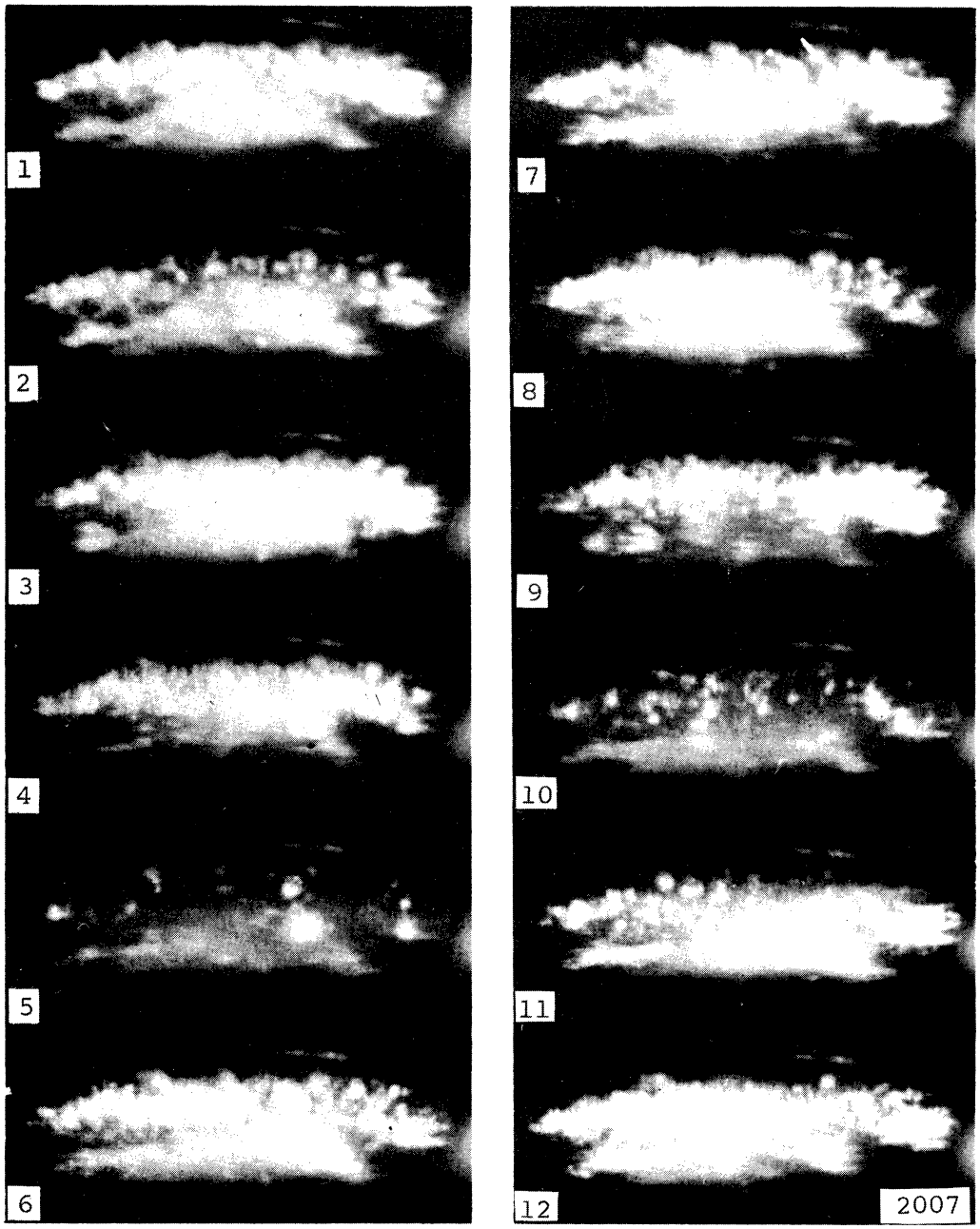

Fig. 16.--High speed photographic sequence (5X), 1 through 12, of a polished type 304 stainless steel specimen in freshly drawn tap water, amplitude of 2 mils, exposure time per frame of 27 μ seconds, time between frames of 79 μ seconds (12,600 fps), frequency 20,200 cps. f-8.0.

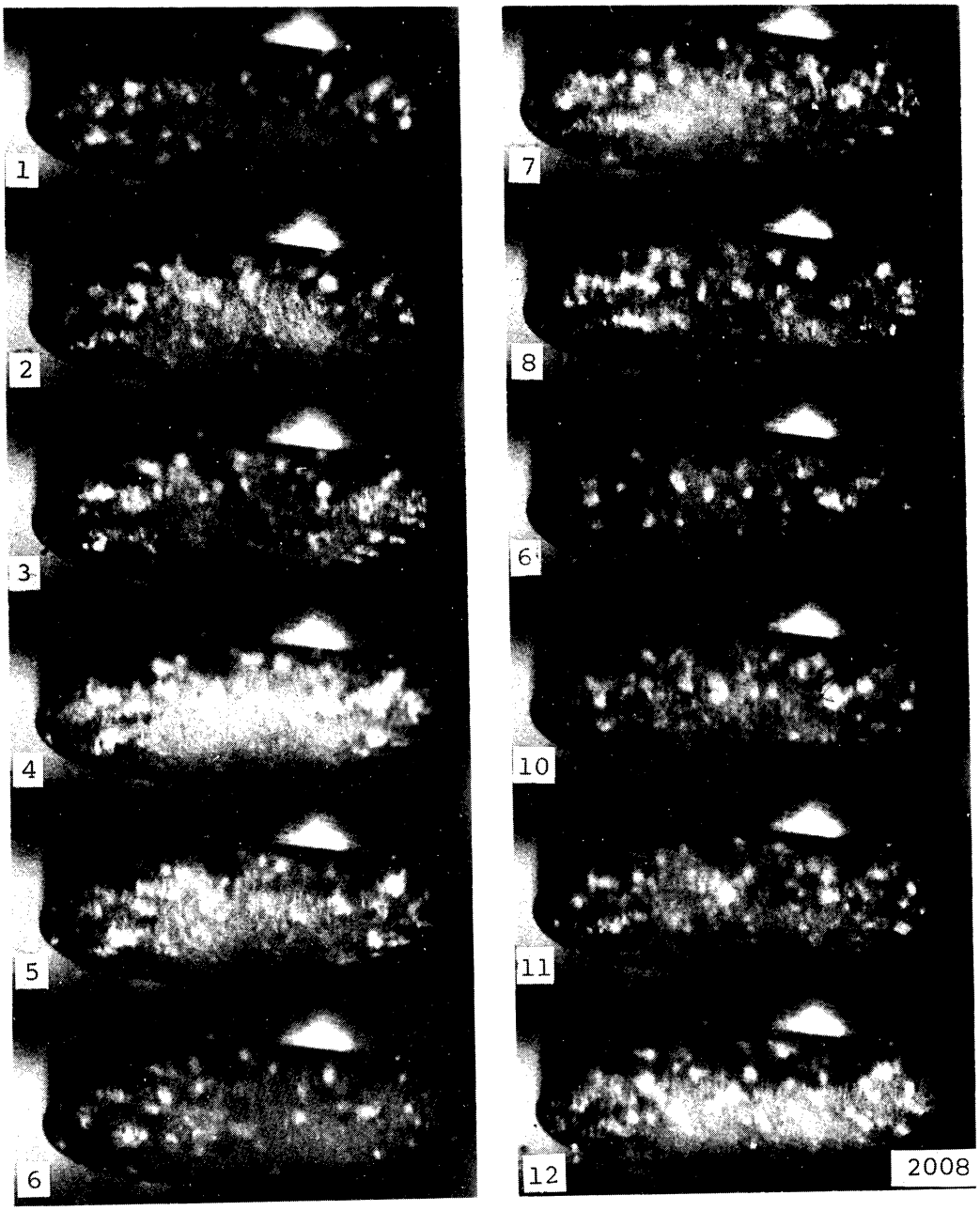

Fig. 17.--High speed photographic sequence (5X), 1 through 12, of a polished type 304 stainless steel specimen in freshly drawn tap water, amplitude of 2 mils, exposure time per frame of 25 μ seconds, time between frames of 75 μ seconds (13,400 fps), frequency 20,200 cps. f-5.6.

sequences from high speed Fastax photographs taken at 12,600 and 13,400 frames per second respectively, and with a time between individual frames of 79 and 75 μseconds. Exposure times per frame were 27 and 25 μseconds respectively. Since the acoustic period was 50 μseconds, the individual photograph was exposed for half or more of the acoustic cycle and thus could have sampled portions of either one or two different cycles. Hence, definition of the individual bubbles that make up the cavitation cloud would be expected to be poor. Both the photographic sequences shown in Figs. 16 and 17 were made using ordinary, freshly drawn tap water, exposing a polished stainless steel specimen, but with 2 different f-stop settings. They thus show the effect of minor variations in photographic settings. Fig. 16 was made using less light than Fig. 17 in which the fringes of the bubble cloud are "washed out" by too much light. The remaining photographs of this section were made using the f-stop which proved to allow too much light for polished surfaces; but sufficient for abrased specimens. As previously mentioned in Chapter III, Section H. 1, development of Fastax film was by a commercial processor and required a considerable time delay. Hence minor lighting corrections often could not be made before several films had been exposed. It was often necessary to guess the correct f-stop setting. Such guesses tended to produce low f-stops because previous experience had been that there was usually insufficient light for proper exposure.

Fig. 18 is similar to Fig. 17 in that a polished stainless steel specimen was used, but exposure was made at a slightly lower framing rate (12,600 frames per second) and partially de-aerated water taken from the venturi loop (~50% STP saturation) was used. Figs. 17 and 18 were sufficiently similar to indicate that minor changes in the gas content of the water would not cause noticeable changes in the bubble field when using a polished specimen.

Figs. 19 and 20 are sequences where freshly drawn tap water and partially de-aerated water are compared. The specimen was type 304 stainless steel with a lightly abrased surface. There is no detectable difference in the bubble clouds, so that it can again be concluded that minor gas content variations do not cause detectable bubble population changes when exposing a lightly abrased specimen. Also, there is no substantial difference between the makeup and the total population when comparing polished and abrased specimens. Because of the relatively low camera speed, definite conclusions on this matter cannot be drawn. Further discussion on the effect of minor surface roughness is presented later in this section for photographs made with a much lower exposure time. For cases where extensive damage has occurred on the specimen, but where a concave surface has not yet been generated (as is the case with very long exposures), Plesset and Devine[34] have shown that a large decrease exists in the number of bubbles compared to an undamaged specimen.

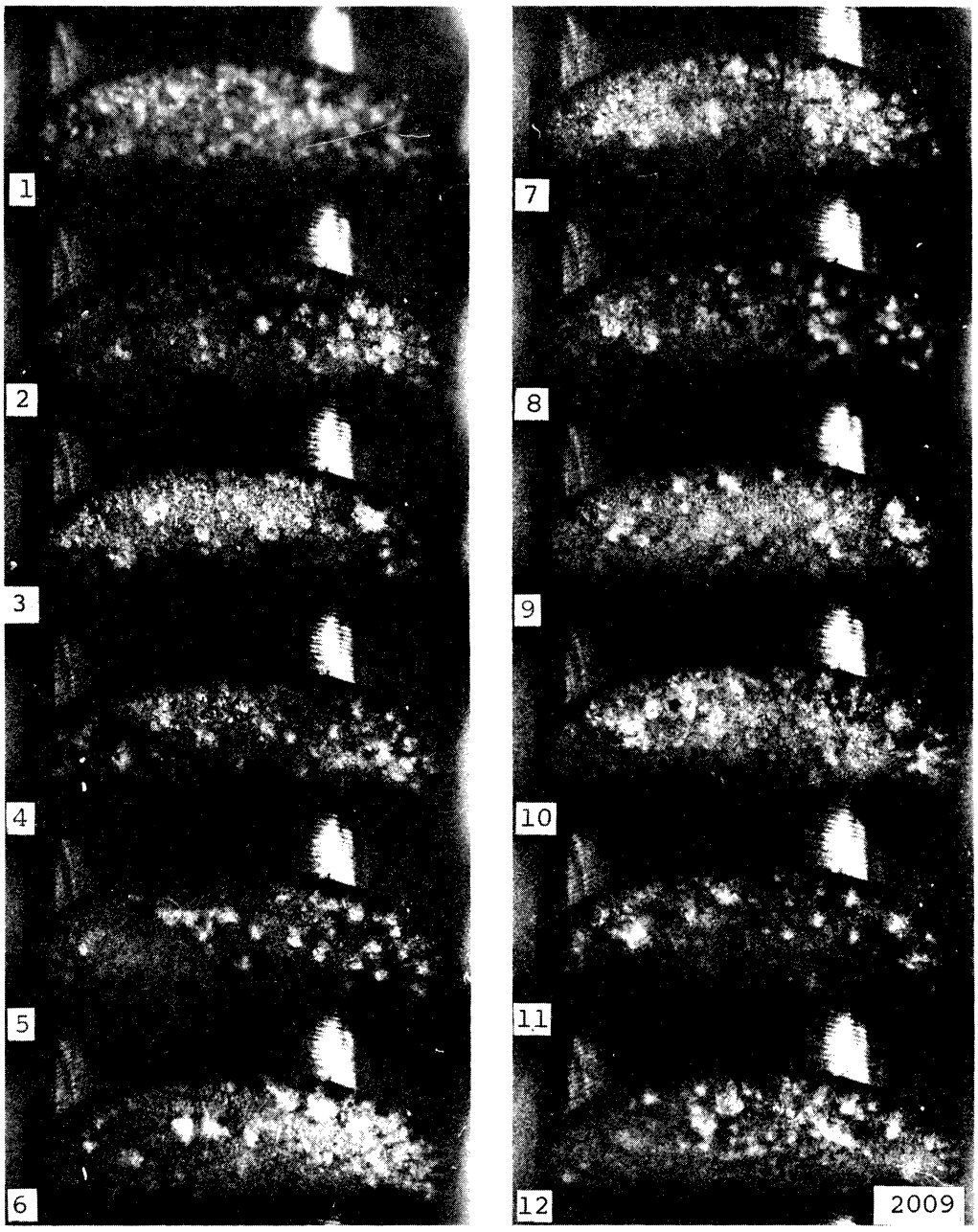

Fig. 18.--High speed photographic sequence (5X), 1 through 12, of a polished type 304 stainless steel specimen in partially de-aerated water (approximately 1.60 vol.%), amplitude of 2 mils, exposure time per frame of 27 μ seconds, time between frames of 79 μ seconds (12,600 fps), frequency 20,200 cps. f-5.6.

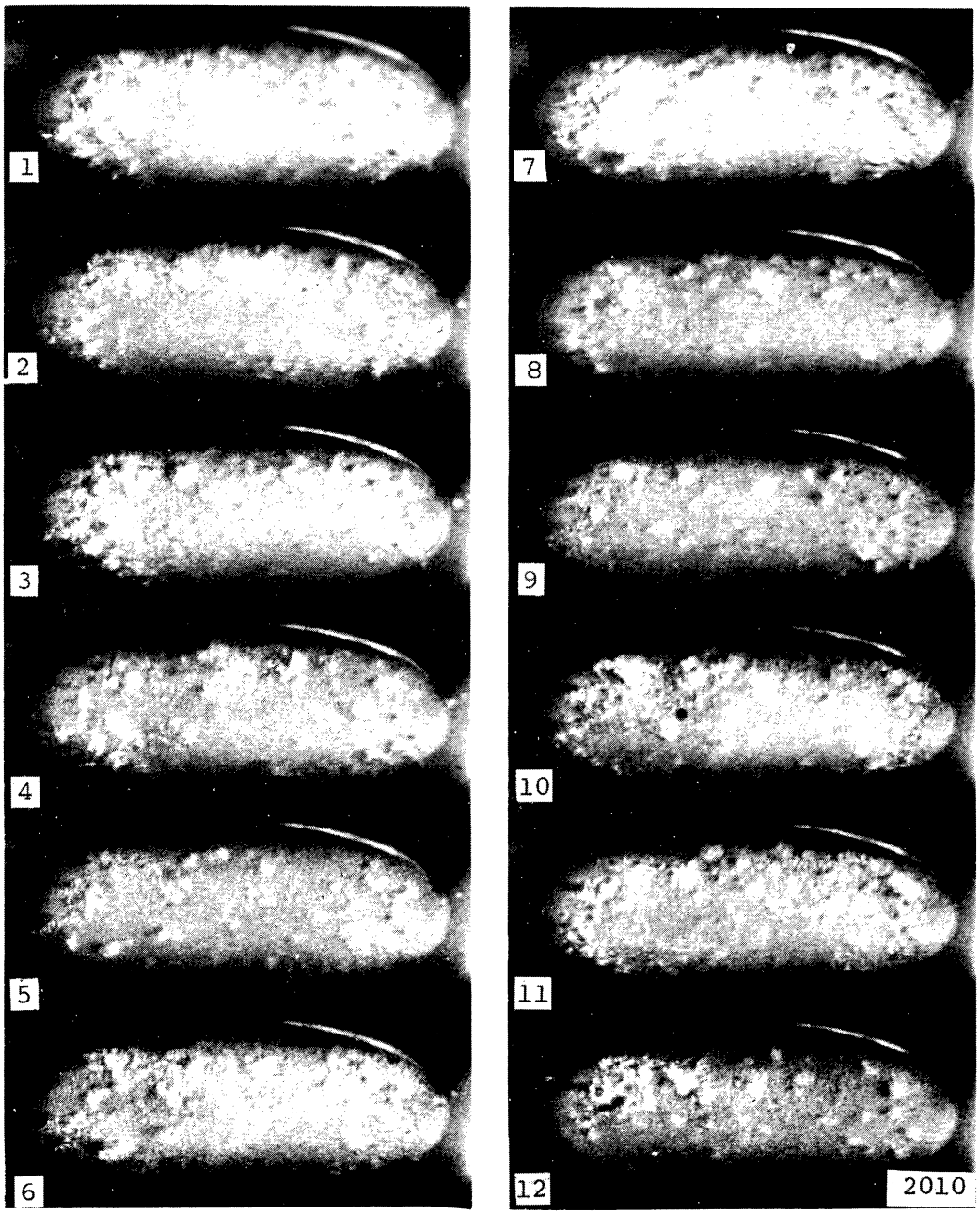

Fig. 19.--High speed photographic sequence (5X), 1 through 12, of a lightly abrased type 304 stainless steel specimen in freshly drawn tap water, amplitude of 2 mils, exposure time per frame of 25 μseconds, time between frames of 76 μseconds, (13,200 fps), frequency 20,200 cps. f-5.6.

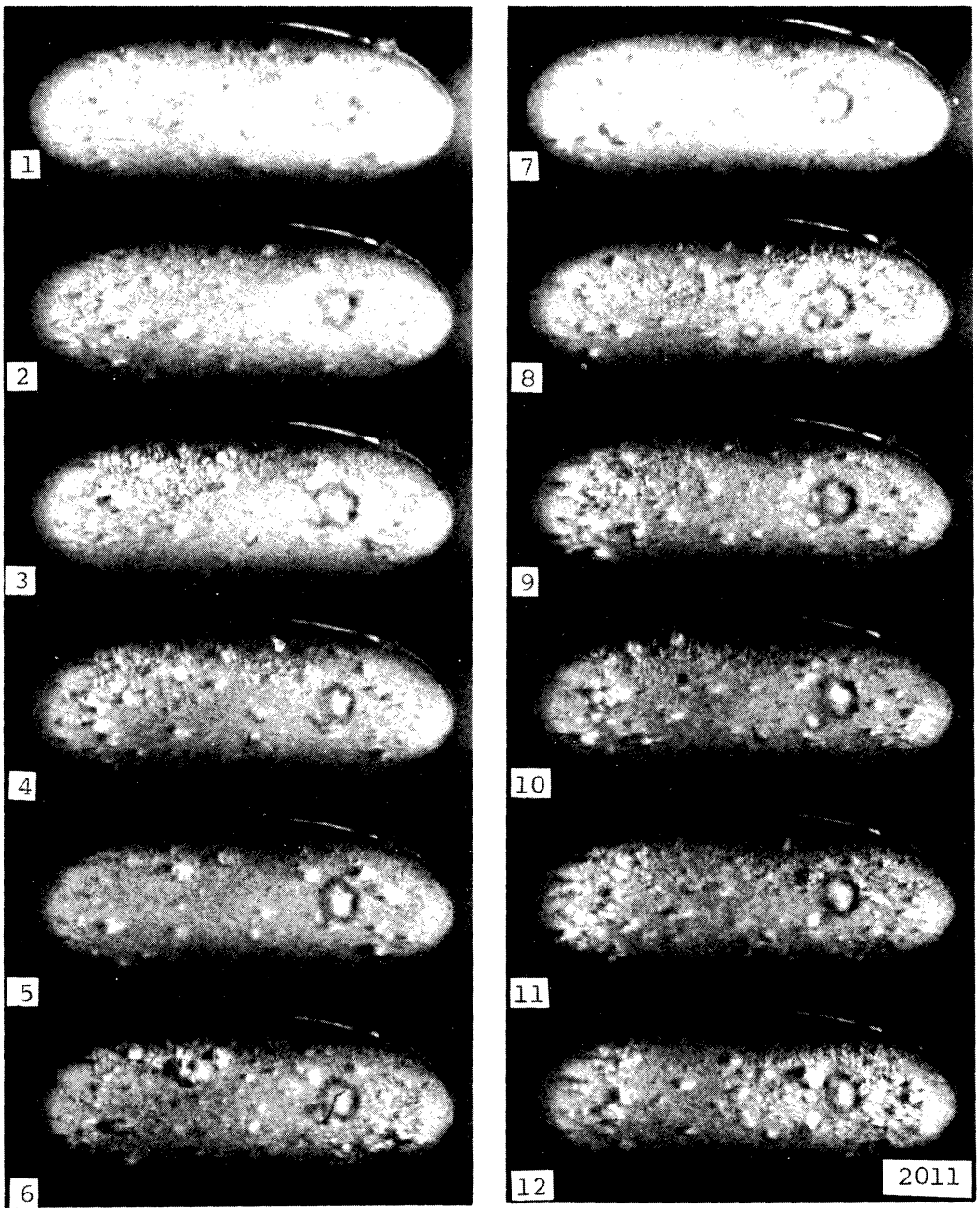

Fig. 20.--High speed photographic sequence (5X), 1 through 12, of a lightly abrased type 304 stainless steel specimen in partially de-aerated water (approximately 1.60 vol.%), amplitude of 2 mils, exposure time per frame of 32 μ seconds, time between frames of 96 μ seconds (10,400 fps), frequency 20,200 cps. f-5.6.

The effect of gross horn amplitude changes was examined in runs using the partially de-aerated water previously described. Runs with a polished specimen were made at amplitudes of 1 mil and 1/2 mil as shown in Figs. 21 and 22, respectively. Comparisons could be made with Fig. 18, which was made at 2 mils amplitude. A drop in bubble population for a decrease in amplitude from 2 mils to 1 mil is apparent. The bubble field is not as full at the lower amplitude. At 1/2 mil as shown on Fig. 22, only slight ring cavitation exists. This can be noticed on the upper left edge of the specimen. The white area at the right is due to reflection. There could be small numbers of cavitation bubbles in this area too, but the light is too intense for their observation. The decrease in bubble population as the applied amplitude decreases is to be expected, because the acoustic pressure also decreases, assuming that other acoustic conditions such as frequency are fixed. As the acoustic pressure decreases, the minimum radius from which cavitation bubbles can be generated increases. Thus a lesser number of bubbles are capable of becoming cavitation bubbles.

Changes in the bubble field due to overall flow pattern variation, perhaps influenced by the proximity of the specimen to the water surface, can be noted by examining photographs of the 75% c. w. nickel (as rec'd) specimen for which three of the four runs were made with the oscillator frequency matched quite closely to the camera framing rate. On the

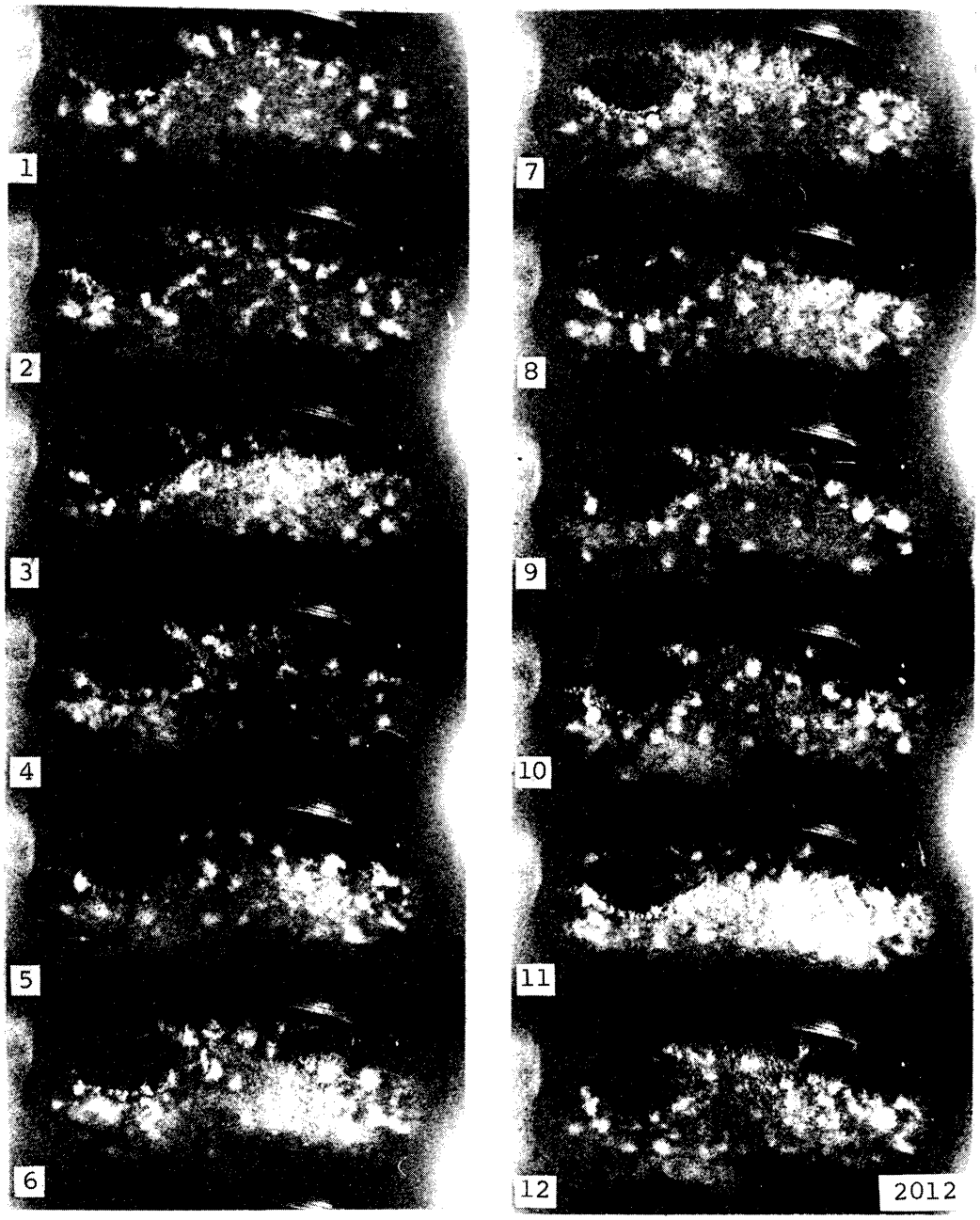

Fig. 21.--High speed photographic sequence (5X), 1 through 12, of a polished type 304 stainless steel specimen in partially de-aerated water (approximately 1.60 vol.%), amplitude of 1 mil, exposure time per frame of 27 μ seconds, time between frames 79 μ seconds (12,600 fps), frequency 20,200 cps. f-5.6.

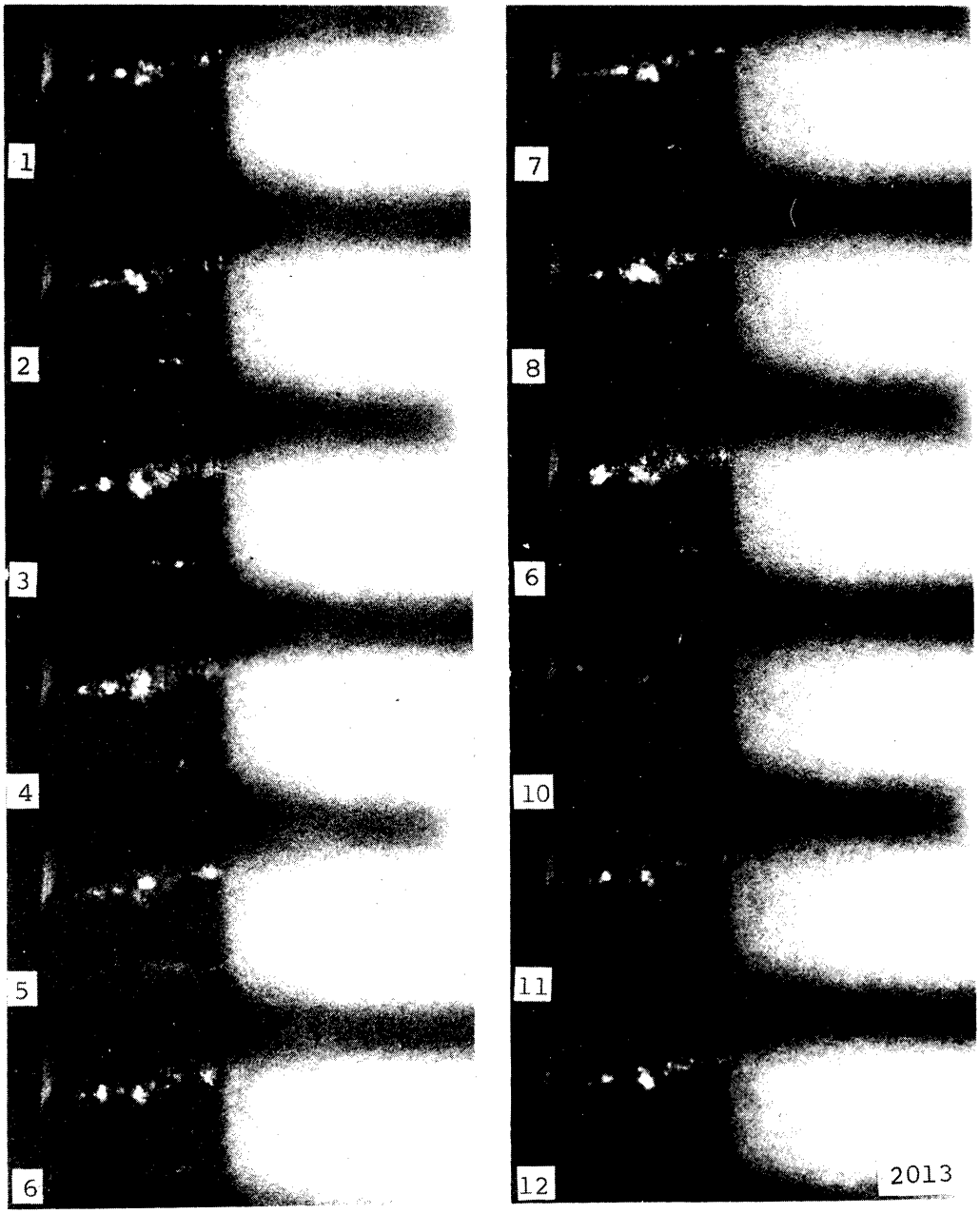

Fig. 22.--High speed photographic sequence (5X), 1 through 12 of a polished type 304 stainless steel specimen in partially de-aerated water (approximately 1.60 vol.%), amplitude of 1/2 mil, exposure time per frame of 34 μseconds, time between frames of 102 μ seconds (9,800 fps), frequency 20,200 cps. f-5.6.

fourth run, the camera speed was set 2% higher than the oscillator frequency so, as previously discussed, the entire acoustic cycle could be explored photographically. Fig. 23 is typical of the first photographic sequence where the run lasted 19 seconds. In this case the match between frequency and framing rate was almost perfect. Thus the bubble field pattern remains almost constant throughout the entire sequence. The scribe mark is visible in this and other photographs, although it shows more clearly in some of the others (e.g. Figs. 24 and 68).

The photographically detectable bubble population varies cyclically with the position in the acoustic cycle. It is not at its maximum point in Fig. 23. The bubble population is low, and the proportion of large diameter bubbles is high. This population change will be further discussed in Section J of this Chapter.

Camera difficulties prevented getting any photographs during the second run with the nickel specimen which was of 9 seconds duration. The photographs for the third run (5 seconds) happen to have been taken in the maximum bubble population portion of the cycle. This is shown in Fig. 68, Section H of this Chapter. Note that the central area at the top of the specimen is free of bubbles. The proximity of the top of the horn to the water surface is believed to cause this pattern. Fig. 24 is for the last run which was for 11 seconds. This photographic sequence of 117 frames had a

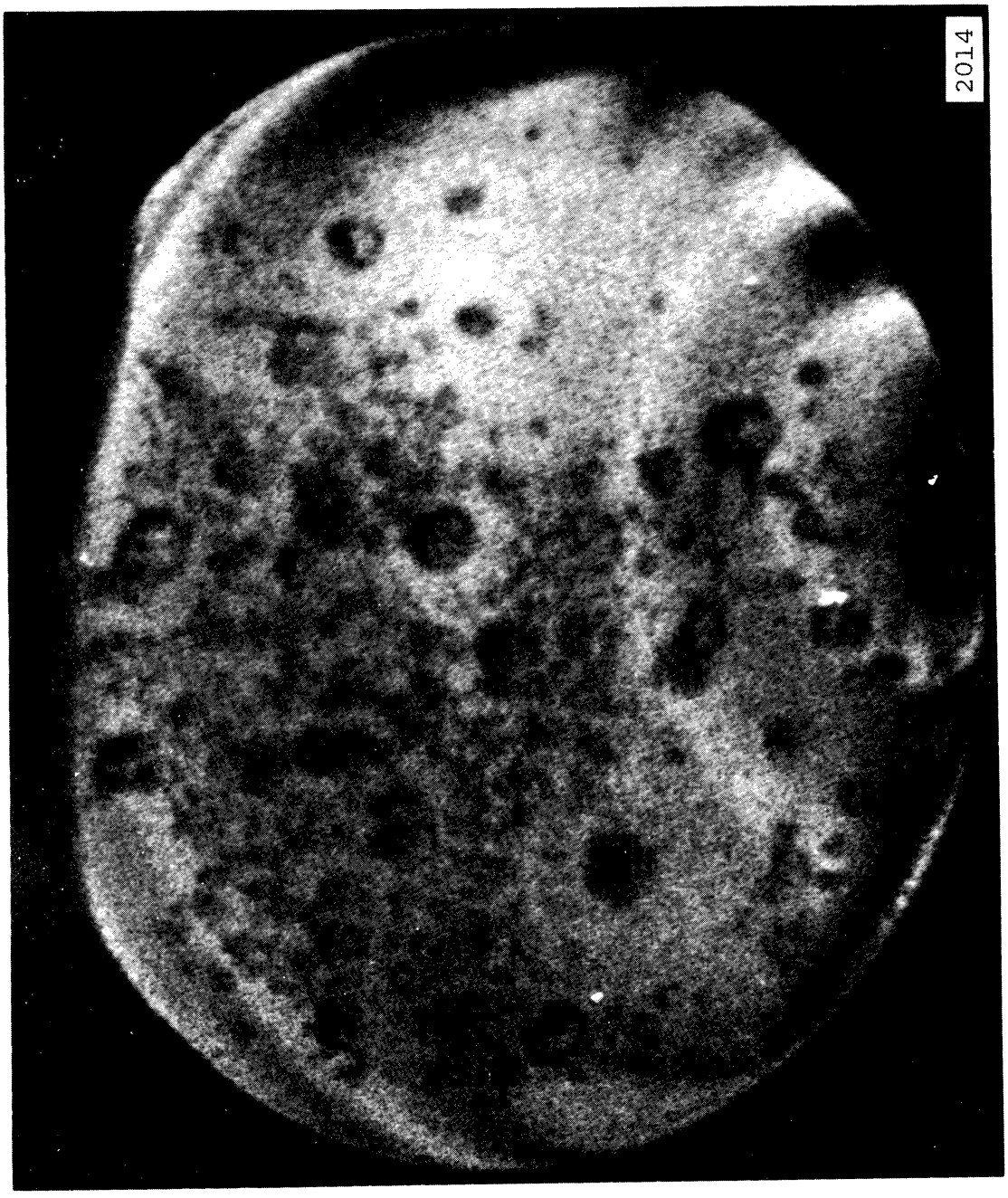

Fig. 23.--High speed photograph (14X) of a 75% c. w. nickel (as rec'd) specimen in water, frequency 20,454 cps, amplitude approximately 2 mils, exposure time per frame of 1.3 μ seconds, photographed at 20,460 fps.

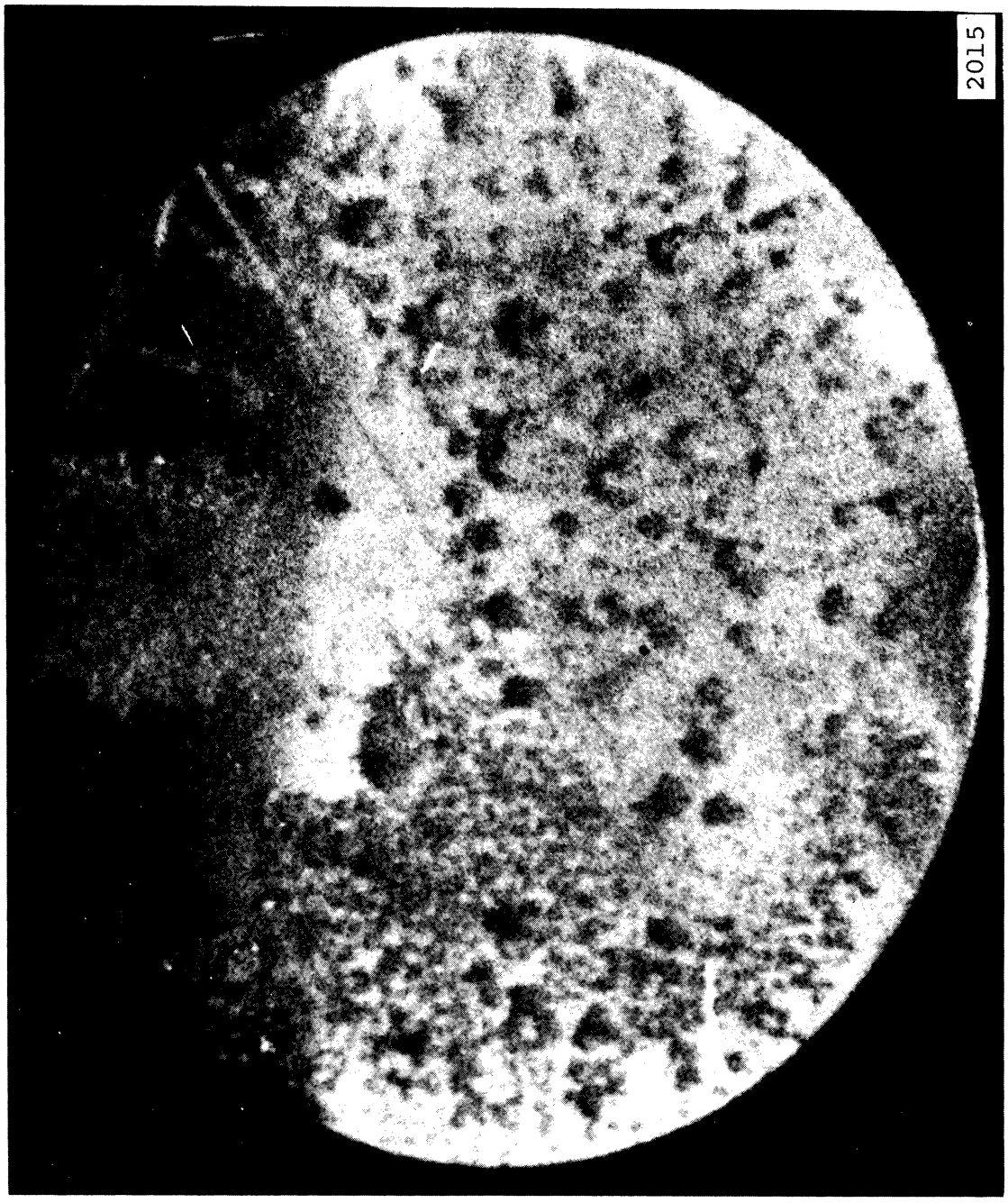

Fig. 24.--High speed photograph (14X) of a 75% c. w. nickel (as rec'd) specimen in water, frequency 20,454 cps, amplitude approximately 2 mils, exposure time per frame of 1.3 μ seconds, photographed at 20,460 fps.

2% advancement with respect to the horn frequency, and hence showed various bubble populations throughout the acoustic cycle. However, Fig. 24 is typical of the maximum population portion of the cycle. Note how the bubble pattern has changed at the top. The area without bubbles in Fig. 68 has now become the preferred bubble area in Fig. 24 and vice versa.

As can be seen from Fig. 5, when the horn is tilted 45° or 60° from the vertical, it is necessary to have only a relatively small depth of water above the top edge of the specimen if mechanical conflict between the horn and the container is to be avoided. The top edge of the inclined specimen is usually within 5 to 10 mm of the surface. Visually, by varying this distance, bubble pattern changes at the top of the specimen can be observed. The motion of the horn when assembled in this position causes a visible indentation in the water surface above the specimen, which vanishes when the water level above the horn is raised. For this case a lesser reduction in bubble population at the top of the specimen was observed. With the horn held vertically (normal position for routine testing) no asymmetrical bubble patterns were noted until the horn was lifted almost out of the water. These asymmetries with the tilted horn are presumably due to the slight difference in pressure between the top and bottom of the specimen because of the small elevation difference as well as non-symmetries introduced by the flat walls and bottom of the container and the proximity of the water surface.

While the horn was designed to resonate at approximately 20,000 cps, there were local peaks of amplitude at lower frequencies. Cavitation was obtainable at about 20,000, 18,500, 10,000 and 6,200 cps.

Fig. 25 is a frame from a sequence taken with the frequency set at 6,200 cps. Only slight cavitation developed because only a small amplitude could be obtained at this reduced frequency. Under stroboscopic illumination occasional bubbles could be seen darting around the specimen surface. Because of the low frequency and a high camera speed of 26,000 fps, up to 5 frames could be made during one acoustic cycle. It was hoped that the individual bubbles could be followed from frame to frame, but they seldom could be traced for more than 2 frames. It is clearly seen though, that most of the bubbles are approximately spherical.

Fig. 26 is from a run at 10,000 cps. The bubble fields at 18,500 and 20,000 cps differed from the runs at 10,000 in that they contained substantially more bubbles and a greater proportion were relatively large. Higher amplitudes were obtainable at the higher horn frequencies which would mean that the threshold radius from which a bubble might attain the status of a cavitation bubble under the influence of the ultrasonic field was lower.*

---

*Neglecting "rectified diffusion" (previously explained) which provides a mechanism where a small gas nucleus can be caused to grow to the threshold radius during an exposure to many periods of the acoustic cycle.

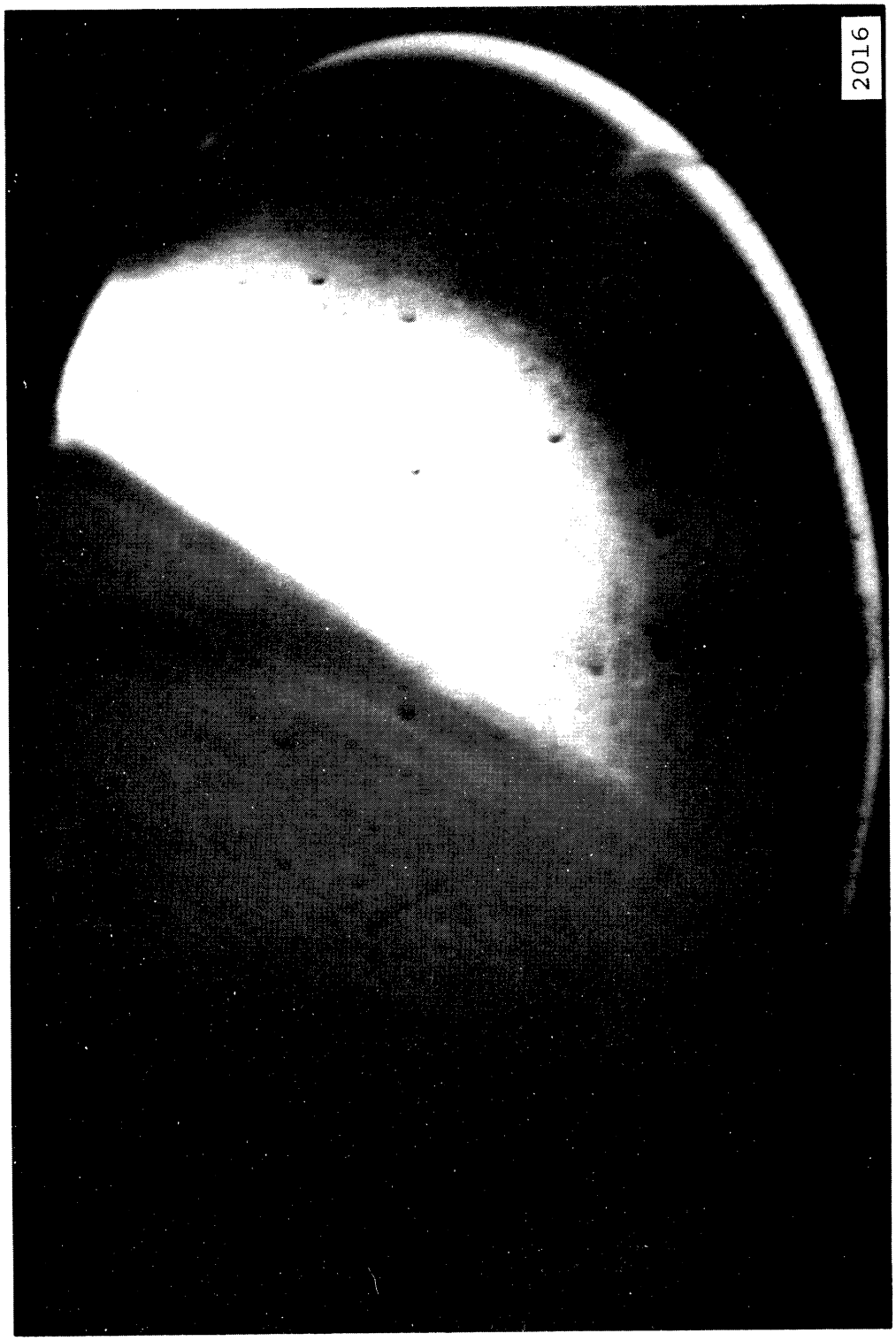

Fig. 25.--High speed photograph (15X) of a partially polished, partially abrased, type 304 stainless steel specimen in water, frequency 6,200 cps, exposure time per frame of 1 μsecond, photographed at 26,000 fps.

Fig. 26.--High speed photograph (15X) of a partially polished, partially abrased, type 304 stainless steel specimen in water, frequency 10,000 cps, exposure time per frame of 1μsecond, photographed at 26,000 fps.

There was no readily detectable difference between the bubble fields at 18,500 and 20,000 cps. A good mechanical resonance (local peak in the horn amplitude vs. frequency curve) at these frequencies was obtained; a poorer, but yet still substantial resonance was obtained at 10,000; and a very weak one existed at 6,200. A comparison between the bubble fields at 10,000 and 20,000 cps will be made in the Section that follows.

To determine the possible effect of minor roughness, as would be incurred by exposure to cavitation for runs up to 60 seconds in length, one half of a polished specimen was lightly abrased, the other half remaining in the polished condition. Several high speed photographic runs were then made. Fig. 26 is typical of these photographs. The abrased section is at the bottom of the photograph. The polished-abrased interface was rotated 90° (see Figs. 41-A and B, Section E of this Chapter) and no change in the bubble pattern from that of Fig. 26 resulted. Thus the roughness was too small to cause any discernable change in the local bubble population, any non-symmetries in the bubble pattern being caused by the non-symmetrical geometry. It was concluded that bubble population changes due to roughness would not occur during the damage runs for this investigation, since the maximum exposure time was to be 60 seconds.

C. Cavitation Bubble Fields

Figs. 27, 28, 29, and 30 are typical of individual high speed photographs taken from various runs with a type 304 stainless steel specimen with an oscillator frequency of 20,300 cps and a camera framing rate of 26,000. Fig. 31 is a typical photograph of a type 2024-T351 aluminum specimen with frequency of 20,200 cps, photographed at 20,150 frames per second and exposed at a time when the bubble population is relatively low.

These photographs and also that of Fig. 26 for 10,000 cps when a stainless steel specimen was used, show the transient bubbles, bubbles at approximately the mean resonance diameter (using equation 3 from Chapter II, the mean resonance diameter for 20,000 is approximately 0.032 cm and approximately 0.064 cm for 10,000 cps), and also those bubbles that are greater in diameter than the mean resonance diameter and apparently have rebounded to this large diameter. A scale on the photographs shows the resonance diameter. The transient bubbles were only slightly larger in diameter at 10,000 cps than at 20,000 cps even though they had a longer time to grow, because the acoustic pressure was less due to smaller horn amplitude (because of a less intense horn resonance) and because the acoustic pressure varies directly as the frequency with other acoustic conditions constant.[54]

Fig. 27 is taken apparently at that portion of the acoustic cycle where the bubble population is at a minimum.

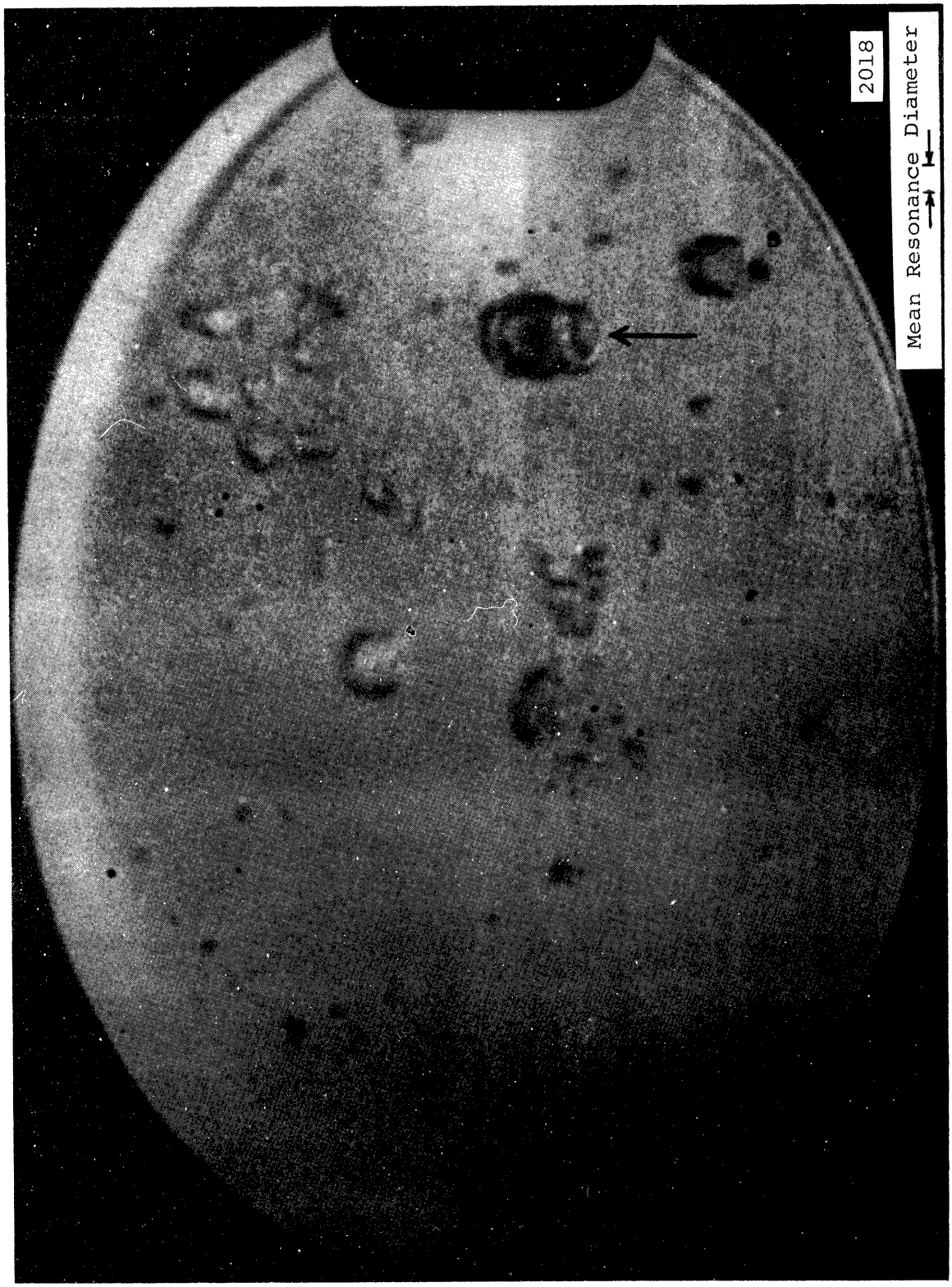

Fig. 27.--High speed photograph (14X) of a partially polished, partially abrased, type 304 stainless steel specimen in water, frequency 20,300 cps, amplitude approximately 2 mils, exposure time per frame of 1 μ second, photographed at 26,000 fps.

Fig. 28.--High speed photograph (14X) of a partially polished, partially abrased, type 304 stainless steel specimen in water, frequency 20,300 cps, amplitude approximately 2 mils, exposure time per frame of 1 μ second, photographed at 26,000 fps.

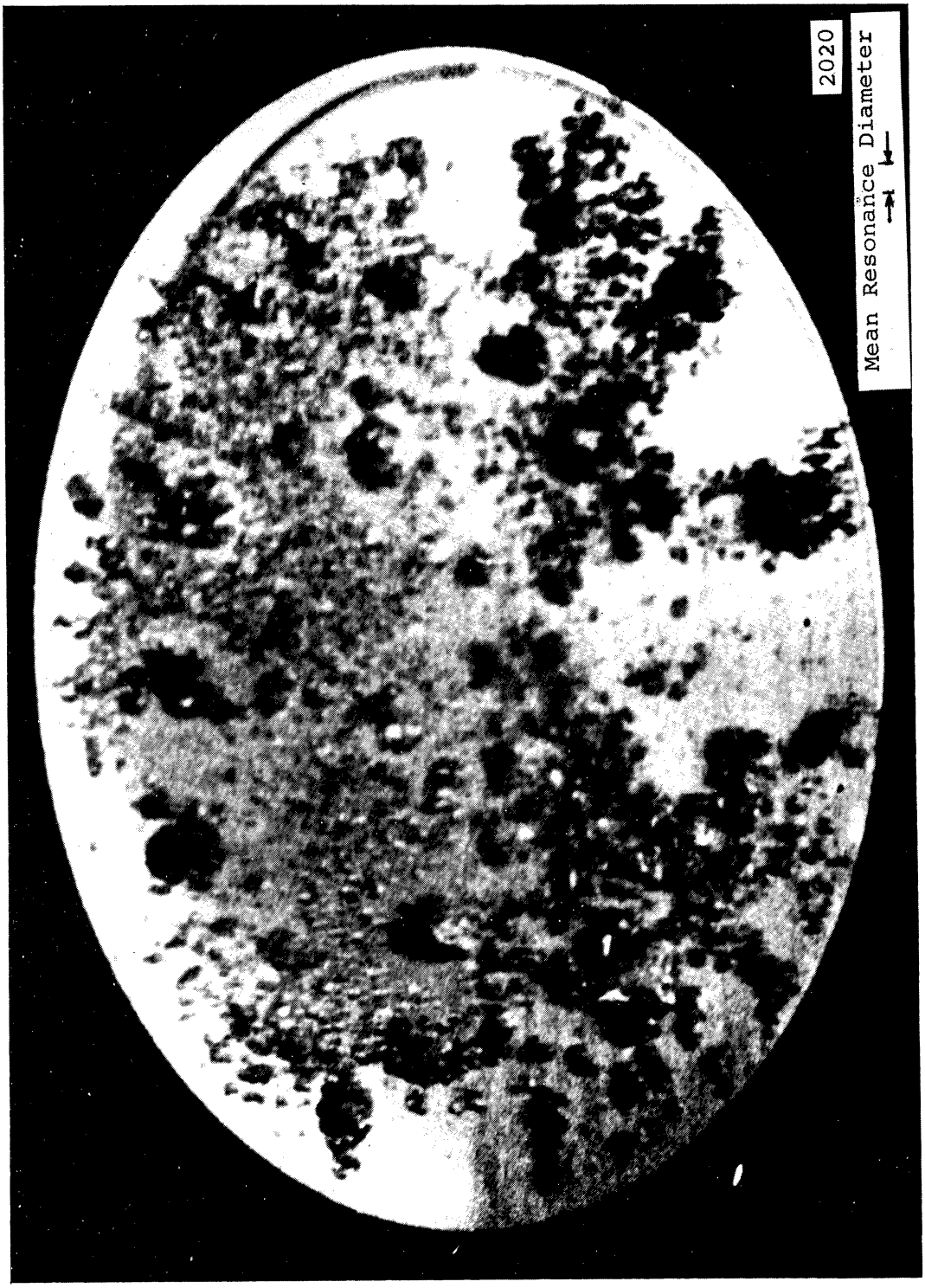

Fig. 29.--High speed photograph (14X) of a partially polished, partially abrased, type 304 stainless steel specimen in water, frequency 20,300 cps, amplitude approximately 2 mils, exposure time per frame of 1 μ second, photographed at 26,000 fps.

Fig. 30.--High speed photograph (14X) of a partially polished, partially abrased, type 304 stainless steel specimen in water, frequency 20,300 cps, amplitude approximately 2 mils, exposure time per frame of 1 μ second, photographed at 26,000 fps.

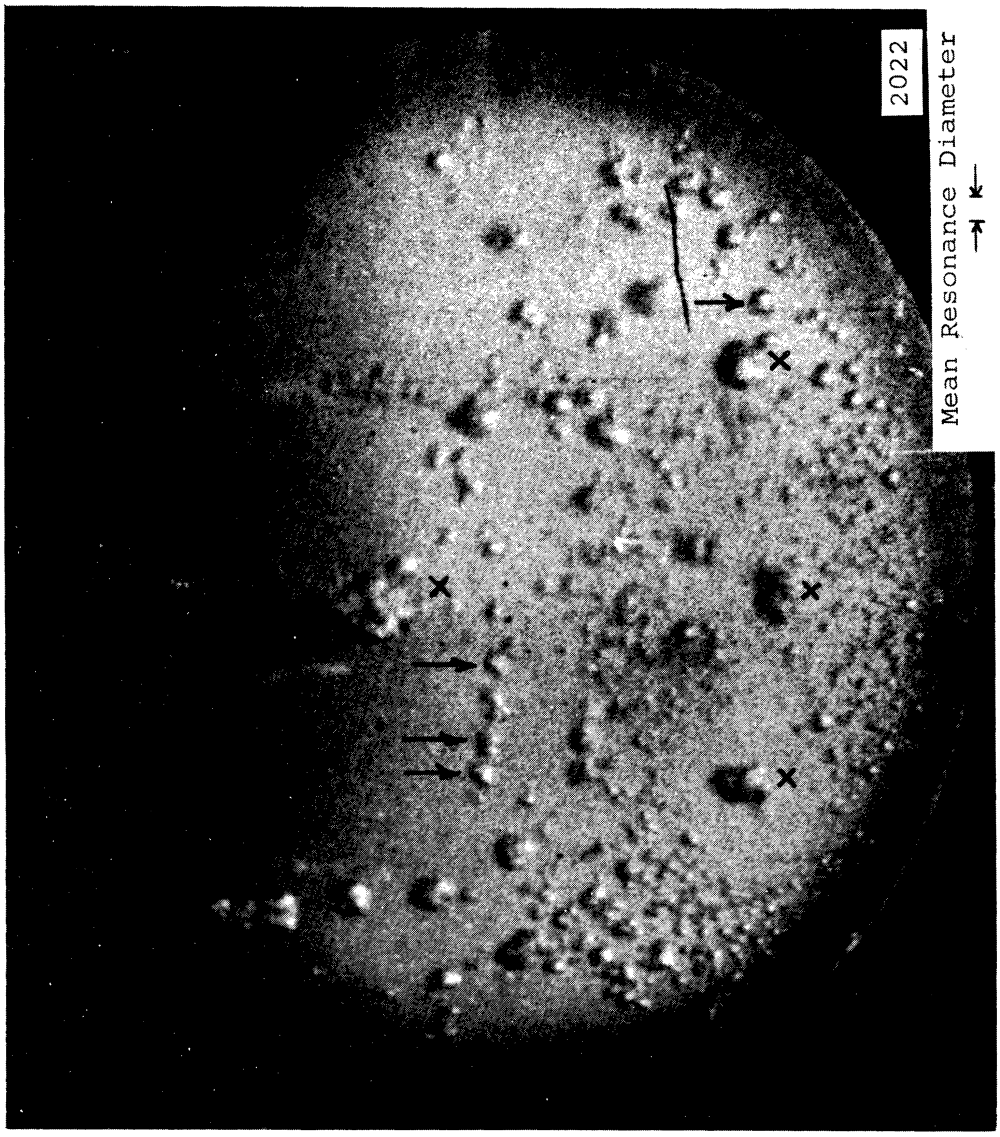

Fig. 31.--High speed photograph No. 79a (12X) of a type 2024-T351 aluminum specimen in water, frequency 20,200 cps, amplitude approximately 2 mils, exposure time per frame of 1.3 μseconds, photographed at 20,150 fps.

A bubble of the same general appearance of that marked with an arrow at the right center of the photograph (appears almost cylindrical) was noticed in many sequences. These "towering" bubbles are discussed in much more detail in Section N of this Chapter. The charcoal-like smudges about 0.2 to 0.3 cm in diameter on the photograph are characteristic of the rebounding bubbles at or near their minimum diameter point (also discussed in more detail in Section D of this Chapter).

Fig. 28 shows a mixture of bubble types where shadows are noted adjacent to the large bubbles in the lower right portion of the photograph. Judging from the shadows, these bubbles are apparently spherical and are just touching or are just off the specimen surface. It is not usual to see shadows of this type nor to see spherical bubbles of this large a diameter in the photographs. The dark trapezoidal shape in the lower center is photographic debris. The protuberances[27] on the bubbles and the large diameters of the bubbles suggests that they have collapsed and rebounded. Some of the larger bubbles are at the predicted mean resonance diameter, but the protuberances existing on them suggest that they have collapsed and rebounded to this size, or else that they have coalesced with smaller bubbles. Again, it has been observed that when the larger bubbles are spherical, they are in, or are approaching, the collapse mode, i.e., they will have disappeared by the next photographic frame. An apparently more stable bubble type is marked by an arrow in Fig. 28. This appears to have

a diameter about twice its height and appears to be on the specimen surface.

Fig. 29 is a typical photograph of that part of the acoustic cycle where the population is a maximum, and all types of bubbles are shown. Visibly, i.e., to the unaided eye, this is a violent type of cavitation and lacks any definite pattern such as the familiar star, which is discussed later. The outer annulus is less heavily populated in that the main body of cavitation breaks into streamers near the edge. These streamers are the only suggestion of a pattern.

Fig. 30 is believed to show that point in the acoustic cycle where collapse of the bubbles has been completed and the expansion part of the acoustic cycle has just been started. This conclusion is due to the small diameters of the transient bubbles in the lower part of the photograph (as will be explained in Section N of this Chapter, these could be rebounding sections resulting from toroidal collapses) and also to the two apparent "shock rings" around rebounding bubbles. These are marked with arrows in Fig. 30. The "shock ring" observation will be further discussed in Section E of this Chapter. Note the large number of bubbles that apparently have survived the collapse. These are glossy, while the charcoal-like smudges are probably the rebounding bubbles.

Fig. 31 again shows bubbles of different diameters. The damage pattern as marked by the lighter shaded area can be seen on the specimen even though it has been exposed to

cavitation for less than a minute. Some of the bubbles that persist through 2 or 3 acoustic cycles are shown on this photograph (marked with arrow), and their diameters are approximately equal to the mean resonance diameter for the applied acoustic frequency.* The largest diameter bubbles (marked with X's) have apparently been formed from bubbles that have collapsed and rebounded.

High speed photographic proof of Noltingk and Nepiras's[41,42] hypothesis that bubbles from nuclei with radii in a range greater than a certain threshold radius and less than a resonant radius grow and collapse in one acoustic cycle, while some bubbles with radii greater than the resonant radius remain for more than one cycle, is seen in Fig. 32. This is a sequence of 6 photographs, A through F, for a type 304 stainless steel specimen oscillated at 10,000 cps. The amplitude was approximately 1 mil (at the time of this test no accurate means of measuring amplitude was available), and camera speed was 26,000 frames per second. Thus two to three photographs were obtained in every acoustic cycle.

Fig. 32-A shows a fully developed star pattern. This general pattern is often observed visually and exists at medium acoustic pressures. The transient bubbles are intermingled with the larger bubbles. One of these larger bubbles,

---

*These are probably transient bubbles that have collapsed and rebounded to the approximate mean resonance diameter. Because of the few bubbles at this mean resonance diameter it seems less probable that they existed as nuclei of resonance size.

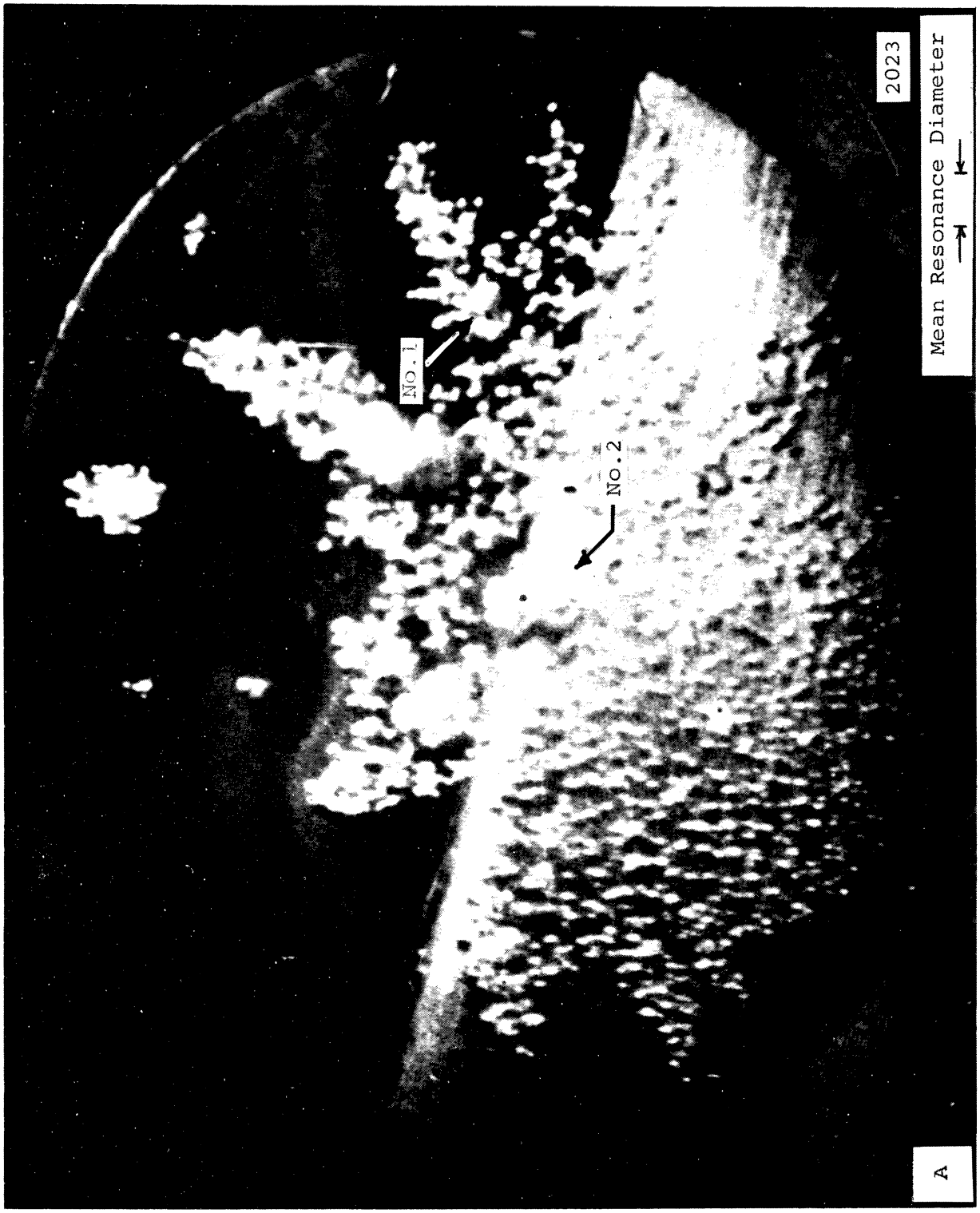

Fig. 32.--High speed photographic sequence (14X), A through F of a partially polished, partially abrased, type 304 stainless steel specimen in water, frequency 10,000 cps, exposure time per frame of 1μsecond, photographed at 26,000 fps.

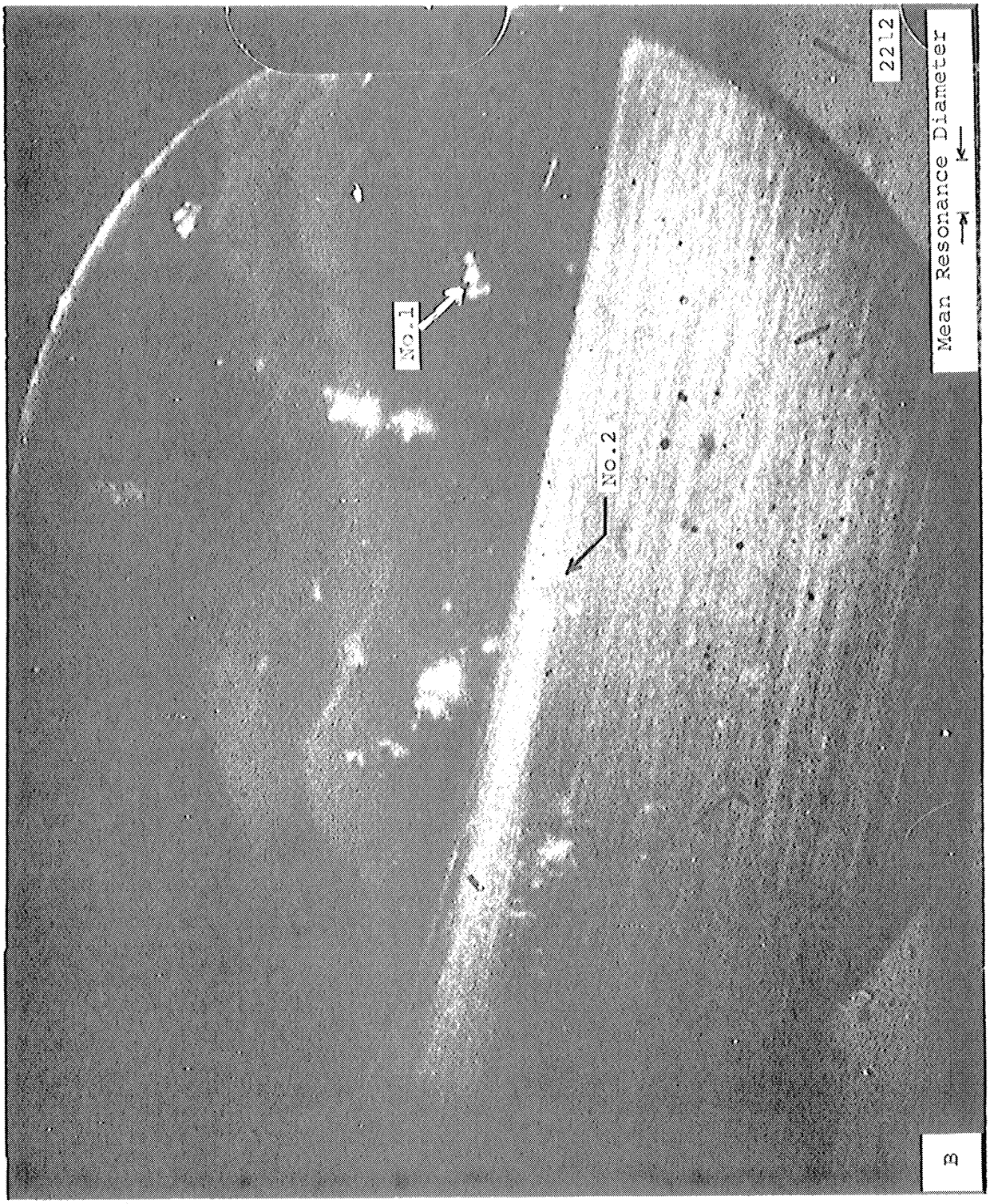

Fig. 32.--Continued

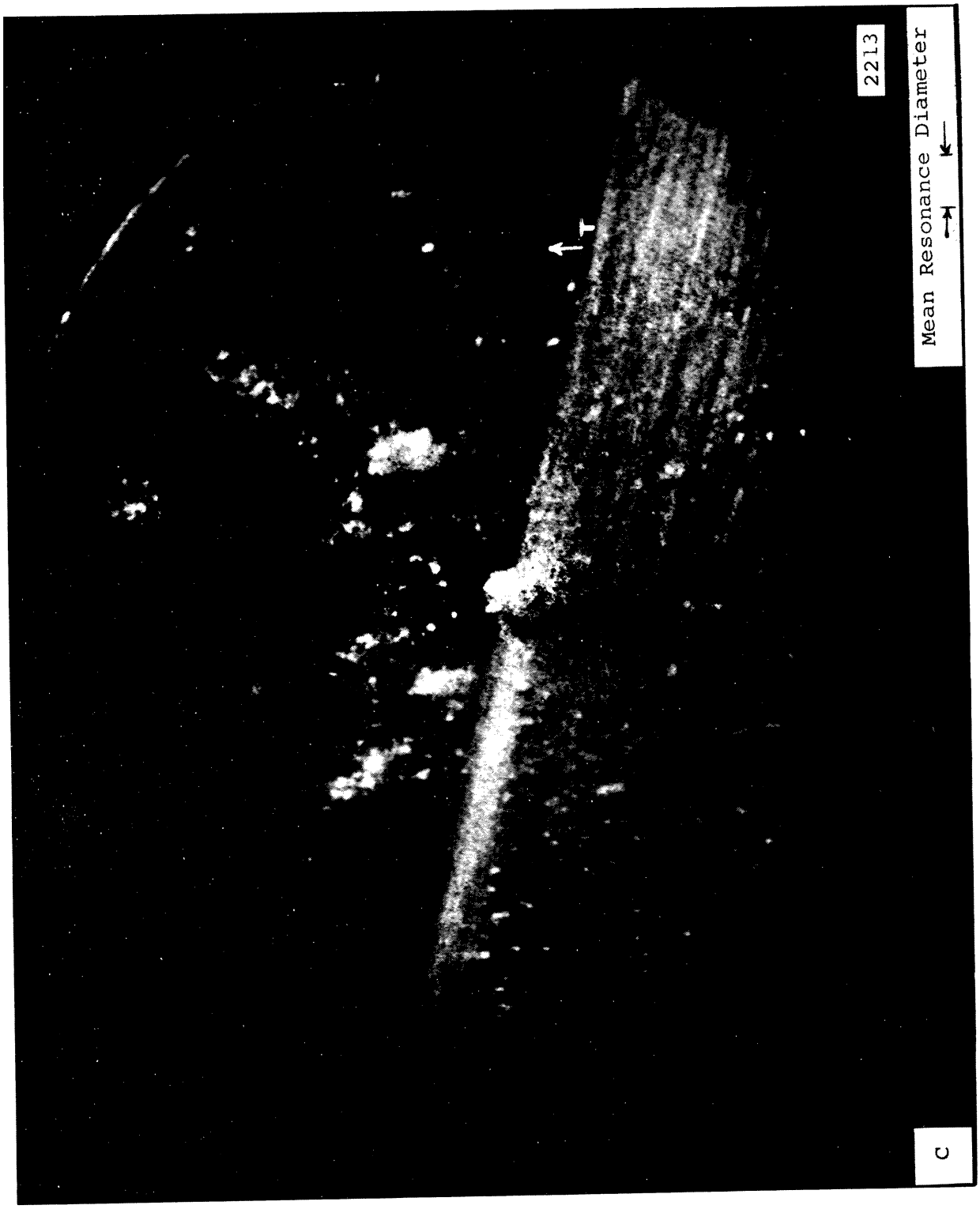

Fig. 32.--Continued

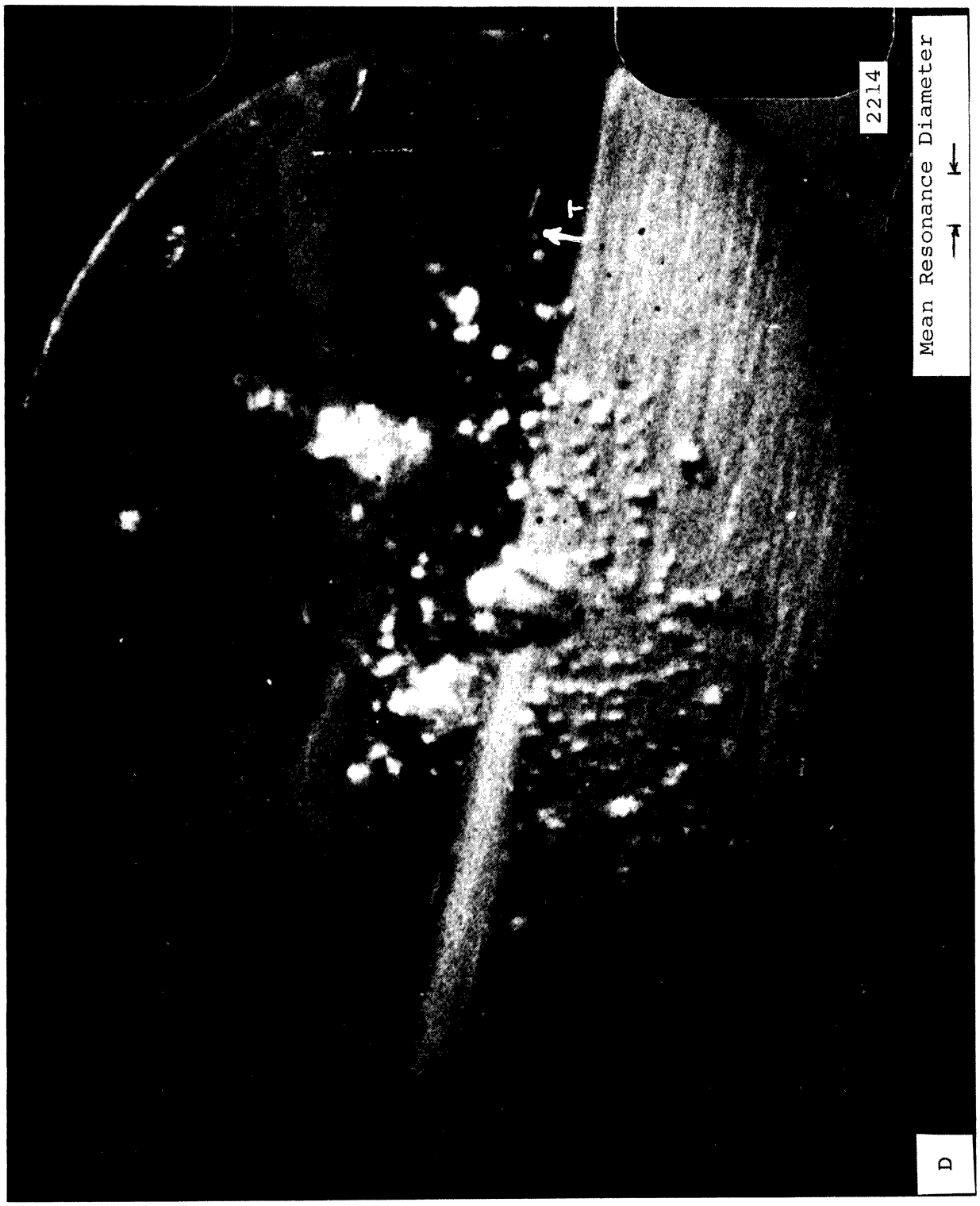

Fig. 32.--Continued

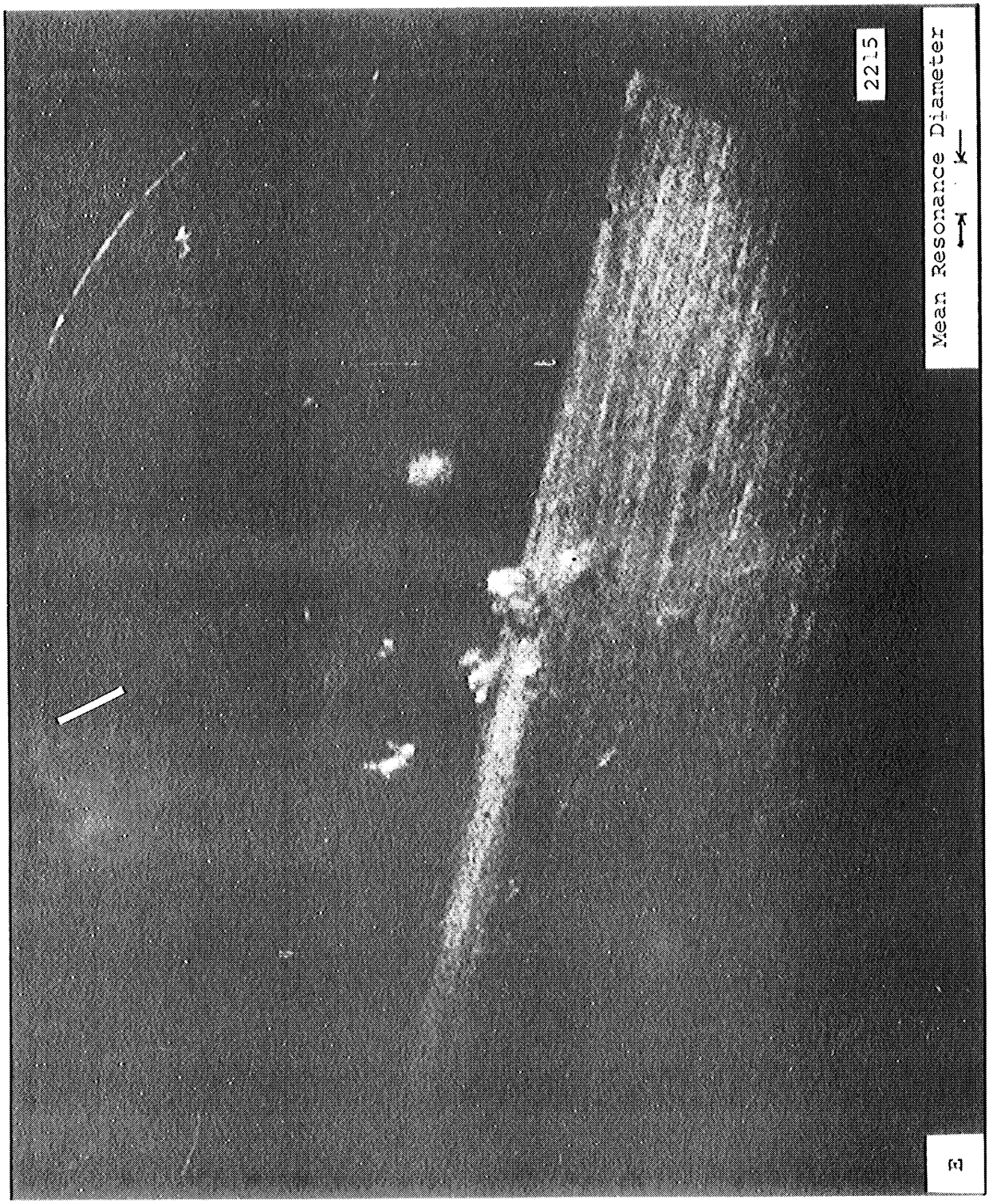

Fig. 32.--Continued

Fig. 32.--Continued

labeled no. 1 on Fig. 32-A is about at the predicted mean resonance diameter. There are also 3 other bubbles that are considerably larger than the predicted resonance diameter. One of these is labeled no. 2 on Fig. 32-A. In Fig. 32-B, 38.5 μseconds later in an acoustic cycle that is 100 μ seconds in length, it is seen that practically all of the transient bubbles are gone as predicted by Noltingk and Neppiras.[41,42] The dominant survivors are the aforementioned larger bubbles which are much smaller in diameter than in Fig. 32-A. Nos. 1 and 2 from Fig. 32-A are also labeled in Fig. 32-B. Bubble no 2 is barely visible. Possibly Fig. 32-B was taken at some instant between the peak of the positive pressure part of the cycle and the start of the negative pressure part. Assuming it was taken at the positive pressure peak, then Fig. 32-C should be at a position early in the negative portion of the cycle showing development of the transient bubble field and expansion of the larger bubbles that were at reduced diameters in Fig. 32-B. Fig. 32-D shows the larger bubbles near their maximum diameters as are the transient bubbles. The larger bubbles of Fig. 32-D can be readily matched as to relative size and position with Fig. 32-C, as can some of the transient bubbles by careful comparison. One of these is marked "T" in both Fig. 32-C and Fig. 32-D for easy identification. Fig. 32-E then shows the bubble field in the positive pressure part of the acoustic cycle, apparently after the collapse of the transient bubble field. Fig. 32-F shows the large bubbles,

still easily identifiable because of their relative positions, and a new group of transient bubbles. It appears as if bubble no. 2 continued throughout the sequence, but no. 1 disappeared after Fig. 32-B.

A sinusoidal acoustic cycle and the probable approximate cycle positions which best match the photographic evidence regarding bubble population and the known frequency and framing rate of Figs. 32-A through F are shown in Fig. 33. From this arrangement, one would deduce that Figs. 32-A and F and Figs. 32-B and E should be roughly similar and they are. Fig. 32-C should show a growing transient bubble group with expanding larger bubbles and it does. Fig. 32-D should show all bubbles at or near their maximum diameters and apparently this too is true. This construction provides evidence that reinforces the model that predicts the existence of both transient bubbles and larger bubbles that persist through more than one acoustic cycle.

Fig. 34-A (37X) shows various types of bubbles on a type 304 stainless steel specimen where the frequency was 20,390 cps and the camera was operated at 20,800 frames per second, at that part of the acoustic cycle where the population is a minimum. The scribe marking line cuts diagonally through the bottom of the photograph. The white vertical line is a scratch on the negative. The large spherical bubble at the upper right is an actual 0.08 cm in diameter. The bubble could be the rebound of a toroidal section and the string of

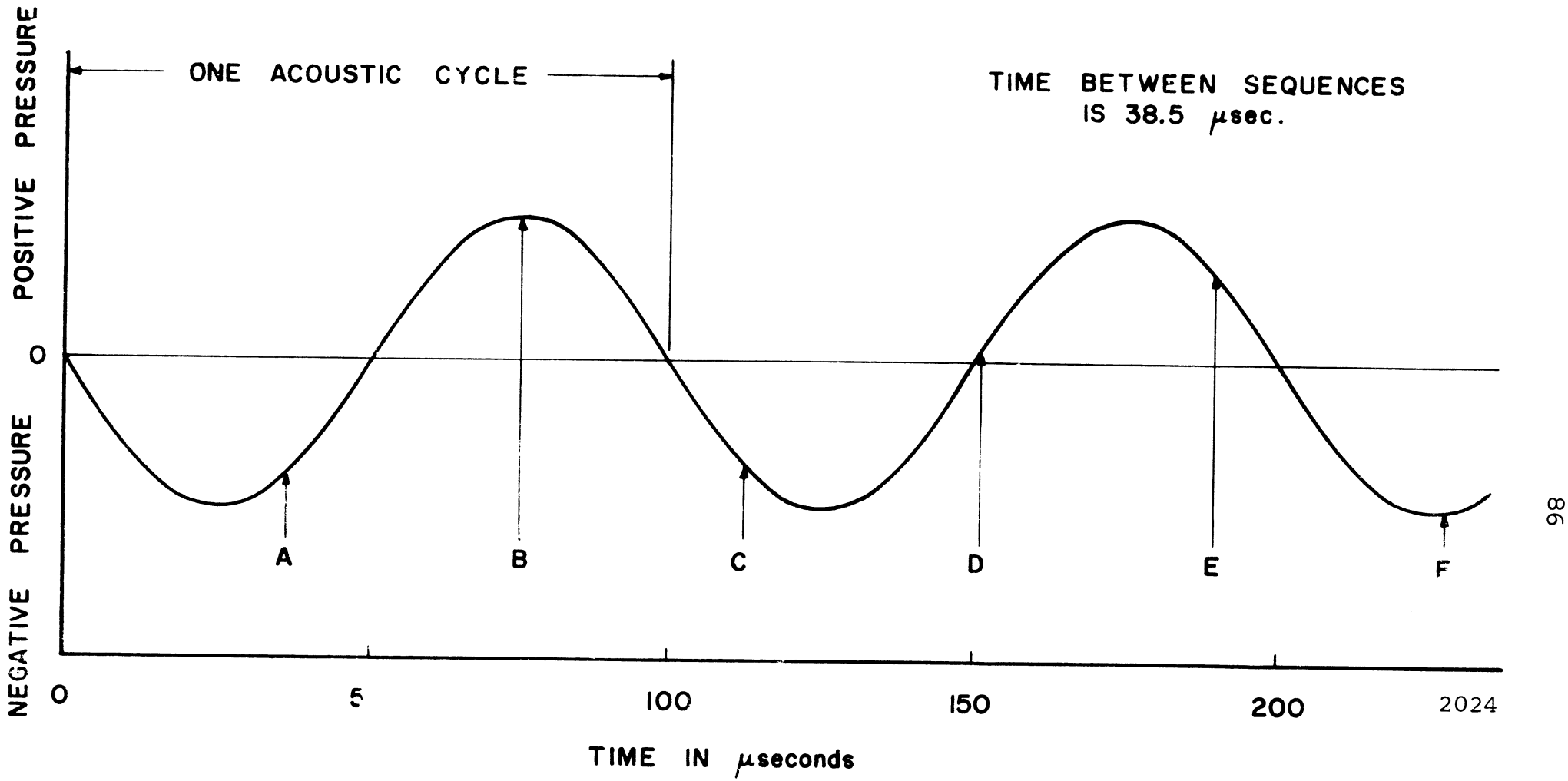

Fig. 33.--Predicted positions in the acoustic cycle of 6 high speed photographs, frequency 10,000 cps, exposure time per frame of 1 μ second, photographed at 26,000 fps.

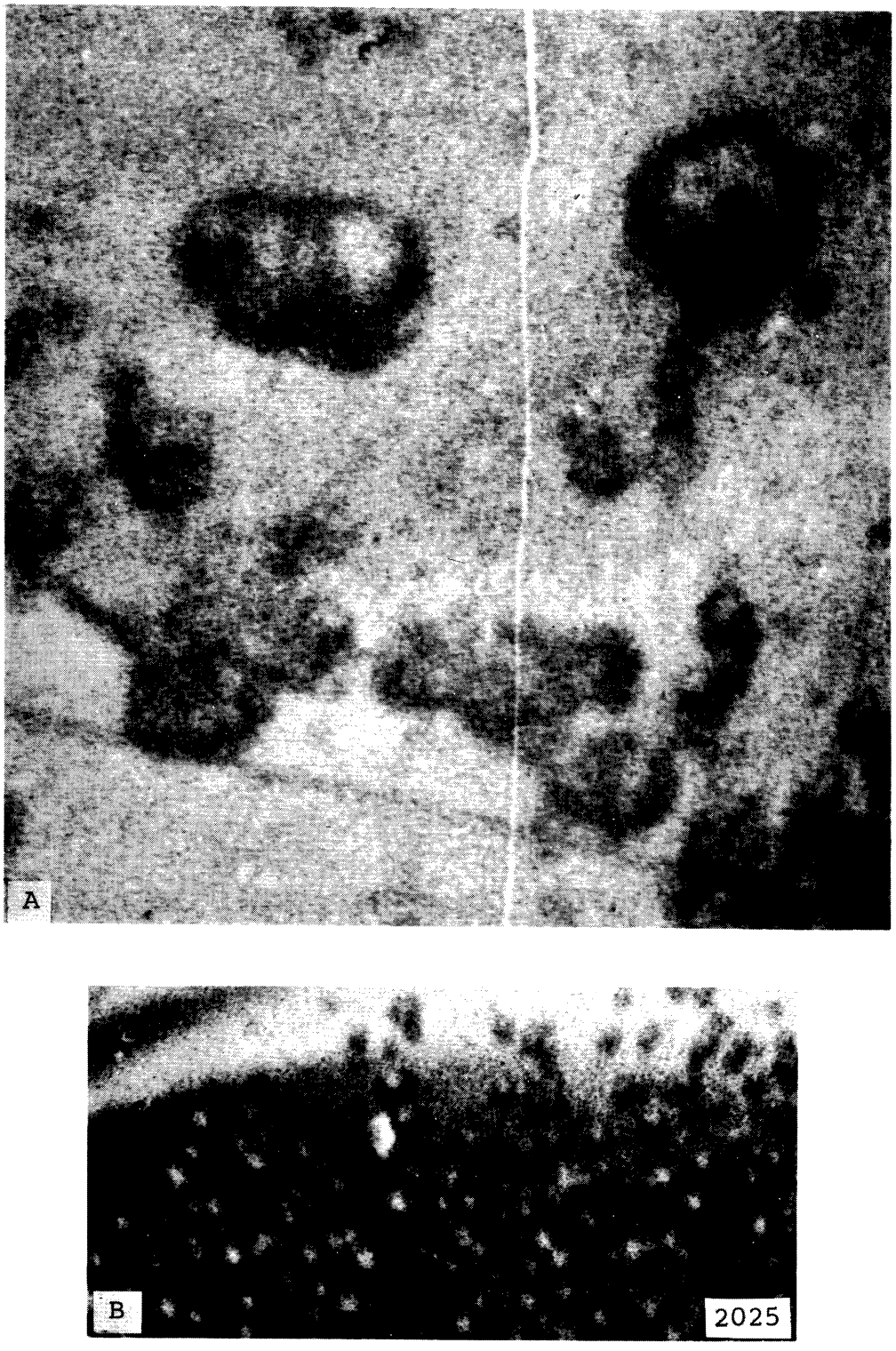

Fig. 34.--High speed photograph (37X) of a type 304 stainless steel specimen in water, A, frequency 20,390 cps, amplitude approximately 2 mils, exposure time per frame of 1.3 μ seconds, photographed at 20,800 fps; B, frequency 10,000 cps, exposure time per frame of 1 μ second, photographed at 26,000 fps.

bubbles below it the rebound of the arrested jet (see Section N of this Chapter). Fig. 34-B (37X) shows transient bubbles, also on a stainless steel specimen. This run was made at a frequency of 10,000 cps and the camera operated at 26,000 frames per second. These bubbles are an actual 0.003 to 0.015 cm in diameter. They are part of a large star pattern that covered most of the specimen surface. They are apparently spherical and are positioned on, or close to, the specimen surface. These bubbles disappeared during each acoustic cycle as the transient bubbles did in the sequence of Figs. 32-A through F.

D. Larger Bubbles

Figs. 35-A through O show individual sections cut from various high speed photographs of larger bubbles whose mean diameters in all cases are greater than the predicted mean resonance diameters for the frequencies used (18,500 and 20,300 cps). All were from runs which used a type 304 stainless steel specimen and the photographic sections were taken from various parts of the overall specimen photograph. All are at (16X). Fig. 35-K shows the result of the collapse of a large bubble about 0.1 cm in diameter which involuted into a torus and rebounded. The form of the torus can be clearly noted. The specimen is so located that the smaller ring to the upper left is probably the rebound of the splash from the central jet of the torus which hit the specimen

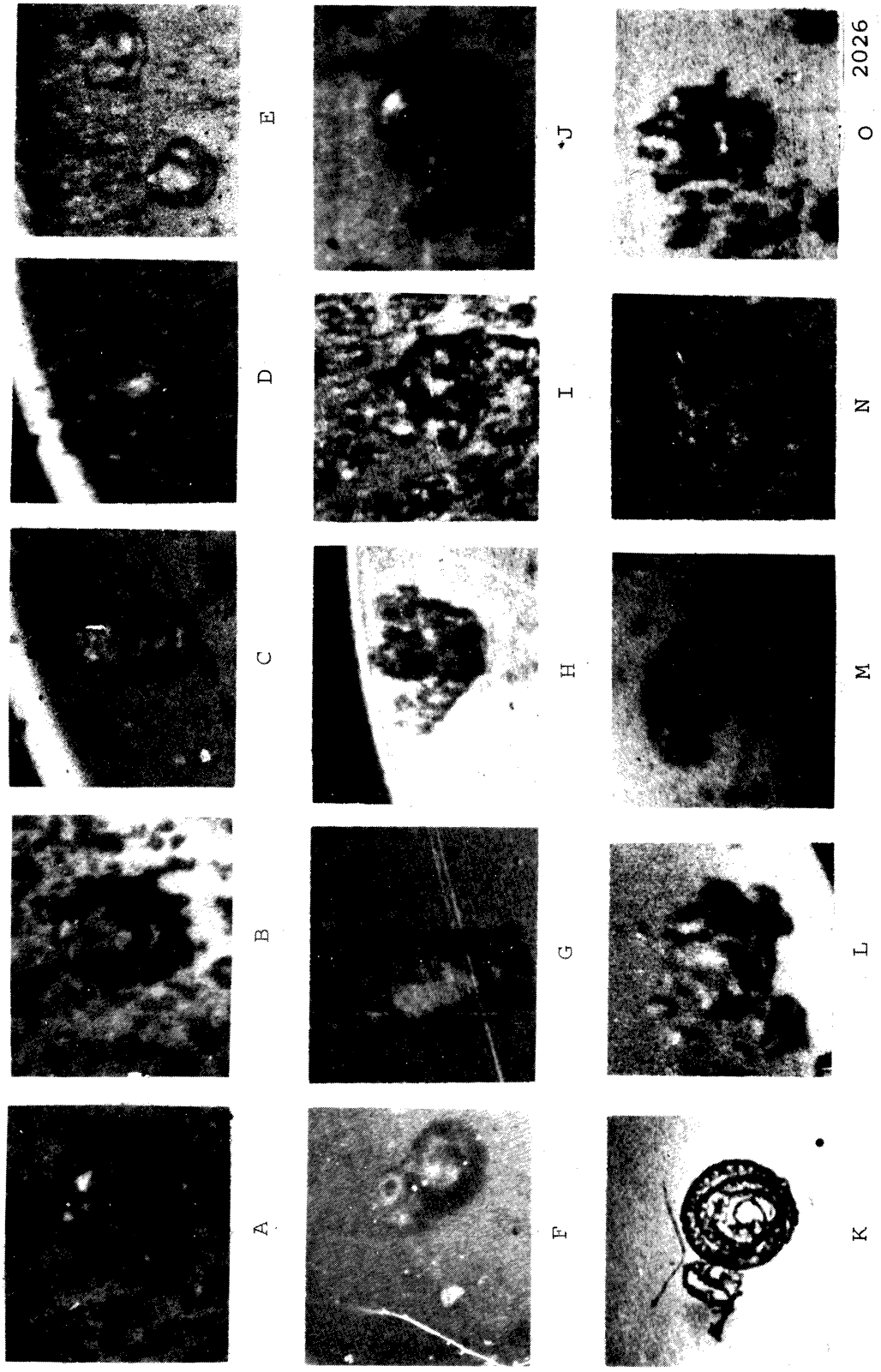

Fig. 35.--High speed photographs (16X) of a type 304 stainless steel specimen in water; A through F, frequency 18,500 cps; G through O, frequency 20,300 cps, amplitude approximately 2 mils; exposure time per frame for all but K of 1 μsecond, photographed at 26,000 fps; exposure time for K of 1.3 μ seconds, photographed at 20,800 fps.

surface precisely as required by this collapse mechanism. Both the large and the small rings have large numbers of protuberances attached to or within them, which appear to be very small bubbles. Fig. 35-F also suggests that a toroidal collapse has occurred. The peculiar separation or cut around the bubbles as shown in Figs. 35-A through G, I, M, N and O, the balooning shapes of H, J, L and M all suggest some form of rebound from a toroidal collapse. Many of the bubbles shown in Fig. 35 exhibit the protuberances reported by Schmid[27] in his single bubble experiments.

Figs. 36, 37 and 38 show plots of diameter vs. time taken from high speed photographic sequences of larger bubbles that could be followed from frame to frame in the sequence. The oscillator frequency was 20,200 cps. The photographic sequences used to plot Figs. 36 and 37 were made with the horn frequency and the camera framing rate almost matched. For Fig. 38 the framing rate was 2% greater than the frequency. Since there was only one data point per acoustic cycle (there is a small probability that there will be two points per cycle in one or two of the cycles for a run when the framing rate is 2% greater than the frequency), these plots show only that the bubbles tend to grow and oscillate increasingly in diameter before they disappear. In all cases their mean diameter is greater than that predicted for resonance (from equation 3 in Chapter II the mean resonance diameter would be approximately

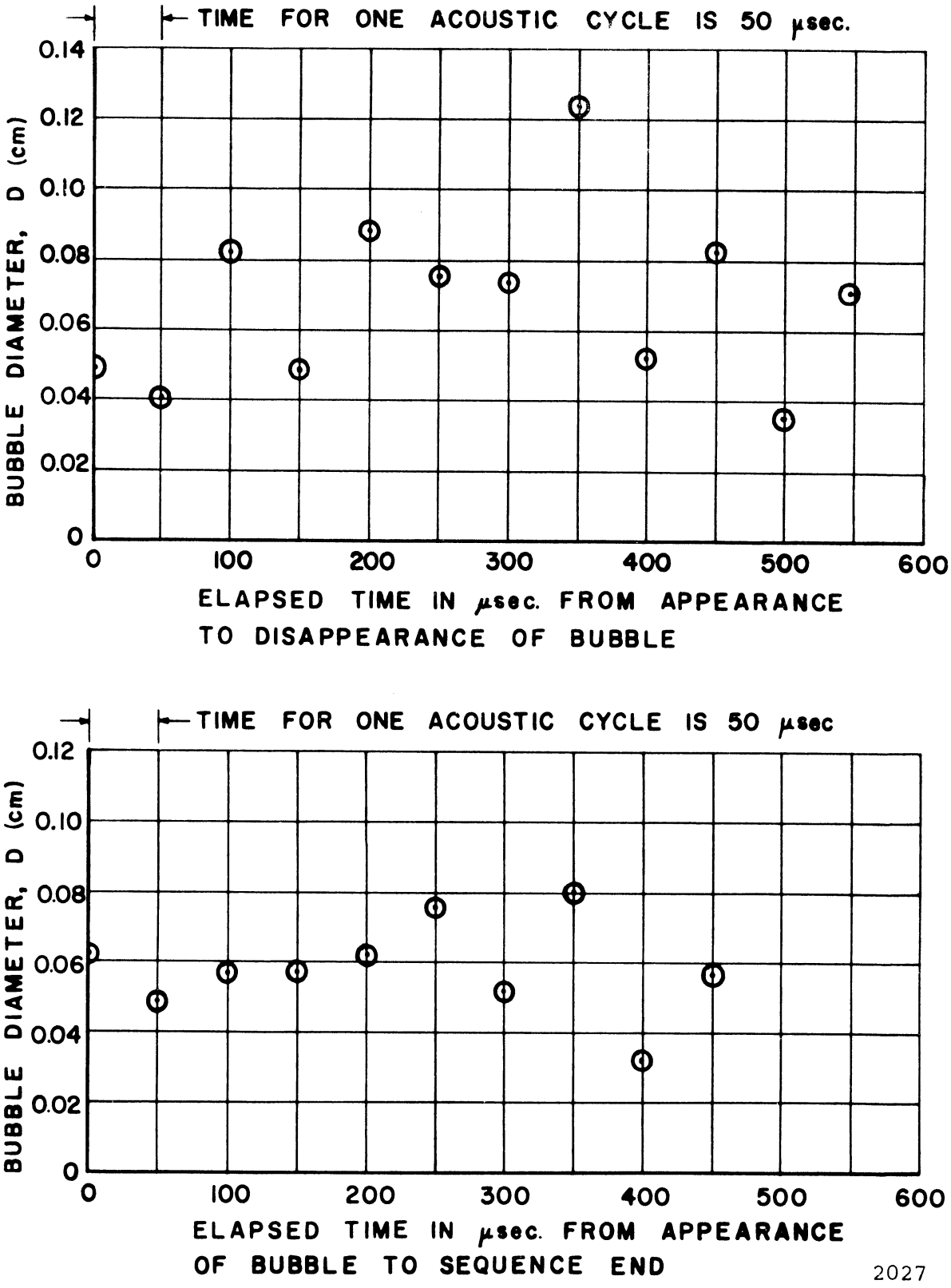

Fig. 36.--Bubble diameter vs. time for individual bubbles on a type 2024-T351 aluminum specimen in water, frequency 20,200 cps, amplitude approximately 2 mils, from photographs having an exposure time per frame of 1.3 μ seconds, photographed at 20,150 fps.

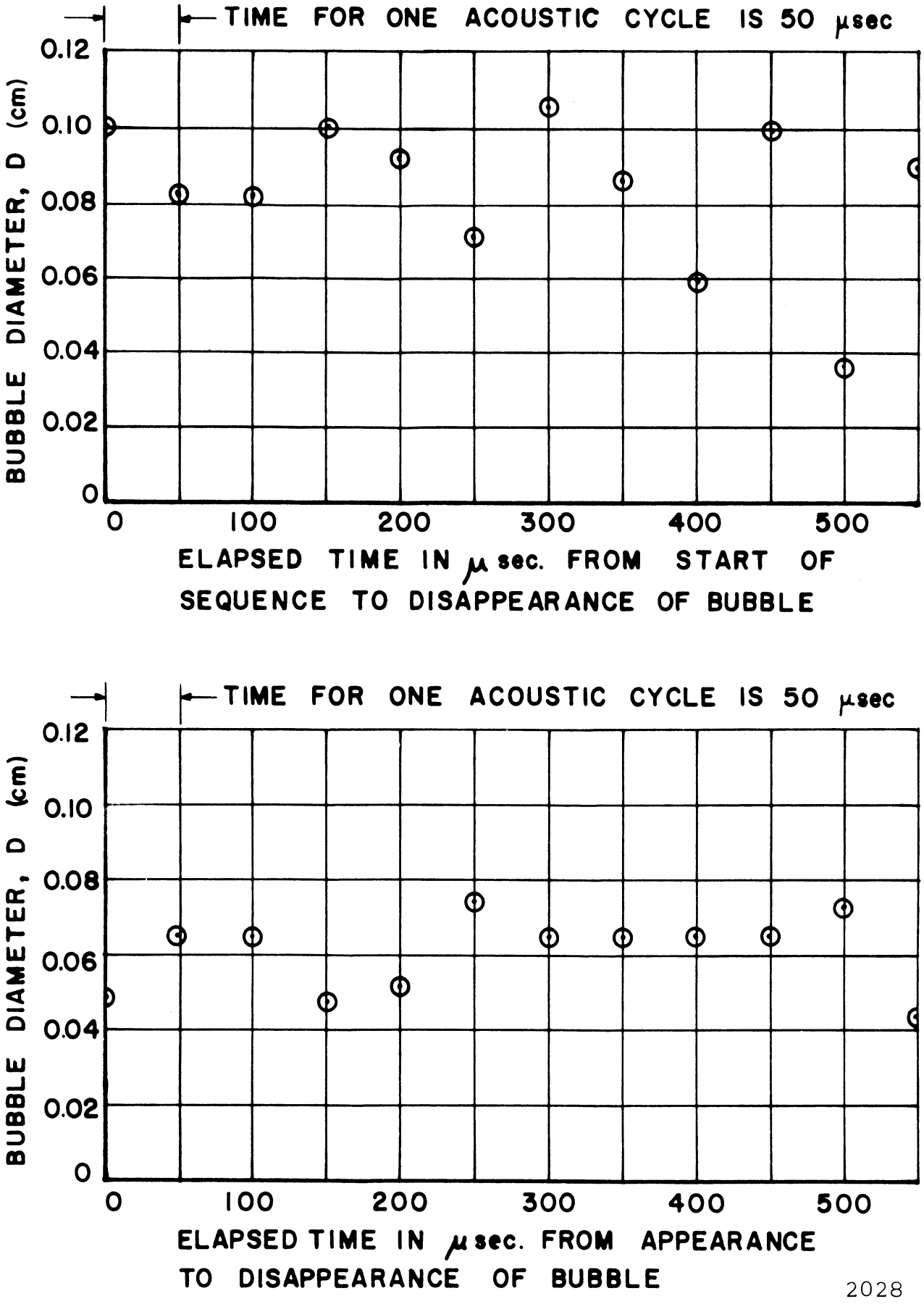

Fig. 37.--Bubble diameter vs. time for individual bubbles on a type 304 stainless steel specimen in water, frequency 20,200 cps, amplitude approximately 2 mils, from photographs having an exposure time per frame of 1.3 μ seconds, photographed at 20,150 fps.

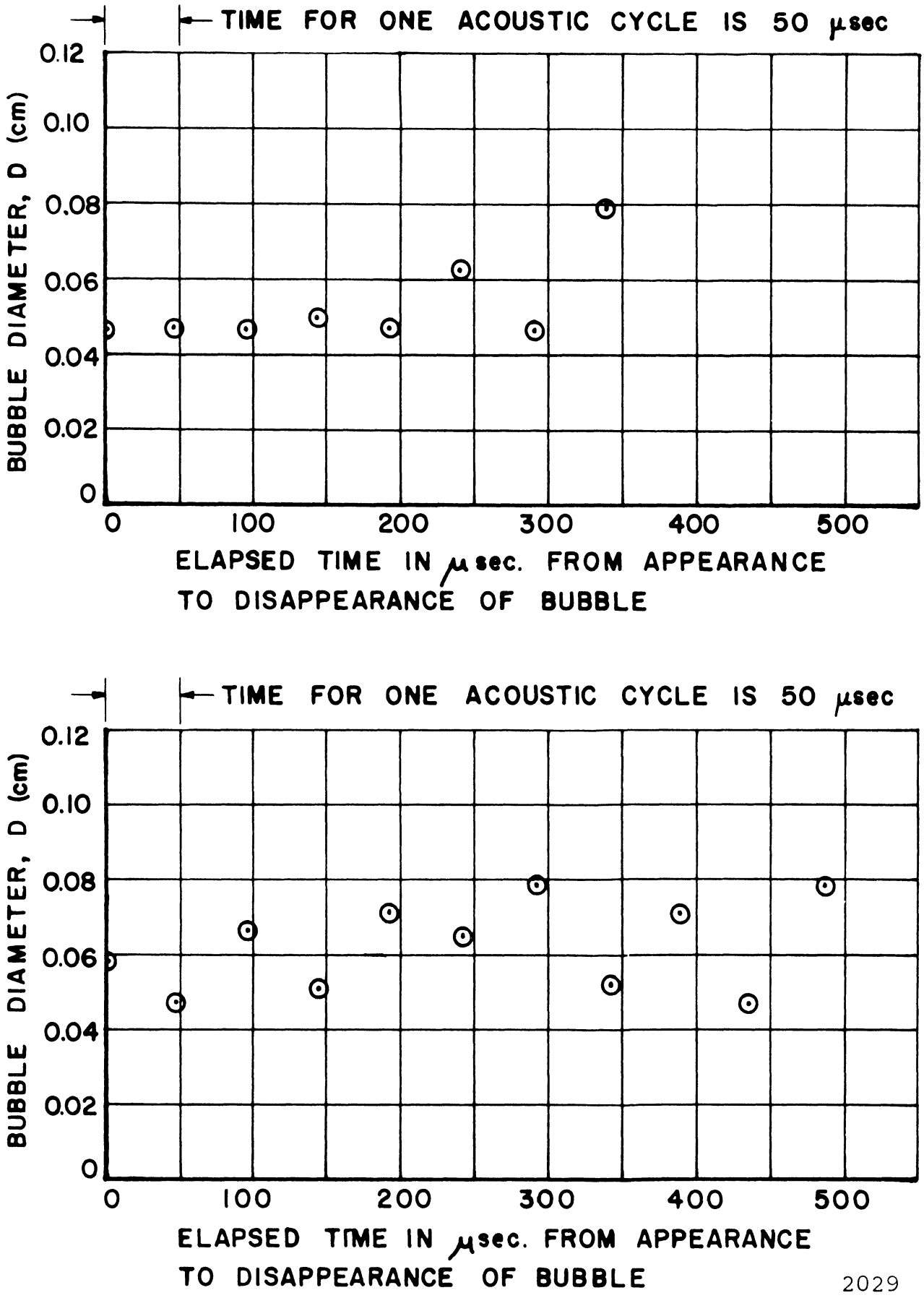

Fig. 38.--Bubble diameter vs. time for individual bubbles on a type 304 stainless steel specimen in water, frequency 20,390 cps, amplitude approximately 2 mils, from photographs having an exposure time per frame of 1.3 μ seconds, photographed at 20,800 fps.

0.032 cm for 20,000 cps). Apparently these large bubbles result from rebounds occurring after a cavitation collapse.

Fig. 39, constructed similarly, contains more photographs per acoustic cycle, since the data was from a run with the frequency at 10,000 cps and the camera at 26,000 frames per second. Since the acoustic period for this run was 100 μ seconds, and the time between frames 38.5 μ seconds, there are two or three data points per cycle. Diameter-time histories are shown for four bubbles. Most of the bubble diameters for all these bubbles remain greater than the predicted mean resonance diameter (0.064 cm for 10,000 cps). However, bubble no. 4 grew slowly from a diameter about half of the mean resonance diameter, then maintained itself at about the mean resonance diameter for two frames, and then grew slightly and disappeared. There could, of course, still be wide variations in diameter of this bubble between the observed data points. A plausible explanation would be that bubble no. 4 started as a transient bubble, collapsed, rebounded, and then oscillated at the resonance diameter, finally expanding and disappearing. There are still insufficient data points to ascertain whether or not these large diameter bubbles oscillate with the acoustic frequency. In Fig. 39 they appear to do so. Interestingly, bubbles no. 2 and 3 merged, contracted to almost the mean resonance diameter, expanded again, then disappeared. There does seem to be an upper limit in diameter for the bubbles observed on Fig. 39. Perhaps at this upper limit the

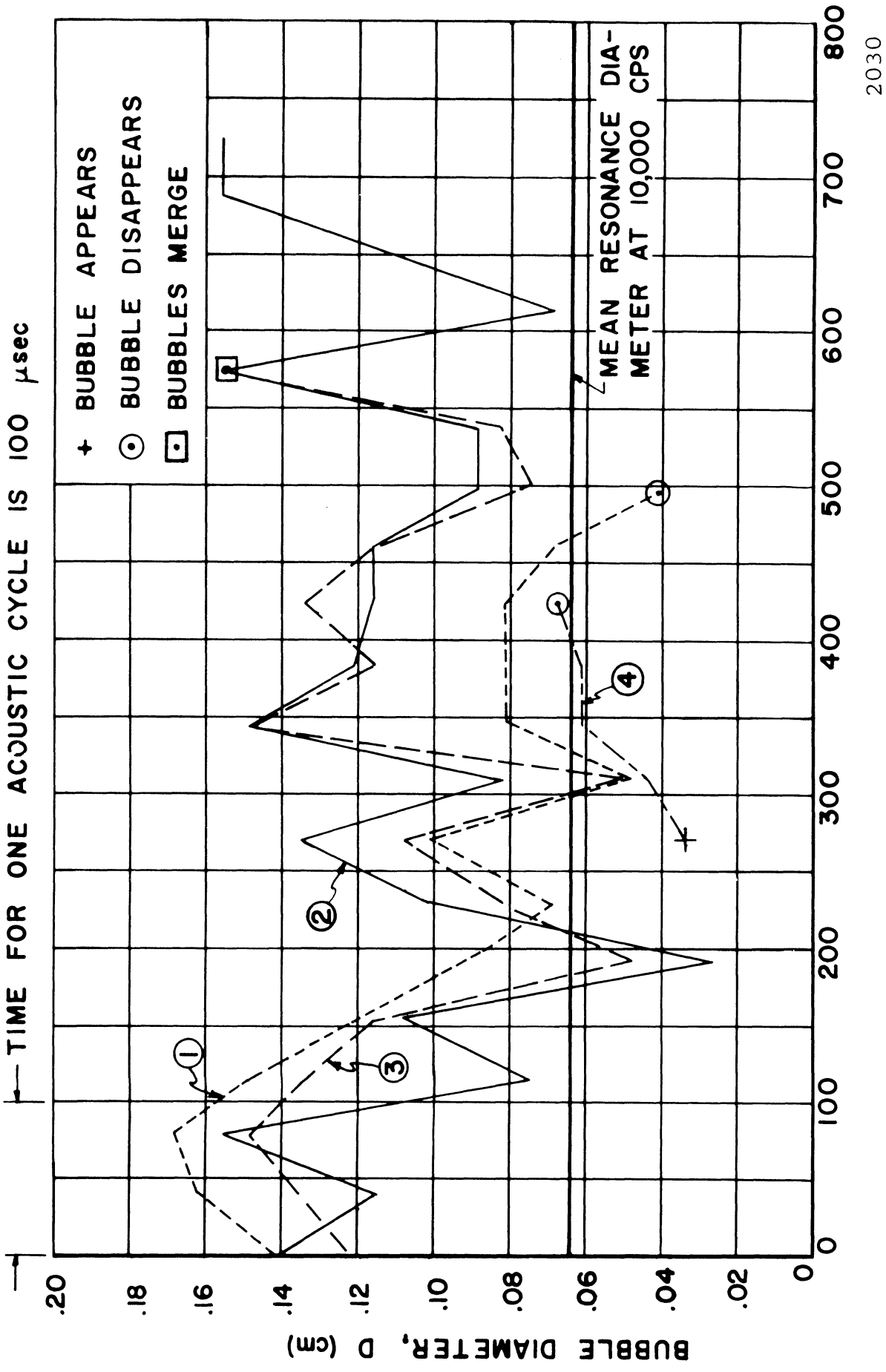

Fig. 39.--Bubble diameter vs. time for 4 selected bubbles on a type 304 stainless steel specimen in water, frequency 10,000 cps, from photographs having an exposure time per frame of 1 μsecond, photographed at 26,000 fps.

collapse speed is sufficient to complete the collapse before the onset of the next negative pressure cycle.

The charcoal-like smudges which appear during early growth on the high speed photographs are thought to be rebounding bubbles. They have a roughened surface that absorbs the light, causing this appearance, which itself suggests that the surface, or possibly the entire vaporous mass, could be composed of a myriad of very small diameter bubbles. Some of the large rebounding bubbles during growth are extremely dark on the photographic prints, but still show a roughened or almost spiny surface if sufficient filters are used during the printing process to practically eliminate that portion of the photograph that is normally printed.

A possible explanation for this very great capability for light absorption in this type bubble is that the cluster of bubbles so thoroughly diffuses the light (very probably the spherical surfaces of the minute bubbles act as lenses) that little is reflected back to the camera, and the bubble appears on the negative almost as unexposed film. The smooth bubbles are highly reflective and do return considerable light to the film. After the bubble has fully rebounded and oscillates in the acoustic field it recovers its smooth, glossy appearance.

E. Shock Waves from Rebounding Bubbles

Schmid's[27] photographic sequence taken in a somewhat similar cavitation field in that bubbles were generated by the sudden deceleration of a fast moving liquid column, showed for a single bubble the collapse, rebound, and resultant shock wave. These pictures were taken at 58,000 frames per second and it was noted by Schmid that the shock wave persisted for approximately 10 μ seconds. This collapse and rebound sequence is reproduced in Fig. 40. The shock ring is visible in frame no. 22. It occurs at that point in the cycle where the bubble is at its minimum diameter, but persists for a portion of the rebound.

Photographic evidence of the effect of such shock waves in a cavitation bubble field is shown in Figs. 41-A and B, taken from the same photographic run of this investigation, but out of sequence. The frequency was 10,000 cps and the camera operated at 26,000 frames per second. Fig. 41-A shows the full cavitation cloud with some bubbles out of focus since they apparently are at an appreciable distance from the specimen surface. Fig. 41-B shows a mist in the central area of the photograph which may be interpreted as smaller bubbles which are the debris from larger bubbles that were collapsed by the shock wave from the rebounding bubble.

Fig. 41-A is no. 11 of a sequence and Fig. 41-B is no. 6. By reconstructing the sequence as was done in Fig. 33, Fig. 41-B preceeds Fig. 41-A in the acoustic cycle by 8.5 μ

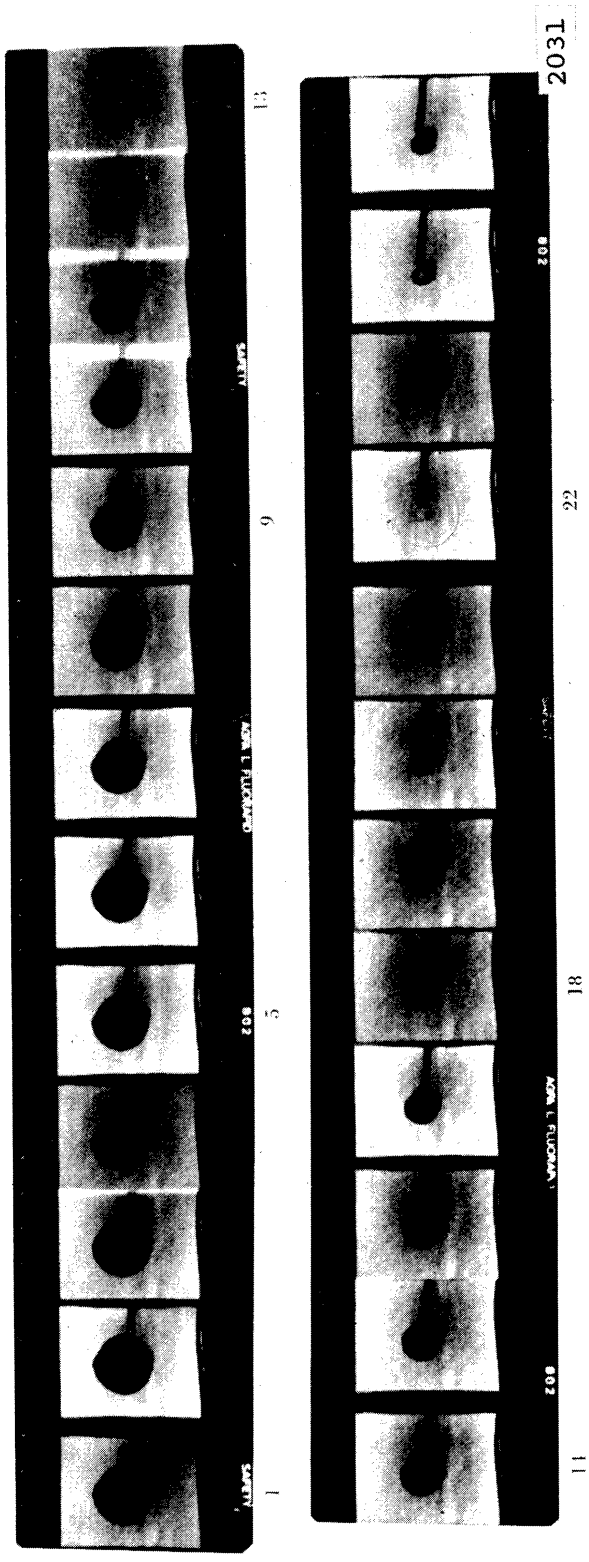

Fig. 40.--High speed photographic sequence by Schmid[27] photographed at 58,000 fps.

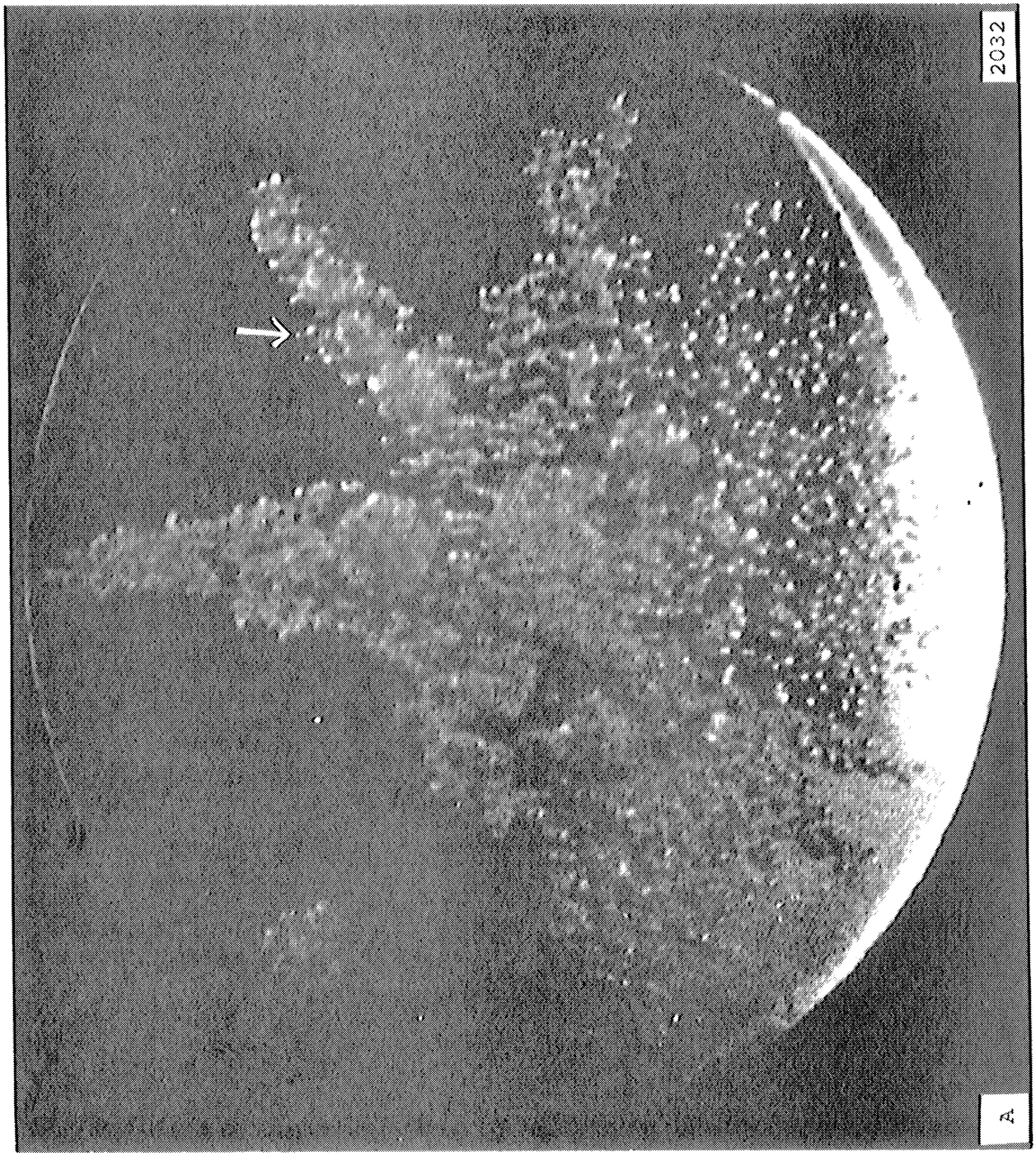

Fig. 41--High speed photographs (14X), A and B, not in sequence of a partially polished, partially abrased, type 304 stainless steel specimen in water, frequency 10,000 cps, exposure time per frame of 1 μ second, photographed at 26,000 fps.

Fig. 41.--Continued

seconds. As brought out in Section N of this Chapter the condition of the "bar-bell" bubble (marked by arrow) shows that Fig. 41-A is precisely at the collapse point. Fig. 41-B passed through Fig. 41-A's phase 8.5 μ seconds previously and apparently has experienced a collapse.

Figs. 42-A, B, and C are a sequence of three photographs taken from a run using a type 2024-T351 aluminum specimen where the oscillator frequency and the camera framing rate were almost matched at 20,200 cps and 20,150 frames per second respectively. Fig. 42-A shows a fairly heavily populated bubble field, apparently from some portion of the negative pressure part of the cycle, judging by the size of both the transient and the larger bubbles. Note the cleared area around the large bubble in the center (indicated by an arrow). It is thought that this area has been swept clear of bubbles momentarily by the local high pressure region surrounding the large, apparently rebounding bubble, and/or by the outward liquid velocity induced by this rebounding bubble. Fig. 42-B shows a large number of bubbles (also marked with arrows) that have apparently collapsed fairly completely, judging from their light-absorbing roughened contours, and are rebounding. Since Figs. 42-A and B are successive frames and the frequency and framing rates are matched, they show the same part of the acoustic cycle. Thus the difference in population is important. Fig. 42-C, one cycle later than Fig. 42-B, shows large, roughly circular cleared areas, and also a heavy bubble population in outer

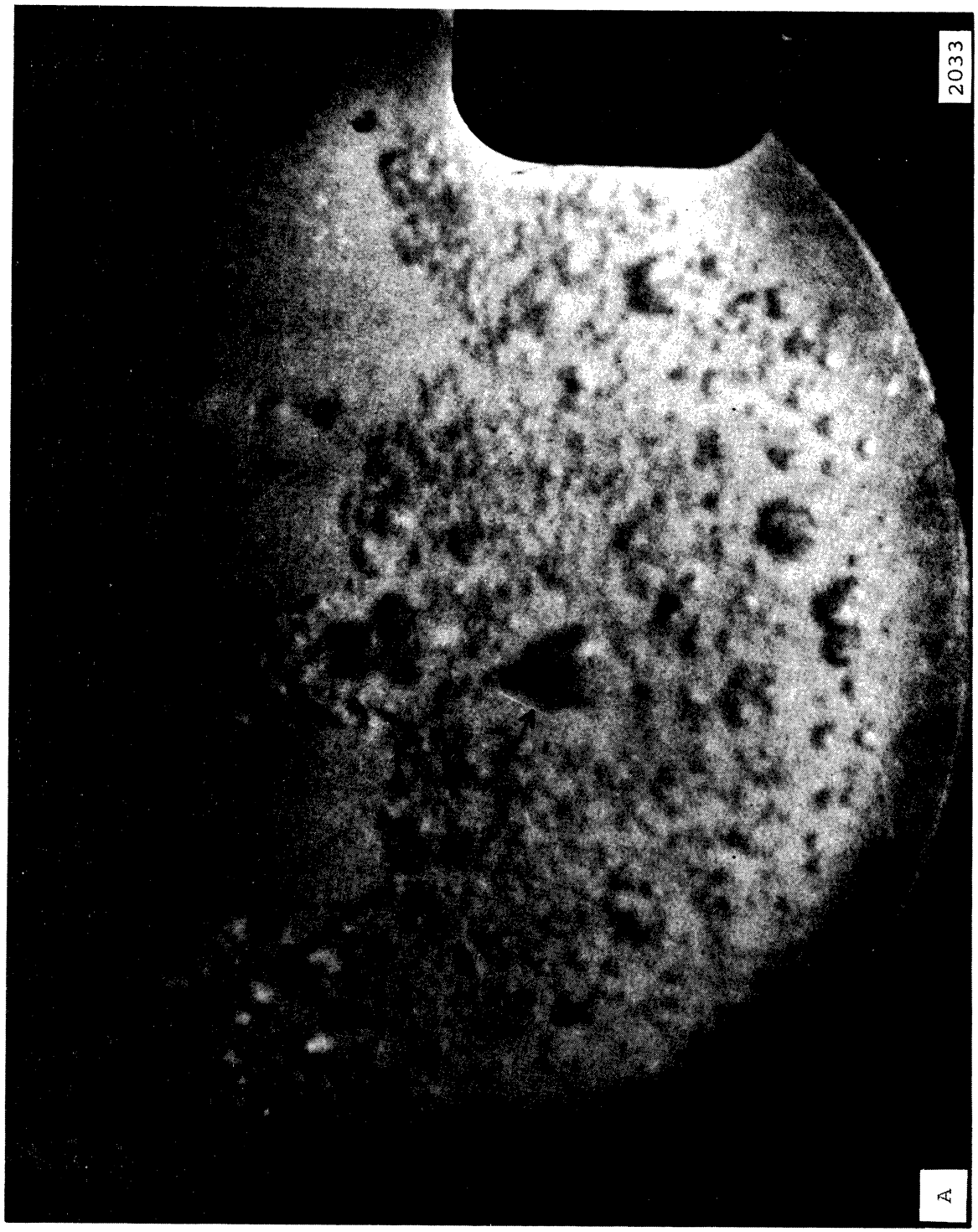

Fig. 42. High speed photographic sequence (14X), A, B, and C, of a type 2024-T351 aluminum specimen in water, frequency 20,200 cps, amplitude approximately 2 mils, exposure time per frame of 1.3 μseconds, photographed at 20,150 fps.

Fig. 42.--Continued

Fig. 42.--Continued

areas. Some of the rebounding bubbles in Fig. 42-B can be matched with those in Fig. 42-C (see parallel-slanted arrows), but their appearance is different. In Fig. 42-B they were apparently rebounding after a collapse. In Fig. 42-C, judging by their size and glossy surface, they probably have survived without collapse during the last positive pressure portion of the cycle. However, there are now two new rebounding bubbles (marked "X"'s) which have apparently cleared the small bubbles from their vicinity.

The rebounding bubbles, at least in their early and intermediate growth stages, certainly appear as if they were composed of many smaller bubbles. Schmid[27] thought that the reason the shock wave persisted so long is that there were successive implosions from many different bubbles. This does not seem too plausible, even though the rebounding bubble appears with a roughened surface that suggests that it could be made up of many small bubbles, since the collapsing bubble may not have been composed of these small bubbles. Another possible explanation for the persistance of the shock wave and the spiny appearance of the rebounding bubbles is proposed in Section N of this Chapter. As the rebounded bubble oscillates in the acoustic field, its surface becomes shiny without individual bubble definition. Smaller bubbles could exist on the coutour, however.

Figs. 43-A through F, six photographs taken from another portion of the run used for Figs. 42-A, B and C, indicate that

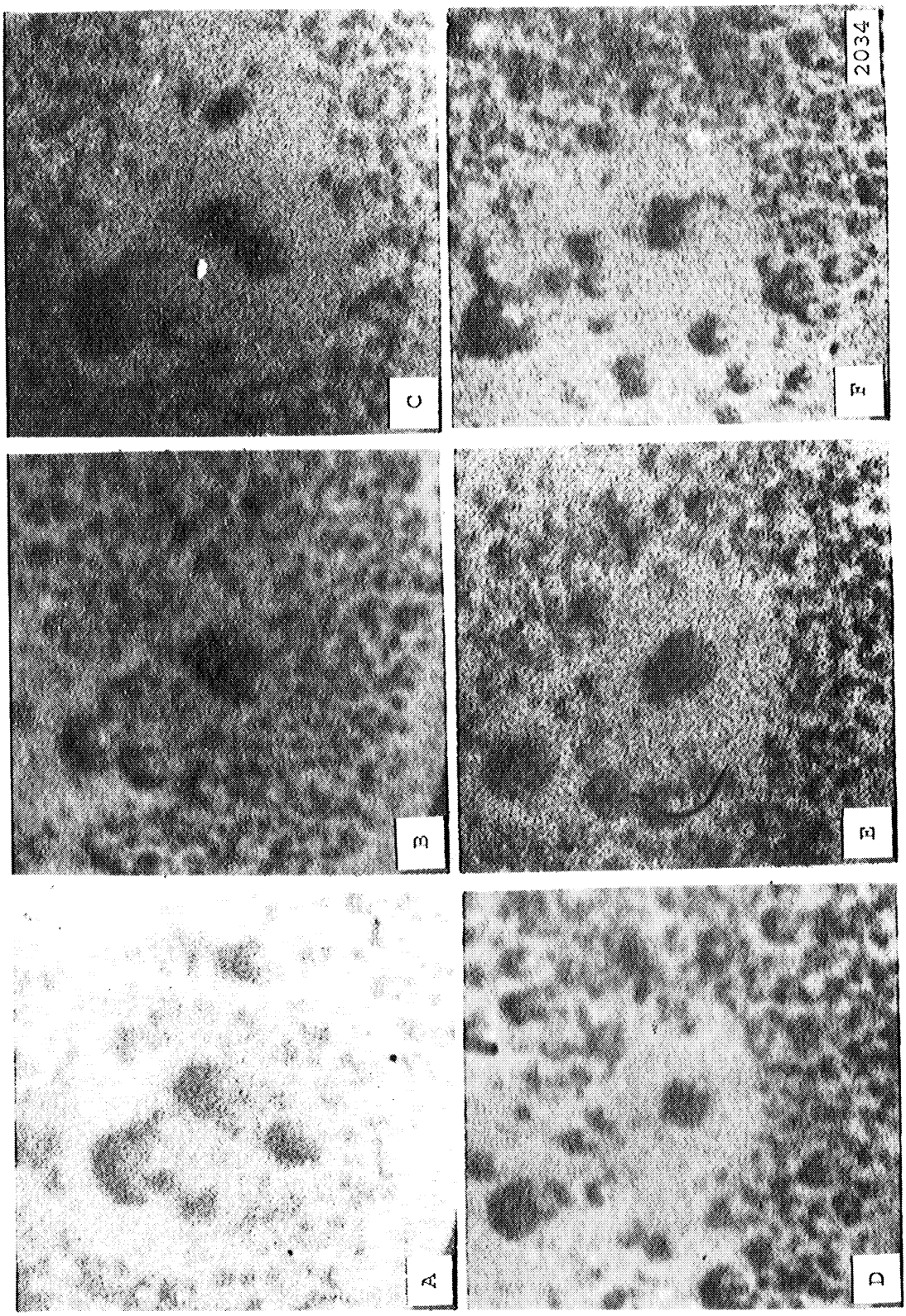

Fig. 43.--High speed photographic sequence (14X), A through F, of a type 2024-T351 aluminum specimen in water, frequency 20,200 cps, amplitude approximately 2 mils, exposure time per frame of 1.3 μ seconds, photographed at 20,150 fps.

the area around a rebounding bubble may remain clear of bubbles through many cycles. In this way the rebounding bubbles greatly affect the bubble population and its pattern. The local over-pressure resulting from a rebounding bubble presumably collapses the transient bubbles that have started to expand in the negative pressure part of the cycle. In addition, the outward liquid velocity around a rebounding bubble may contribute to the existence of a circular bubble-free area. However, the spherical symmetry that almost always exists around the rebounding bubble makes doubtful the importance of this velocity effect since other velocities induced by the horn motion might upset the symmetry if velocity effects were important. Also the bubble population density around the cleared areas would presumably be increased as bubbles were swept into the adjacent area. This has not been observed.

F. Profile Photographs

A series of true profile photographs (frames from high speed photographic sequences), and also a series where the horn was tilted slightly towards the camera (angle of tilt of about 2°) so that a portion of the specimen surface was visible, have been obtained. All were made using a type 304 stainless steel specimen.

Fig. 44 is a sequence of five true profile photographs. Since the acoustic period is 50 μseconds and the time between frames is 38.5 μseconds, there will be one, or possibly two,

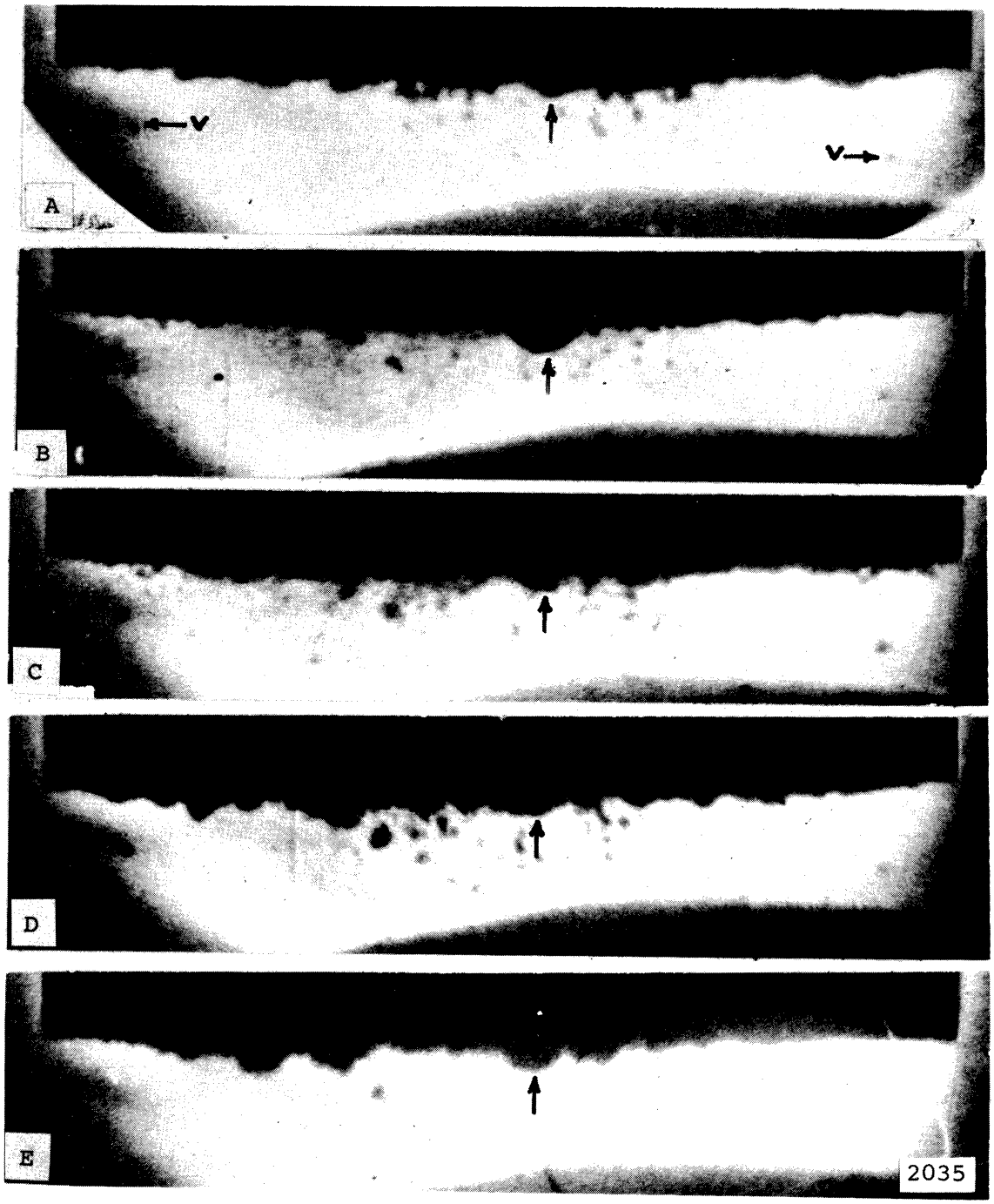

Fig. 44.--High speed photographic sequence (11X), A through E, of a type 304 stainless steel specimen in water, frequency 20,300 cps, amplitude approximately 2 mils, exposure time per frame of 1μ second, photographed at 26,000 fps.

photographs per acoustic cycle. This sequence shows the growth, collapse and rebound of a hemispherically-shaped bubble (marked by the arrow).

Fig. 45 is a sequence of 11 profile photographs showing formation, first collapse, rebound, second collapse, rebound, and final collapse of a bubble that is in a semistable position below the specimen surface. The frequency is 20,300 cps and the camera framing rate 26,000 frames per second. Nos. D, F, G, H, and I of the sequence strongly suggest that the bubbles are in a toroidal shape with the axis normal or almost normal to the specimen surface above (this will be further discussed in Section N of this Chapter). The appearance of these bubbles is remarkably similar to those photographed by Ivany[20] in a venturi diffuser.

Fig. 46 is a sequence of three profile photographs taken from a run where the frequency was 20,300 cps and the framing rate 26,000 frames per second. This sequence shows an oblong type of bubble (see arrows), which is long in the vertical direction. Bubbles of this type are highly unstable, since when they do appear, they are generally gone (although not in the present case) from the next photograph in the sequence. This type of non-spherical bubble was discussed by Rattray[55] who predicted that such perturbations would increase the collapse time. The appearance in three successive frames of an elongated bubble of this type is not usual. Fig. 47, a sequence of three profile photographs made under similar

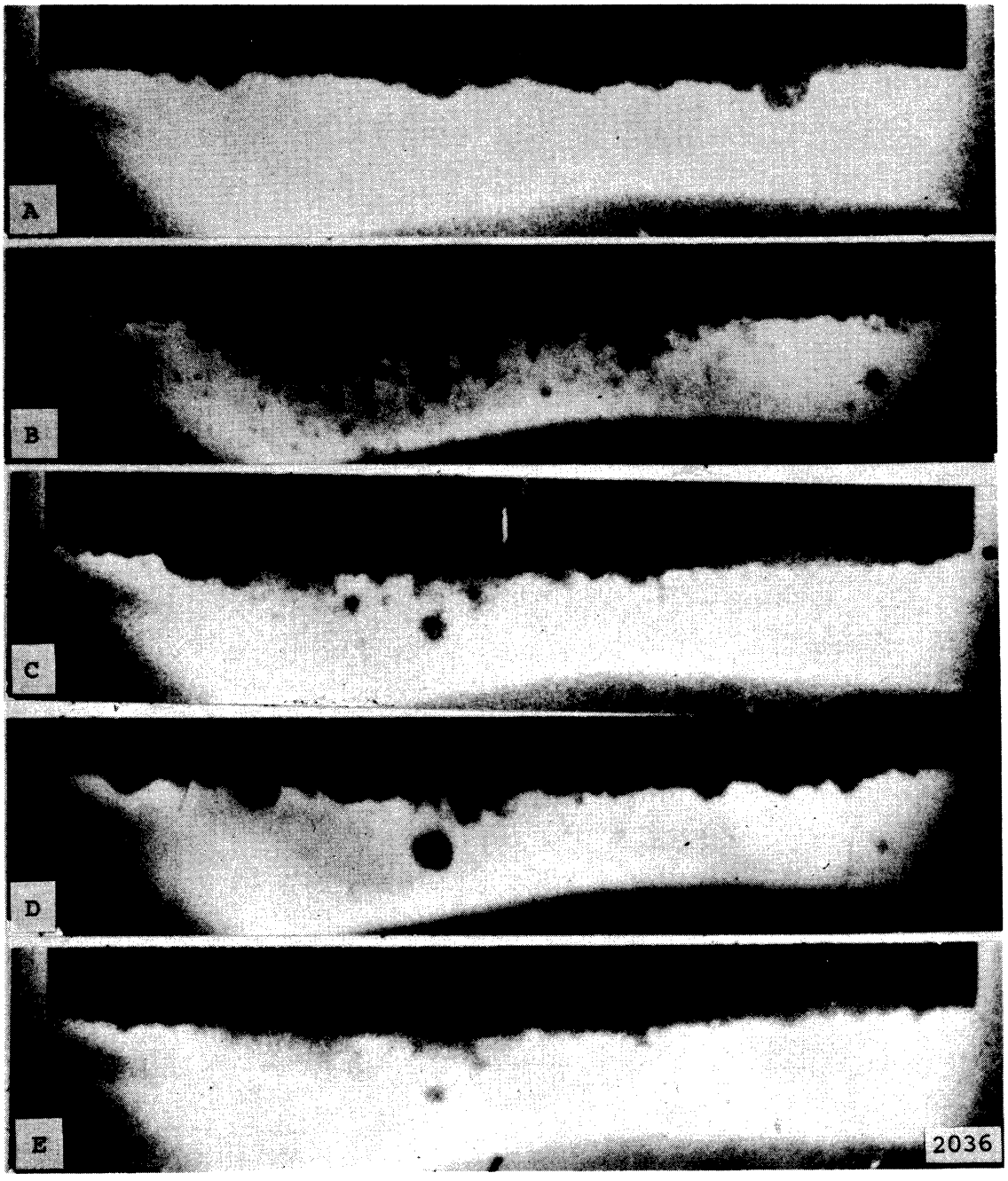

Fig. 45.--High speed photographic sequence (11X), A through K, of a type 304 stainless steel specimen in water, frequency 20,300 cps, amplitude approximately 2 mils, exposure time per frame of 1 μsecond, photographed at 26,000 fps.

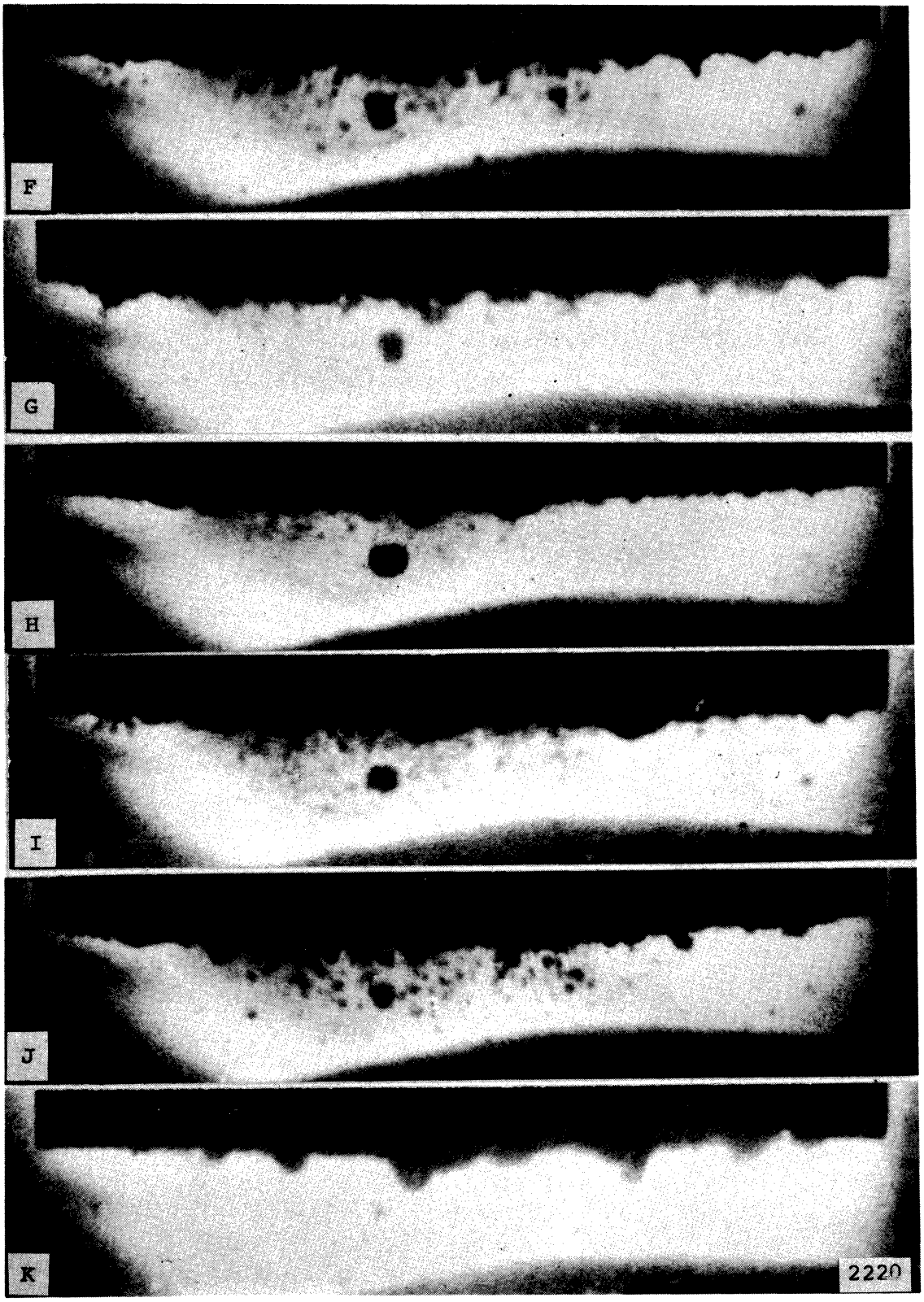

Fig. 45.--Continued

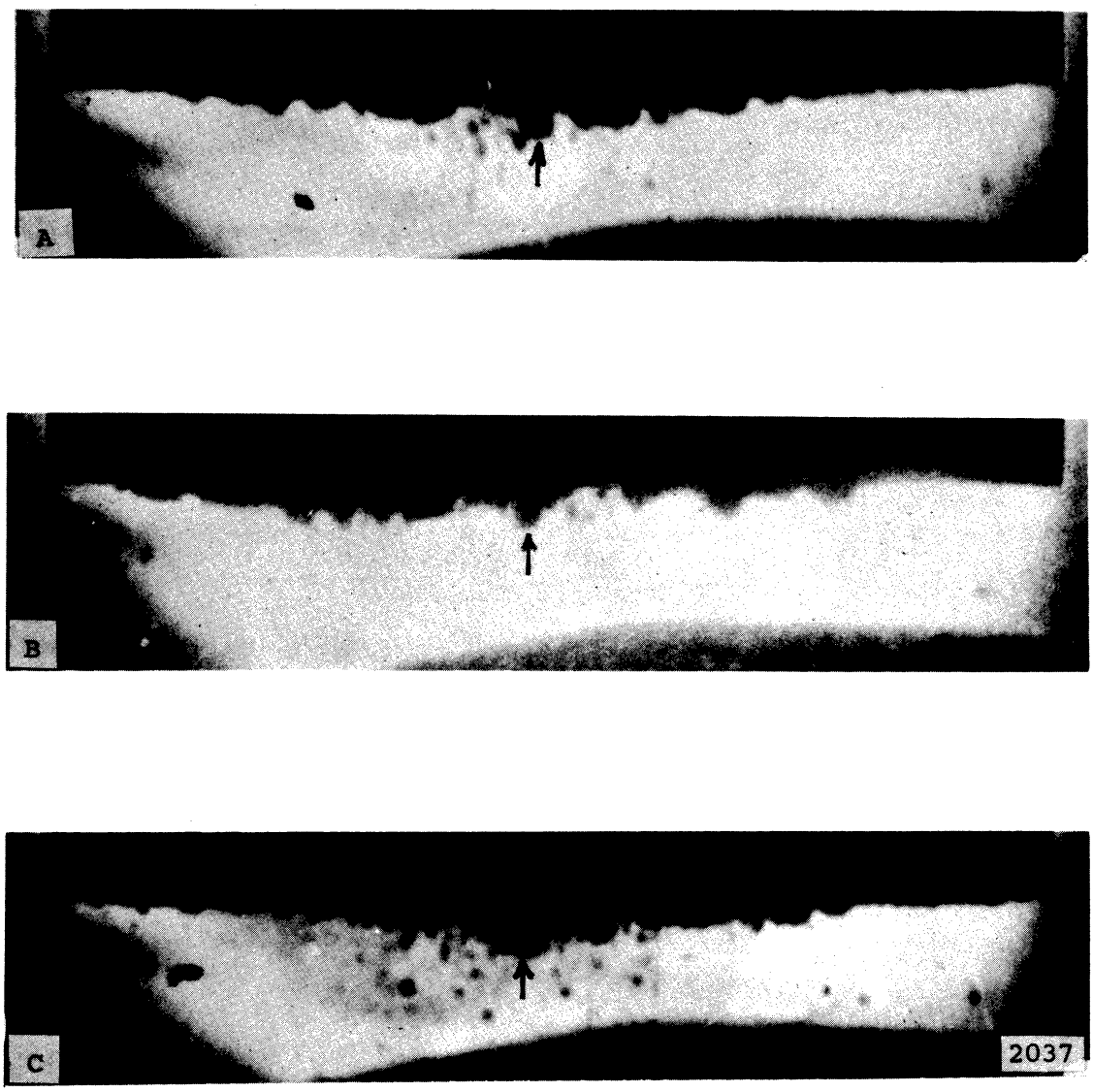

Fig. 46.--High speed photographic sequence (11X), A through C, of a type 304 stainless steel specimen in water, frequency 20,300 cps, amplitude approximately 2 mils, exposure time per frame of 1 μsecond, photographed at 26,000 fps.

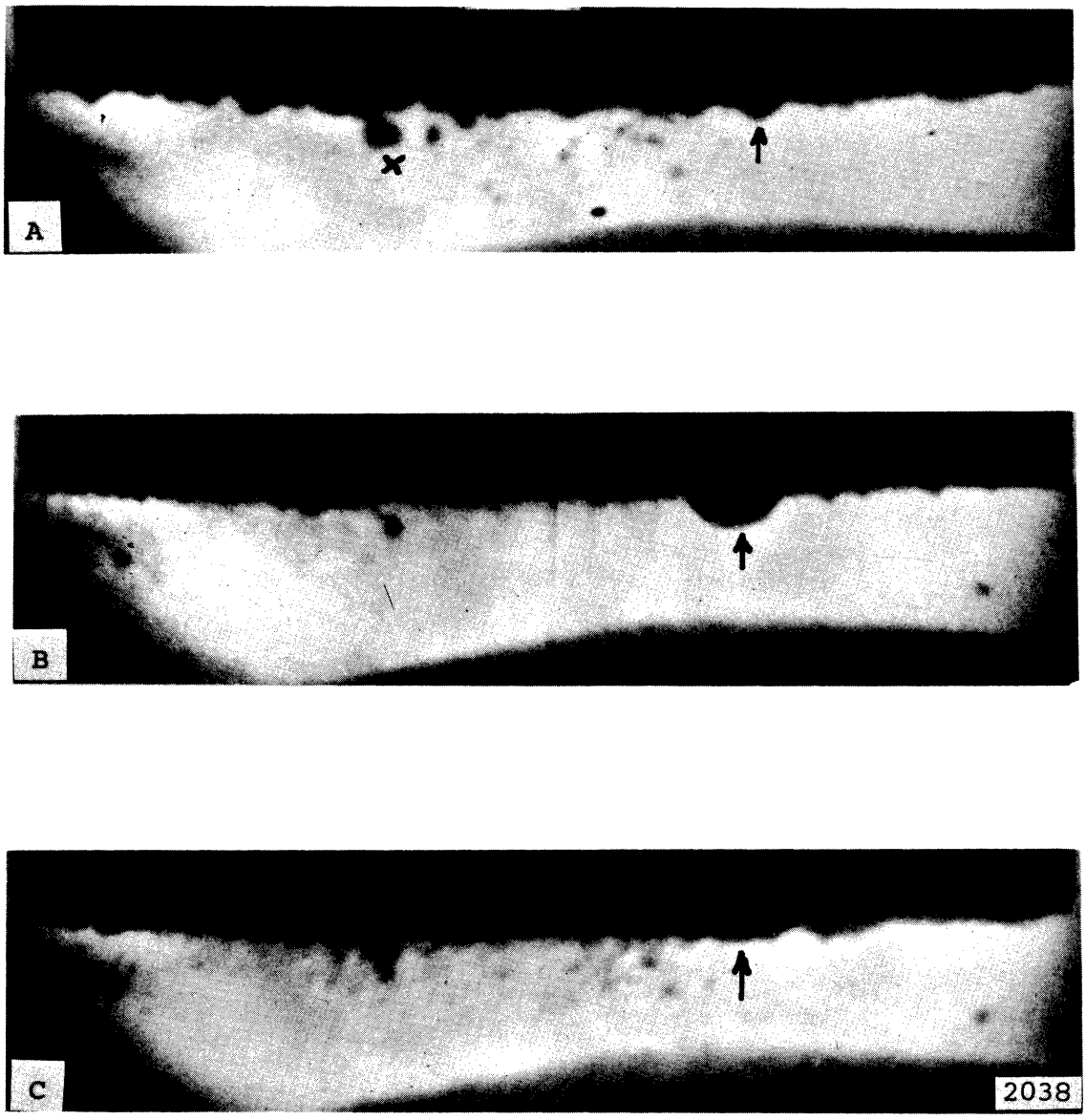

Fig. 47.--High speed photographic sequence (11X), A through C, of a type 304 stainless steel specimen in water, frequency 20,300 cps, amplitude approximately 2 mils, exposure time per frame of 1 μsecond, photographed at 26,000 fps.

conditions to Fig. 46, shows the growth and collapse of a hemispherically-shaped bubble without rebound. The bubble at left in Fig. 47-A marked "X" suggests that it is in a toroidal collapse. If so, the streamer from this bubble in Fig. 47-B to the upper left could be a cavitation vapor trail left by the high speed central jet from the toroidal collapse, as is discussed later in Section N of this Chapter.

Fig. 48, photographed with the frequency set at 20,300 cps and with a framing rate of 26,000 frames per second, illustrates the method used to determine photographically the horn amplitude. It also shows interesting hemispherical bubbles of various diameters on the specimen surface in the left-hand part of the picture.

Fig. 49 is a sequence of two photographs from a run with the frequency set at 20,300 cps, and the camera speed at 26,000 frames per second. Fig. 49-A shows a large bubble (see arrow) apparently collapsing toroidally. In Fig. 49-B the elongated bubble that is marked appears to indicate that a toroidal collapse has taken place and this bubble could be the same one as in Fig. 49-A.

Similarly, all of the next series (Figs. 50 through 53) were photographed with the frequency at 20,300 cps and the camera speed at 26,000 frames per second, but the horn was tilted slightly from the vertical (angle of about 2°). The individual photographs are shown out of sequence. The particular bubbles that are discussed are indicated with an

Fig. 48.--High speed photograph (14X) used to determine amplitude of a type 304 stainless steel specimen in water, frequency 20,300 cps, amplitude approximately 2 mils, exposure time per frame of 1 μ second, photographed at 26,000 fps.

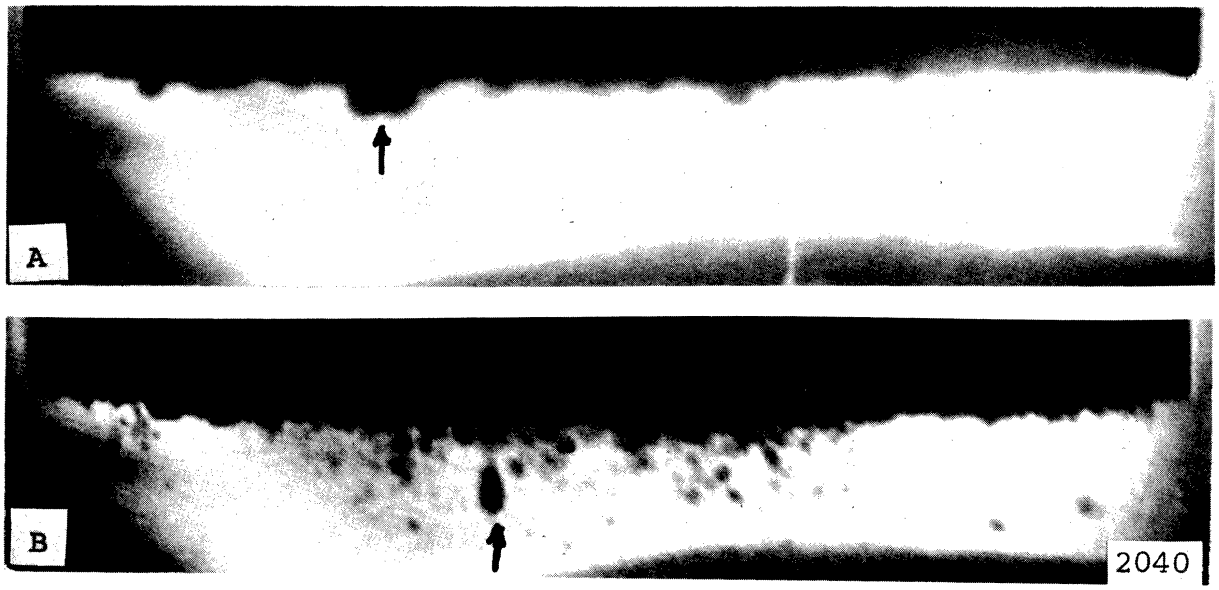

Fig. 49.--High speed photographic sequence (11X), A and B, of a type 304 stainless steel specimen in water, frequency 20,300 cps, amplitude approximately 2 mils, exposure time per frame of 1 μsecond, photographed at 26,000 fps.

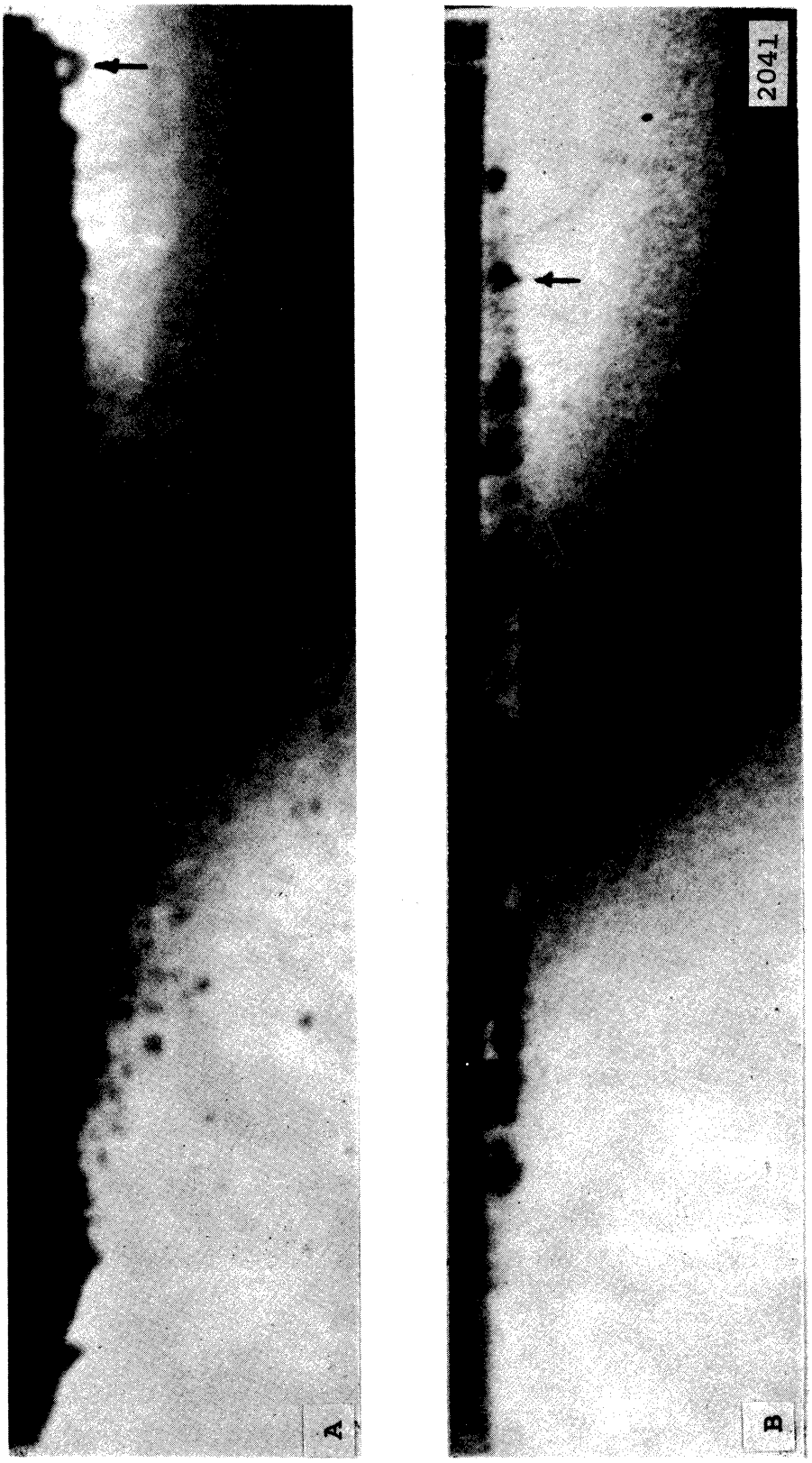

Fig. 50.--High speed photographs (15X), A and B, not in sequence, of a type 304 stainless steel specimen in water, frequency 20,300 cps, amplitude approximately 2 mils, exposure time per frame of 1 μsecond, photographed at 26,000 fps.

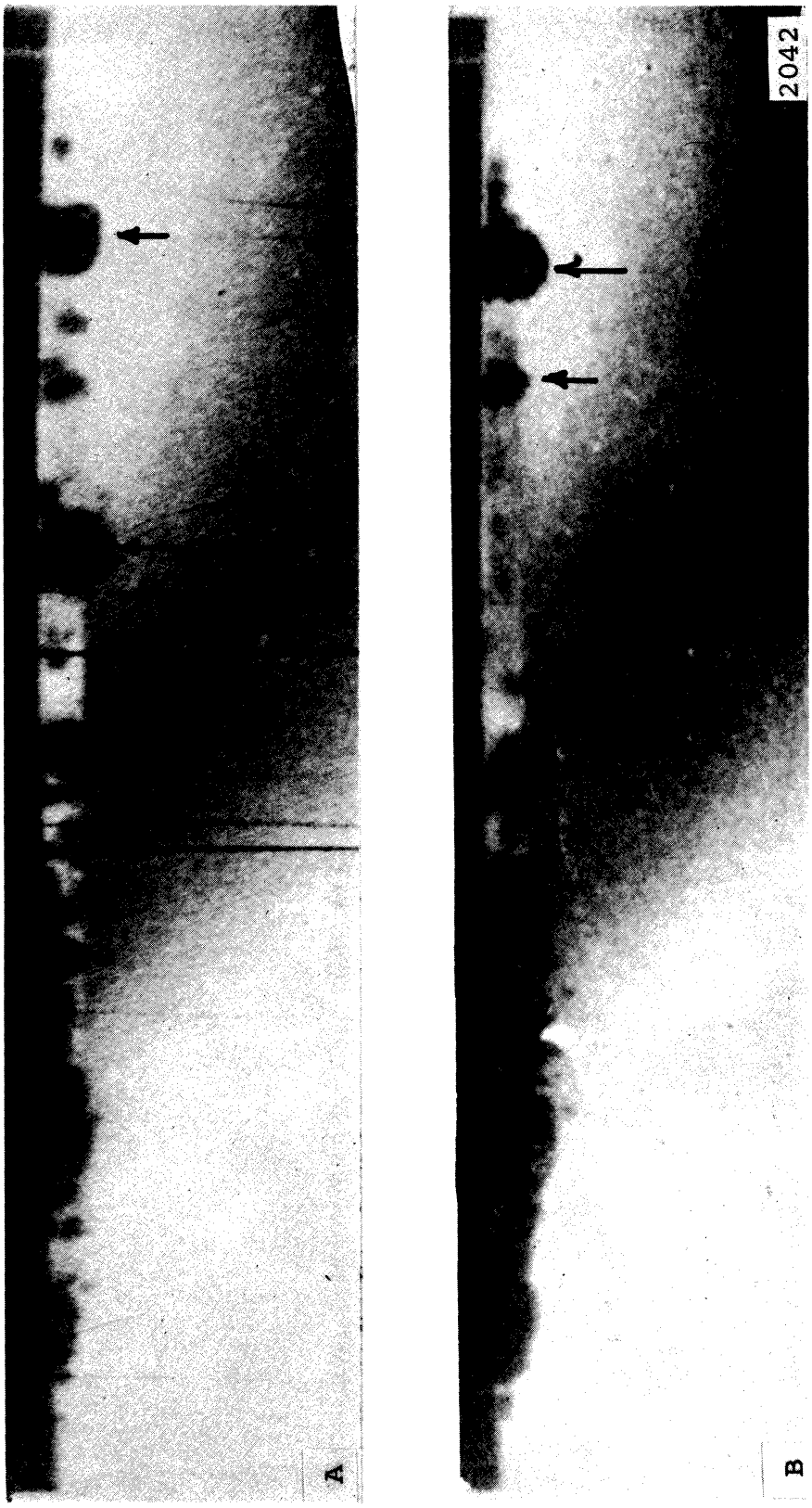

Fig. 51.--High speed photographs (15X), A and B, not in sequence, of a type 304 stainless steel specimen in water, frequency 20,300 cps, amplitude approximately 2 mils, exposure time per frame of 1 μsecond, photographed at 26,000 fps.

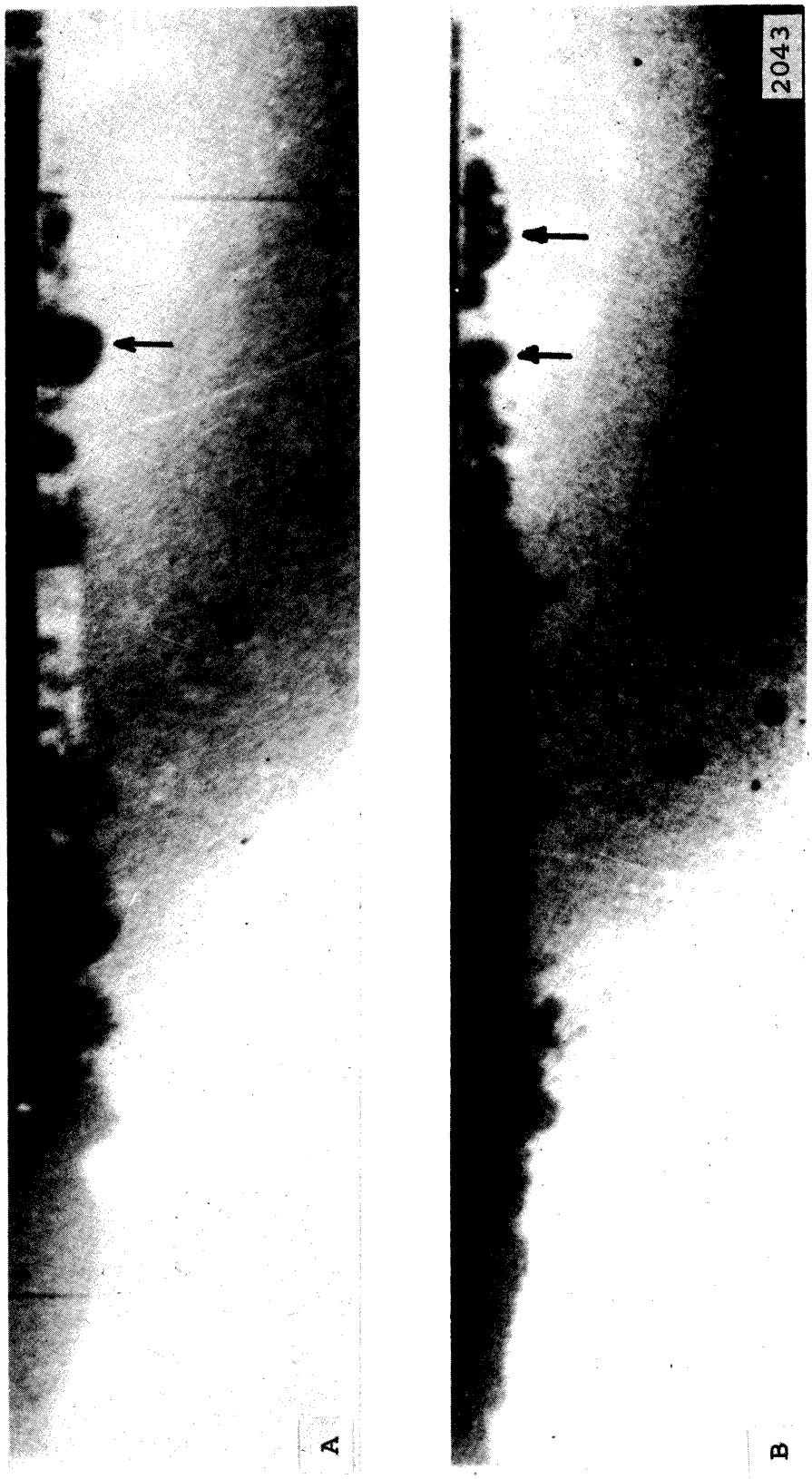

Fig. 52.--High speed photographs (15X), A and B, not in sequence, of a type 304 stainless steel specimen in water, frequency 20,300 cps, amplitude approximately 2 mils, exposure time per frame of 1 μ second, photographed at 26,000 fps.

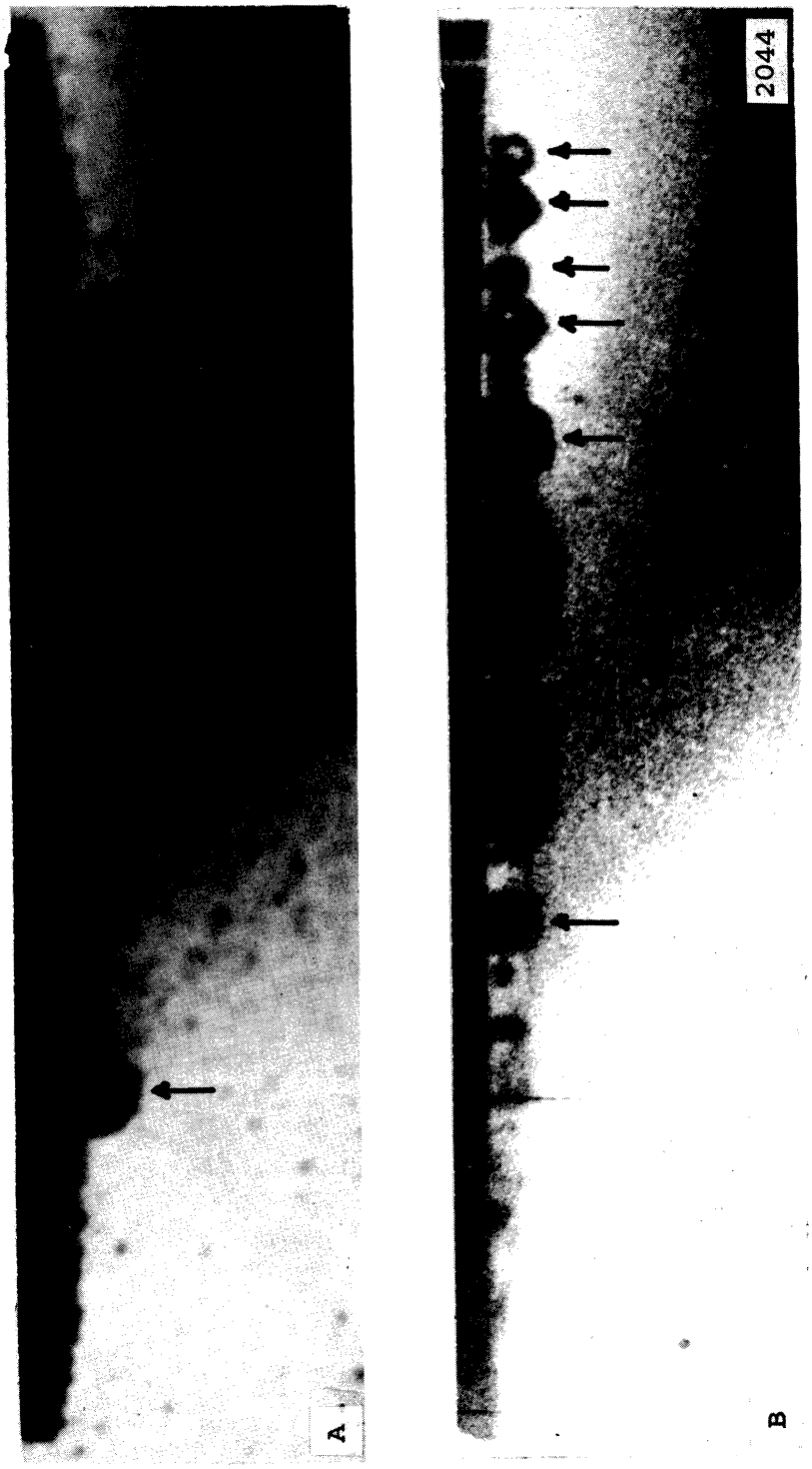

Fig. 53.--High speed photographs (15X), A and B, not in sequence, of a type 304 stainless steel specimen in water, frequency 20,300 cps, amplitude approximately 2 mils, exposure time per frame of 1 μ second, photographed at 26,000 fps.

arrow on the photographs. Fig. 50-A shows a large bubble at the outer right edge, a position where they are seldom seen (an area incidentally where damage is greatly reduced). Fig. 50-B shows the low bubble population portion of the acoustic cycle. The bubble indicated is believed to be in the final phase of collapse as is discussed in Section N of this Chapter. The areas at the right could have been cleared by rebounding bubbles as previously discussed. The large bubbles in Figs. 51-A and B, 52-A and B, and 53-A and B are almost identical in shape to many of the spark-induced bubbles in the Shutler and Mesler[23] experiments that were shown to be in a toroidal collapse mode. The bubbles marked were highly unstable and were gone in each case in the next frames. It is more difficult to study the shapes of the smaller bubbles that are shown, because their profiles are not as well defined as those of the larger ones, though generally their shapes are the same. This is especially noticeable in Fig. 51-B in the cluster of bubbles at the right part of the photograph.

Fig. 54 is a sequence of six photographs with the horn tilted slightly ($\sim 2°$), from a run with the frequency set at 20,300 cps and the camera at 26,000 frames per second. The individual bubbles in the cluster below the center portion of the specimen held their relative positions quite closely through the entire sequence, even though their size and shape changed.

Fig. 55, taken from a run made with the frequency set at 20,300 cps and the camera at 26,000 frames per second, with

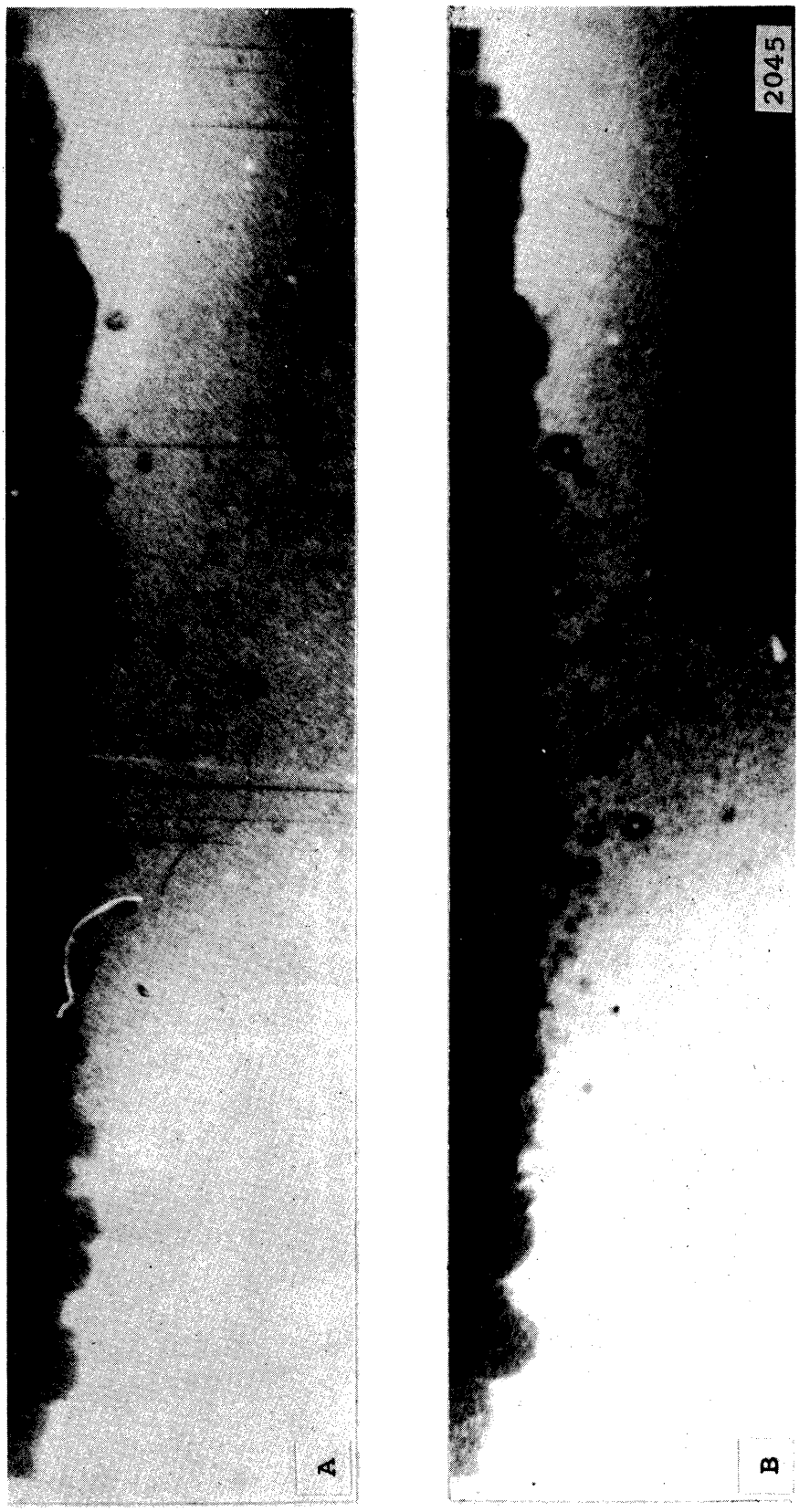

Fig. 54.--High speed photographic sequence (15X), A through F, of a type 304 stainless steel specimen in water, frequency 20,300 cps, amplitude approximately 2 mils, exposure time per frame of 1 μ second, photographed at 26,000 fps.

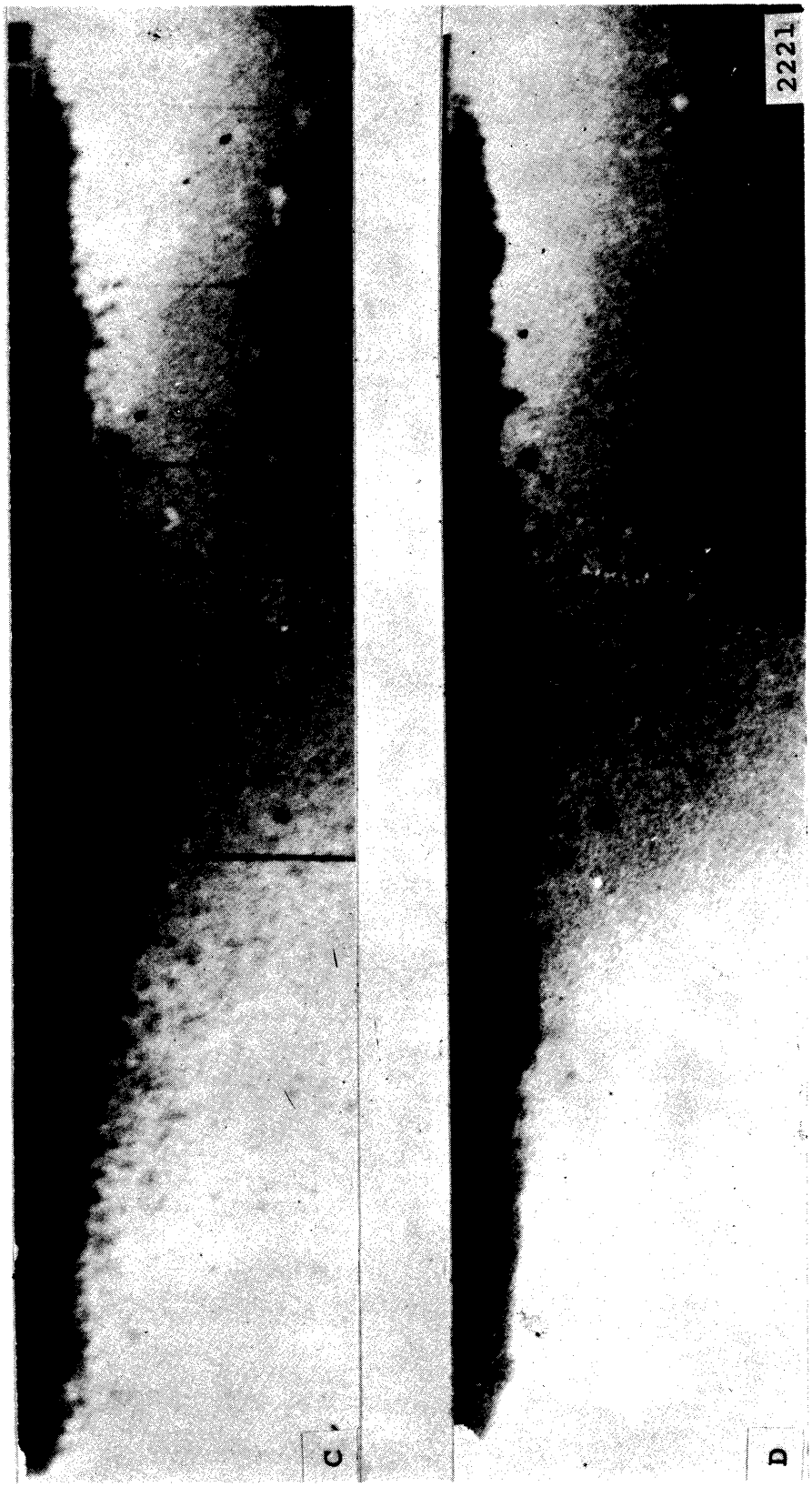

Fig. 54.--Continued

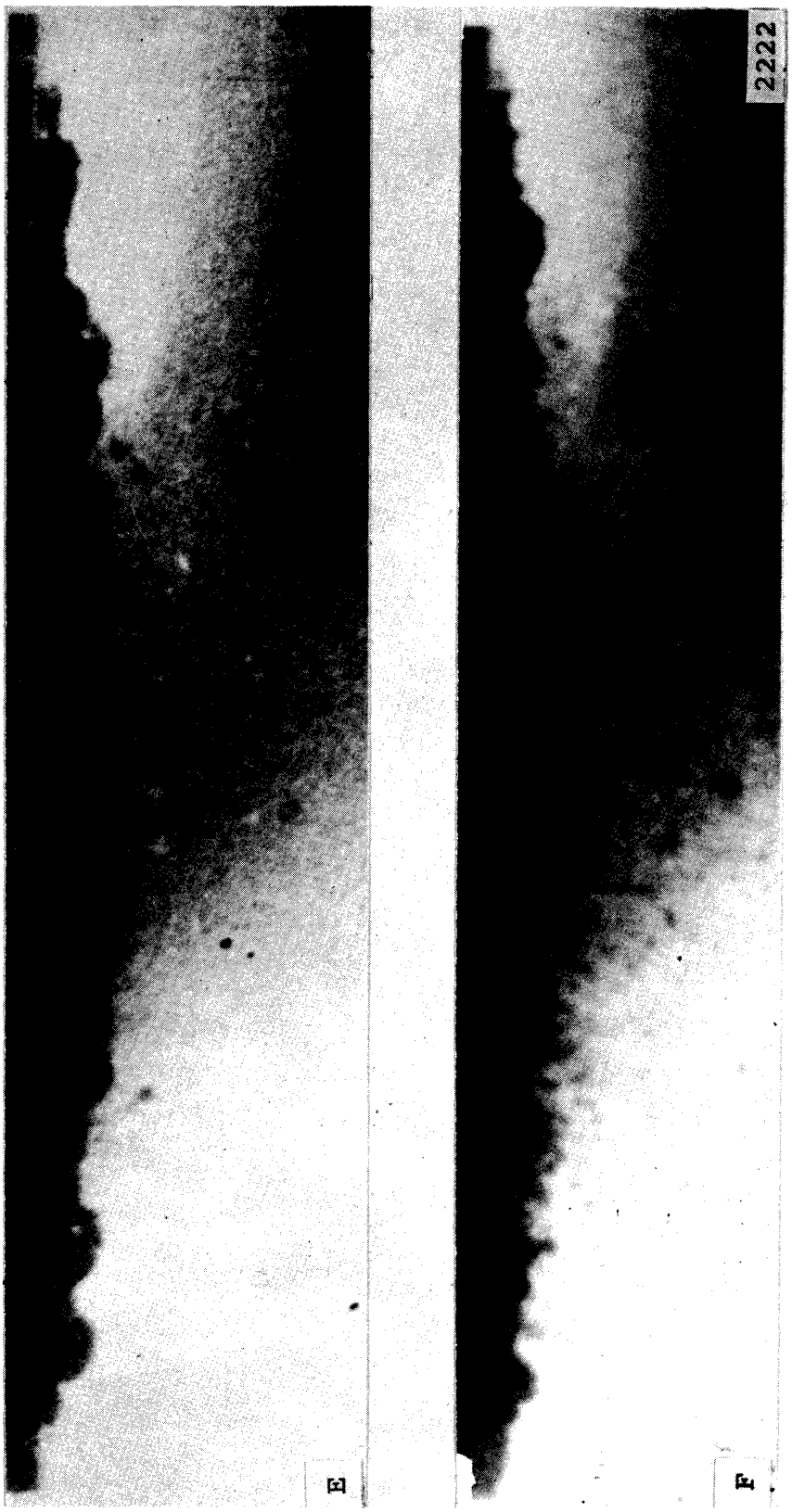

Fig. 54.--Continued

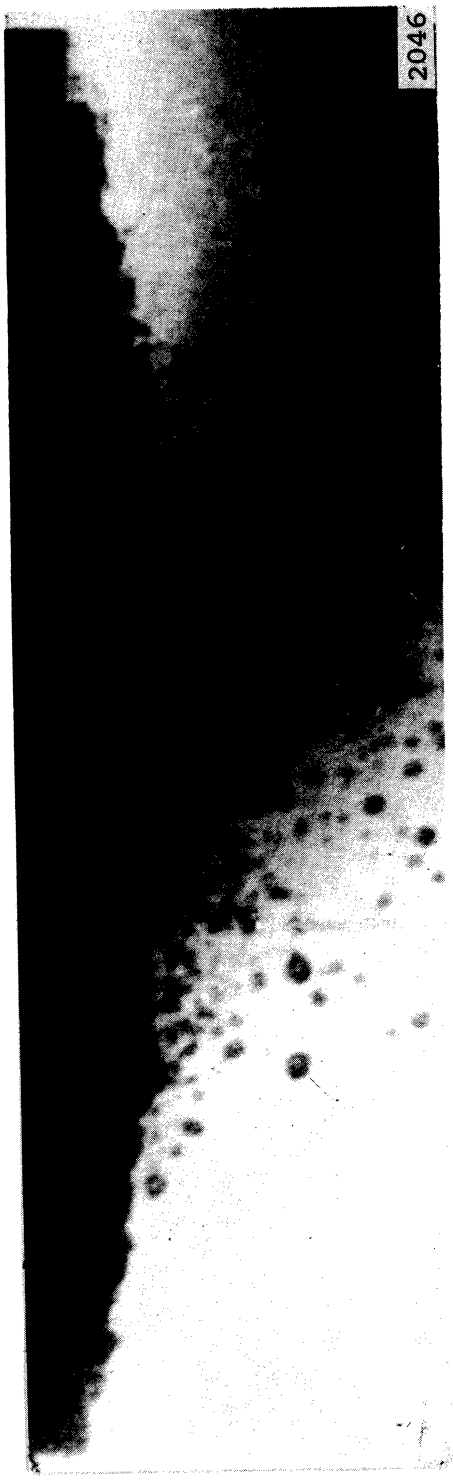

Fig. 55.--High speed photograph (15X) of a type 304 stainless steel specimen in water, frequency 20,300 cps, amplitude approximately 2 mils, exposure time per frame of 1 μsecond, photographed at 26,000 fps.

the horn tilted (~2°) shows the occasional heavy bubble population that occurs below the specimen surface. In general, as shown by the photographs in this section, most of the bubbles are on the specimen surface. This information was of value when assembling bubble populations to compare with pit counts.

G. Flow Patterns

The existence of a vortex ring around the edge of the specimen, which is induced by the vertical motion of the specimen, has been shown experimentally by Jackson and Nyborg[36,37,38]. This vortex ring and others detected by them are shown in Fig. 56. Their experiments showed that the A and A' vortices are clearly a function of the curvature of the specimen edge. Since in this investigation a sharp edge was used, the vortices were substantial as determined experimentaly by Jackson and Nyborg, and they extended well out into the water away from the specimen. They also reported that as h, the distance from the bottom of the water container, is increased beyond approximately 1 cm (their horn diameter was 5.7 cm), the B and B' circulations almost disappear. A and A' are not a function of h, however, until it becomes quite small compared to the horn diameter. The existence of the edge vortex, A', may explain the usual lack of damage on the outer annulus of the specimen surface (see Fig. 56). The pressure around the outside of such a vortex would be higher than that in the core, while the core pressure would be roughly that pressure

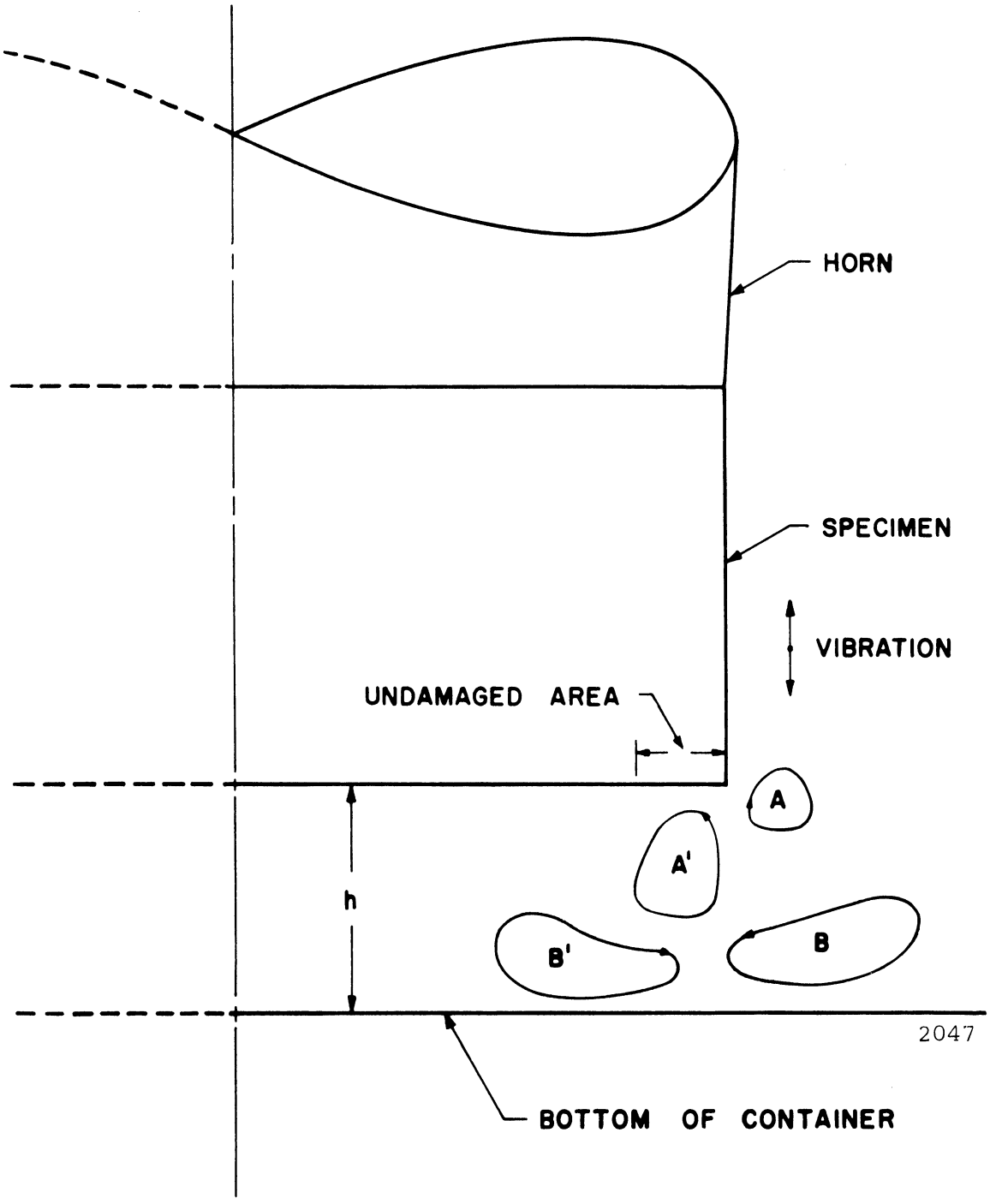

Fig. 56.--Ultrasonically-induced eddy currents near a horn vibrating in the vertical direction in a water container[36].

necessary to nucleate a cavity. Hence bubbles in the outer portion of the vortex ring, i.e., along the edge annulus of the specimen, would be reduced in number.

The vaporous core of the A' ring vortices on each side of the specimen center line can be detected by studying the profile sequences, Figs. 44 through 47, and 49. The two core regions on each side of the horn in Fig. 44-A are indicated by an arrow and a "V." They hover below the specimen surface, one near each outer edge, maintaining their relative positions throughout the entire photographic run, moving and changing in diameter only slightly. That they are not equidistant from the specimen may be due to the asymmetrical geometry of the water container relative to the horn location.

Star-like bubble patterns as shown typically in Figs. 41-A and B are observed only at certain, usually small amplitudes. These patterns have been observed to change with frequencies. The star patterns such as shown on Figs. 41-A and B for a type 304 stainless steel specimen at 10,000 cps frequency generally had 4 or 6 prongs. At 20,419 cps as typified by the copper 900°F annealed specimen in Fig. 57, there were some fine fingers in the bubble pattern at the outer edge annulus, but whether these are similar in nature and origin to the more pronounced star patterns is not known. However, they may be. At the lower frequency the prongs contained large numbers of bubbles, while at the higher frequency they were often only one bubble in width.

Fig. 57.--High speed photograph (14X) of a copper 900°F annealed specimen in water, frequency 20,419 cps, amplitude approximately 2 mils, exposure time per frame of 1.3 μ seconds, photographed at 20,430 fps.

The experimentally recorded trail of a large bubble on a lightly abrased type 304 stainless steel specimen where a heavy bubble population was induced over the entire specimen surface by a 2 mil amplitude at approximately 20,300 cps, is shown in a photographic sequence of 15 frames in Fig. 58. The exposure time per frame is high, 32 μ seconds, since the Fastax camera was used and operated at only 10,400 frames per second. The bubble required 44 milliseconds to move across the top of the tilted specimen starting in the upper right-hand corner, pursuing an arc-like path, and then leaving the specimen in the upper left-hand corner (starting and finishing points are indicated by arrows). Fig. 58 is made with 32 frames removed between each of the frames shown to simplify the presentation. Thus the time between frames is 3.07 milliseconds. The 44 milliseconds required to traverse the specimen corresponds to 880 acoustic cycles, so that the existence of this bubble through so many frames is indeed remarkable. That this type of sequence has not been commonly observed is due to the fact that only with the Fastax camera are enough frames available (and this camera was only seldom used due to its less favorable optical properties) to observe the slow net drift of bubbles in this fashion. Also it may be only very seldom that a bubble will be able to survive collapse for such a long period.

Such arc-like flows across the specimen face may explain the star-like formations, assuming a pattern of the flow paths

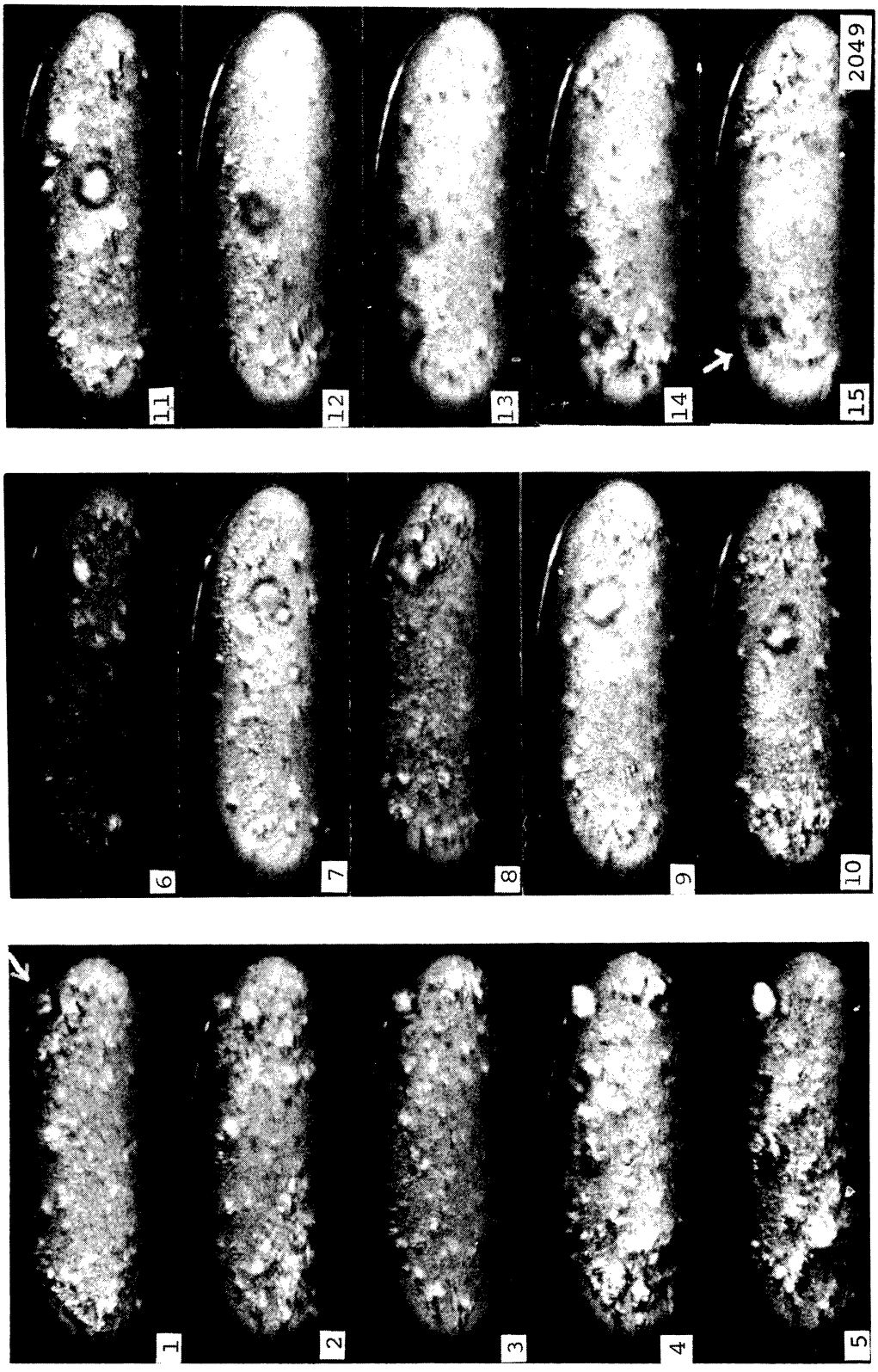

Fig. 58.--High speed photographic sequence (5X), 1 through 15, of a lightly abrased, type 304 stainless steel specimen in partially de-aerated water (1.60vol.%), amplitude of 2 mils, frequency 20,200 cps, exposure time per frame of 32 μ seconds, time between frames of 3.07 milliseconds, photographed at 10,400 fps.

across the specimen to exist where the flows enter through one of the prongs and exit through an adjacent prong. The higher velocity in the vicinity of the prong would result in reduced local pressures giving rise to a high local bubble population. This explanation requires an even number of prongs on the stars. This is generally the case at 10,000 cps if the stubs, or underdeveloped prongs, of the pattern are counted.

Fig. 59 shows the apparent start of a star-like formation on a type 2024-T351 aluminum specimen with the frequency at 20,195 cps and the camera operating at 20,200 frames per second. This pattern repeated itself throughout most of the recorded sequence of 117 acoustic cycles, and it appears to have paired prongs. Its existence only on a portion of the specimen is no doubt due to asymmetries introduced by the surface, bottom, walls, etc.

The copper specimen,(Fig. 57), shows only a partially developed star-like pattern at the lower left, but the prongs do appear to be paired. Fig. 60 shows paired star-like prongs that have been sectioned from photographs. For each photograph they were the only portion of a star pattern apparent.

Movement, and in this case a coalescence of 2 larger bubbles on a type 304 stainless steel specimen, is shown in Figs. 61-A, B and C. The frequency was 10,000 cps and the camera operated at 26,000 frames per second. Fig. 61-A shows two large bubbles well separated. Fig. 61-B shows movement by

Fig. 59.--High speed photograph (14X) of a type 2024-T351 aluminum specimen in water, frequency 20,195 cps, amplitude approximately 2 mils, exposure time per frame of 1.3 μ seconds, photographed at 20,200 fps.

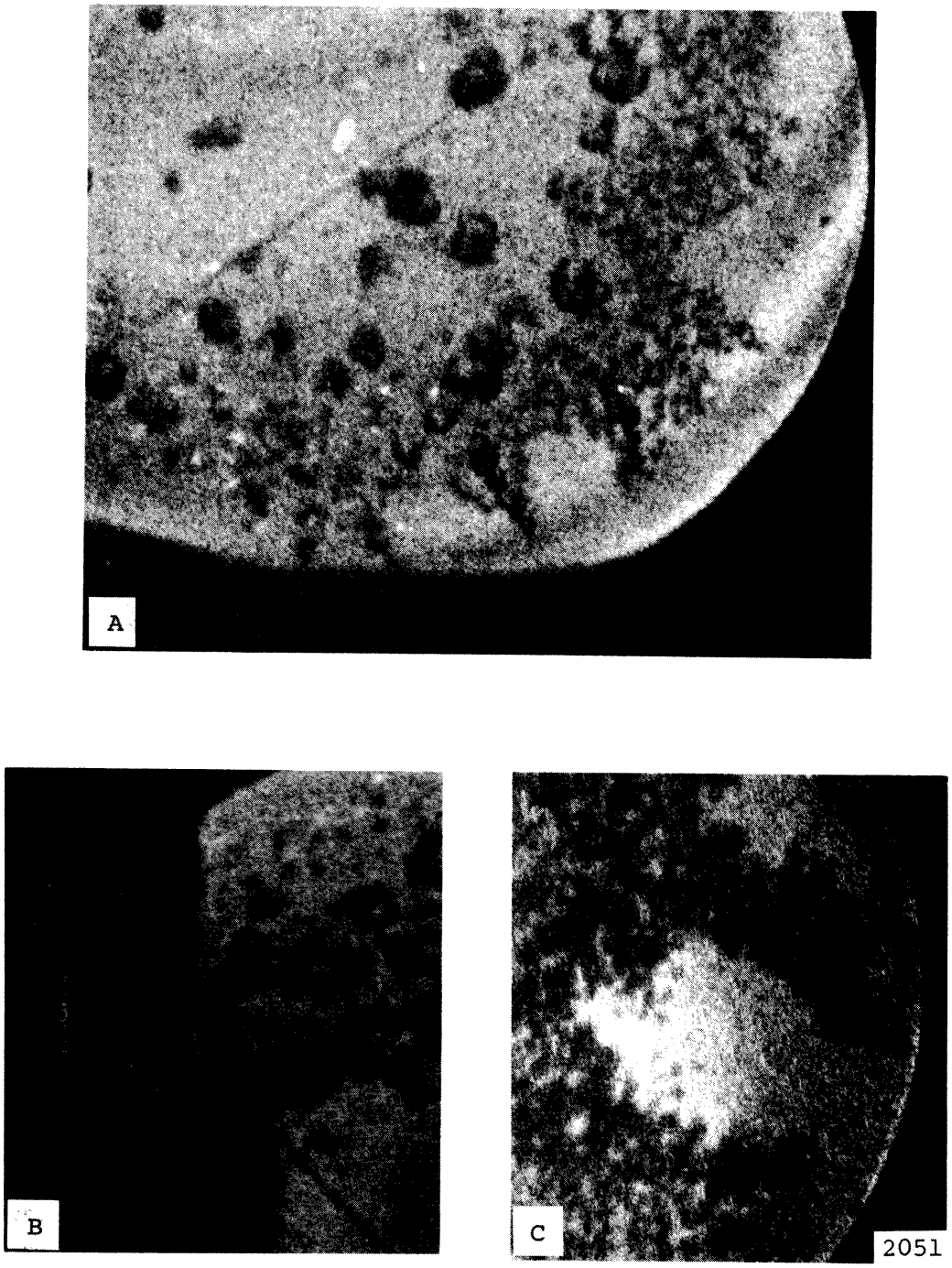

Fig. 60.--High speed photographs (16X) of specimens in water; A, 75% c.w. nickel (as rec'd) frequency 20,454 cps, exposure time per frame of 1.3 μ seconds, photographed at 20,460 fps; B, 75% c.w. nickel (as rec'd), frequency 20,454 cps, exposure time per frame of 1.3 μ seconds, photographed at 20,470 fps; C, type 304 stainless steel, frequency 20,325 cps, exposure time per frame of 1.3 μ seconds, photographed at 20,700 fps; amplitude for A, B, and C approximately 2 mils.

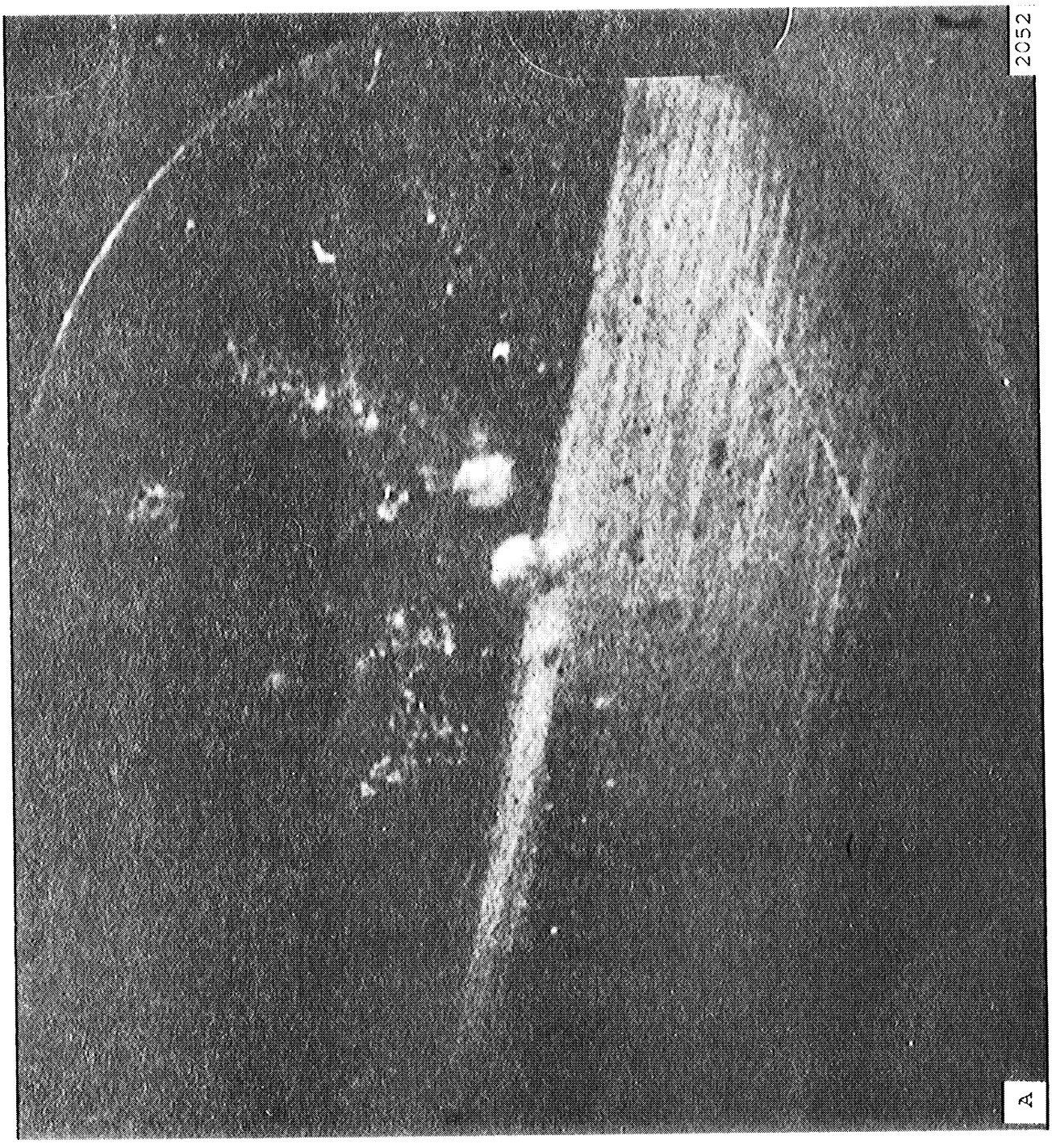

Fig. 61.--High speed photographic sequence (14X), A, B, and C of a type 304 stainless steel specimen in water, frequency 10,000 cps, exposure time per frame of 1 μ second. Photographed at 26,000 fps.

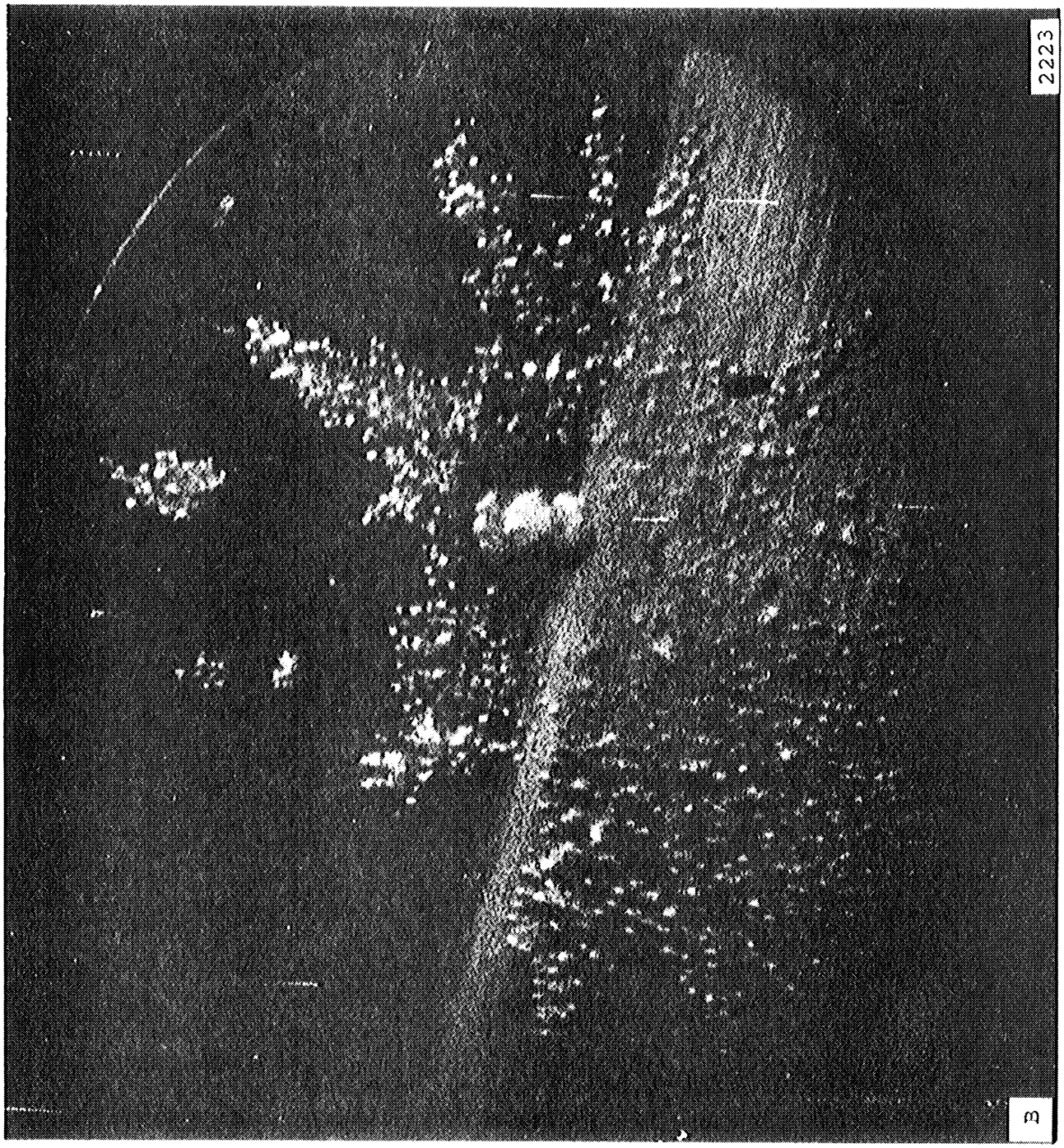

Fig. 61.--Continued

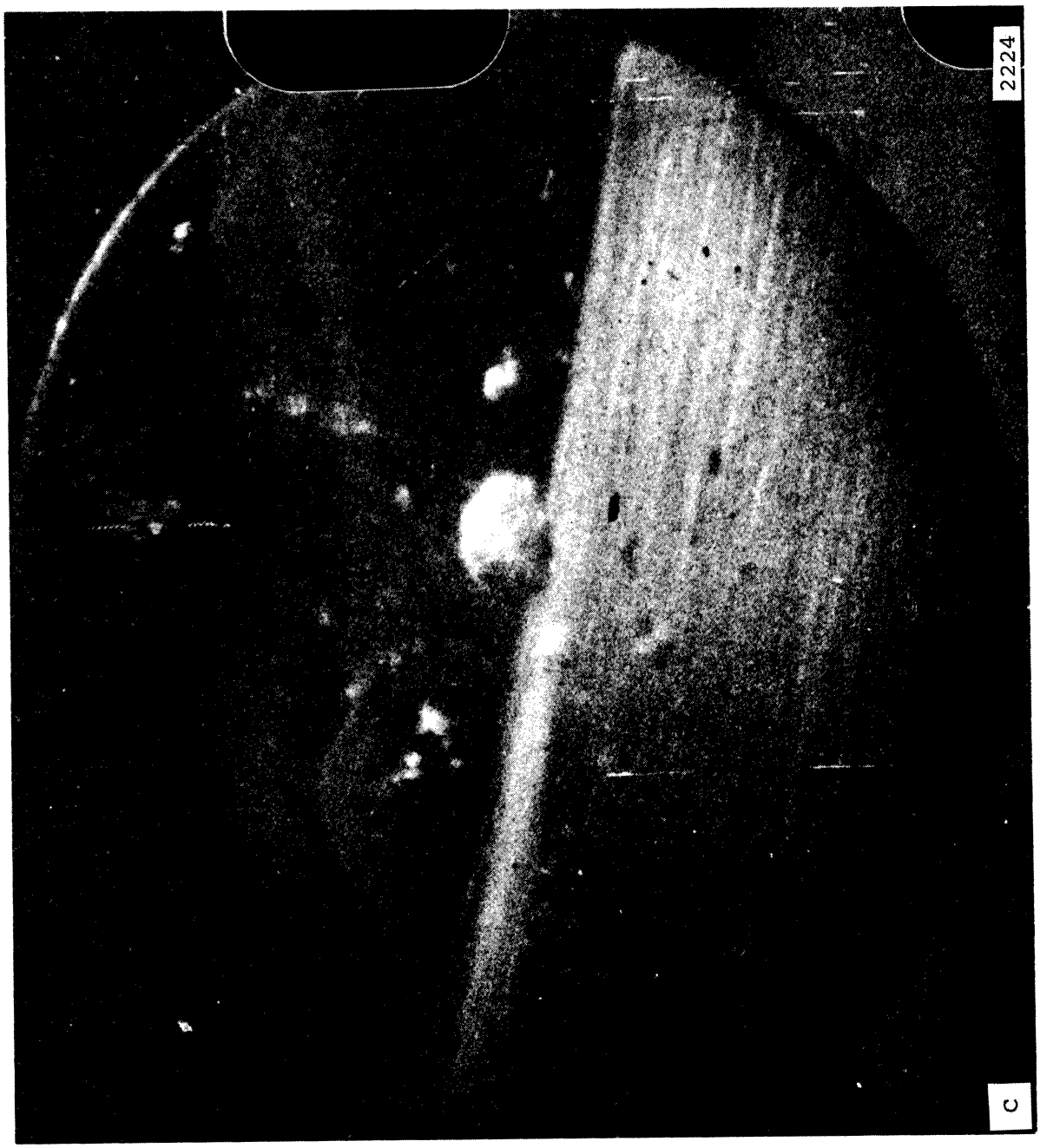

Fig. 61.--Continued

both bubbles towards each other, and Fig. 61-C shows only one larger bubble remaining, apparently the result of coalescence of the two original bubbles. Note that even though the bubbles apparently merged, the new bubble retains the bumpy surface exhibited by the single ones. Note also the very clear star pattern of small bubbles in Fig. 61-B.

Visible flow patterns on the surface of the water can be easily observed in the 7-1/2 cm square by 2-1/2 cm deep water container when the horn is held vertically and operated at 20,000 cps with 2 mil amplitude. With the horn tip about 1-1/2 cm below the water surface, clockwise or counter-clockwise vortices with axes normal to the surface around the horn, depending on the proximity of the various sides, can be seen. When the horn is located near a corner, a figure-8 type of flow results with the flow pursuing a circular path around the horn, then looping in the corner. These patterns are sketched below.

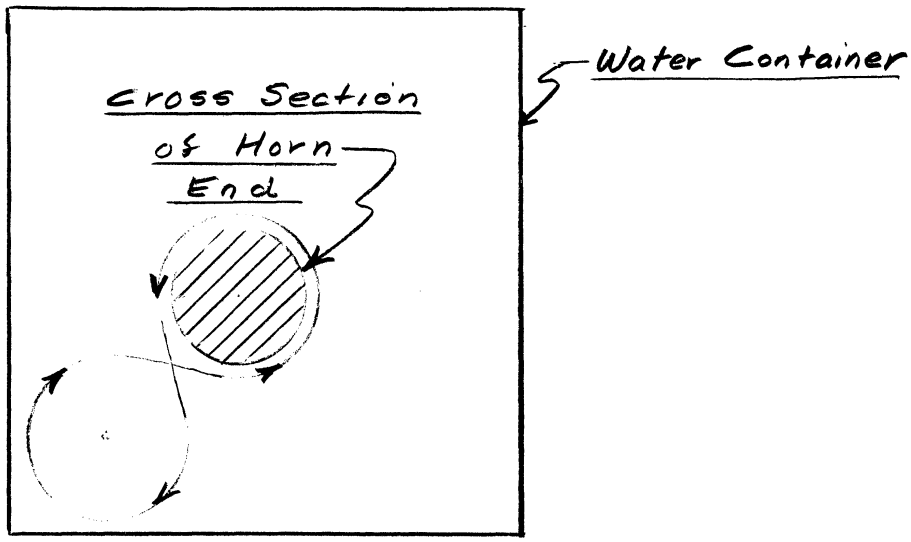

H. Approximate Maximum Bubble Populations

Fig. 62 and Figs. 64 through 69 show the cavitation bubble cloud at the approximate maximum population point for all of the eight materials except for type 1100-0 aluminum. For this material only a ring bubble pattern could be obtained over extended periods. Apparently the threaded stud in this very soft material does not have sufficient strength to provide the required mechanical bond between specimen and horn. The maximum population condition for this material is shown in Fig. 63-A. In a change noticeable to the unaided eye, the cavitation pattern shifted at the beginning of the run from a reasonably full one to a thin ring just inside the outer annulus as shown in Fig. 63-A.

Fig. 63-B also for 1100-0 aluminum shows the bubble population of an apparently full cavitation cloud, at least from the visual appearance, at a point in the acoustic cycle where only a few large bubbles have survived.

Prints of the highest possible enlargement were made for each photographic run showing the approximate maximum bubble population. These were then used to obtain bubble counts for the various bubble diameter ranges. The approximate maximum ring cavitation pattern population was used for the 1100-0 aluminum specimen. On some photographs the bubbles were so heavily packed that it was necessary to assume for the purpose of counting that maximum packing of a typical bubble diameter existed.

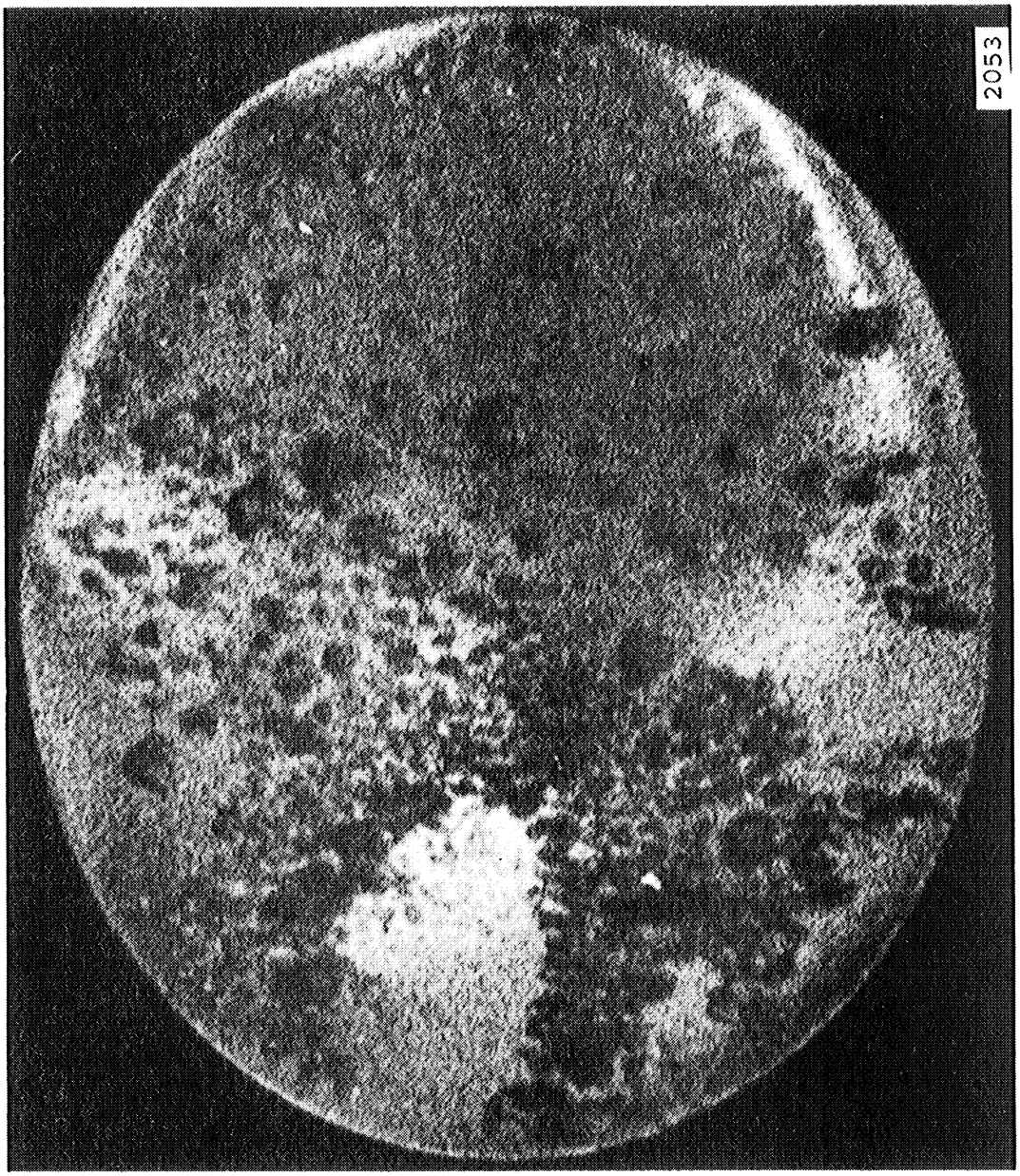

Fig. 62.--High speed photograph (12X) of the approximate maximum bubble population of a type 304 stainless steel specimen in water, frequency 20,325 cps, amplitude approximately 2 mils, exposure time per frame of 1.3 μseconds, photographed at 20,700 fps.

Fig. 63.--High speed photographs (12X), A and B, not in sequence, of A, the approximate maximum ring bubble population and B, at the minimum bubble population, both of a type 1100-0 aluminum specimen in water, frequency 20,244 cps, amplitude approximately 2 mils, exposure time per frame of 1.3 μ seconds, photographed at 20,250 fps.

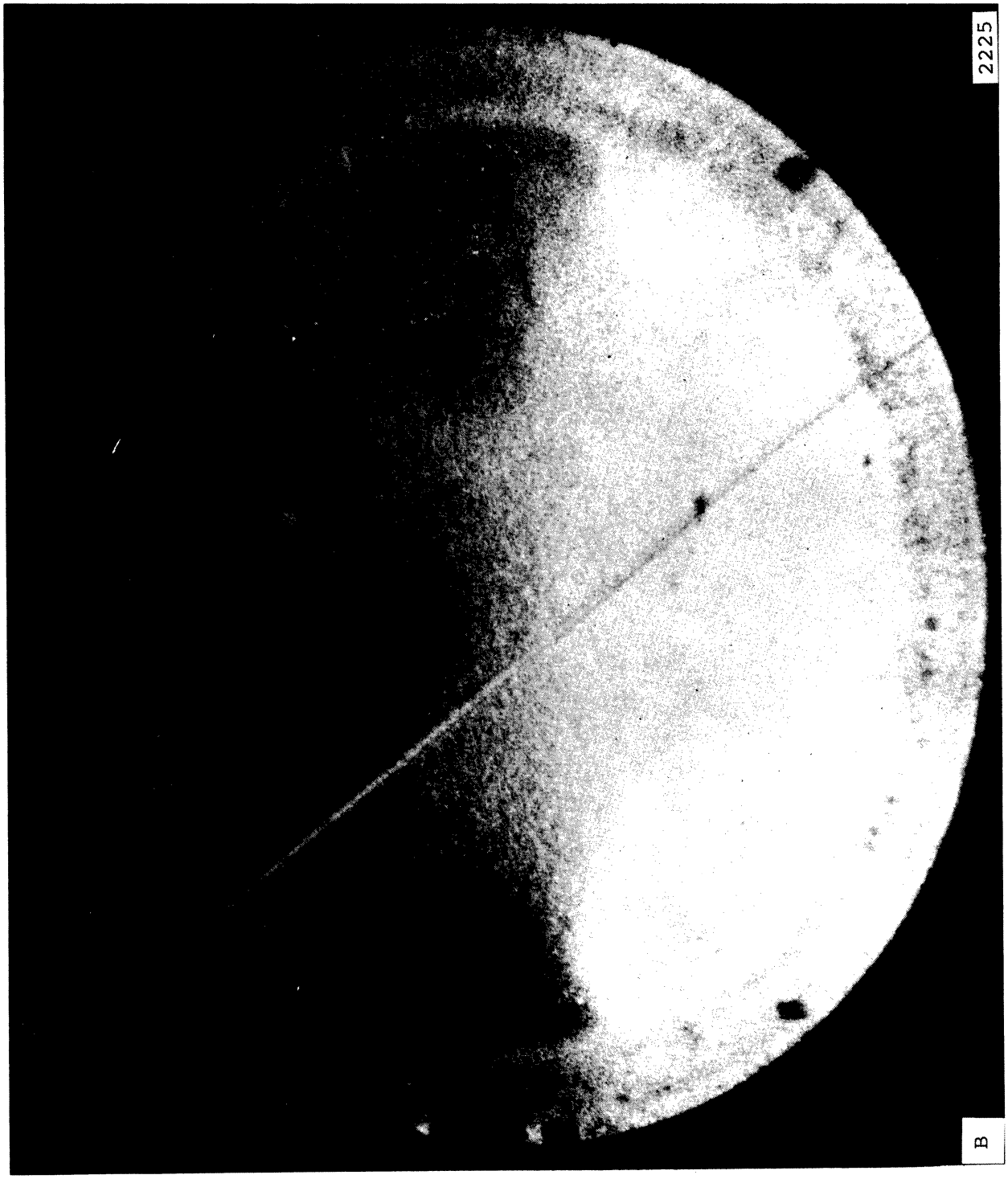

Fig. 63.--Continued

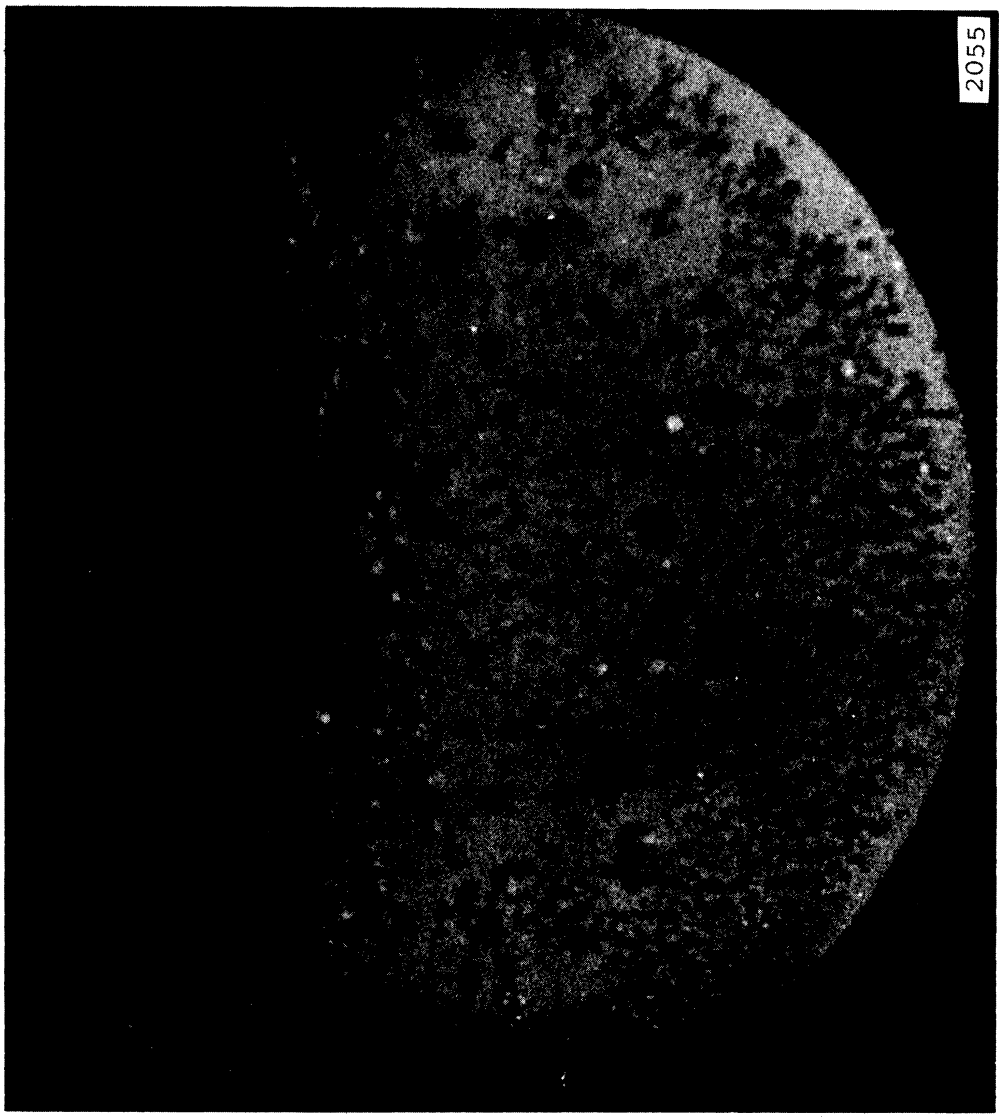

Fig. 64.--High speed photograph (11X) of the approximate maximum bubble population of a type 2024-T351 aluminum specimen in water, frequency 20,200 cps, amplitude approximately 2 mils, exposure time per frame of 1.3 μ seconds, photographed at 20,150 fps.

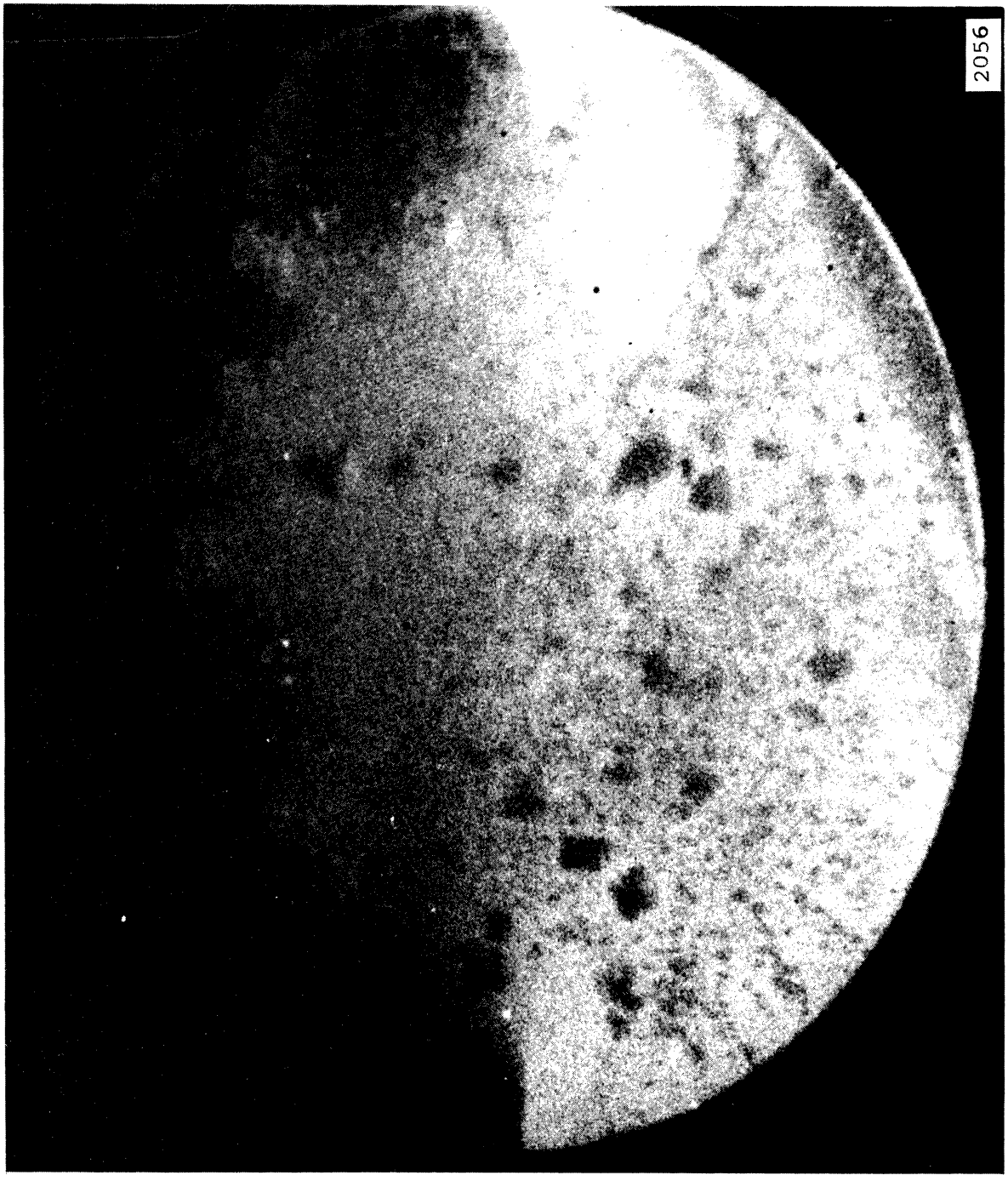

Fig. 65.--High speed photograph (12X) of the approximate maximum bubble population of a type 6061-T651 aluminum specimen in water, frequency 20,243 cps, amplitude approximately 2 mils, exposure time per frame of 1.3 μseconds, photographed at 20,200 fps.

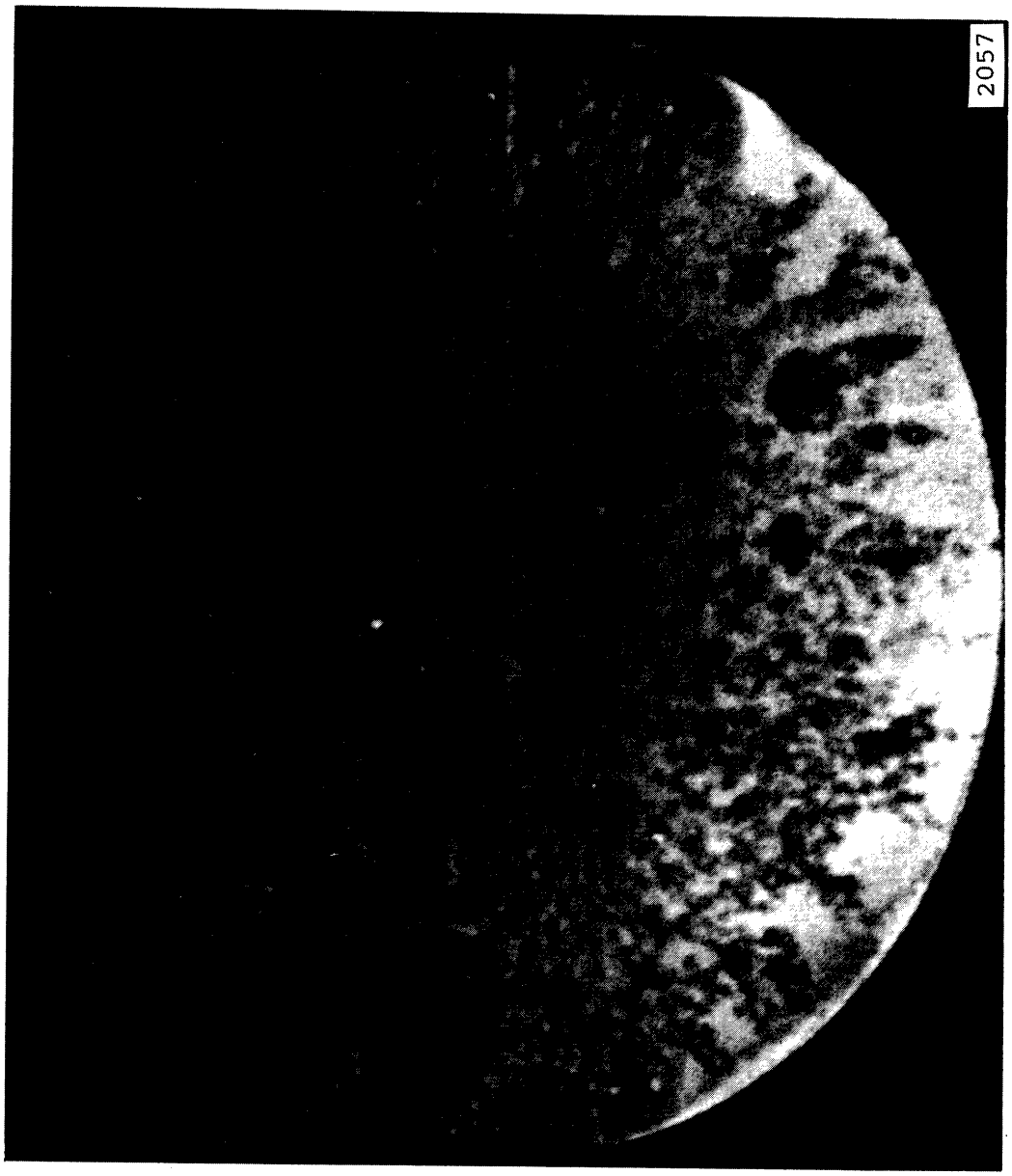

Fig. 66.--High speed photograph (12X) of the approximate maximum bubble population of a 60% c.w. copper (as rec'd) specimen in water, frequency 20,542 cps, amplitude approximately 2 mils, exposure time per frame of 1.3 μseconds, photographed at 20,530 fps.

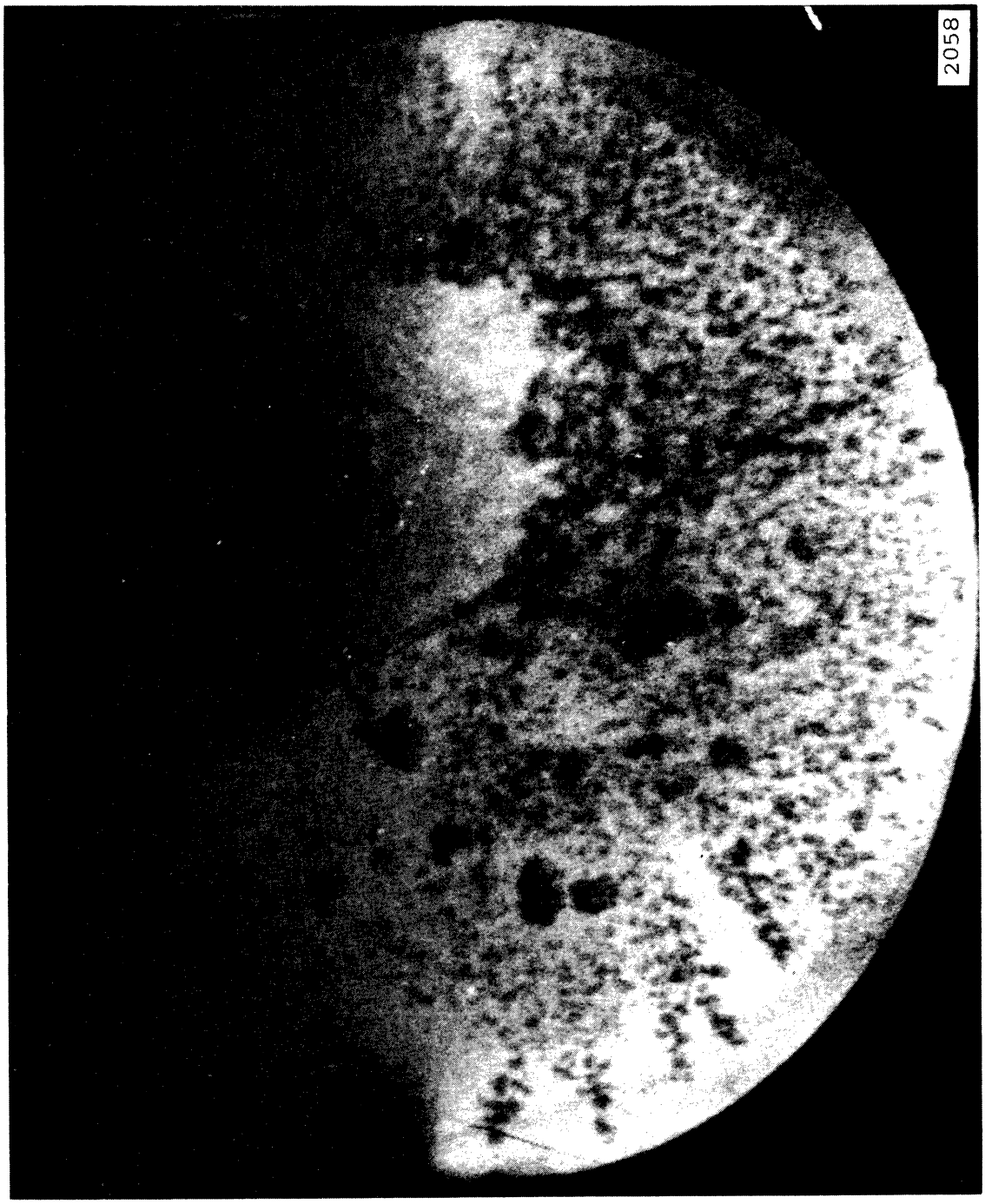

Fig. 67.--High speed photograph (12X) of the approximate maximum bubble population of a copper 900°F annealed specimen in water, frequency 20,419 cps, amplitude approximately 2 mils, exposure time per frame of 1.3 μ seconds, photographed at 20,430 fps.

Fig. 68.--High speed photograph (12X) of the approximate maximum bubble population of a 75% c. w. nickel (as rec'd) specimen in water, frequency 20,454 cps, amplitude approximately 2 mils, exposure time per frame of 1.3μ seconds, photographed at 20,470 fps.

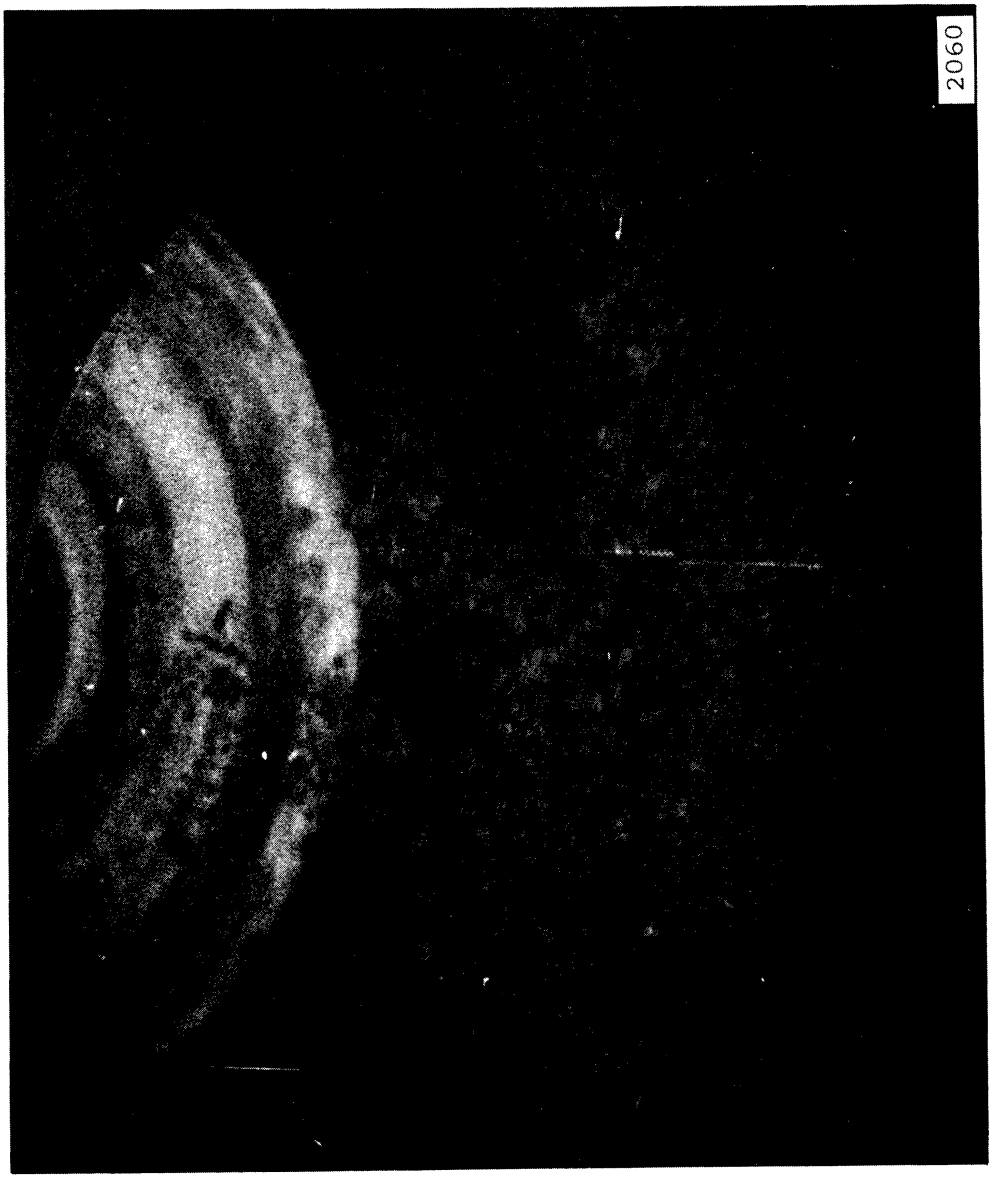

Fig. 69.--High speed photograph (11X) of the approximate maximum bubble population of a Plexiglas specimen in water, frequency 20,564 cps, amplitude approximately 2 mils, exposure time per frame of 1.3 μ seconds, photographed at 20,560 fps.

Considerable variation was noted in the approximate maximum bubble population for the 7 specimens (see Table 1). (1100-0 aluminum was excluded since no photograph of the maximum population in a full-surface pattern was obtained.) These varied from 967 bubbles for Plexiglas to 5,386 for the 75% c. w. nickel (as rec'd). Since all were exposed at an approximate amplitude of 2 mils, with the exception of Plexiglas for which the amplitude was 1.6 mils, this difference in population is of considerable interest.* The rings that are evident in the Plexiglas photograph (Fig. 69) are the threaded end of the specimen seen through the transparent Plexiglas.

Amplitude measurements in air using a stroboscope and microscope have shown[7] that the calibration between the accelerometer at the top of the horn and the specimen amplitude is the same (within ± 10%, which is the precision obtainable with the microscope) for all the materials except Plexiglas. As a result, the accelerometer setting which was used for these runs corresponded to 2 mils (± 10%) for all specimens except Plexiglas for which it was 1.6 mils. Frequency varies only negligibly from specimen to specimen. The reduced amplitude with Plexiglas is apparently due to the lack of a good mechanical bond between specimen and horn for this material. Apparently the bond is worse with Plexiglas than with 1100-0 aluminum, since the full amplitude was attained with the

---

*See Appendix "D."

TABLE 1

EXPOSURE AND DAMAGE PARAMETERS

Materials	Duration (sec)	No. of Oscillations	Approx Max. Bubble Population per Cycle	Total Bubbles for Run	Pit sizes in cm. Very very large >0.0120	Very large <0.0120 >0.0034	Large <0.0034 >0.0010	Approx. small <0.0010	Total No. of Pits	Bubbles per Pit	Wt. Loss (mg)	gms. per sec.
304 SS	54	1,097,550	4,872	5.35×10^9	1	3	15	62,000	62,000	8.71×10^4	0.07 (a)	1.3×10^{-6}
1100-0 Aluminum	22	141,708 303,660	1,884(b) 734(c)	$.27 \times 10^9$ $.22 \times 10^9$	3	3	75	71,800	71,900	$.68 \times 10^4$	1.72	78×10^{-6}
2024-T351 Aluminum	60	1,212,036	1,854	2.25×10^9	4	22	50	122,800	122,900	1.75×10^4	0.17	2.83×10^{-6}
6061-T651 Aluminum	15	303,638	1,913	$.58 \times 10^9$	1	9	50	88,400	88,500	$.66 \times 10^4$	0.75	50×10^{-6}
Copper 60% C.W. (As Rec'd)	32	657,344	4,111	2.70×10^9	3	7	38	101,800	101,900	2.65×10^4	0.48	15×10^{-6}
Copper 900°F Annealed	33	673,811	2,160	1.46×10^9	4	7	31	71,600	71,700	2.03×10^4	0.36	10.9×10^{-6}
Nickel 75% C.W. (As Rec'd)	44	899,976	5,386	4.85×10^9	3	4	52	107,000	107,100	4.53×10^4	0.30	6.8×10^{-6}
Plexiglas	27	555,215	967	$.54 \times 10^9$	3	50	60	-	113	475×10^4	0.45	16.7x10-6

(a) Weight corrected by an additional run.
(b) Average maximum of other 2 aluminum specimens used because high speed photographs did not show transient bubbles.
(c) "Ring" cavitation only.

aluminum. Since the acoustic intensity varies as the square of both the amplitude and the frequency, a decrease in one or both would reduce the bubble population.

A very poor bond existed with the type 1100-0 aluminum specimen during the test as was already mentioned. The initial, reasonably full "maple leaf" pattern which was obtained is shown in the center of the photograph of Fig. 70. The ring pattern which occurred is also shown in this photograph. Apparently the ultrasonic vibration weakens the specimen-horn bond, and the amplitude then diminishes, accompanied by a change in pattern.

As previously discussed in Section G of this Chapter, proximity of the specimen to the sides or bottom of the water container or the water surface could also effect the fullness of the cavitation pattern, and thus the maximum bubble population.

The size distribution of the approximate maximum bubble populations of the 7 specimens (excepting 1100-0 aluminum) are shown in Fig. 71 and Figs. 73 through 78. The size distribution of the approximate maximum ring population for 1100-0 aluminum is shown in Fig. 72. To construct these spectra, the number of bubbles in each size range is plotted at the range median.

The spectra all show very few bubbles with diameter greater than 0.02 cm, but large numbers at less than this diameter. The number density, with the exception of Plexiglas,

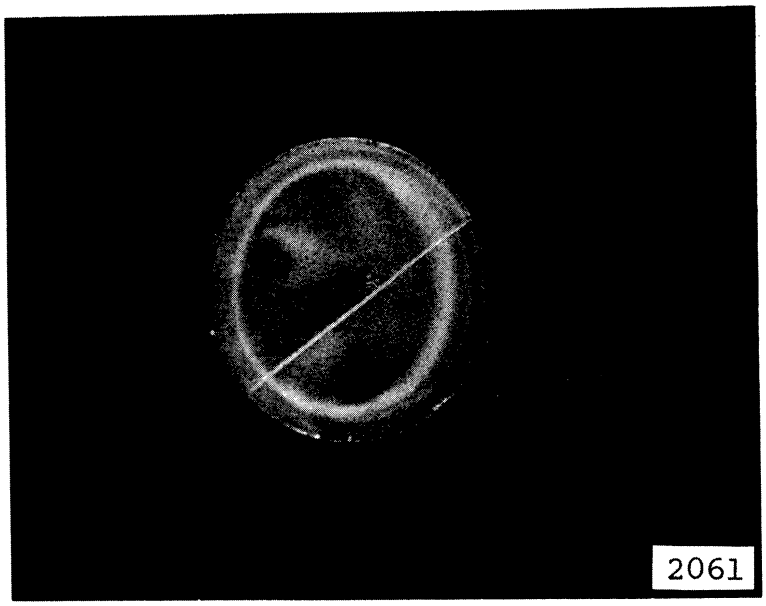

Fig. 70.--Still photograph (2.5X) of a type 1100-0 aluminum specimen after 22 seconds of exposure to cavitation in water with frequency at 20,244 cps and amplitude approximately 2 mils.

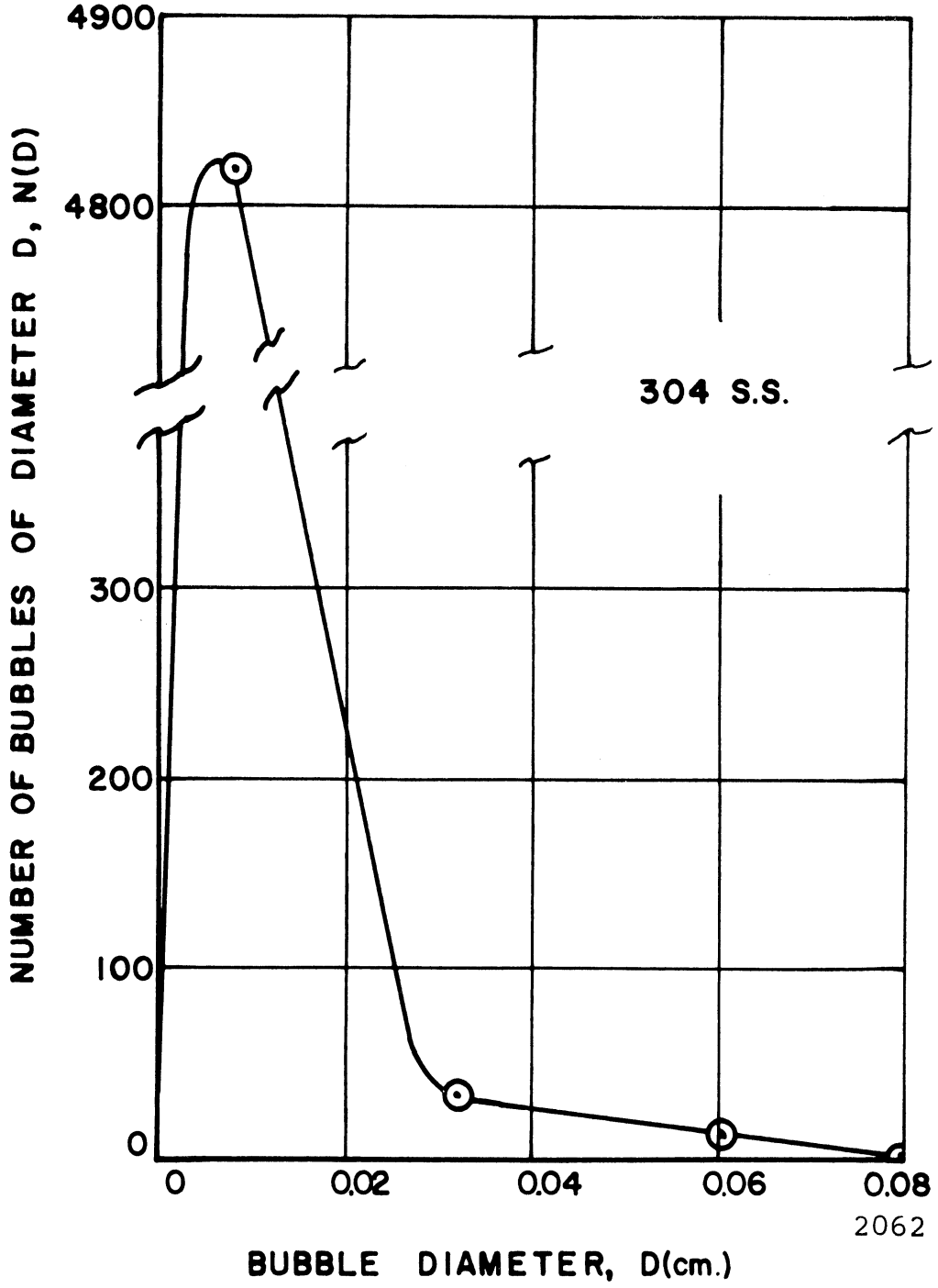

Fig. 71.--Size distribution of the approximate maximum bubble population of a type 304 stainless steel specimen exposed to cavitation in water for 54 seconds with frequency at 20,325 cps and amplitude approximately 2 mils.

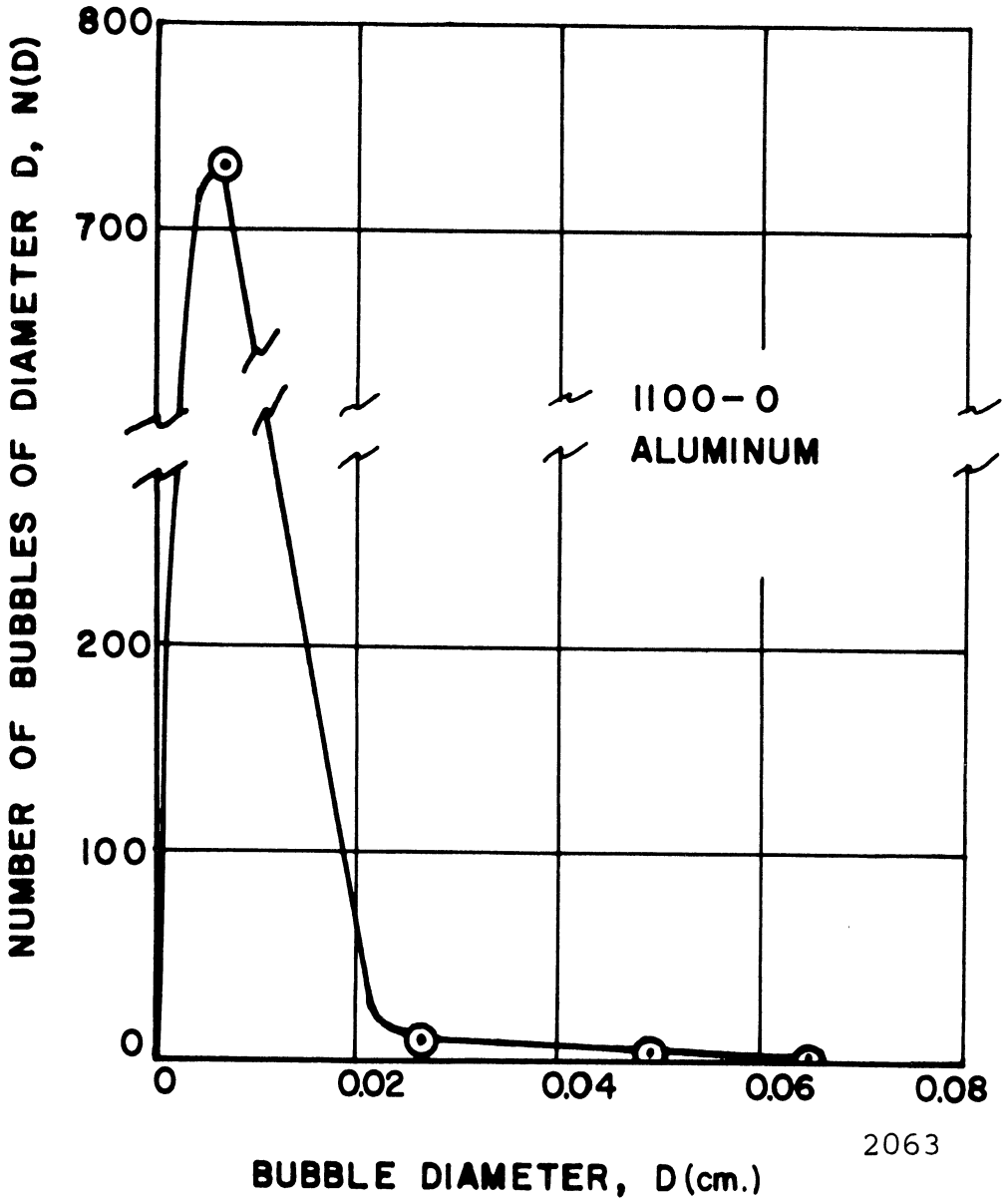

Fig. 72.--Size distribution of the approximate maximum ring bubble population of a type 1100-0 aluminum specimen exposed to cavitation in water for 22 seconds with frequency at 20,244 cps and amplitude approximately 2 mils.

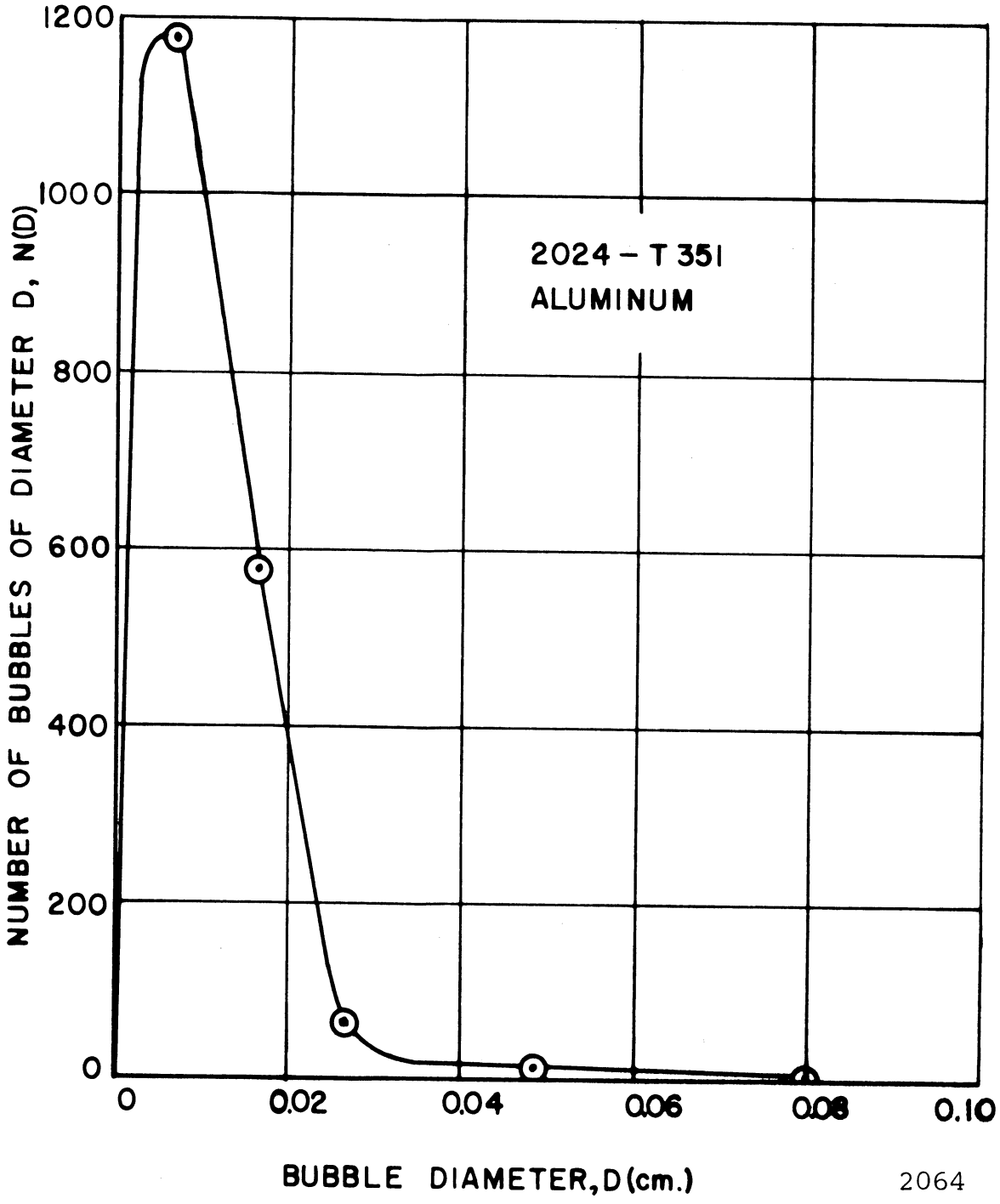

Fig. 73.--Size distribution of the approximate maximum bubble population of a type 2024-T351 aluminum specimen exposed to cavitation in water for 60 seconds with frequency at 20,200 cps and amplitude approximately 2 mils.

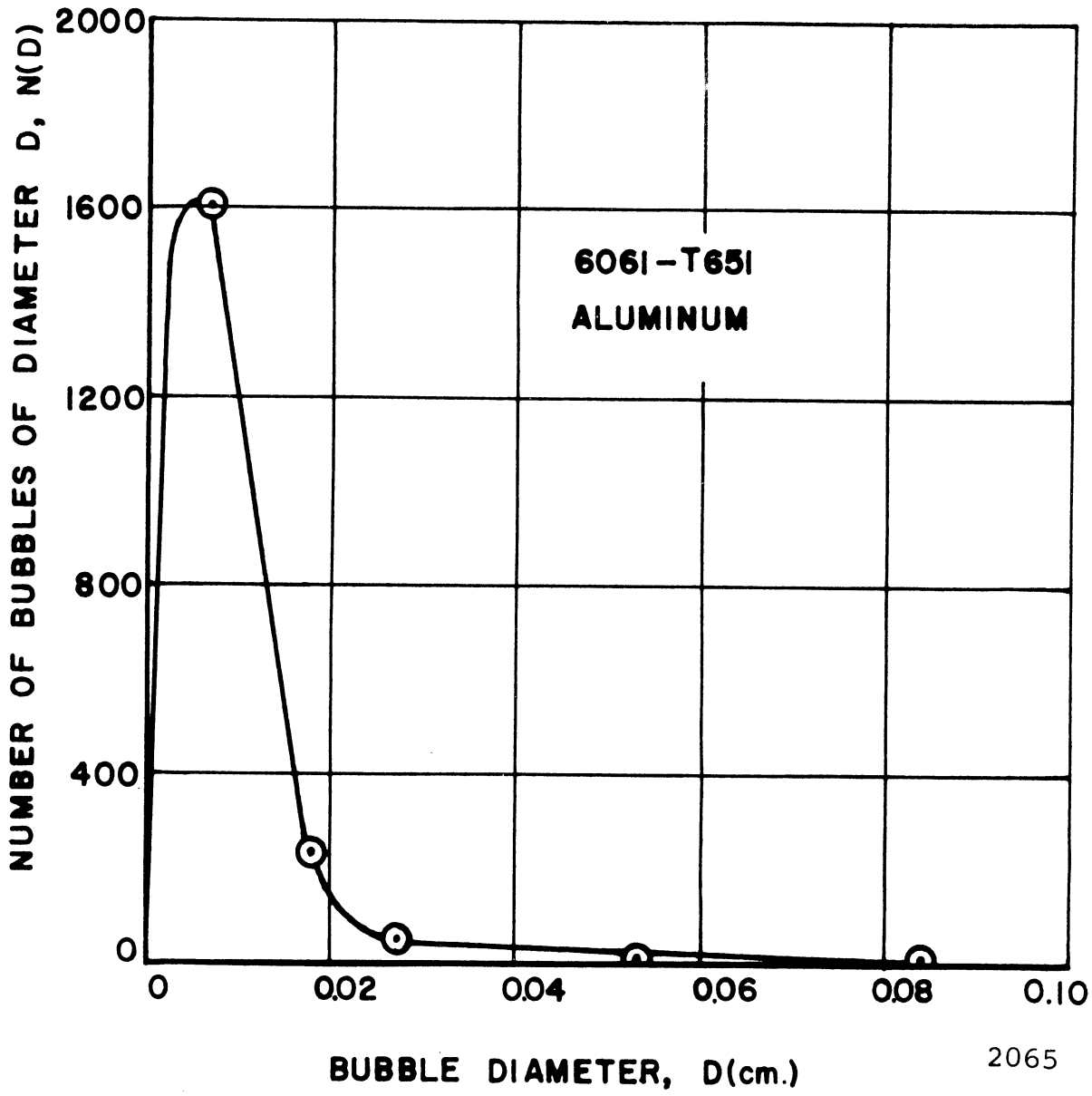

Fig. 74.--Size distribution of the approximate maximum bubble population of a type 6061-T651 aluminum specimen exposed to cavitation in water for 15 seconds with frequency at 20,243 cps and amplitude approximately 2 mils.

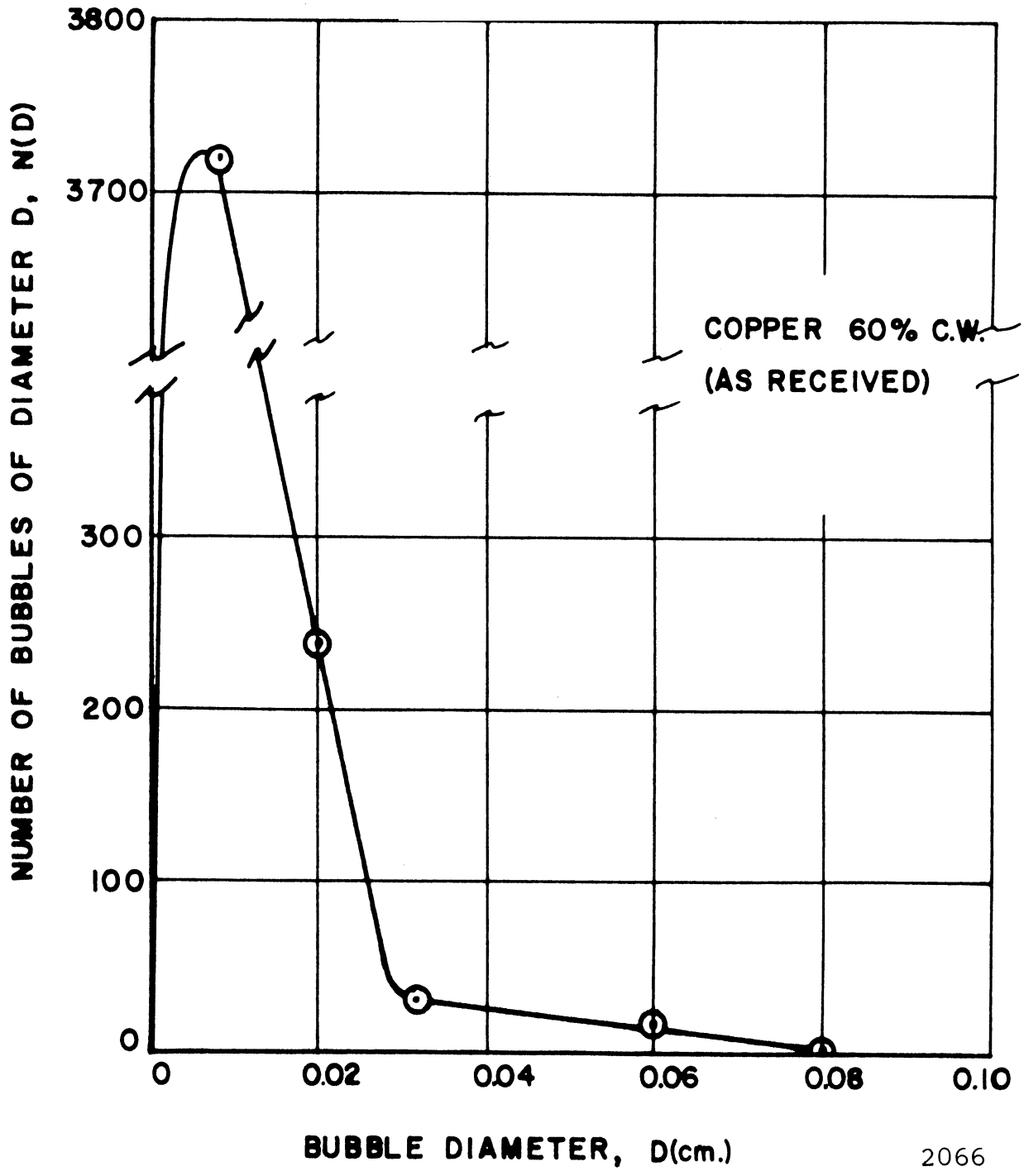

Fig. 75.--Size distribution of the approximate maximum bubble population of a 60% c. w. copper (as rec'd) specimen exposed to cavitation in water for 32 seconds with frequency at 20,542 cps and amplitude approximately 2 mils.

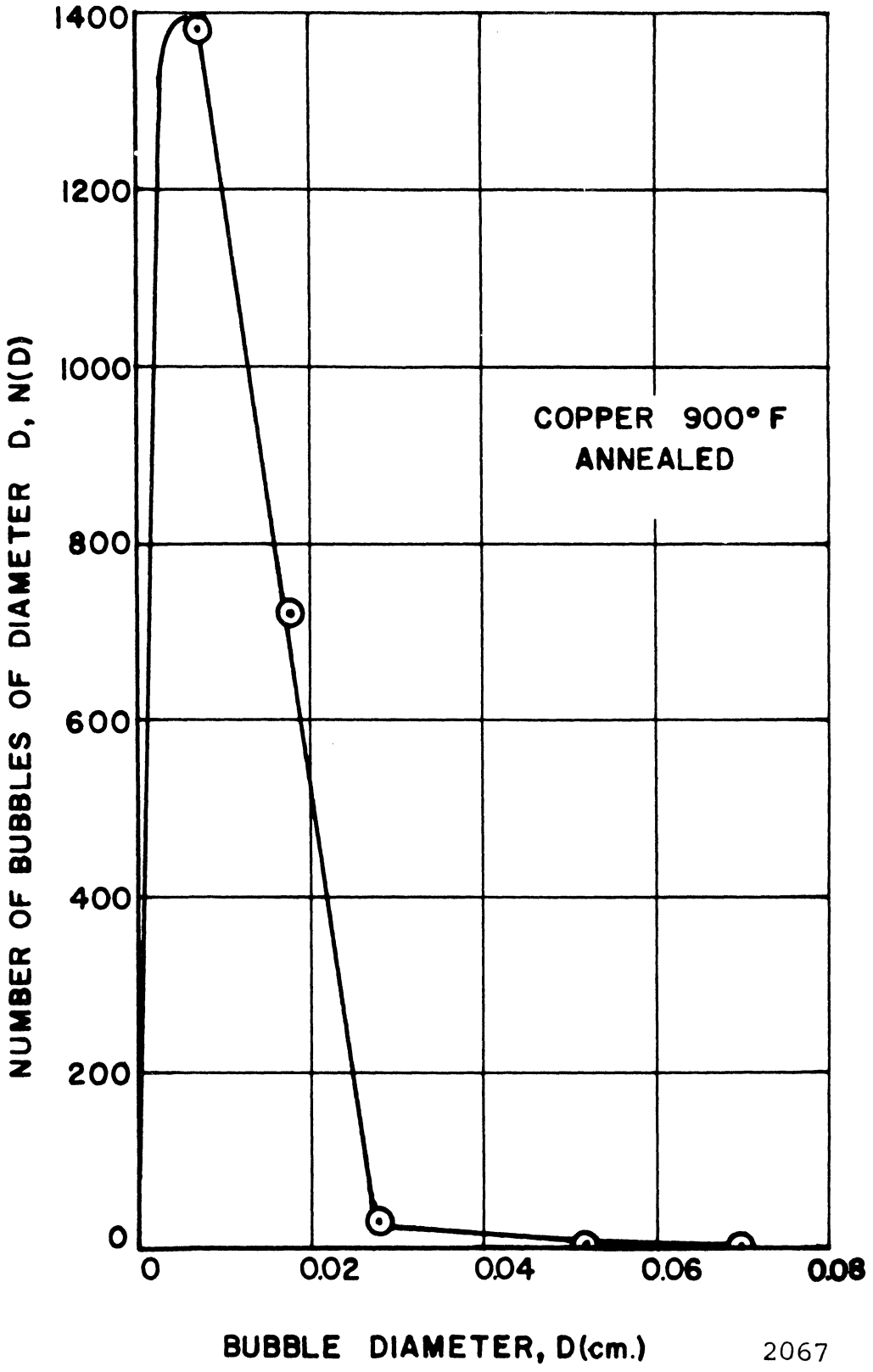

Fig. 76.--Size distribution of the approximate maximum bubble population of a copper 900°F annealed specimen exposed to cavitation in water for 33 seconds with frequency at 20,419 cps and amplitude approximately 2 mils.

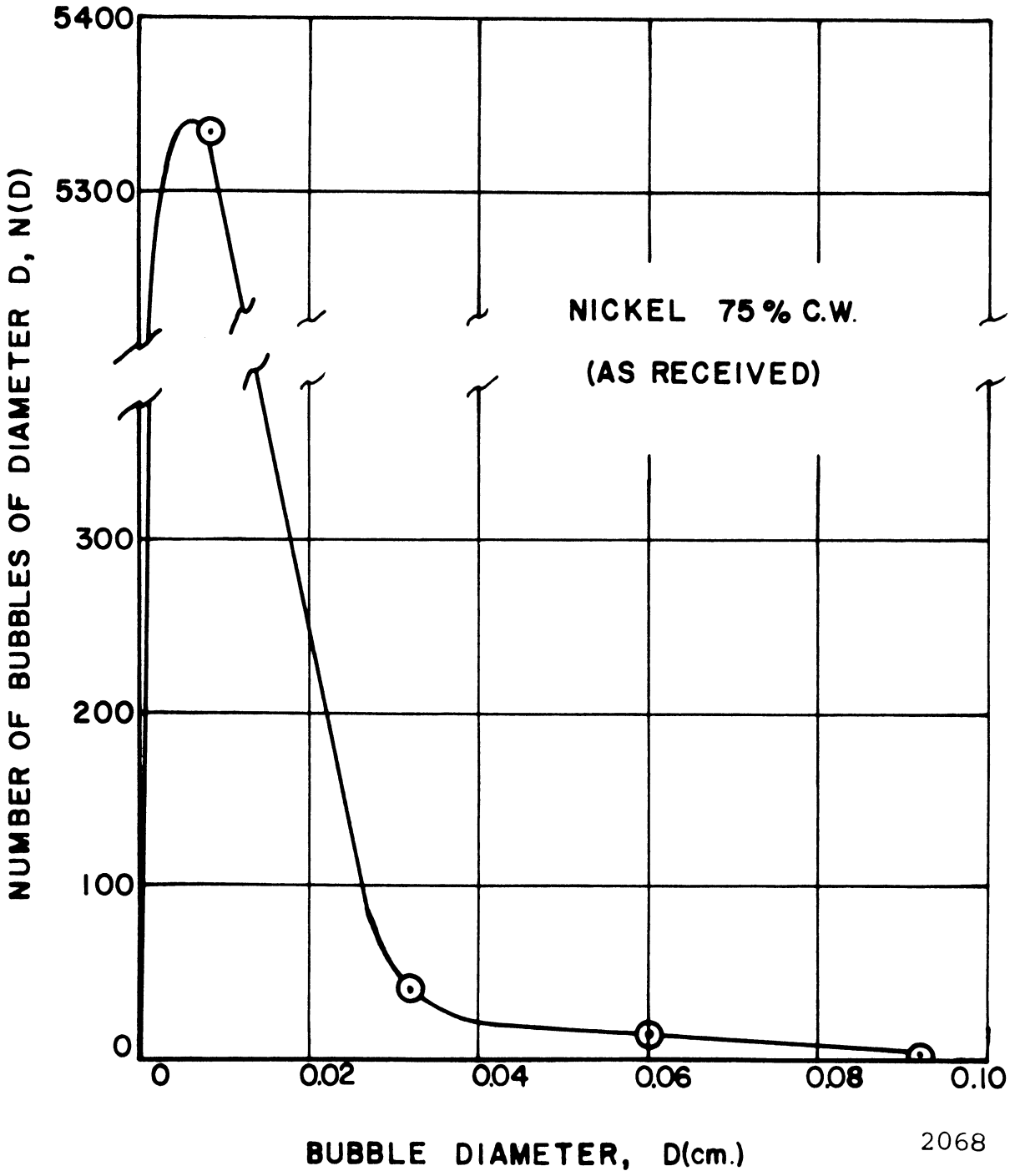

Fig. 77.--Size distrubution of the approximate maximum bubble population of a 75% c. w. nickel (as rec'd) specimen exposed to cavitation in water for 44 seconds with frequency at 20,454 cps and amplitude approximately 2 mils.

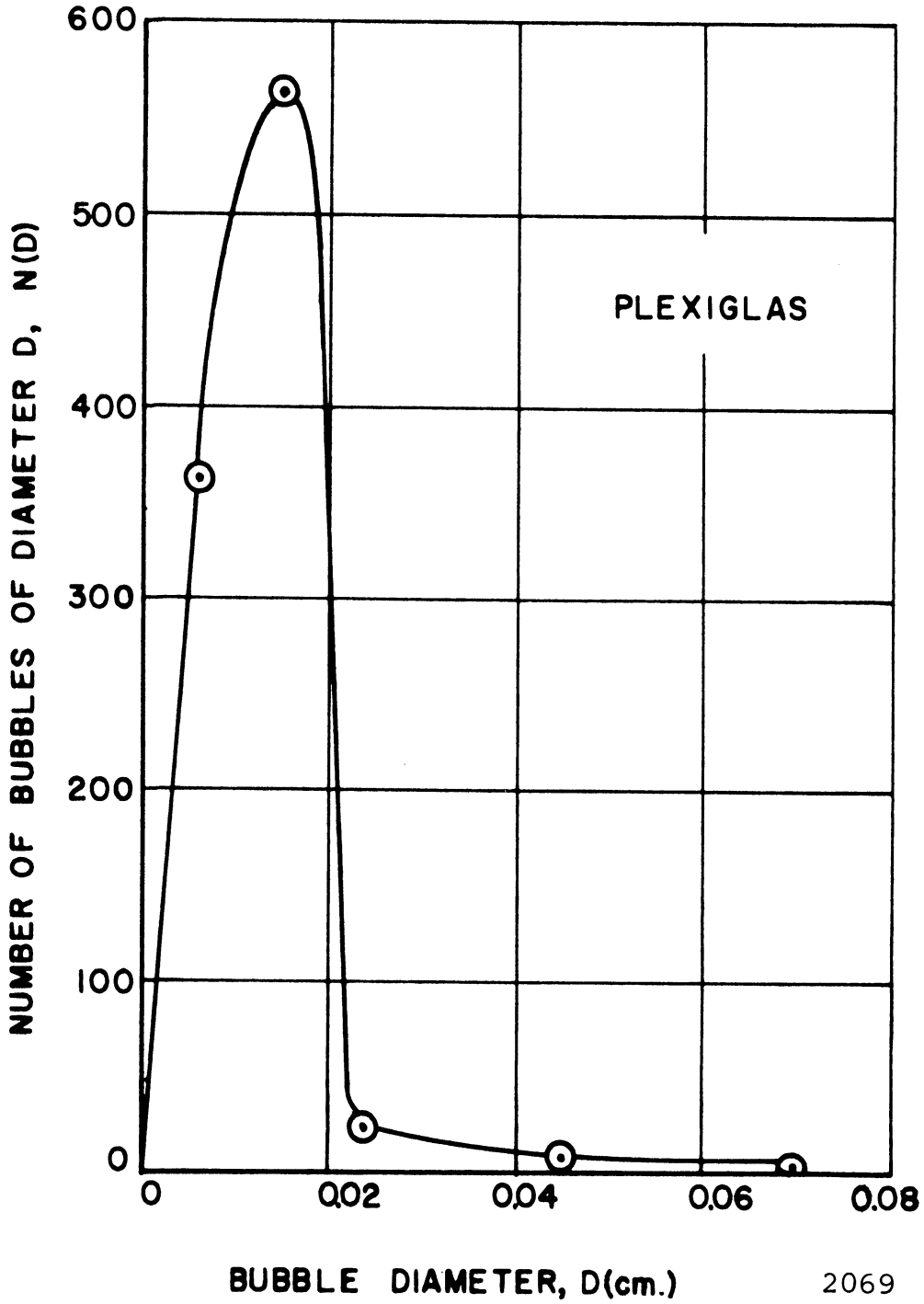

Fig. 78.--Size distribution of the approximate maximum bubble population of a Plexiglas specimen exposed to cavitation in water for 27 seconds with frequency at 20,564 cps and amplitude approximately 2 mils.

increases as the diameter of the bubble lessens. The Plexiglas population shows a maximum at a diameter of approximately 0.018 cm and then decreases for lower diameters, since with its relatively low approximate maximum population it was possible to segregate smaller diameter bubbles. All of the curves are shown passing through the origin, although except for Plexiglas, no data on the very small bubble portion of the spectra could be obtained due to limitations in photographic resolution. The spectra show that the cavitation bubble field at the approximate maximum population point is almost entirely made up of transient bubbles. There is no discernible difference among the specimens with respect to the bubble size distribution or the diameters of the transient bubbles.

I. Bubble Spectra at Various Populations

The type 2024-T351 aluminum specimen provided high speed photographs of exceptional resolution. Five of the photographic frames were selected at random from the two sequences of 117 frames each, for which the frequency was 20,200 cps and the camera was operated at 20,150 frames per second. On these typical photographs, assignment of bubbles to the various size ranges at the median of that range was made to construct bubble size spectra. Figs. 79 through 83 show the bubble population when it was not at the recorded maximum. Figs. 84 through 88 show the corresponding spectra, which will be discussed in greater detail later on.

Fig. 79.--High speed photograph No. 93-a (11X) of a type 2024-T351 aluminum specimen in water, frequency 20,200 cps, amplitude approximately 2 mils, exposure time per frame of 1.3 μseconds, photographed at 20,150 fps.

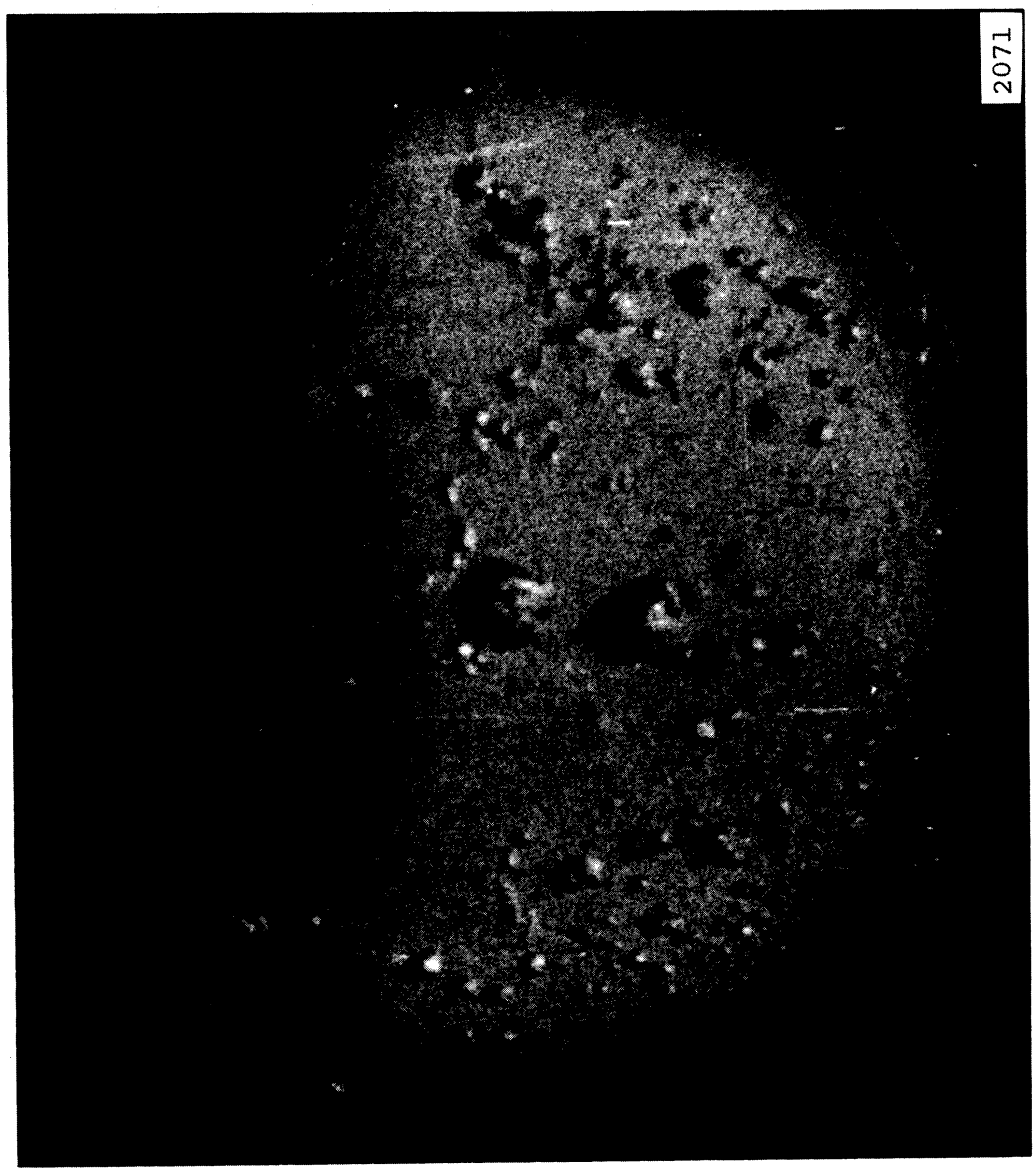

Fig. 80.--High speed photograph No. 97-a (11X) of a type 2024-T351 aluminum specimen in water, frequency 20,200 cps, amplitude approximately 2 mils, exposure time per frame of 1.3 μ seconds, photographed at 20,150 fps.

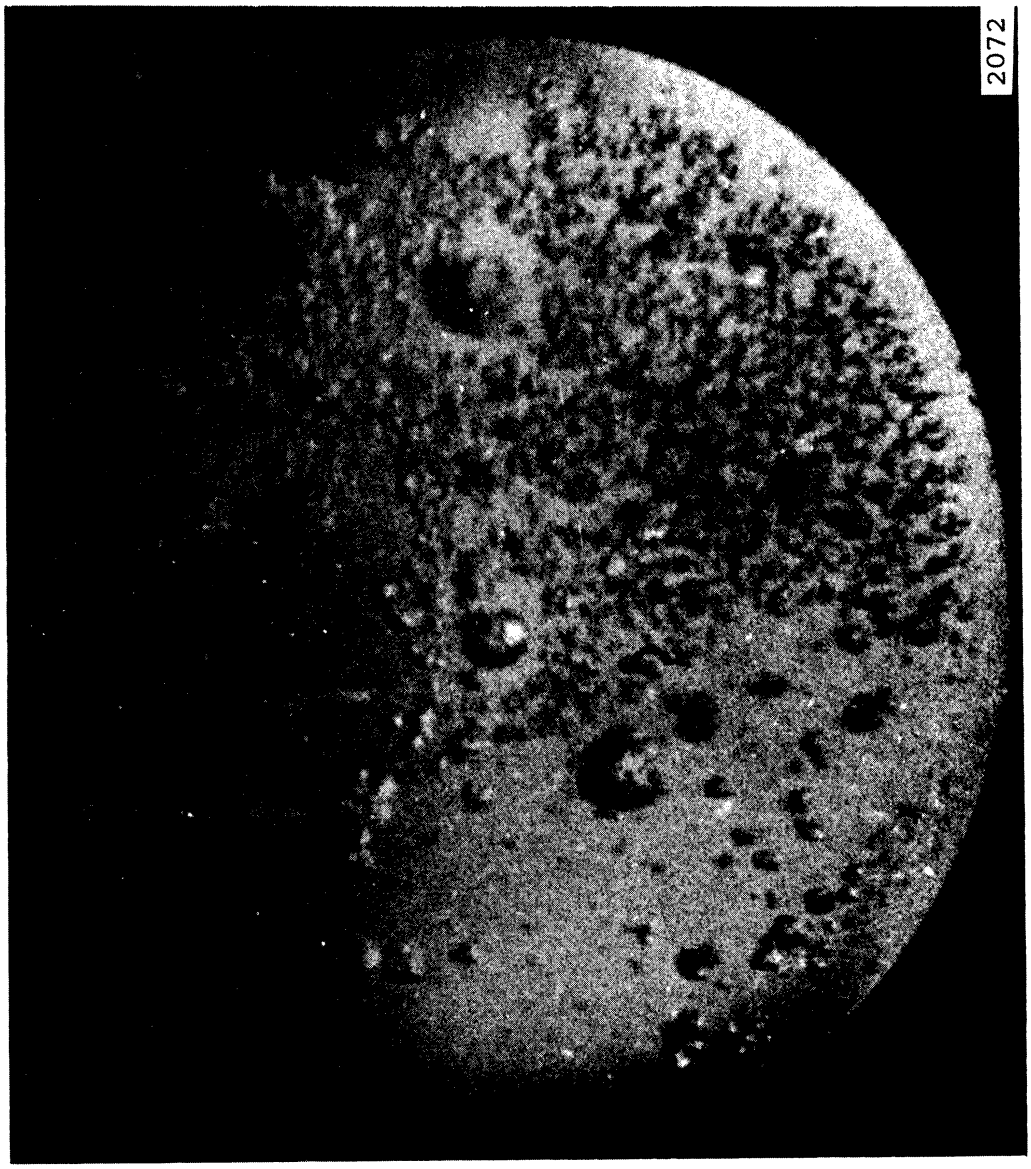

Fig. 81.--High speed photograph No.97 (11X) of a type 2024-T351 aluminum specimen in water, frequency 20,200 cps, amplitude approximately 2 mils, exposure time per frame of 1.3 μ seconds photographed at 20,150 fps.

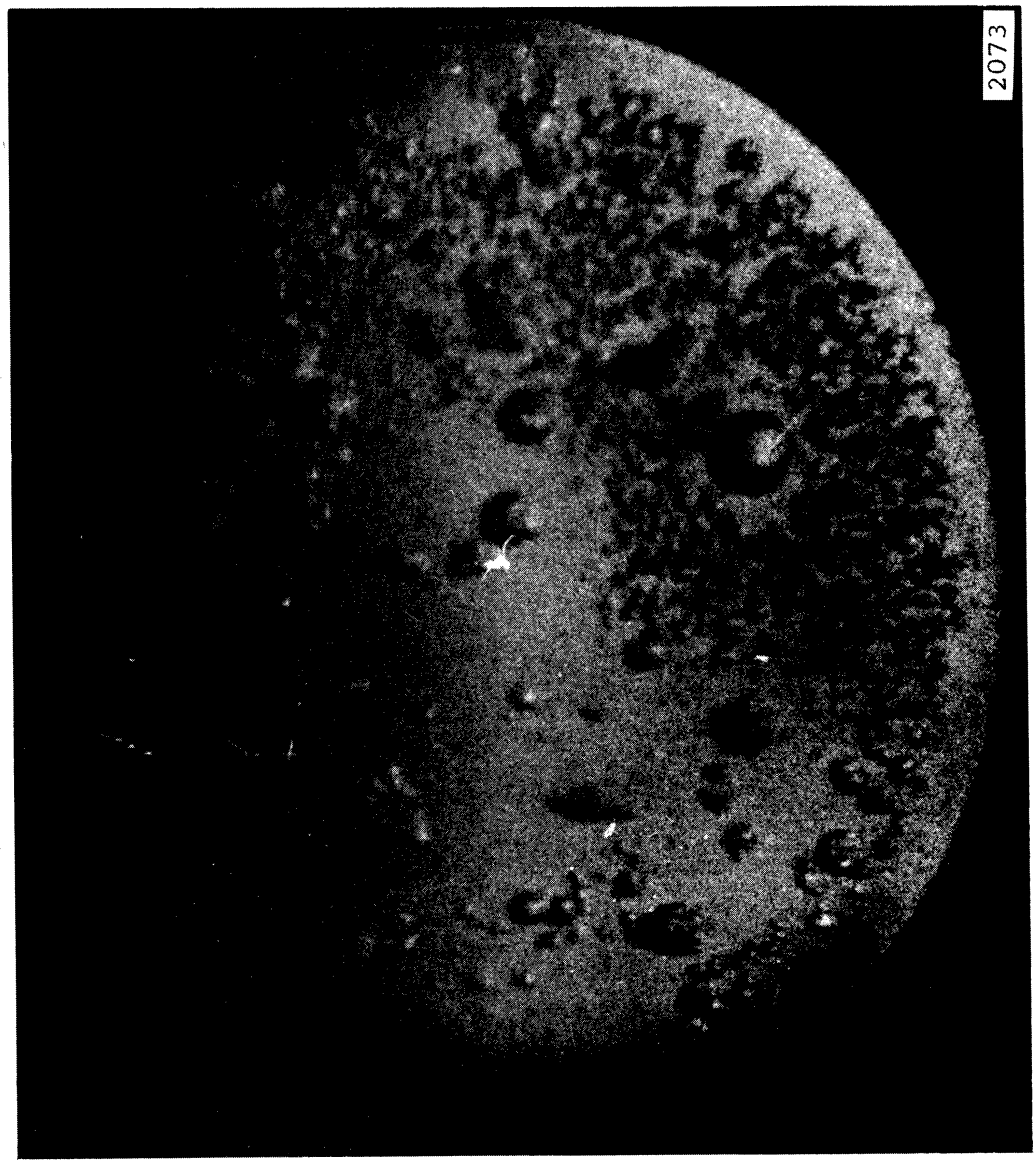

Fig. 82.--High speed photograph No. 111 (11X) of a type 2024-T351 aluminum specimen in water, frequency 20,200 cps, amplitude approximately 2 mils, exposure time per frame of 1.3 μ seconds photographed at 20,150 fps.

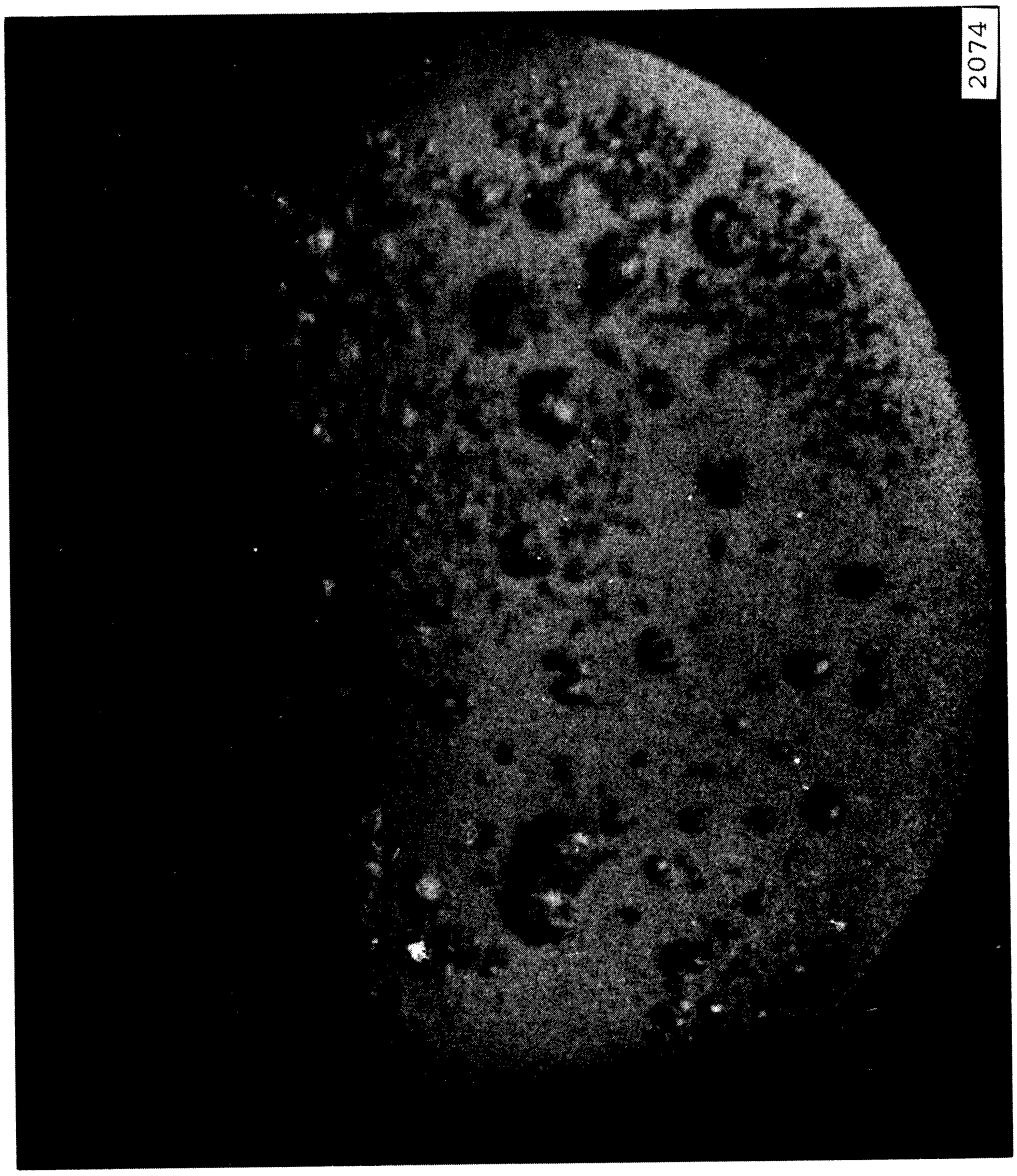

Fig. 83.--High speed photograph No. 115 (11X) of a type 2024-T351 aluminum specimen in water, frequency 20,200 cps, amplitude approximately 2 mils, exposure time per frame of 1.3 μseconds, photographed at 20,150 fps.

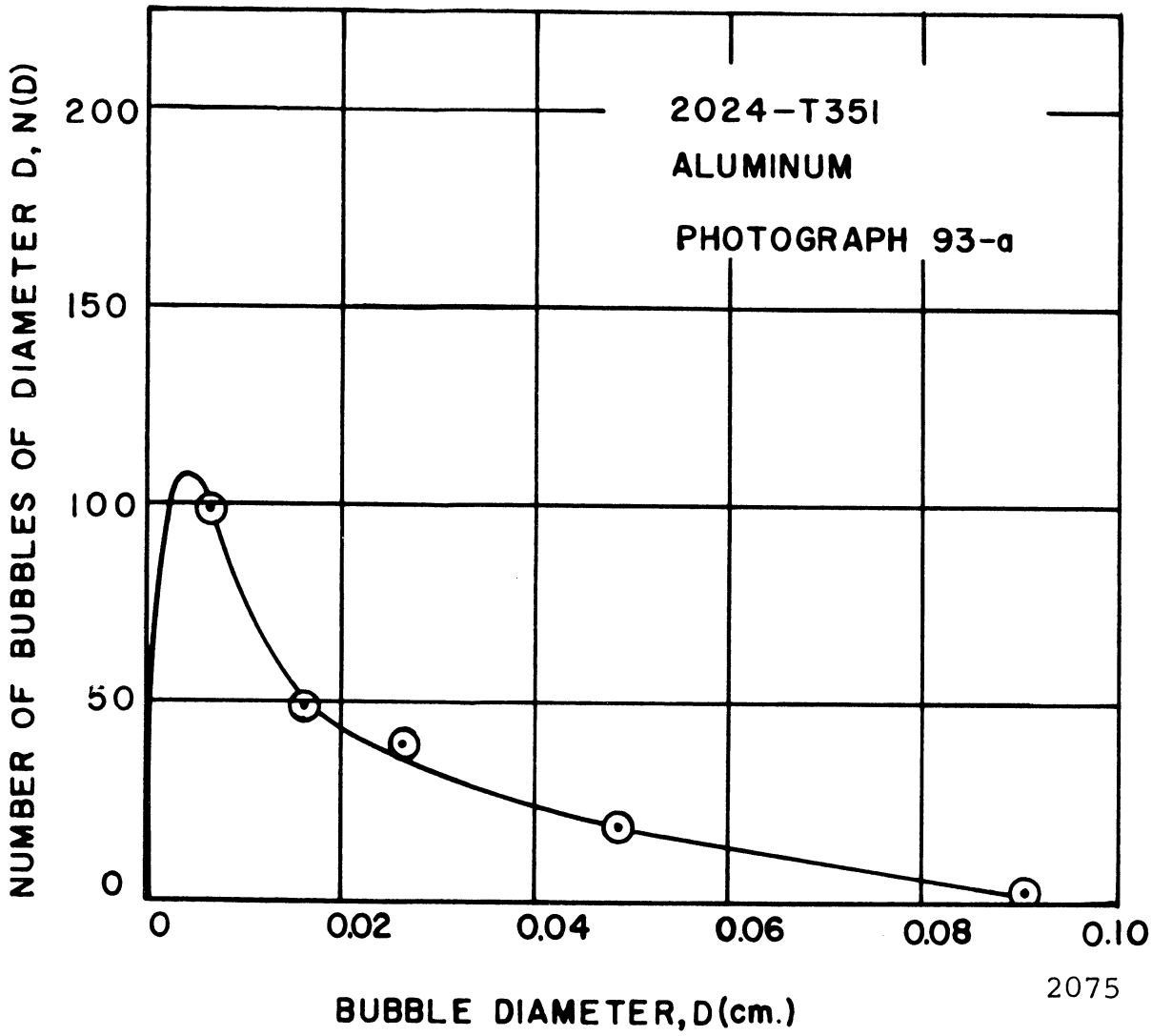

Fig. 84.--Size distribution of the bubble population from photograph No. 93-a of a type 2024-T351 aluminum specimen in water, frequency 20,200 cps, amplitude approximately 2 mils, exposure time per frame of 1.3 μ seconds, photographed at 20,150 fps.

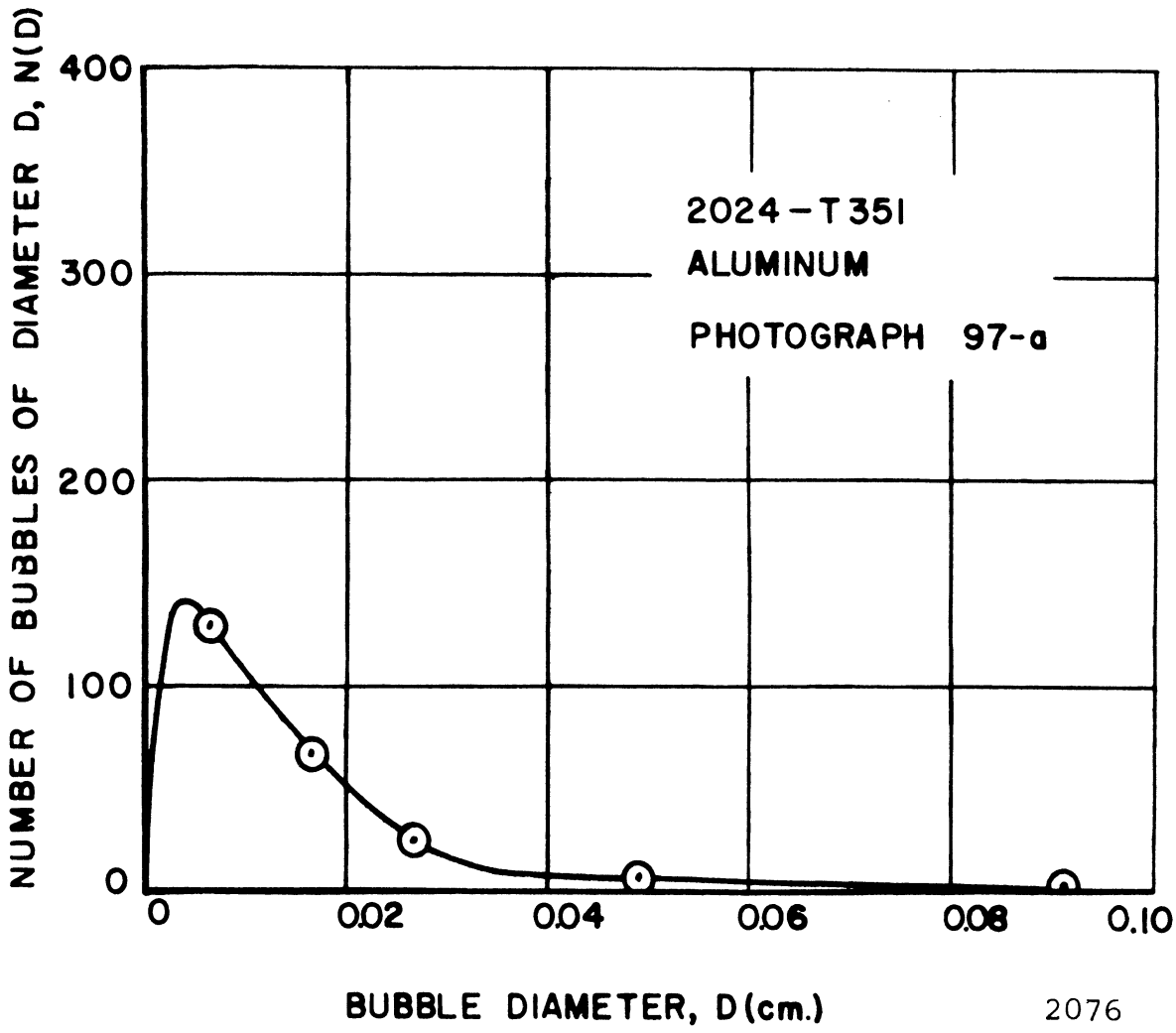

Fig. 85.--Size distribution of the bubble population from photograph No. 97-a of a type 2024-T351 aluminum specimen in water, frequency 20,200 cps, amplitude approximately 2 mils, exposure time per frame of 1.3 μ seconds, photographed at 20,150 fps.

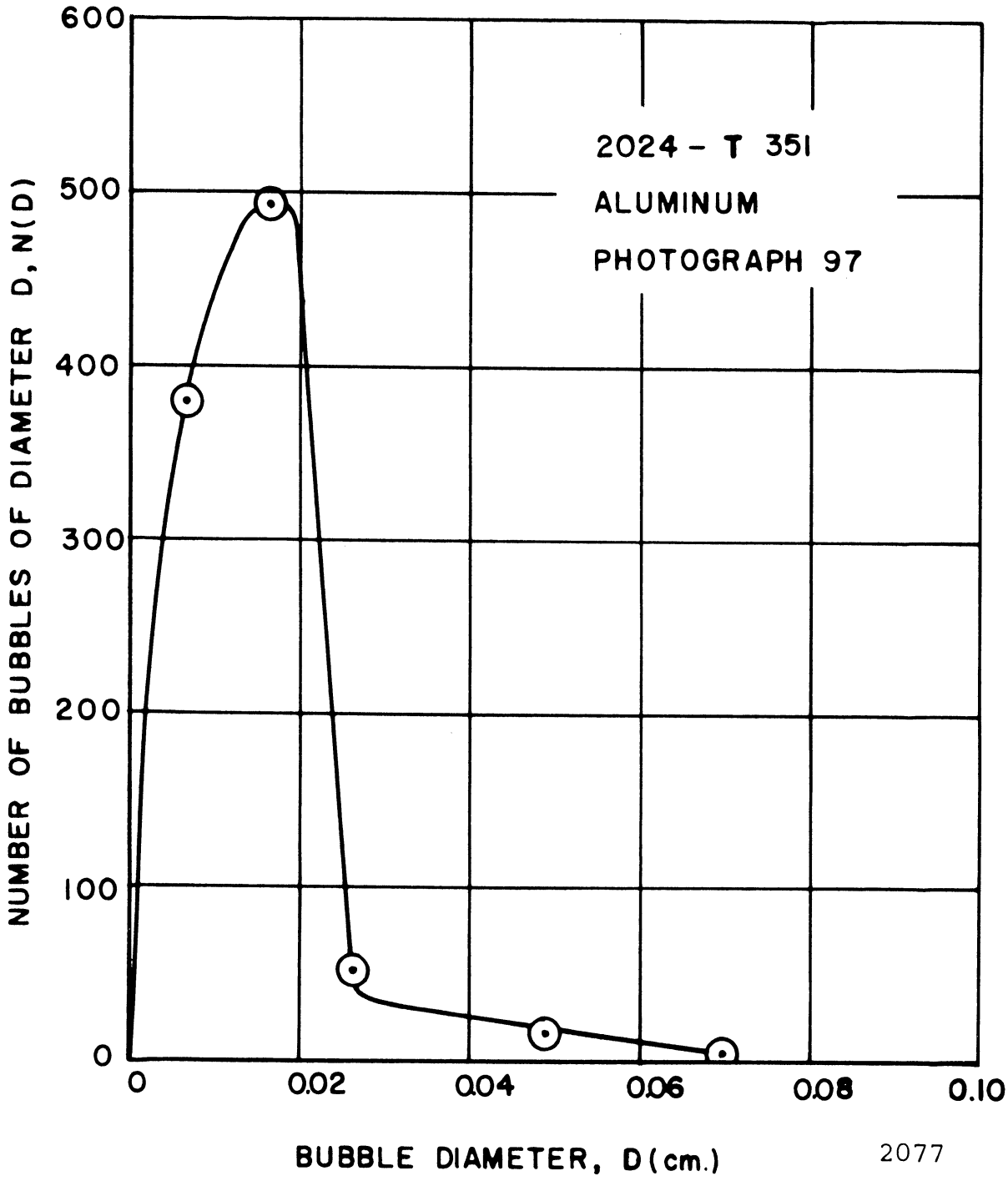

Fig. 86.--Size distribution of the bubble population from photograph No. 97 of a type 2024-T351 aluminum specimen in water, frequency 20,200 cps, amplitude approximately 2 mils, exposure time per frame of 1.3 μ seconds, photographed at 20,150 fps.

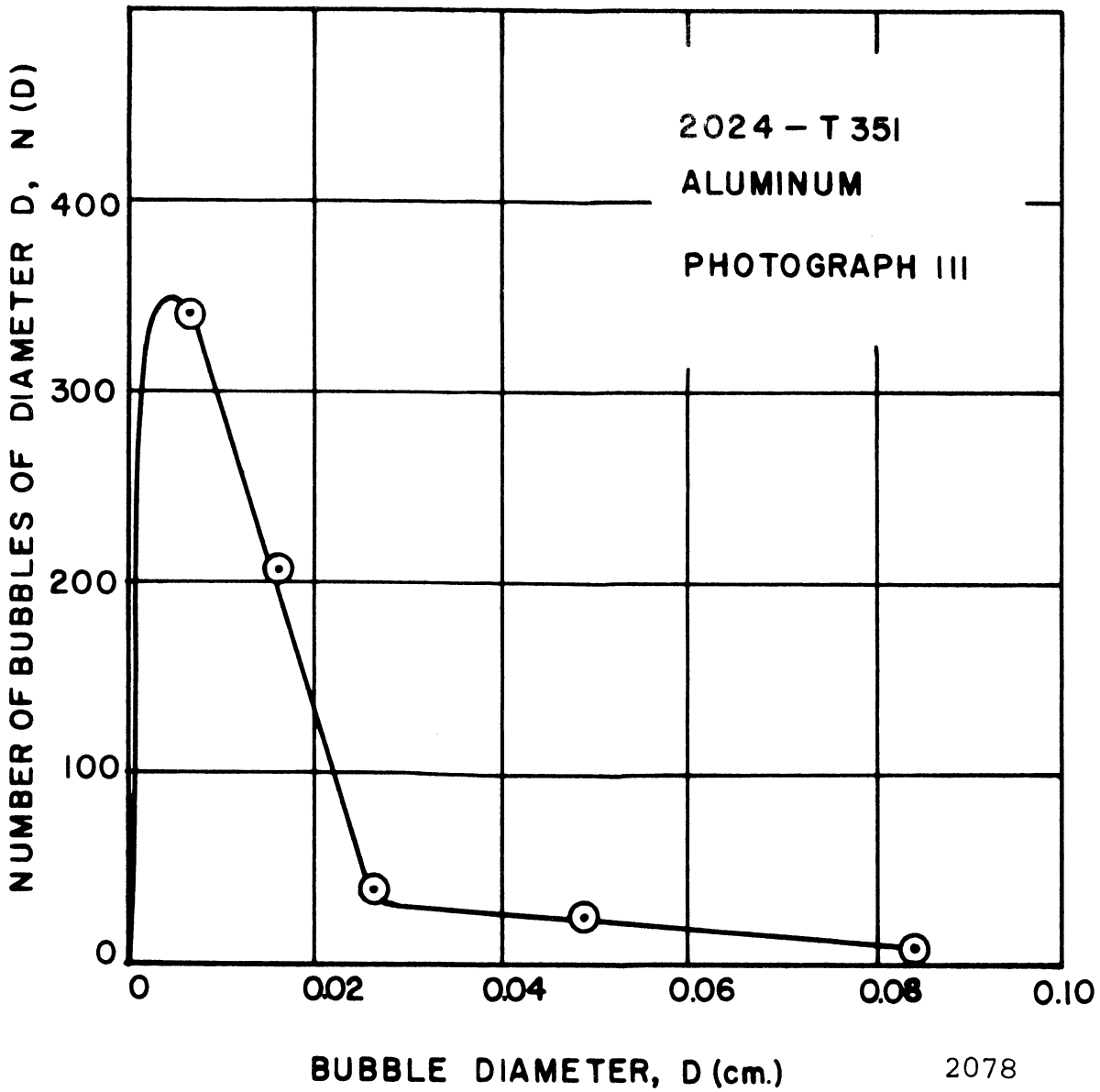

Fig. 87.--Size distribution of the bubble population from photograph No.111 of a type 2024-T351 aluminum specimen in water, frequency 20,200 cps, amplitude approximately 2 mils, exposure time per frame of 1.3 μ seconds, photographed at 20,150 fps.

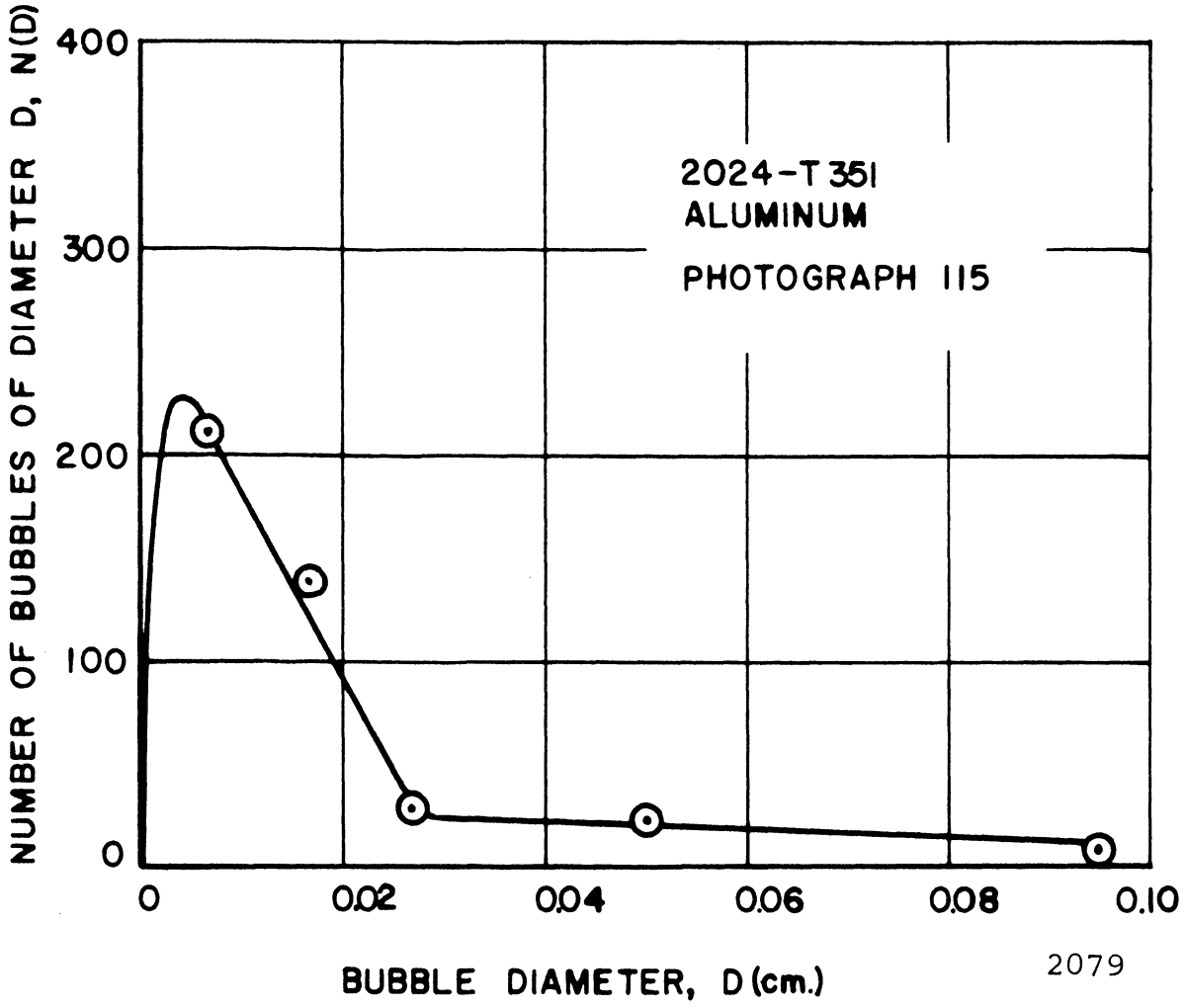

Fig. 88.--Size distribution of the bubble population from photograph No. 115 of a type 2024-T351 aluminum specimen in water, frequency 20,200 cps, amplitude approximately 2 mils, exposure time per fraome of 1.3 μ seconds, photographed at 20,150 fps.

The photographs show vividly how the population varies substantially even though, as was true in these experimental runs, the oscillator frequency and the camera framing rate were closely matched. Because of this matching, the photographs were exposed at about the same part of the acoustic cycle for each frame. However, the population difference is large and the corresponding spectra differ considerably. It may be that the pressure waves from rebounding bubbles have an important effect on the transient bubble population in the near vicinity. In fact, the "cleared area" around some of the large bubbles in Figs. 81, 82, and 83 show this effect.

Thus the use of the maximum bubble count to compute the total number of bubbles per experimental run may be somewhat inaccurate on this account.

The bubble size distributions of Figs. 84, 85, and 88 are quite similar to each other with respect to the form of the curves and the total number of bubbles. Fig. 87 has a similar distribution, but the maximum number of bubbles is higher in the small size range. The most numerous size of bubble for all four curves is in a range of which the median diameter is $\sim$ 0.007 cm and the average diameter $\sim$ 0.018 cm. This compares quite well with the other 7 specimens.

Fig. 86 shows a number decrease in the lower size range, accompanied by a heavy increase in transient bubbles in the size range for this specimen ($<$ 0.025 cm). The average diameter drops slightly to approximately 0.016 cm.

J. Bubble Population Throughout the Acoustic Cycle

High speed photographs of the bubble cloud were taken with the camera framing rate 2% greater than the oscillator frequency for a type 304 stainless steel specimen and the numbers of bubbles in selected size ranges obtained. Integer millimeter diameters were used for size ranges in the photographic enlargement, but the diameters shown in Fig. 89 have been corrected to true sizes. These show the bubble population per frame for four selected diameter ranges and also the total bubbles per frame. A total of fifty consecutive frames were used for counting.

Ordinarily, freshly drawn tap water was used, so some visible bubbles would be expected to exist at all points in the cycle because of the large quantity of entrained air. This has been reported by Saneyoshi and Okushima[35] and others as discussed in Section B of this Chapter. However, at certain points in the acoustic cycle the graphs in Fig. 89 show that there are few or no transient bubbles, which is, again, proof of Noltingk and Neppiras's hypothesis[41,42] that the transient bubbles (which make up the vast majority of the bubble field population) grow and collapse in one acoustic cycle. The only survivors in some of the frames were a few very large bubbles whose characteristic shape suggested that they had rebounded during a previous cycle, and some bubbles that were apparently beginning their first rebound as shown by their characteristic size and surface.

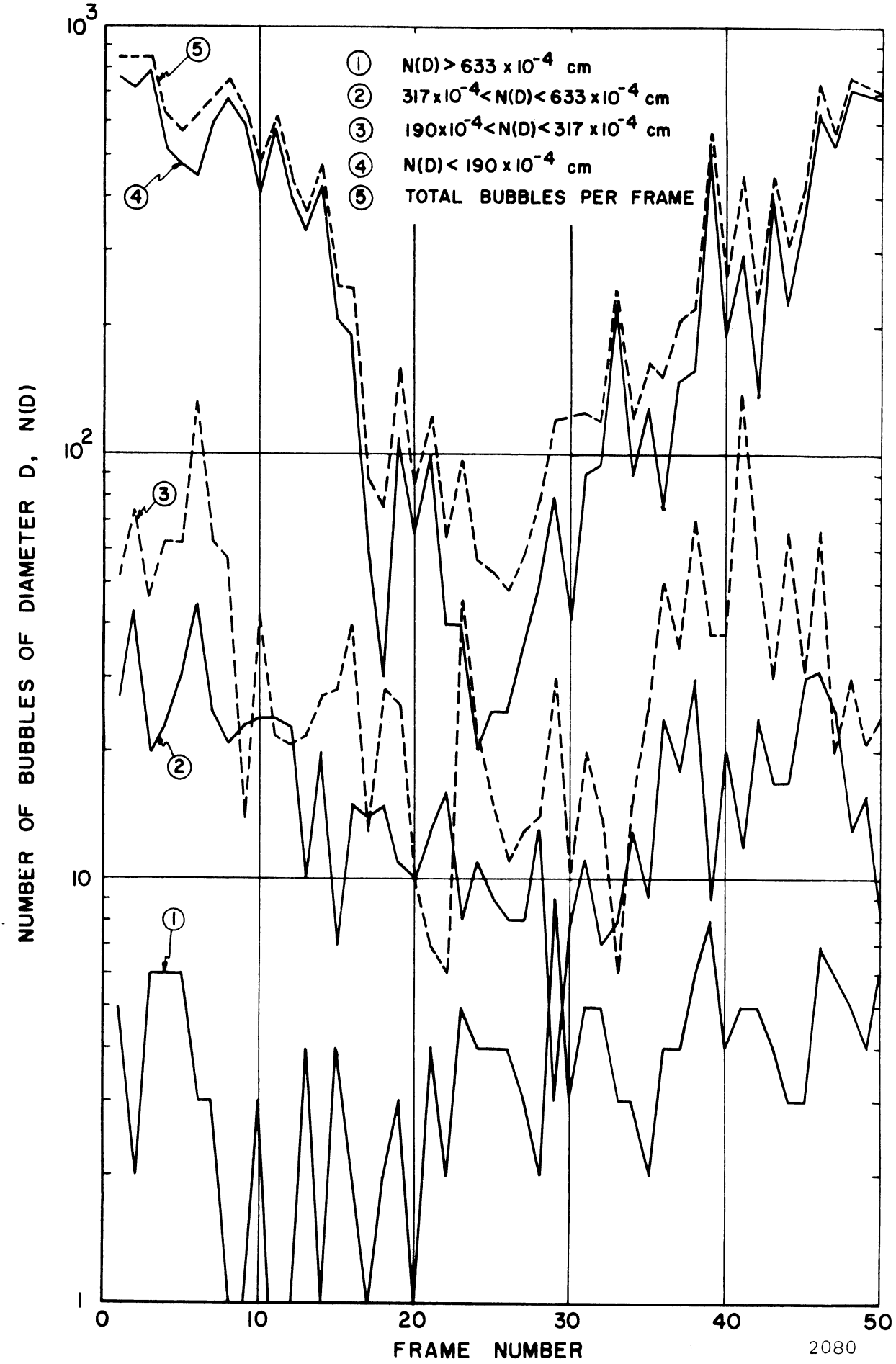

Fig. 89.--Size distribution of the bubble population of frames 1 through 50 of a type 304 stainless steel specimen in water, frequency 20,390 cps, amplitude approximately 2 mils, exposure time per frame of 1.3 μ seconds, photographed at 20,800 fps.

Wide variations in the total bubble population were often noted in successive frames. These changes were almost entirely due to changes in the number of transient bubbles. These population changes may well be due to the occurrence of pressure waves that are emitted by the rebounding bubbles and inhibit the growth of new transient bubbles in the high pressure areas.

Fig. 89 shows that the total bubble population drops heavily in a portion of the acoustic cycle. This portion apparently covers the period occurring after the transient bubbles of one cycle have collapsed up to the point in the successive cycle where the new group of transient bubbles become visible on the high speed photographs.

K. Material Damage

1. Weight Loss

Previous investigators[6] have measured cavitation weight loss in a vibratory facility on specimens for exposures as low as 5 minutes, but not with great precision. Exposure times of 60 seconds and less have been used in this investigation to examine the premise that a nucleation period is required for weight loss to occur.

The weight loss of the various specimens along with other data is shown in Table 1. Although the data is relatively imprecise because of the very small weight differences involved (from 0.07 to 1.7 mg), still the measured losses are large

compared to the precision of the Mettler balance (~0.01 mg). Removel of wiped metal or polishing compounds from cracks or scratches on the specimen surface by the action of the cavitation field may be responsible for part of the weight loss. Fig. 90 shows the scratches that appeared on the 75% c. w. nickel (as rec'd) specimen after exposure for 44 seconds at a frequency of 20,454 cps and an amplitude of approximately 2 mils. These were not visible before the test. The frosty surface shows the location of the heaviest damage, indicating that even in this very short run, pitting has occurred. The center line is a marking scribe.

2. Number of Pits

Appendix "A" shows in detail the variation of the pit population density over various parts of the surface of an individual specimen. Pitting was so heavy on all the specimens except Plexiglas that it was necessary to use estimates of pit population density for small (S) pits to arrive at the estimated total number of pits, even for these very short runs.

Table 1 shows the number of pits for the selected diameter ranges as well as the estimated totals for each specimen.

Counting accuracy, even at 500X, was limited because of multiple pit damage, i.e., superposition of pits which occurs as damage increases. On some specimens the larger pits may be caused by some form of mechanical damage other than cavitation. These pits could occur in the handling process.

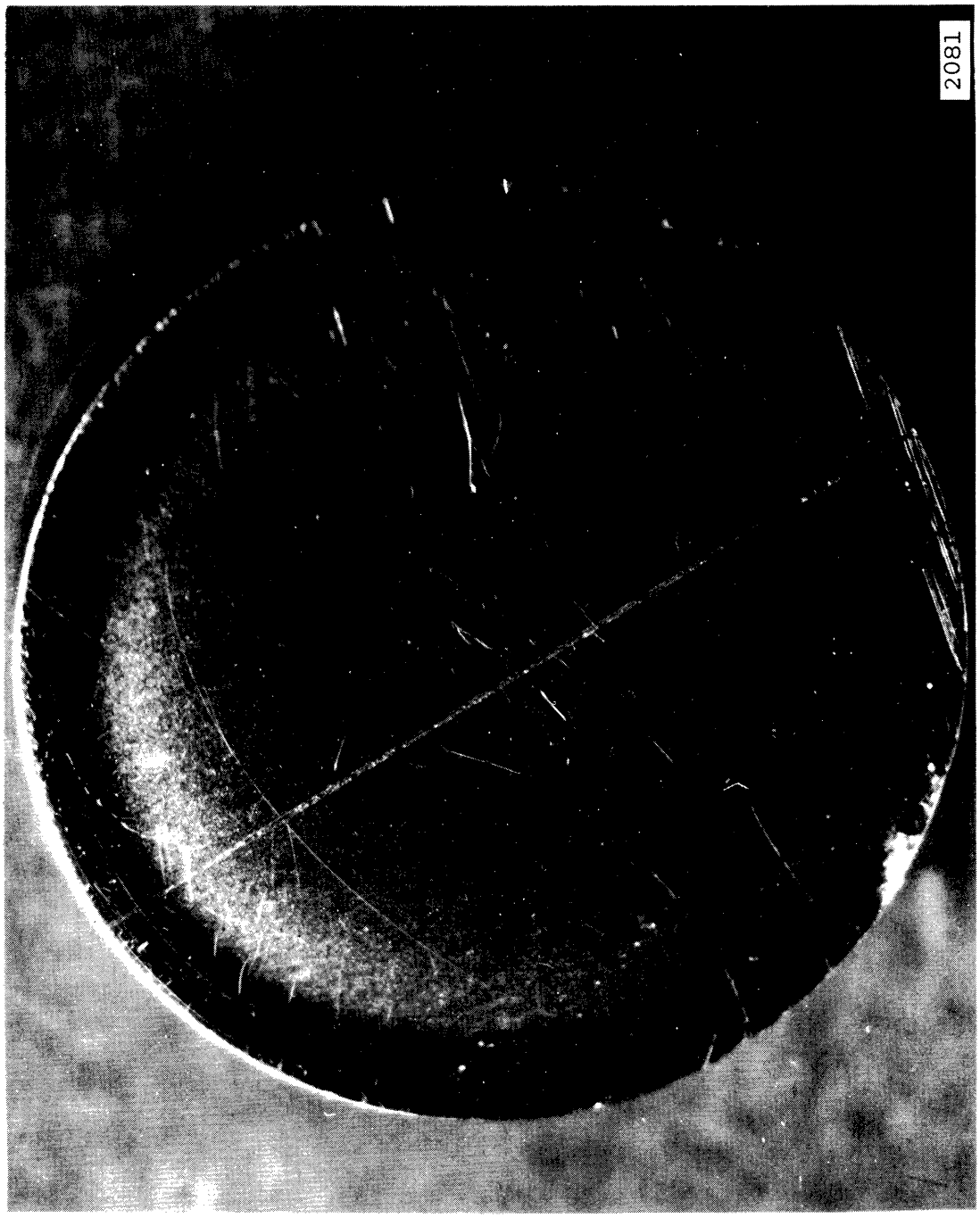

Fig. 90.--Still photograph (2.5X) of a 75% c.w. nickel (as rec'd) specimen after 44 seconds of exposure to cavitation in water with frequency at 20,454 cps and amplitude approximately 2 mils.

The number of pits ranges from 113 on Plexiglas to approximately 123,000 on type 2024-T351 aluminum. Since the run duration for the aluminum was 60 seconds, this corresponds to a formation of ~2,000 pits/sec. or ~1 pit every 10 cycles. On the average ~3-1/2 cycles were required to form a pit on type 6061-T651 aluminum and ~ 4,000 cycles on Plexiglas.

When making the actual cavitation exposure runs starting with a polished specimen, up to 5 seconds of running time was required to accomplish minor amplitude adjustments. After this period the ultrasonic equipment was shut off while preparations were completed for a high speed photographic run. While the specimens were not removed for metallographic examination after this adjustment period because a fixed position of the specimens in the water container for all runs on each specimen was considered mandatory, a frosty damage pattern was evident even after this short adjustment period on all of the specimens.

3. Pit Spectra

The number of pits in various size ranges was determined from selected groups of typical photomicrographs (500X) for all materials but Plexiglas. This information was used to plot pit size distribution spectra. For Plexiglas the entire specimen surface was examined to obtain data for a pit spectrum, since the total number of pits was relatively small.

Examination of the photomicrographs (500X) permitted far greater accuracy in determining the pit size distribution

than that obtainable using a microscope. With the microscope, because of optical and measuring limitations, the majority of the pits could only be categorized as having diameters < 0.0010 cm, while using the photomicrograph it was possible to select six discreet diameter ranges < 0.0010 cm, with the lowest being < 0.0002 cm. Tabulation of this data is shown in Appendix "B" and the corresponding spectra are shown in Figs. 91 through 97. Fig. 98 is for Plexiglas, with the data being obtained from Appendix "A." For Plexiglas the proportion of pits with diameters < 0.0010 cm was only about 50%, i.e., the pits in Plexiglas are larger in diameter by a factor ~ 10, so that the volume per pit may be larger by $> 10^3$ (since the depth to diameter ratio is also larger), but the pits are considerably fewer in number.

The spectra for the metals are quite similar, showing an increasing number of pits as the pit diameter decreases (which is also the case for Plexiglas). The extreme number of small pits for the copper 900°F annealed specimen is not readily explainable. Perhaps it is due to the selection of photomicrographs which may have been atypical in this case. These photomicrographs were taken only from areas where there was no, or at worst little, evidence of miltiple pitting, and then three locations were chosen at random.

As shown in Appendix "B," all pits with diameters > 0.0004 cm were counted, and compared with the measured hardness of the specimens (Table 2), to see whether a correlation between the number of larger pits and hardness might

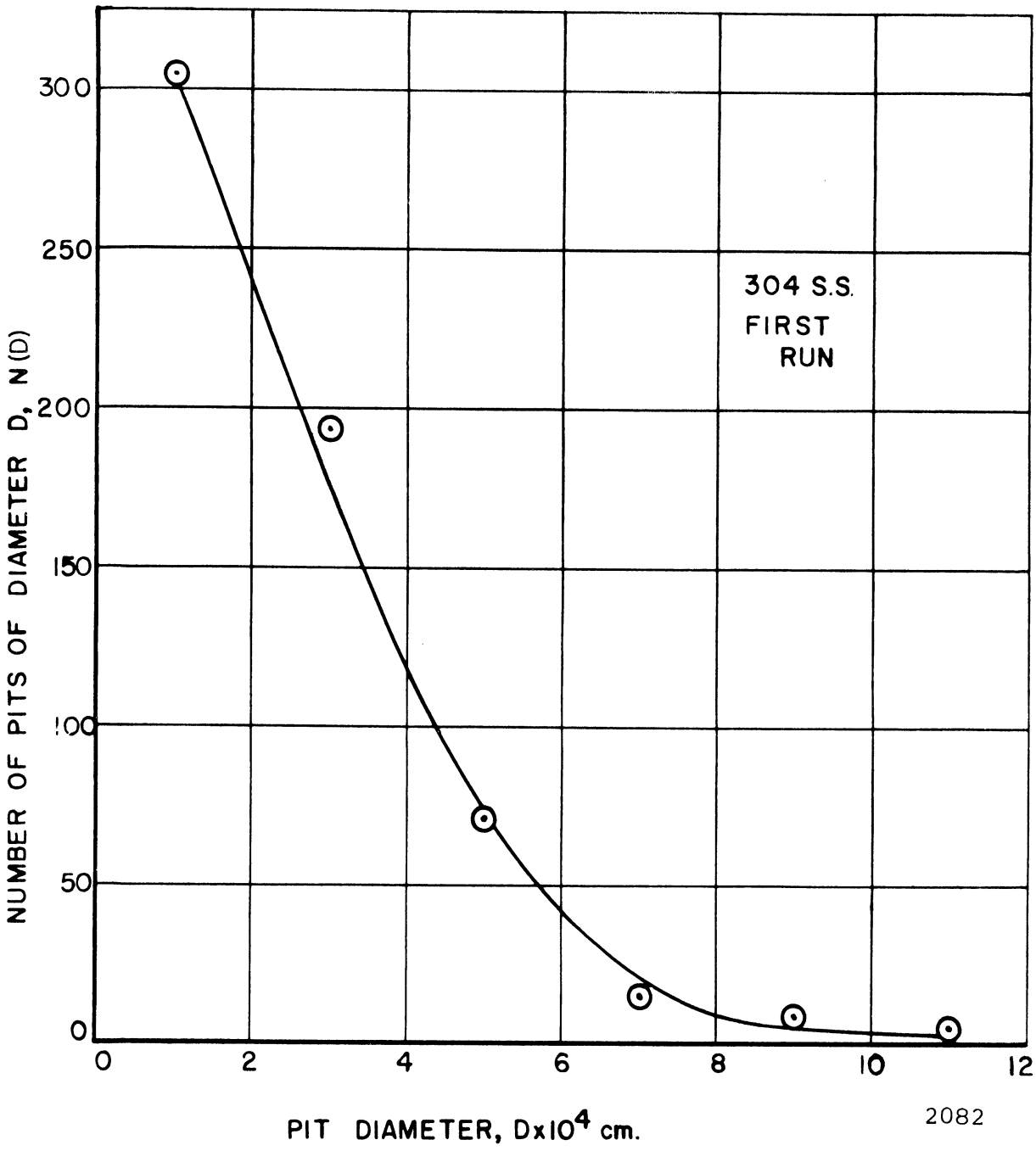

Fig. 91.--Pit size distribution for a type 304 stainless steel specimen exposed to cavitation in water for 54 seconds, frequency 20,325 cps, and amplitude approximately 2 mils.

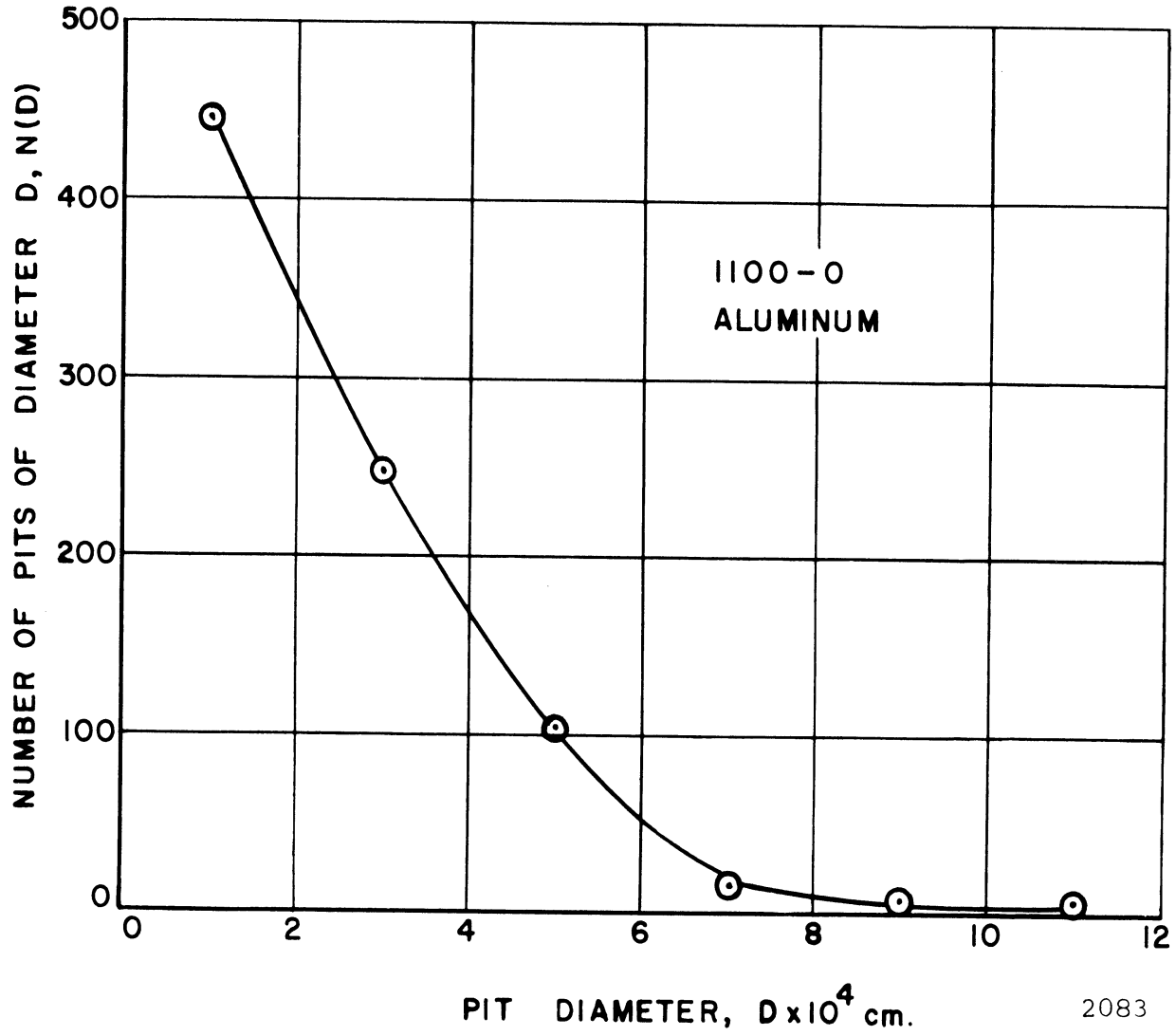

Fig. 92.--Pit size distribution for a type 1100-0 aluminum specimen exposed to cavitation in water for 22 seconds, frequency 20,244 cps, and amplitude approximately 2 mils.

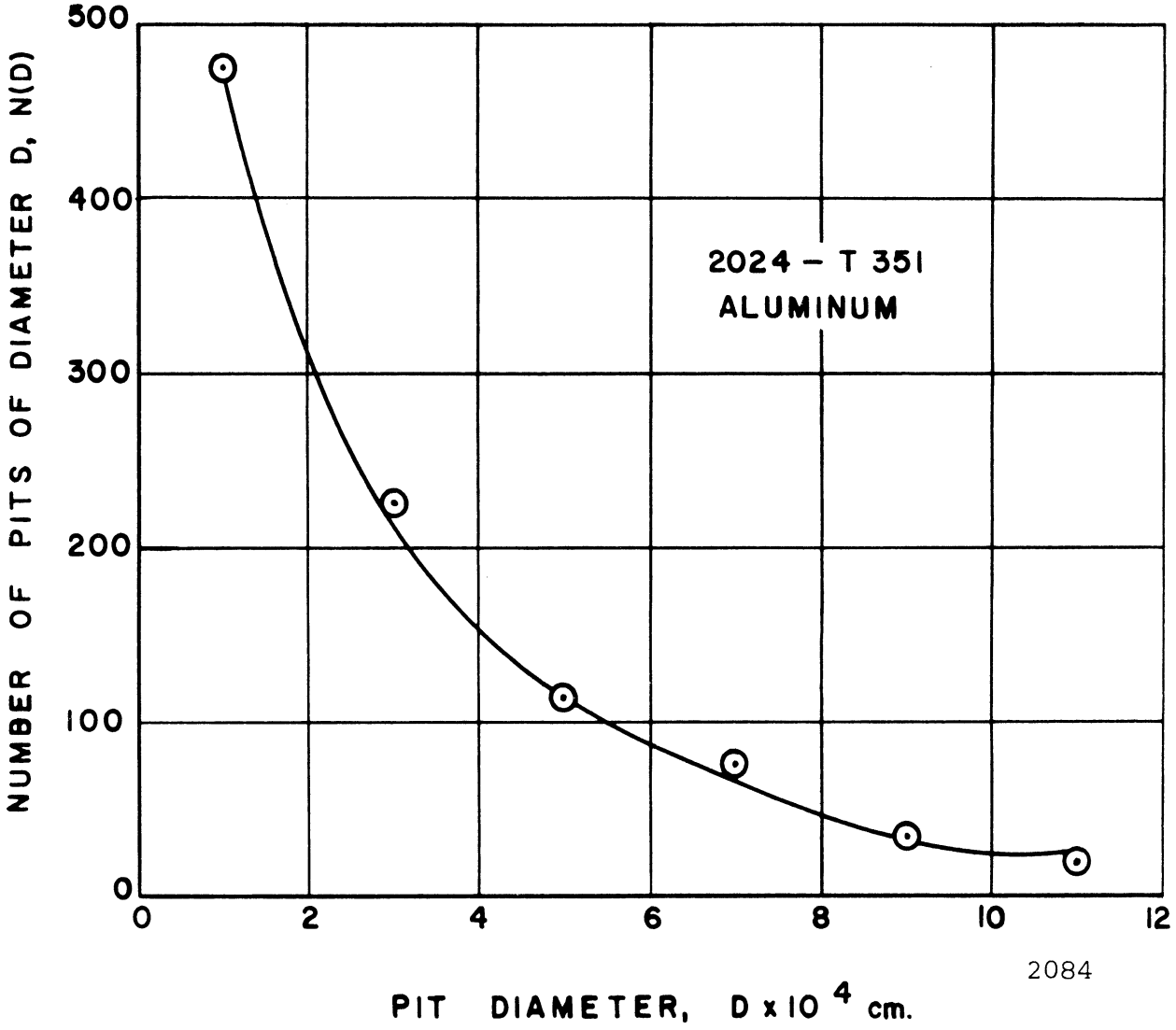

Fig. 93.--Pit size distribution for a type 2024-T351 aluminum specimen exposed to cavitation in water for 60 seconds, frequency 20,200 cps, and amplitude approximately 2 mils.

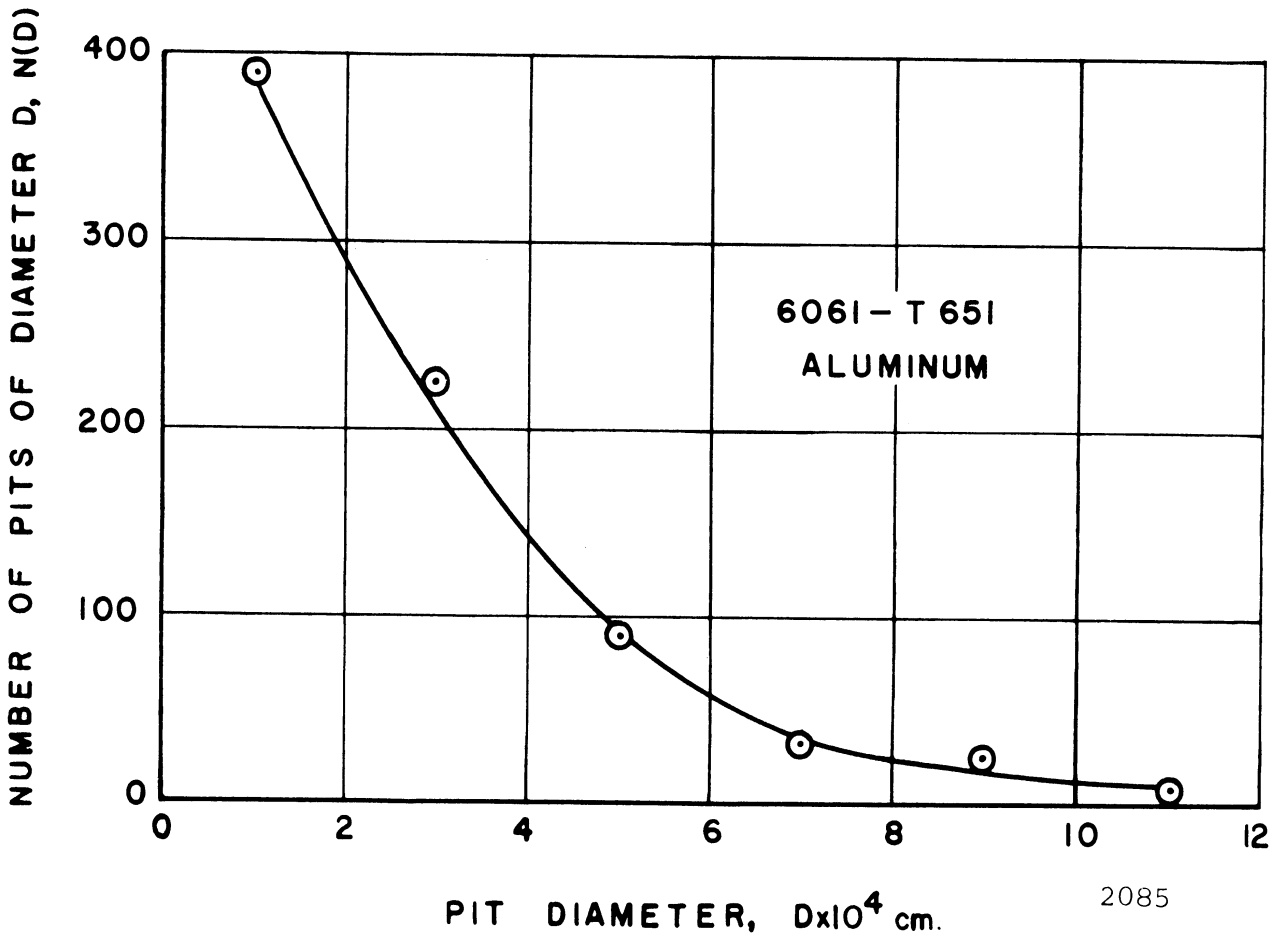

Fig. 94.--Pit size distribution for a type 6061-T651 aluminum specimen exposed to cavitation in water for 15 seconds, frequency 20,243 cps, and amplitude approximately 2 mils.

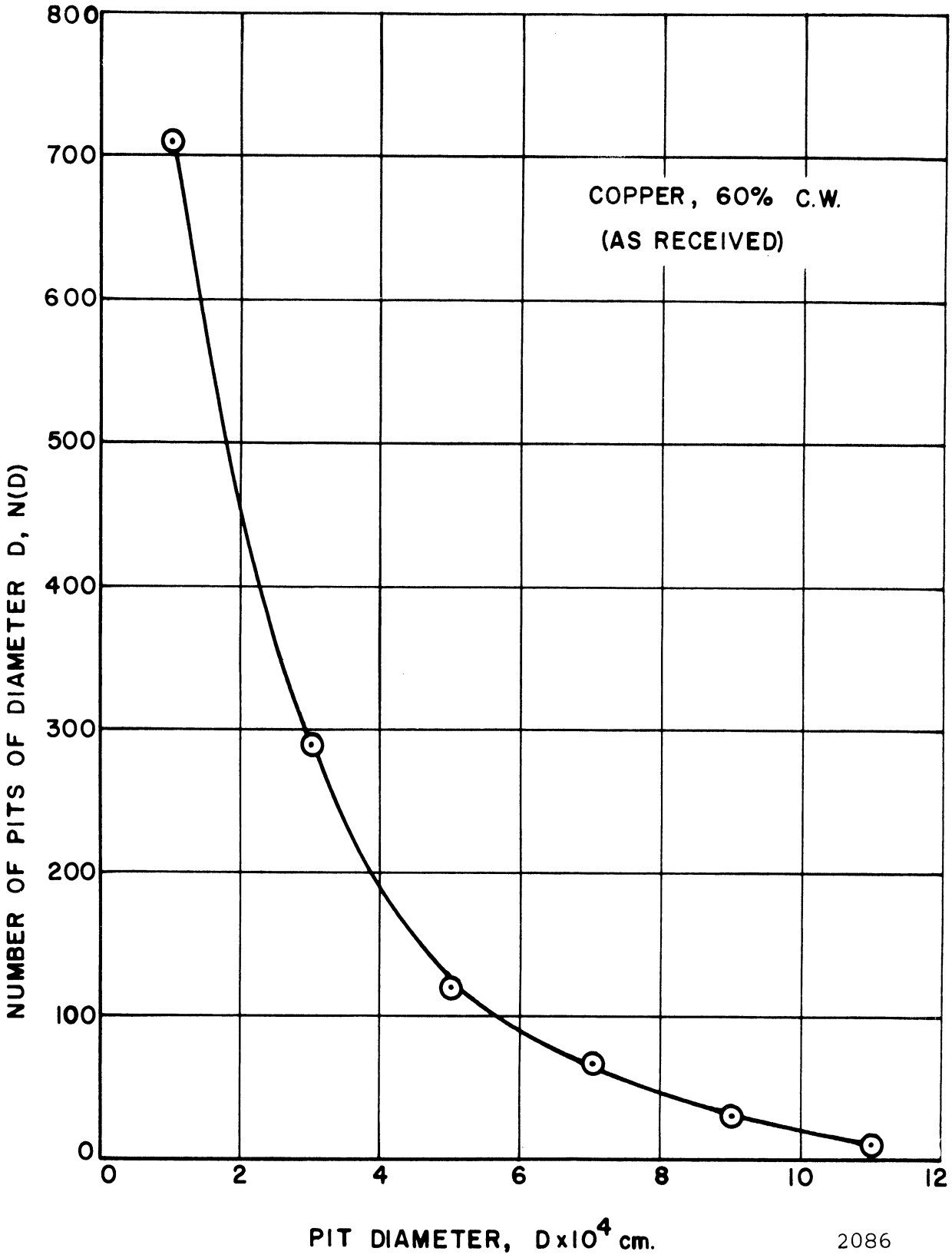

Fig. 95.--Pit size distribution for a 60% c.w. copper (as rec'd) specimen exposed to cavitation in water for 32 seconds, frequency 20,542 cps, and amplitude approximately 2 mils.

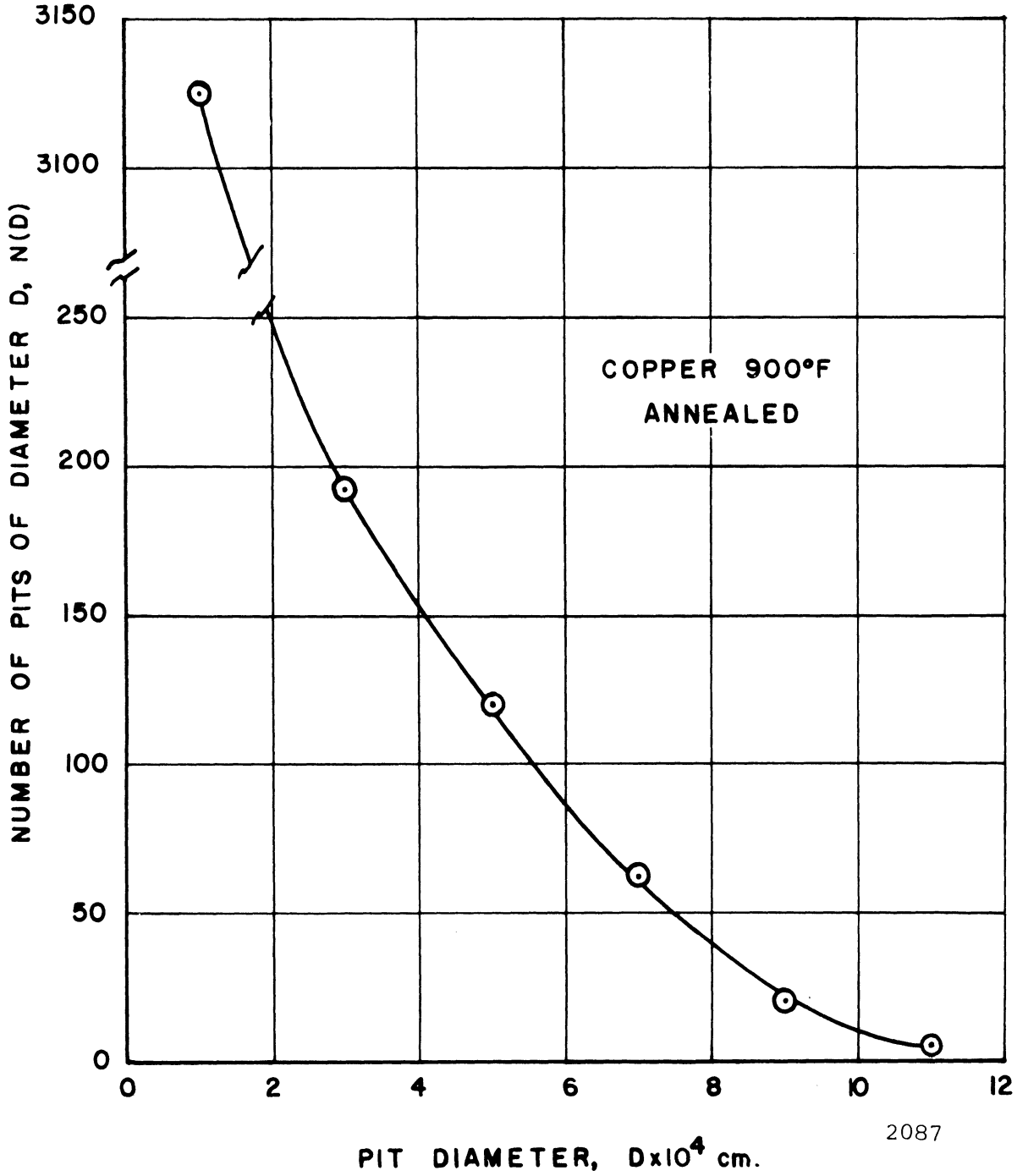

Fig. 96.--Pit size distribution for a copper 900°F annealed specimen exposed to cavitation in water for 33 seconds, frequency 20,419 cps, and amplitude approximately 2 mils.

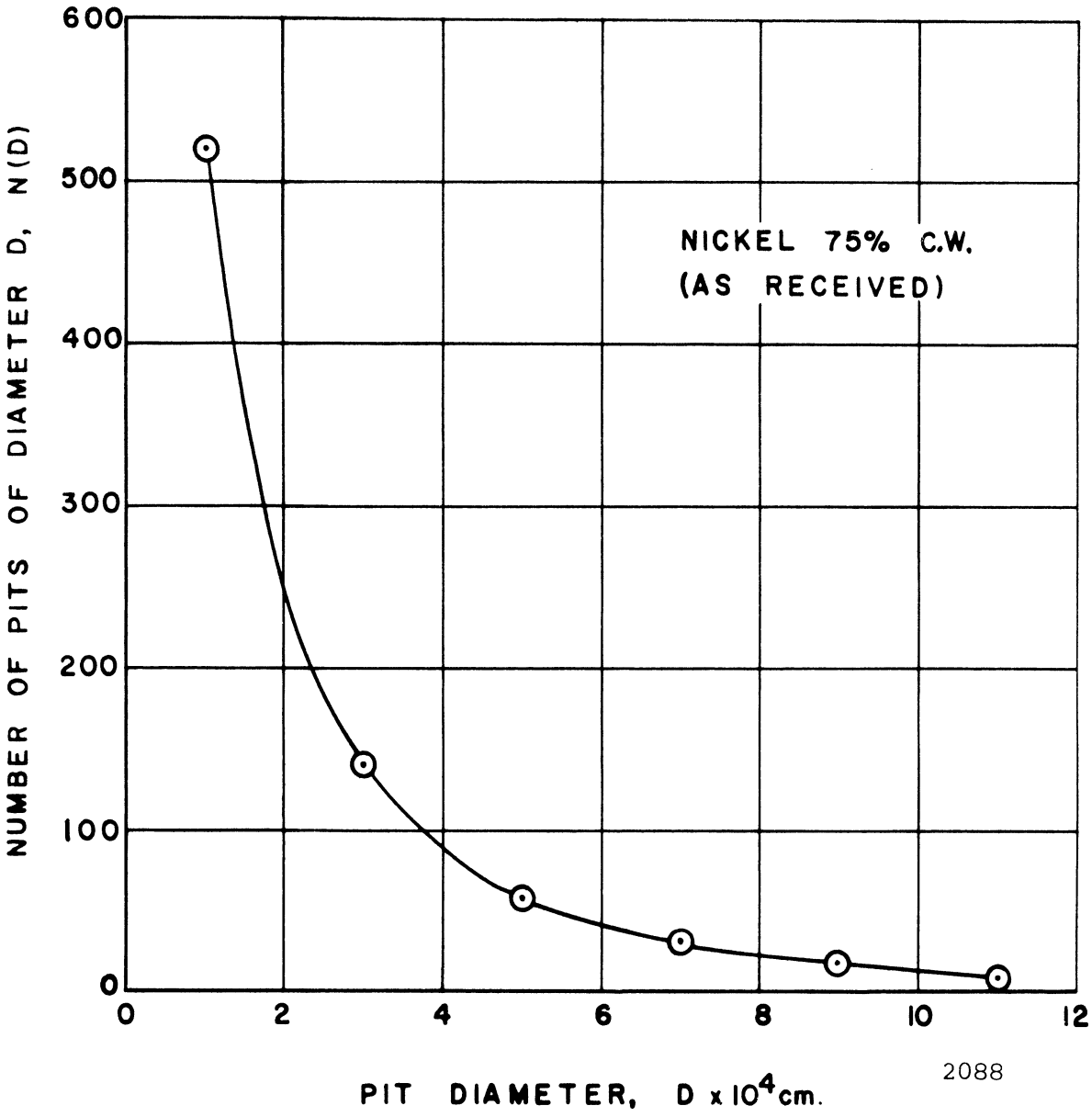

Fig. 97.--Pit size distribution for a 75% c. w. nickel (as rec'd) specimen exposed to cavitation in water for 44 seconds, frequency 20,454 cps, and amplitude approximately 2 mils.

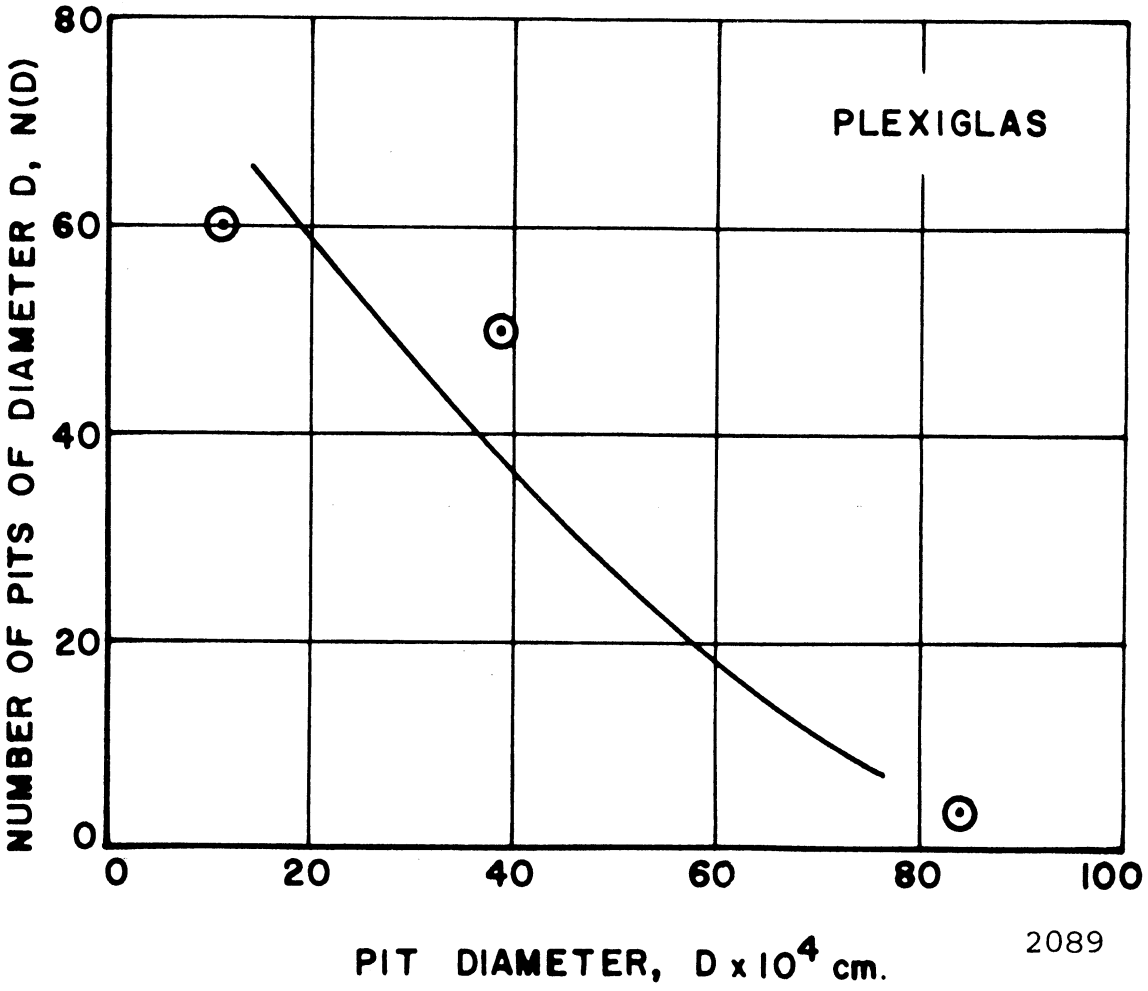

Fig. 98.--Pit size distribution for a Plexiglas specimen exposed to cavitation in water for 27 seconds, frequency 20,564 cps, and amplitude approximately 2 mils.

TABLE 2

MECHANICAL PROPERTIES OF THE SPECIMENS

Material	Tensile Strength psi	Yield Strength psi	Energy Strain Energy psi	True Strain Energy (a) psi	True Strain Energy (b) psi	True Brkng. Stress psi	Hardness (Brinell) No.	Elastic Modulus psi	% Elong.	%Red. Area	Char. Acoustic Imped. lb_2mass/ ft^2-sec	Ultimate[57] Resilience (UR) (in-l . force/in^3) psi
304 SS	94,500	64,700	57,300	41,300	47,500	172,800	184	$29x10^6$	63.8	77.9	$8.11x10^6$	183
1100-0 Aluminum	12,250	7,600	4,950	4,320	22,600	35,600	18	$10x10^6$	44.5	85.5	$2.83x10^6$	13
2024-T351 Aluminum	72,000	57,900	13,300	13,600	31,050	102,500	135	$10x10^6$	20.0	34.5	$2.83x10^6$	414
6061-T651 Aluminum	45,300	40,000	25,800	9,840	38,620	86,800	101	$10x10^6$	19.4	56.7	$2.83x10^6$	246
Copper 60% C.W. (As Rec'd)	53,400	49,500	3,100	3,100	11,800	85,600	106	$17x10^6$	6.2	19.8	$6.66x10^6$	216
Copper 900°F Annealed	31,500	9,500	13,900	13,900	26,900	54,300	38	$17x10^6$	51.3	48.5	$6.66x10^6$	87
Nickel 75% C.W. (As Rec'd)	93,100	82,000	3,200	3,200	8,300	99,100	160	$30x10^6$	3.9	10.2	$8.85x10^6$	164
Plexiglas	10,445	1,600	320	320	320	320	3	$.4x10^6$	4.0	0.0	$.38x10^6$	5

Values obtained from Harrison et al[56] (except Ultimate Resilience)

True Strain Energy (a) is corrected for elongation

True Strain Energy (b) is corrected for elongation and reduction in area

exist. In Table 3 the specimens are ranked according to hardness, and the number of pits with diameters > 0.0004 cm have been normalized to the maximum total number of pits observed (type 2024-T351 aluminum). It was expected that the softer materials would have proportionately more larger pits. However, type 304 stainless steel, the hardest material, had the third highest number of large pits (>0.0004 cm.). Plexiglas, the softest material, had the largest number > 0.0004 cm. Actually the number of pits in this category with the exception of Plexiglas was quite uniform for all materials.

The pit spectrum for type 304 stainless steel, Fig. 91, is quite similar to that obtained by Robinson[10] for the same material in a cavitating water venturi. However, the pits in the venturi were generally $\sim$3 to 10 times smaller, most having diameters ~ 0.0004 cm.

4. Comparison of Bubble and Pit Spectra

Most of the bubbles that were observed in the high speed photographs had diameters < 0.02 cm, while most of the pits that were measured on the photomicrographs had diameters < 0.0002 cm. The 100:1 ratio between these diameters is only approximate (Robinson[10] found for his venturi experiments a ratio of about 300:1), but is of value in furthering understanding of the damaging mechanism. For example, if the pits result from a micro-jet evolving from an asymmetric bubble collapse, then from the above information, the jet diameter must be $\sim$ 1/100 to 1/1000 that of the original bubble. This

TABLE 3

NORMALIZED NUMBER OF PITS WITH DIAMETERS > 0.0004 CM
COMPARED TO BRINELL HARDNESS NUMBER

Specimen	Brinell Hardness No.	Normalized Number of Pits >0.0004 cm*
Type 304 Stainless Steel	184	246
75% C.W. Nickel (As Rec'd)	160	134
Type 2024-T351 Aluminum	135	244
60% C.W. Copper (As Rec'd)	106	281
Type 6061-T651 Aluminum	101	193
Copper 900°F Annealed	38	374
Type 1100-0 Aluminum	18	176
Plexiglas	3	57,000

*Information taken from photomicrographs (500X).

large ratio seems reasonable since if the jet is to have a high enough velocity to be damaging, the kinetic and pressure energy from a much larger mass of water must be concentrated therein. The large bubble to pit diameter ratio is much harder to justify on the basis of a shock wave mechanism, since the bubble collapse center would necessarily be of the order of the maximum bubble radius from the specimen surface, so that the depression created by a spherical shock wave generated at such a position would be likely to cover an area with a diameter of the same order as that of the bubble. See sketch below.

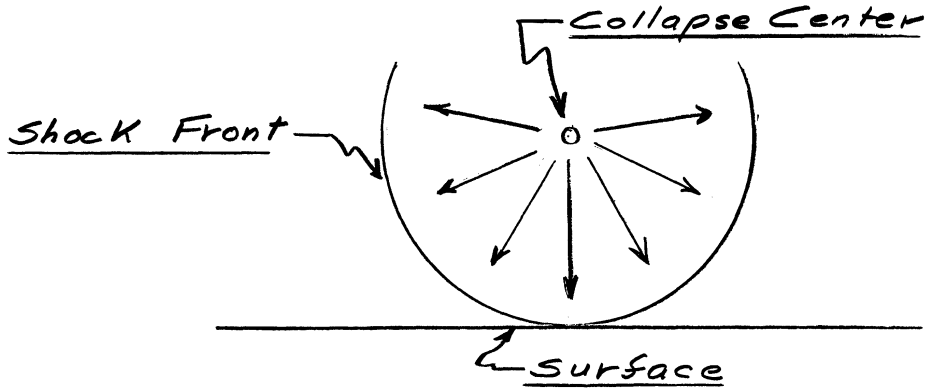

5. Low Power Photomicrographs

A general picture of the pit damage was gained from before and after composite photomicrograph (53X) assemblies. While magnification was too low for the study of individual pits, the damage pattern was quite evident because of the varying pit population density. Additional information was provided by these assemblies when attempting to correlate bubble

patterns with the damage patterns. (The full assemblies are not included.)

For the type 2024-T351 aluminum specimen, the entire surface was mapped at 53X both before and after cavitation-exposure, so that any damage patterns would be evident. Orientation of the damage pattern with the bubble pattern was made possible by the 4 vertical scratches (accidentally acquired) in the lower left section of the specimen shown on Figs. 42-A and B. This specimen was the first to be run. For later runs a center scribe mark greatly assisted in matching the damage pattern to the bubble pattern.

For the 2024-T351 aluminum specimen the damage pattern follows the bubble pattern as shown in the many high speed photographs and as typified by Fig. 64 which shows the approximate maximum bubble population for this specimen. The damage is less at the top where the bubble population is also less, though still extensive. The damage is noticeably heavier at the bottom where a heavy bubble population was almost always evident in the photographs. Fig. 99 is a section from the large composite photomicrograph assembly and shows part of the dense pitting area which corresponds to the heavy bubble population area, as well as part of the relatively undamaged outer annulus. The high speed photographs show few bubbles on this annulus area as is to be expected on physical grounds previously explained.

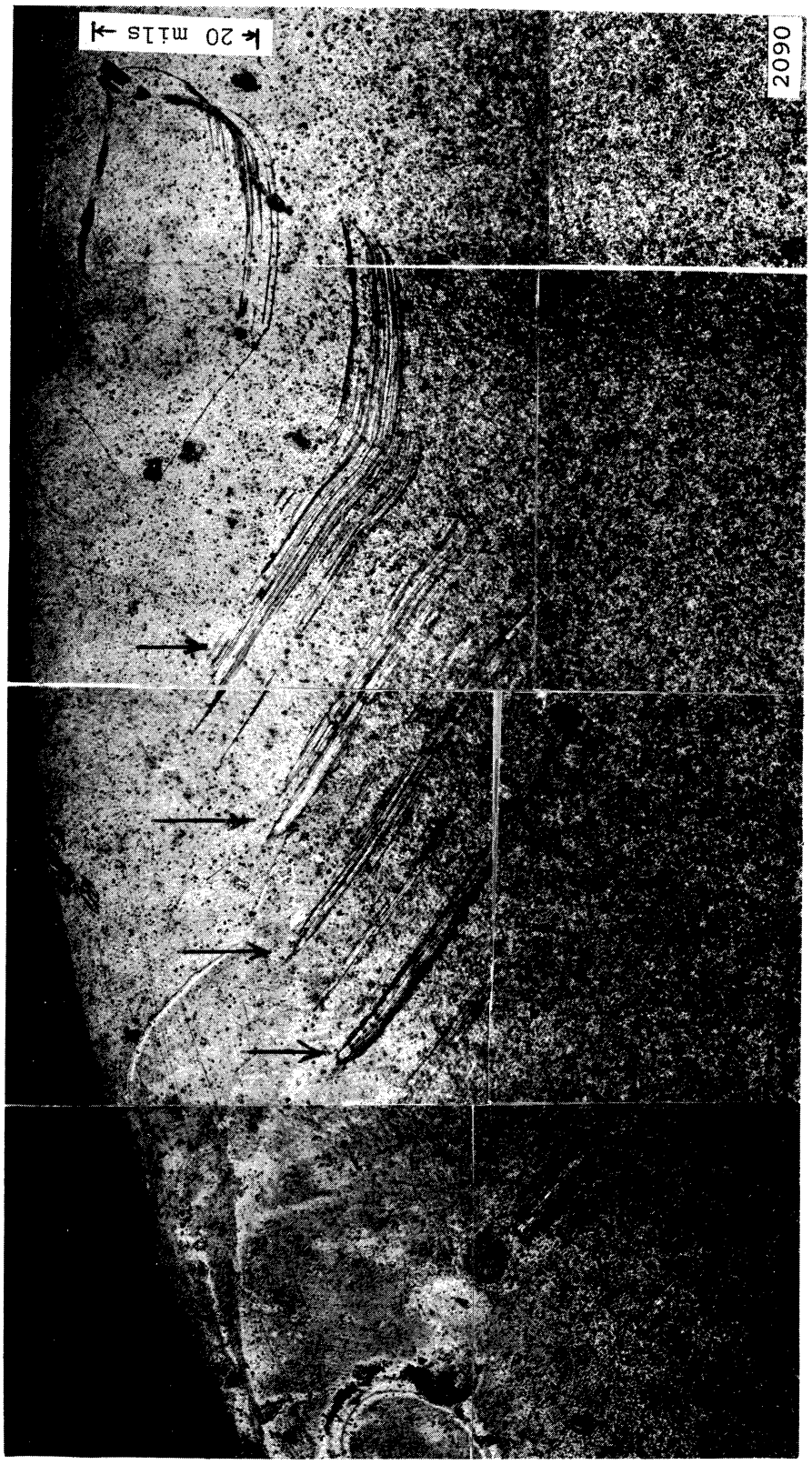

Fig. 99.--Section from a composite photomicrograph assembly (53X) of a type 2024-T351 aluminum specimen exposed to cavitation in water for 60 seconds, frequency 20,200 cps, and amplitude approximately 2 mils.

The four short gouges on the type 2024-T351 aluminum specimen (see arrows in Fig. 99) did not accelerate the damage in their area, but apparently the ridges along the sides of the gouges have some effect on flow patterns parallel to the surface so that damage was somewhat less between them. This suggests definite flow patterns exist across the specimen surface and thus cause bubble motion parallel to the surface, as was previously shown (Fig. 58).

Since this type 2024-T351 aluminum sample was the first to be tested, and multiple pitting was noticed, it was decided to run the remaining seven samples, when possible, less than the 60 seconds which had been used for this specimen.

Fig. 100 is a section from the assembled composite photomicrograph for the type 304 stainless steel specimen after exposure to cavitation for 54 seconds. The large pits that are so noticeable along the outer edge existed before cavitation. These were actually a result of the polishing operation, but it was decided to expose the specimen to cavitation nevertheless in order to see whether or not damage would be localized around existing pits. It was not, as was also observed earlier in the venturi tests.[39] Damage is uniformly heavy with the exception of the outer annulus where damage was light. This run corresponds to a full bubble field (with the exception of the outer annulus) as typified by Fig. 62, a photograph of the approximate maximum bubble population on the stainless steel.

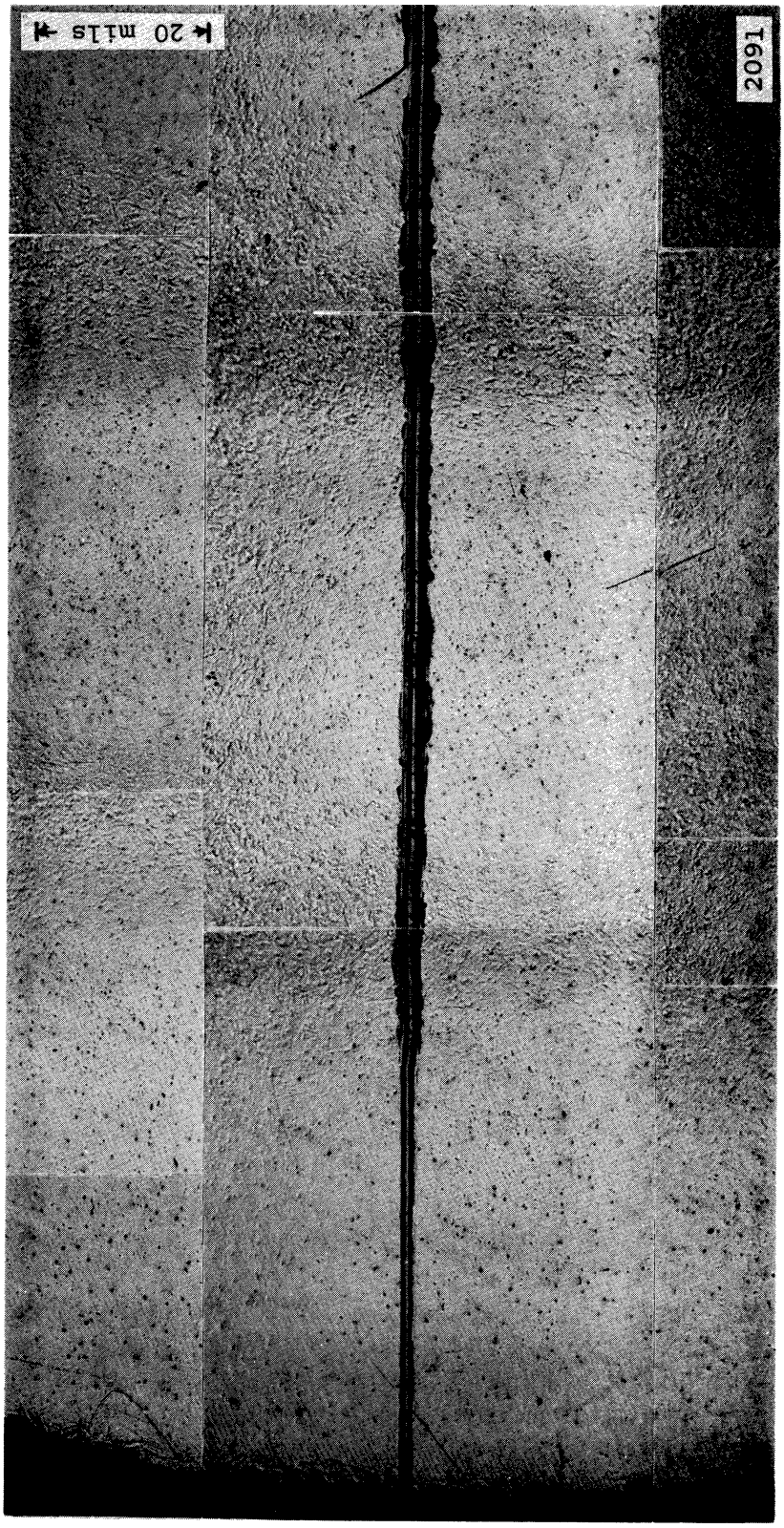

Fig. 100.--Section from a composite photomicrograph assembly (53X) of a type 304 stainless steel specimen exposed to cavitation in water for 54 seconds, frequency 20,325 cps, and amplitude approximately 2 mils.

Fig. 101 is a section from the composite photomicrograph assembly for type 1100-0 aluminum after exposure for 22 seconds. Referring to Fig. 63-A which is a photograph of the approximate maximum ring bubble pattern, to which this specimen was exposed, the section taken from the specimen surface photomicrograph corresponds to the area around the scribe at the lower right. Fig. 101 exhibits two distinct ring patterns near the outer edge, and the usual lightly damaged outer annulus is very narrow. The inner, heavier damage pattern on the photomicrograph corresponds to the heavy bubble pattern evident in Fig. 63-A.

It was difficult to maintain proper cavitation with the type 1100-0 aluminum specimen, as already explained, because the threads in this weak specimen were unable to maintain proper compressive load between the specimen and the horn. Visible cavitation for the first 7 seconds was in a leaf-like pattern accompanied by a weak ring pattern near the outer annulus (Fig. 70). The visible cavitation then shifted to a heavy ring pattern near the outer annulus, but slightly displaced from the previous ring pattern, with no visible pattern in the center. Damage is extremely heavy over the entire specimen, but even heavier where dense bubble concentrations were noticed in the bubble population photographs. The heavy damage to the usually damage-free annulus area is partly due to the very low resistance to cavitation of this soft material. The previously discussed possible lack of good coupling between the

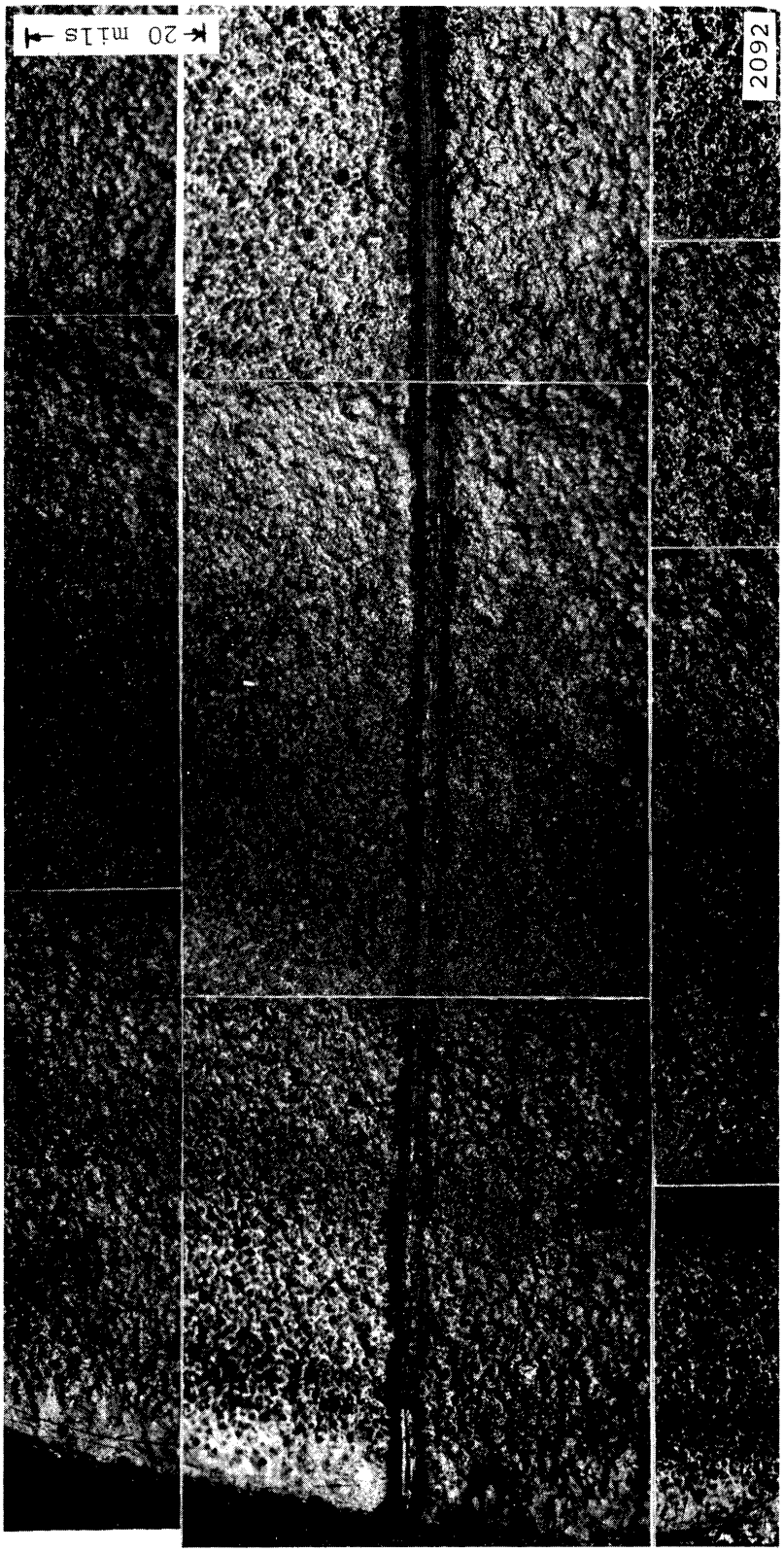

Fig. 101.--Section from a composite photomicrograph assembly (53X) of a type 1100-0 aluminum specimen exposed to cavitation in water for 22 seconds, frequency 20,244 cps, and amplitude approximately 2 mils.

specimen and the horn may have changed the typical flow patterns so that the unusual damage patterns resulted.

Fig. 102 is a section of the composite photomicrograph assembly for type 6061-T651 aluminum after exposure for 15 seconds. The large black pits and some of the pits on the outer annulus existed before exposure to cavitation. These initial pits allow orientation of the photomicrograph sections and the approximate maximum bubble population photograph, Fig. 65. The section in Fig. 102 corresponds with the upper left edge section of Fig. 65. Damage is heavy in this section, increasing toward the center.

Fig. 103 is a section from a composite photomicrograph assembly for a damaged 60% c. w. copper (as rec'd) specimen after 32 seconds of cavitation. Fig. 66 shows the corresponding approximate maximum bubble population. The bend in the scribe mark (Fig. 103) can be seen at the left in Fig. 66. The specimen was extensively damaged with general multiple pitting in the central area. The bubble pattern prongs (Fig. 66) do not correspond to any concentration of pit damage, suggesting that the bubble pattern continually changes. It has also been noticed visually and in photographic enlargements (Fig. 41-A) that these prongs of the bubble cloud sometimes lift away from the specimen surface near the outer annulus.

Fig. 67, a photograph of the approximate maximum bubble population recorded for the copper 900°F annealed specimen, showed, as did other photographs from the experimental sequence

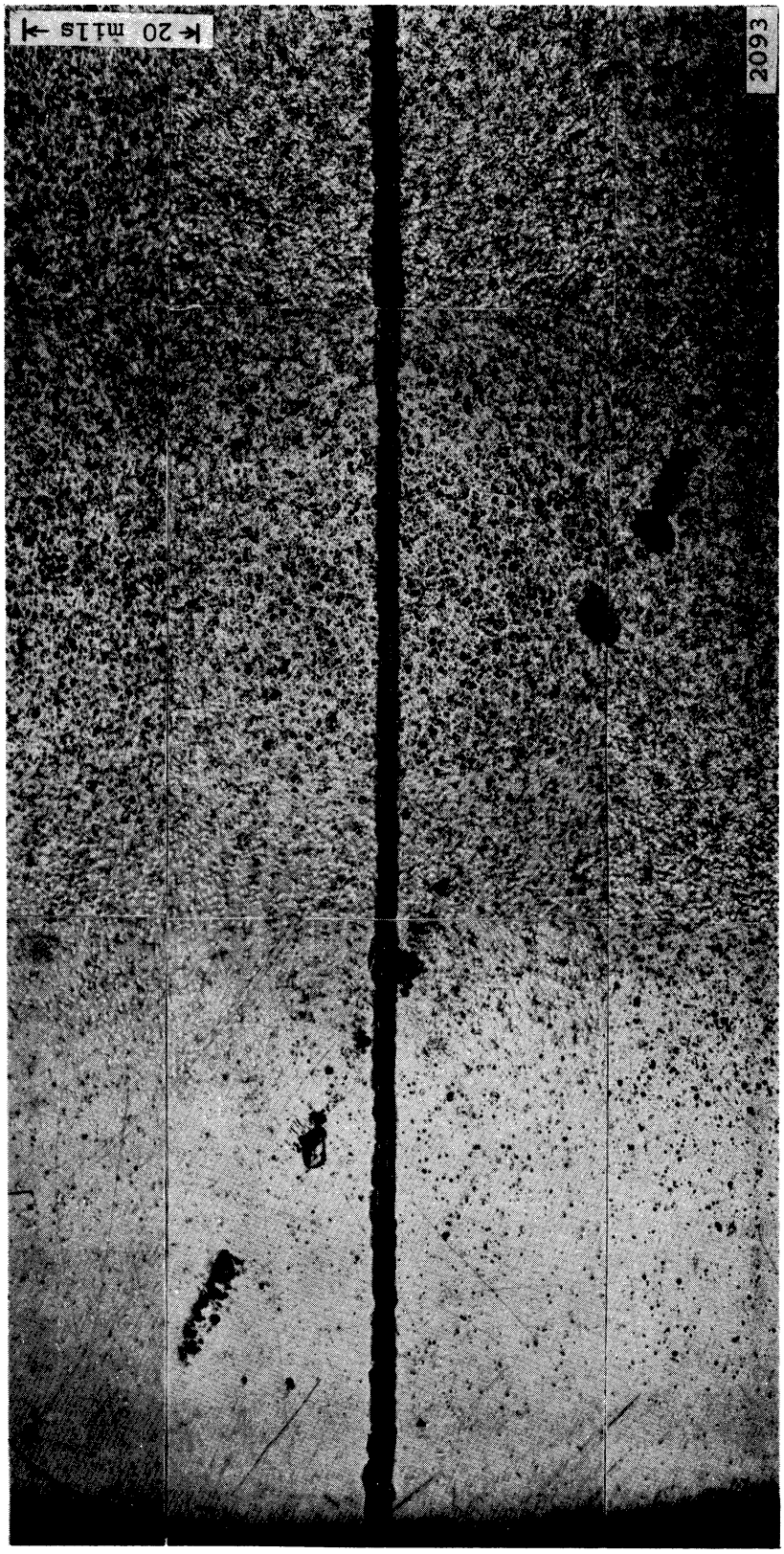

Fig. 102.--Section from a composite photomicrograph assembly (53X) of a type 6061-T651 aluminum specimen exposed to cavitation in water for 15 seconds, frequency 20,243 cps, and amplitude approximately 2 mils.

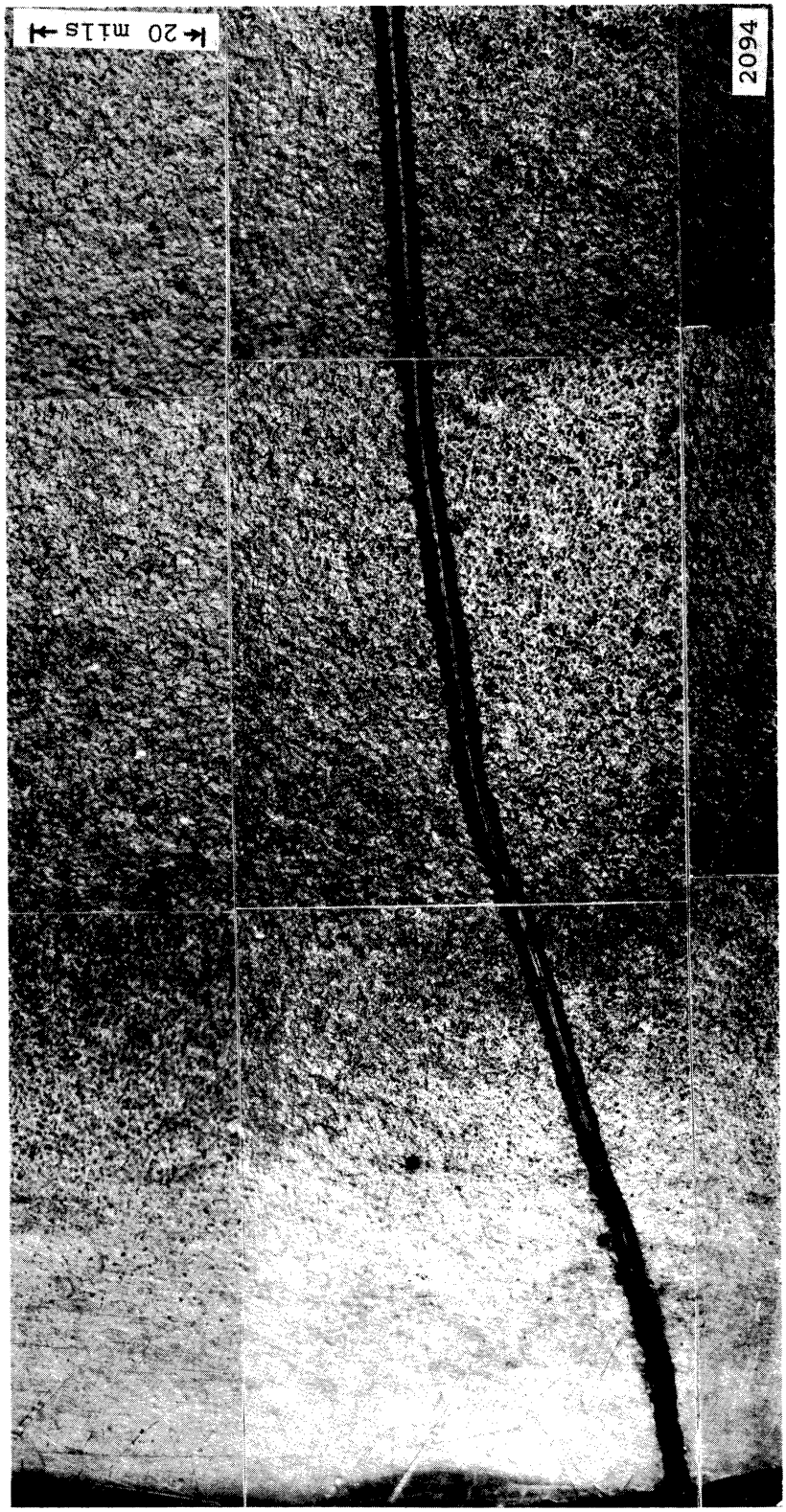

Fig. 103.--Section from a composite photomicrograph assembly (53X) of a 60% c.w. copper (as rec'd) specimen exposed to cavitation in water for 32 seconds, frequency 20,542 cps, and amplitude approximately 2 mils.

of this specimen, a bias of bubble population location occurring to the left of the center scribe mark and at the lower part of the specimen. Figs. 104-A and B are taken from the composite photomicrograph assemblies of this specimen after exposure to cavitation for 33 seconds, and show sections at the left and right ends of the scribe mark, respectively. Again, damage is heavy everywhere, but much heavier at points of bubble concentrations. This observation, and the similar ones in this section, appear to indicate the existence of preferred bubble locations, peculiar to the specimen, water level, etc. However, the bubble pattern can still shift occasionally, or there are damaging bubbles existing in the high speed photographs that are too small to be detected by the techniques used.

Fig. 105 is a section from the composite photomicrograph assembly, for the 75% c. w. nickel (as rec'd) specimen after exposure for 44 seconds. There is no noticeable damage pattern. The bubble pattern at the approximate maximum (Fig. 68) was generally full and uniform, covering the specimen surface.

Fig. 106 is a section from the composite photomicrograph assembly for Plexiglas after it was re-run for 5 minutes to a total exposure of 5 minutes and 27 seconds. The original 27 second run produced only 113 pits, some of which were believed due to handling damage. The pattern shown in Fig. 106 corresponds to the visible bubble cloud and shows heavy surface deterioration along the center of the picture. No high speed photographs were made for this second Plexiglas run.

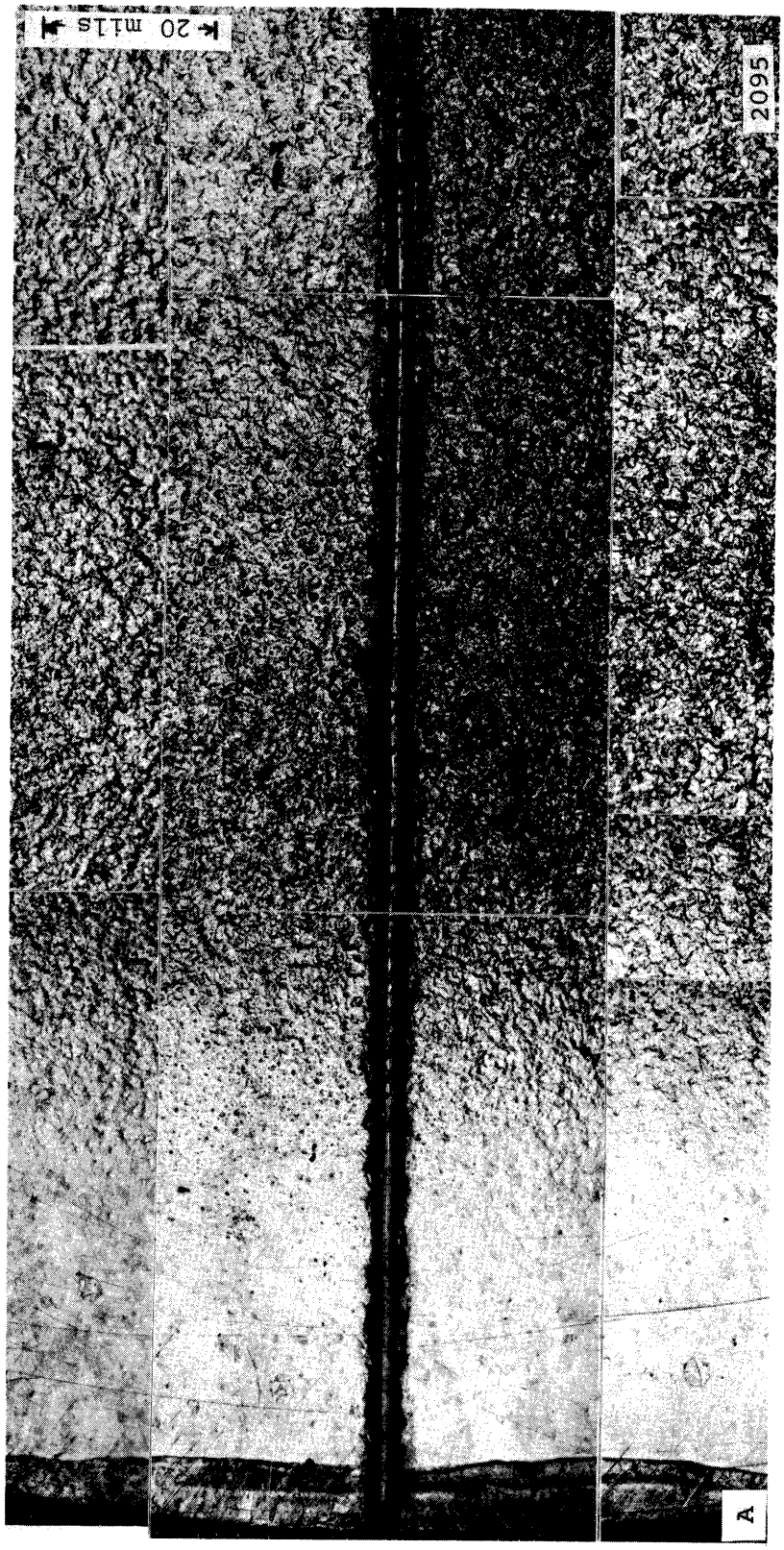

Fig. 104.--A and B. Sections from a composite photomicrograph assembly (53X) of a copper 900°F annealed specimen exposed to cavitation in water for 33 seconds, frequency 20,419 cps, and amplitude approximately 2 mils.

Fig. 104.--Continued

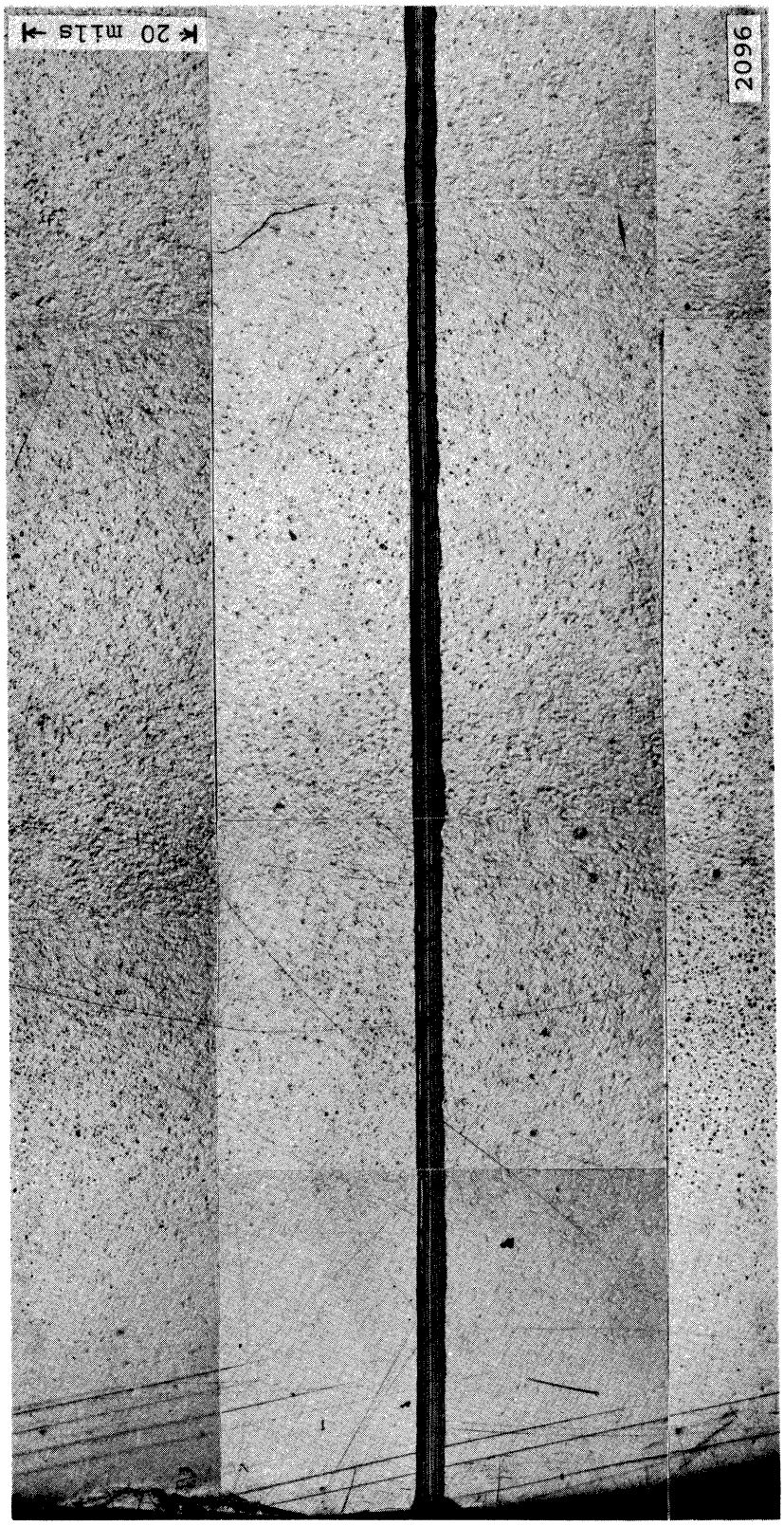

Fig. 105.--Section from a composite photomicrograph assembly (53X) of a 75% c. w. nickel (as rec'd) specimen exposed to cavitation in water for 44 seconds, frequency 20,454 cps, and amplitude approximately 2 mils.

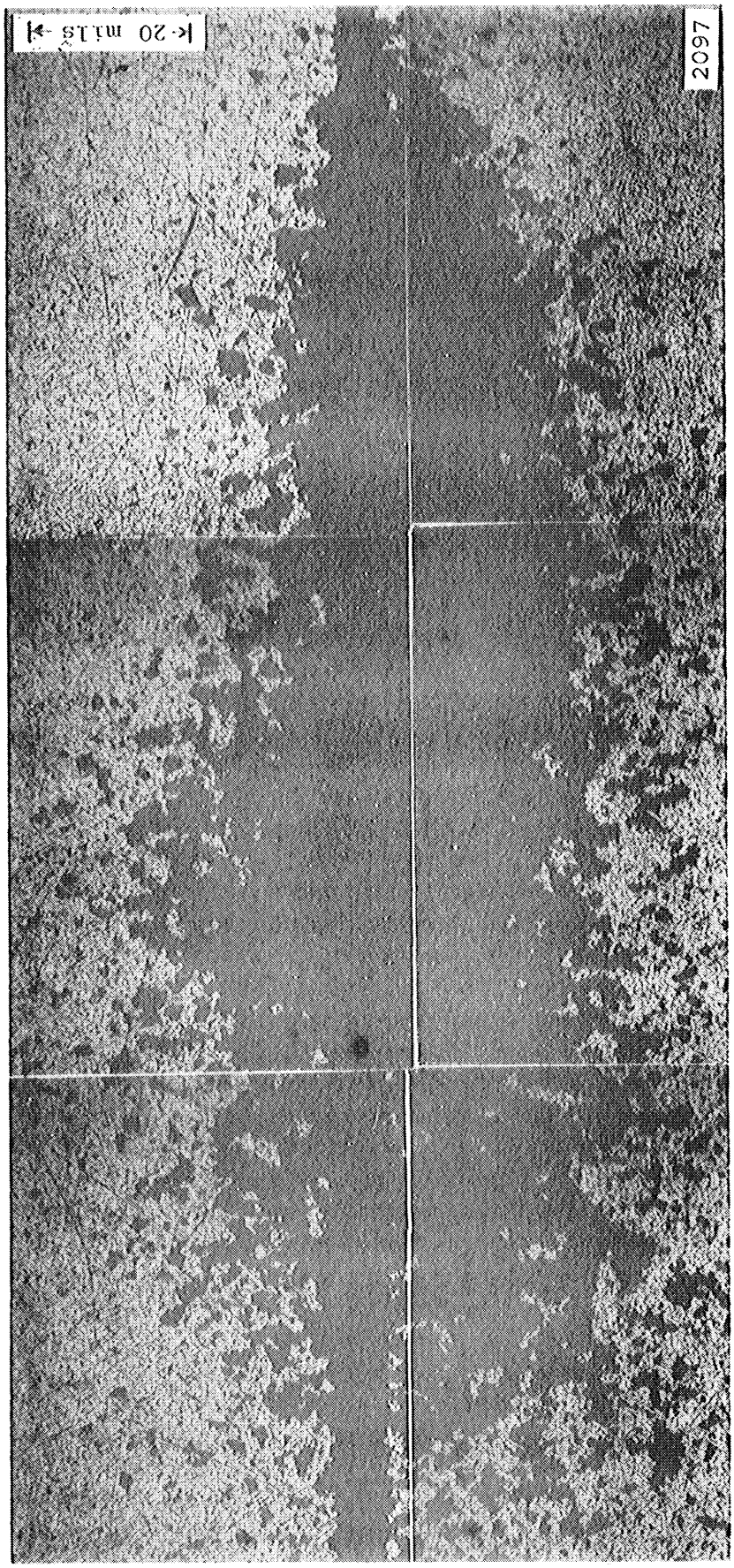

Fig. 106.--Section from a composite photomicrograph assembly (53X) of a Plexiglas specimen exposed to cavitation in water for 27 seconds, frequency 20,564 cps, and amplitude approximately 2 mils.

6. Proficorder Data

Figs. 107 through 113 show Proficorder* traces (indicated by arrows on both ends of the photomicrograph assembly) and corresponding photomicrographs. Fig. 114 of Plexiglas shows only typical traces and photomicrographs of the surface, since a correlation between trace and photomicrograph was not possible. The 27 second cavitation exposure of Plexiglas did not provide sufficient pit damage for a trace, so the trace and photomicrographs shown were made after 5 minute 27 second exposure, but not in the heavily damaged area shown in Fig. 106.

Fig. 107, for the type 304 stainless steel specimen, shows pitting very similar to that of Robinson's[10] venturi experiments (the large pits existed before exposure). The individual pits are similar as to depth and diameter to some of those shown by Robinson, but the rim is much less.

Fig. 108, for the type 1100-0 aluminum specimen, shows the effect of multiple pitting. The traces of the deep pits show steps and other irregularities suggesting that they have experienced multiple pitting.

Fig. 109, for the type 2024-T351 aluminum specimen, shows extremely heavy pitting with a wide range of pit diameters. The deepness of some of the pits suggests multiple pitting.

---

*A precision Profilometer manufactured by Micrometrical Division, The Bendix Corporation, Ann Arbor, Michigan.

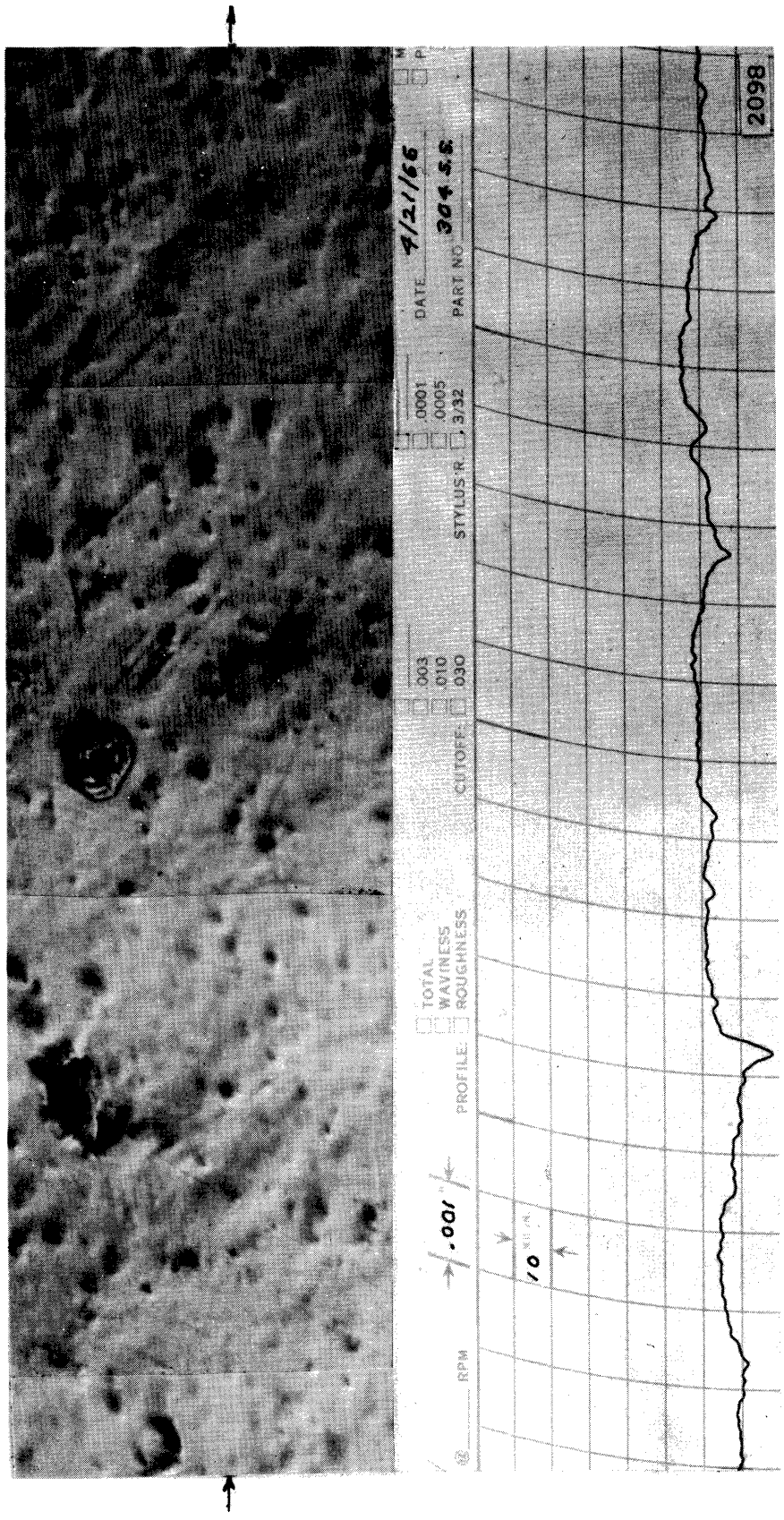

Fig. 107.--Photomicrographs (500X) and matching Proficorder trace of a typical surface of a type 304 stainless steel specimen exposed to cavitation in water for 54 seconds, frequency 20,325 cps, and amplitude approximately 2 mils.

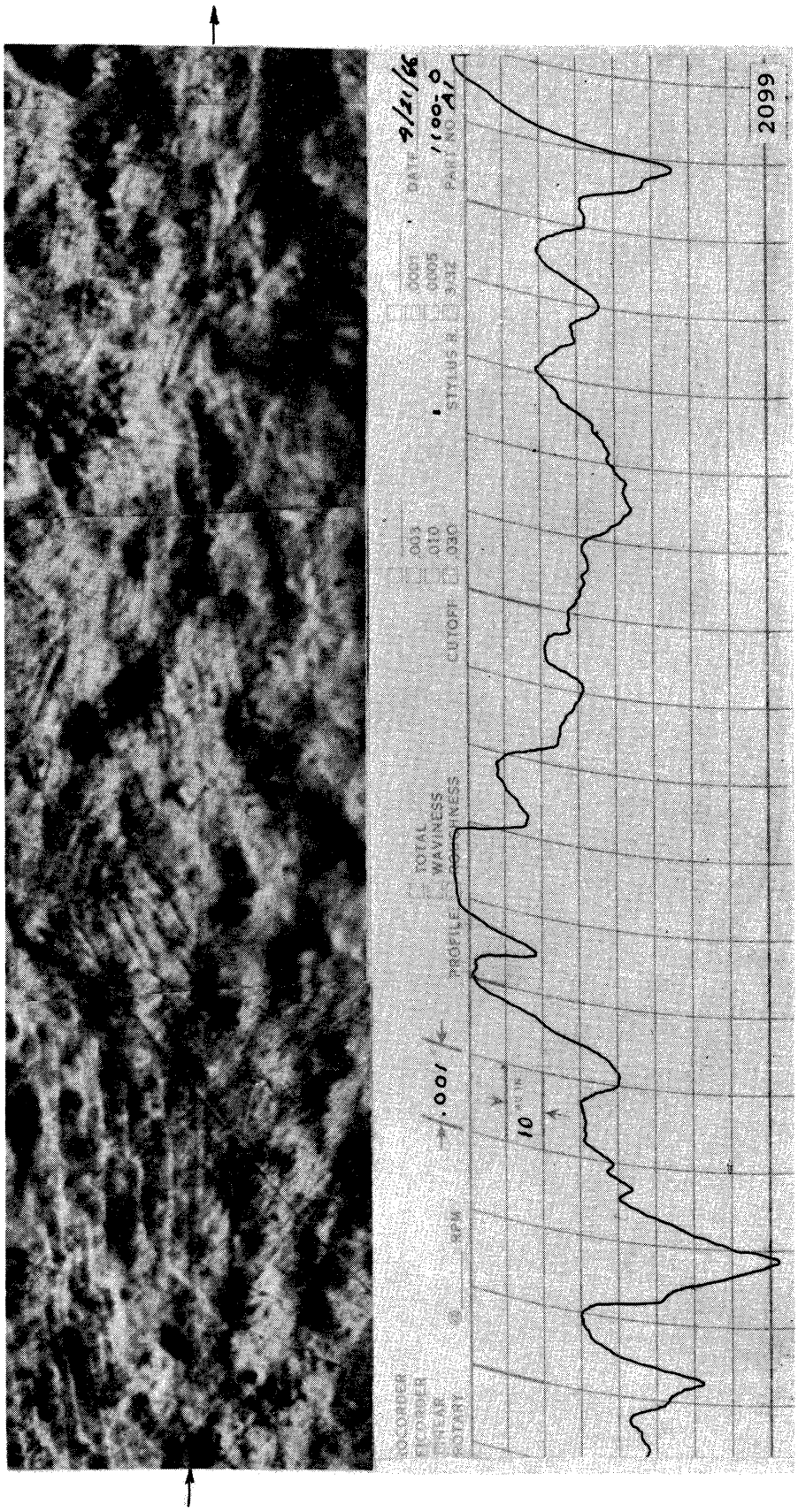

Fig. 108.--Photomicrographs (500X) and matching Proficorder trace of a typical surface of a type 1100-0 aluminum specimen exposed to cavitation in water for 22 seconds, frequency 20,244 cps, and amplitude approximately 2 mils.

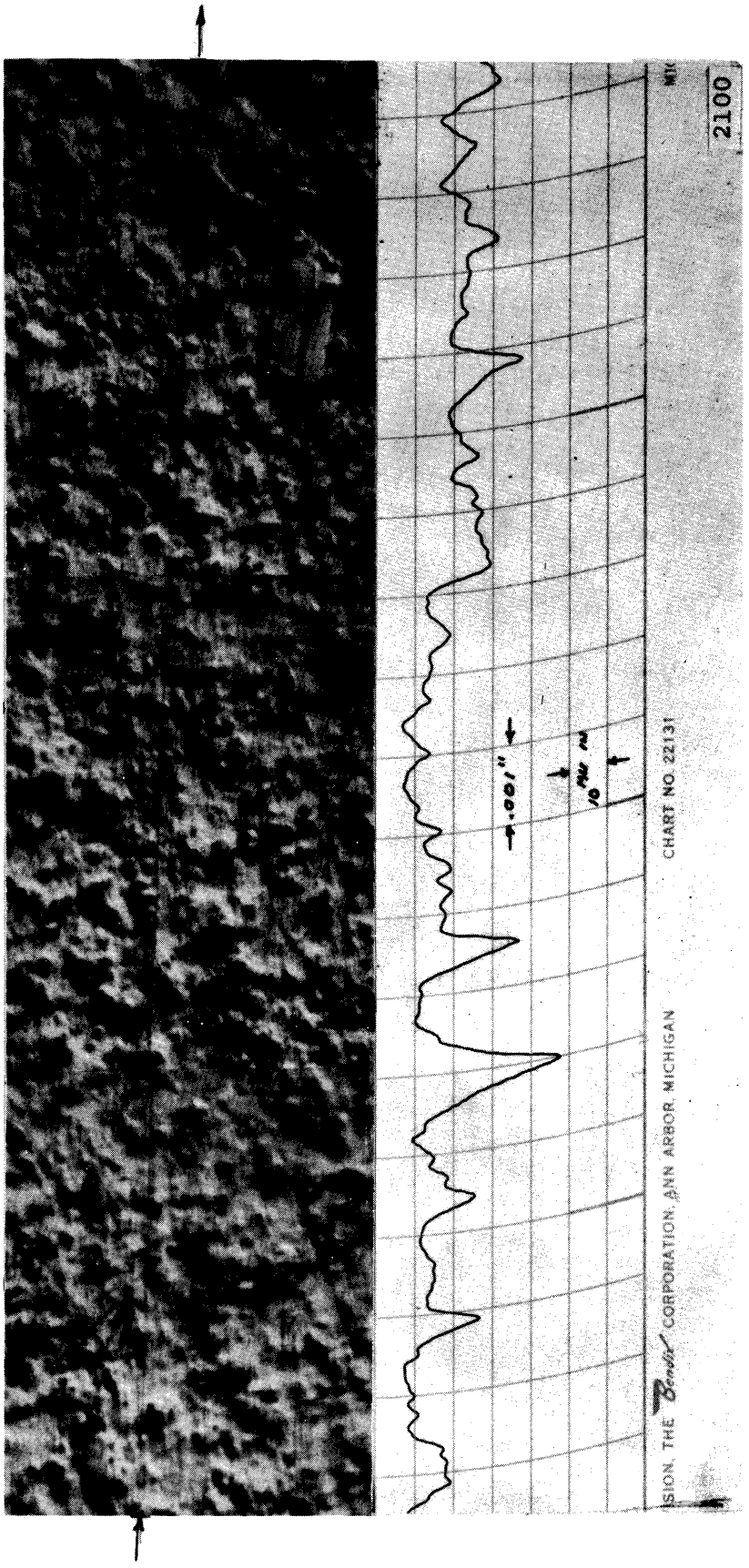

Fig. 109.--Photomicrographs (500X) and matching Proficorder trace of a typical surface of a type 2024-T351 aluminum specimen exposed to cavitation in water for 60 seconds, frequency 20,200 cps, and amplitude approximately 2 mils.

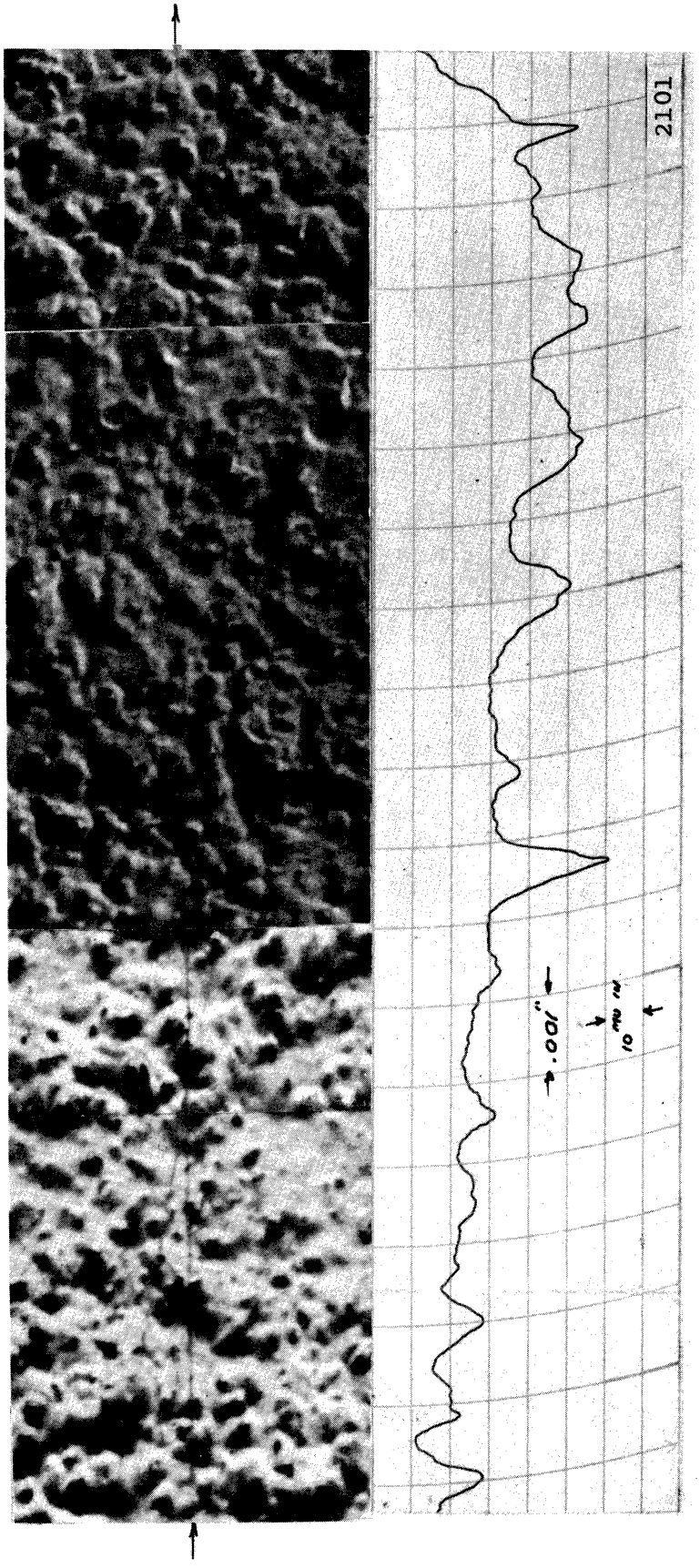

Fig. 110.--Photomicrographs (500X) and matching Proficorder trace of a typical surface of a type 6061-T651 aluminum specimen exposed to cavitation in water for 15 seconds, frequency 20,243 cps, and amplitude approximately 2 mils.

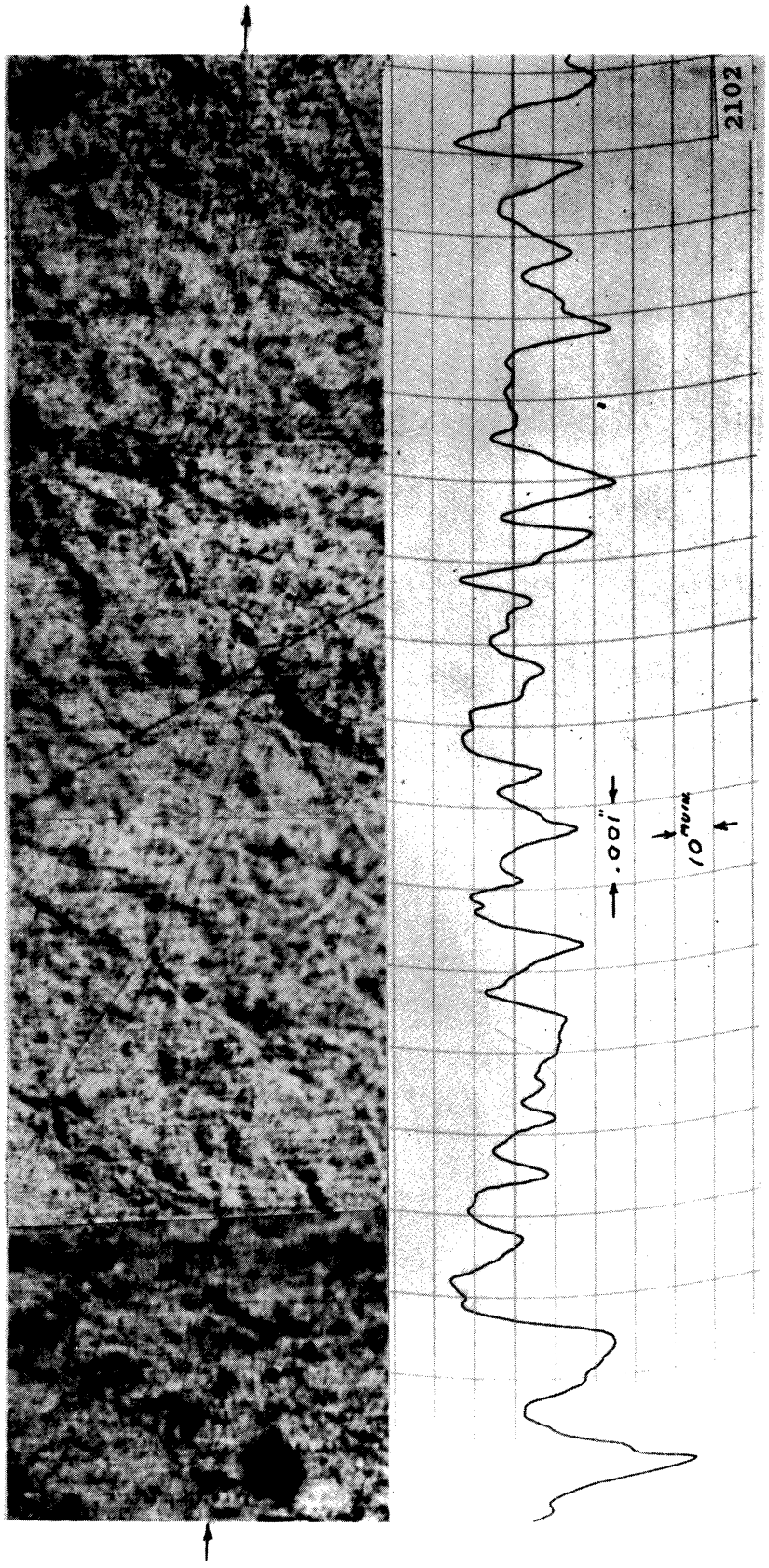

Fig. 111.--Photomicrographs (500X) and matching Proficorder trace of a typical surface of a 60% c.w. copper (as rec'd) specimen exposed to cavitation in water for 32 seconds, frequency 20,542 cps, and amplitude approximately 2 mils.

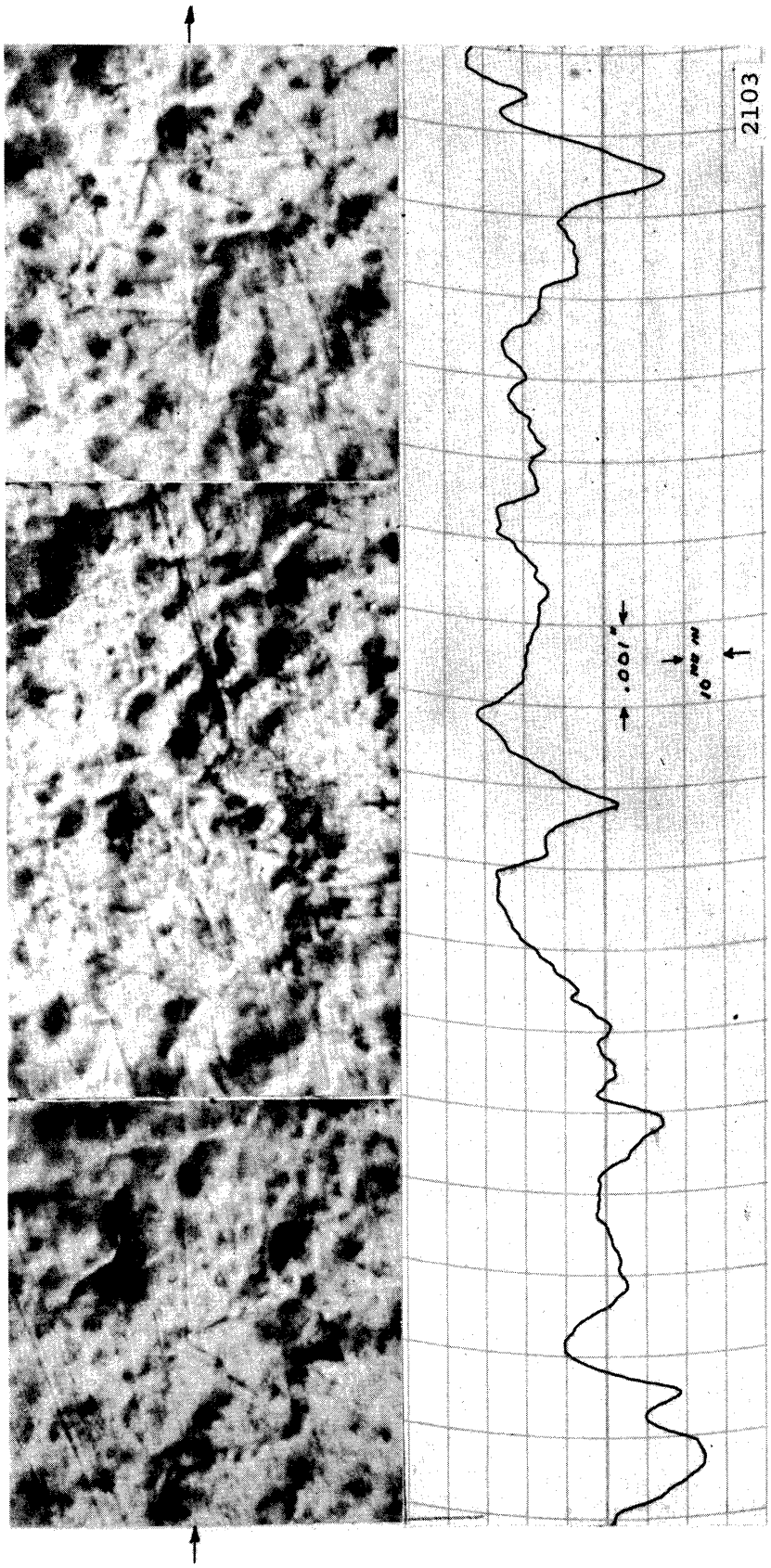

Fig. 112.--Photomicrographs (500X) and matching Proficorder trace of a typical surface of a copper 900°F annealed specimen exposed to cavitation in water for 33 seconds, frequency 20,419 cps, and amplitude approximately 2 mils.

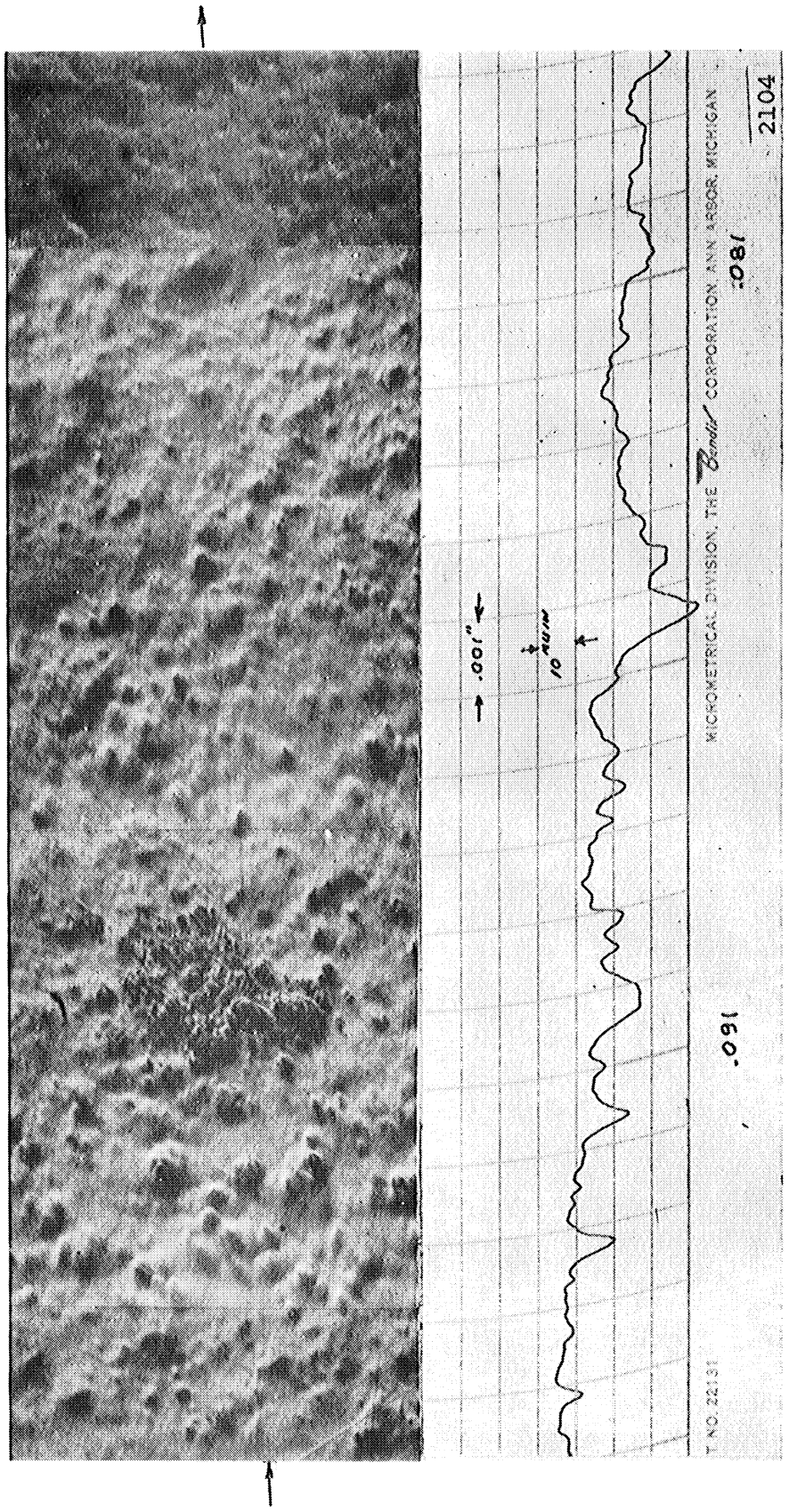

Fig. 113.--Photomicrographs (500X) and matching Proficorder trace of a typical surface of a 75% c.w. nickel (as rec'd) specimen exposed to cavitation in water for 44 seconds, frequency 20,454 cps, and amplitude approximately 2 mils.

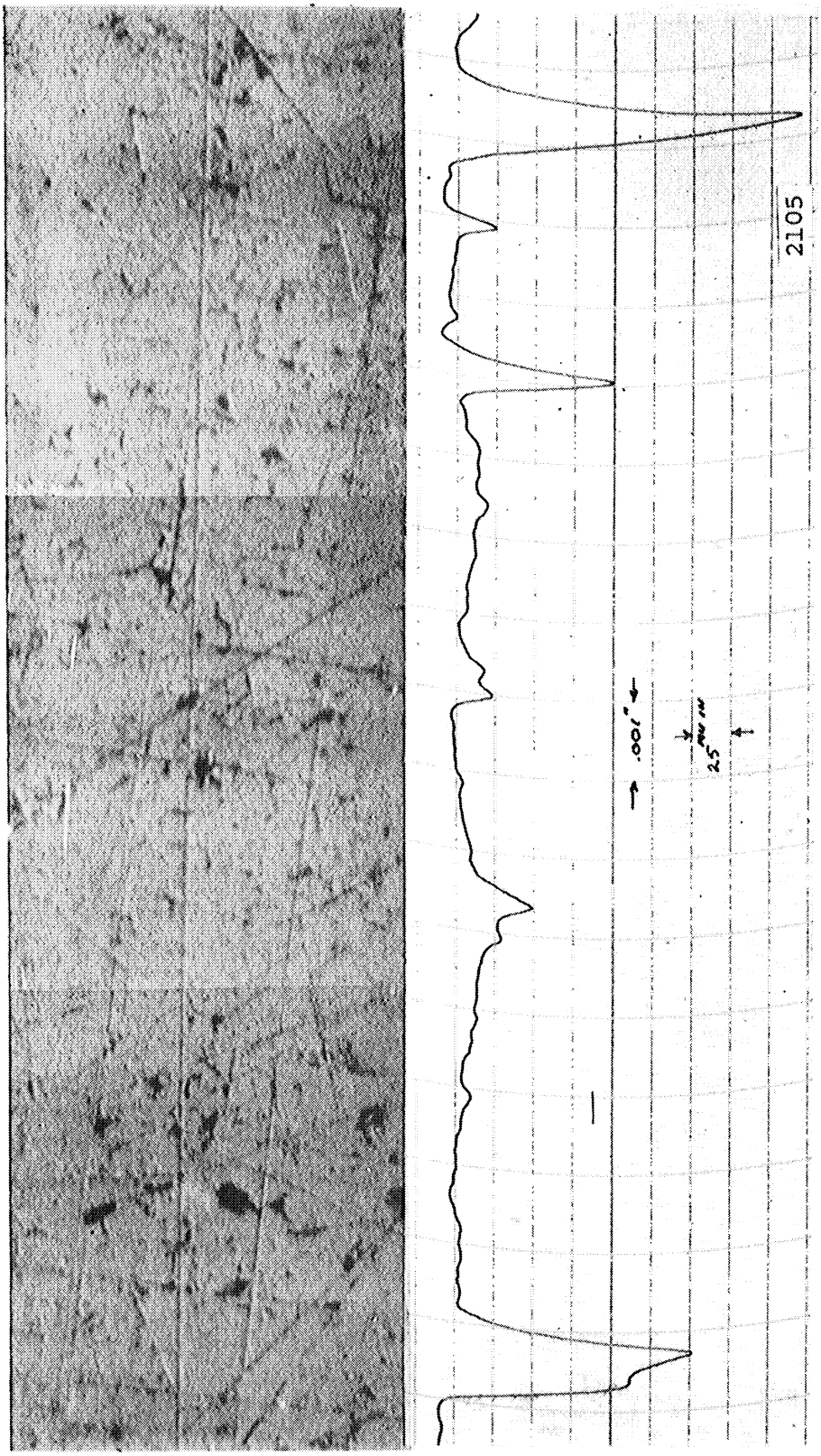

Fig. 114.--Photomicrographs (500X) and selected Proficorder trace of a typical surface of a Plexiglas specimen exposed to cavitation in water for 27 seconds, frequency 20,564 cps, and amplitude approximately 2 mils.

Fig. 110, for the type 6061-T651 aluminum specimen, again shows heavy damage. Note that the deep pit in the center of the Proficorder trace shows evidence of additional pitting because of both the depth of the pit and the irregularity of the trace of the sides indicating "steps." The area to the right of the trace section that was used showed extensive multiple pitting.

Fig. 111, for the 60% c. w. copper (as rec'd) specimen, shows on the photomicrographs a large number of small pits. The deep, compound pits are probably the result of multiple pitting. The dark spots at each extreme of the photomicrograph are pits that were not caused by cavitation.

Fig. 112, for the copper 900°F annealed specimen, shows a heavily damaged surface. A large number of small pits are also evident.

Fig. 113, for the 75% c. w. nickel (as rec'd) specimen, shows extensive, but not too deep pitting. The froth-like mass at the left center of the photomicrograph could have been caused by corrosion, although this is unlikely in the very short exposures used.

Fig. 114, for the Plexiglas specimen, shows a badly damaged surface. A less sensitive height ratio was used on the Proficorder because of the depth of the pits. Note the rims on the pits, suggesting their formation by very local micro-jet impact rather than by a shock wave emanating from a collapse center at some distance (at least a bubble radius). Since such a shock would cover a substantial portion of the surface,

rim formation would tend to be suppressed. Close examination of all the foregoing Proficorder traces shows similar rim formation as was also evident in the venturi tests.[10]

7. Plexiglas Pits

Photomicrographs of certain Plexiglas pits are presented because of their uniqueness or because they were not of the type shown on the photomicrographs of the preceeding section. Fig. 115 (500X) shows a pit near the center marking scribe, that is nearly round, which occurred after 27 seconds of exposure. Fig. 116 (1000X) after 5 minutes and 27 seconds of exposure, shows a pit with some straight line boundaries suggesting that the damage follows some sort of crystalline structure. This could be true even though Plexiglas is a polymer, since orientation of the molecules into strands or fibers could form structures similar to grains, but much larger. Failure could thus occur in preferred shapes and directions.

Fig. 117 (1800X), similarly exposed for 5 minutes and 27 seconds, shows a large pit surrounded by large numbers of smaller ones. Again note the generally hexagonal shape of the pit, with contour formed from approximately straightline sections. The foregoing explanation is applicable. Fig. 118 (1000X) shows the heavy damage that was incurred after 5 minutes and 27 seconds of exposure. The general shattering of the surface, peculiar to Plexiglas for this investigation, is probably due to single-blow impact. Figs. 119 and 120

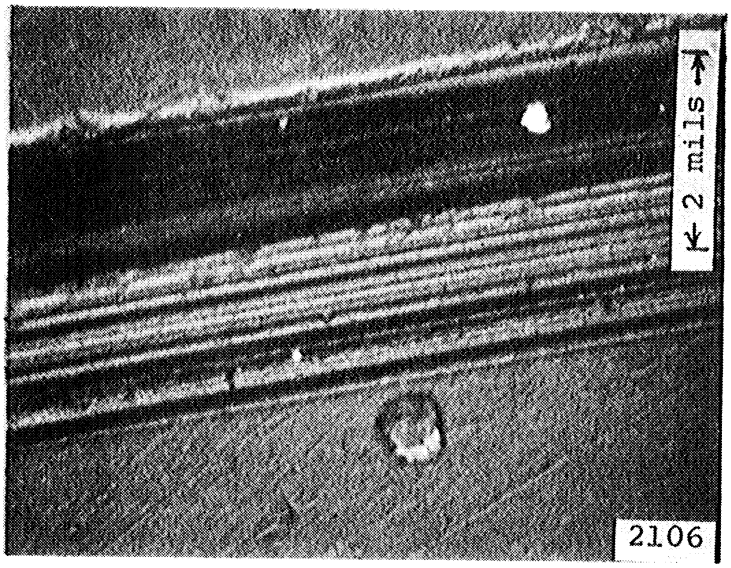

Fig. 115.--Photomicrograph (500X) of a Plexiglas specimen showing a portion of center marking scribe after exposure to cavitation in water for 27 seconds, frequency 20,564 cps, and amplitude approximately 2 mils.

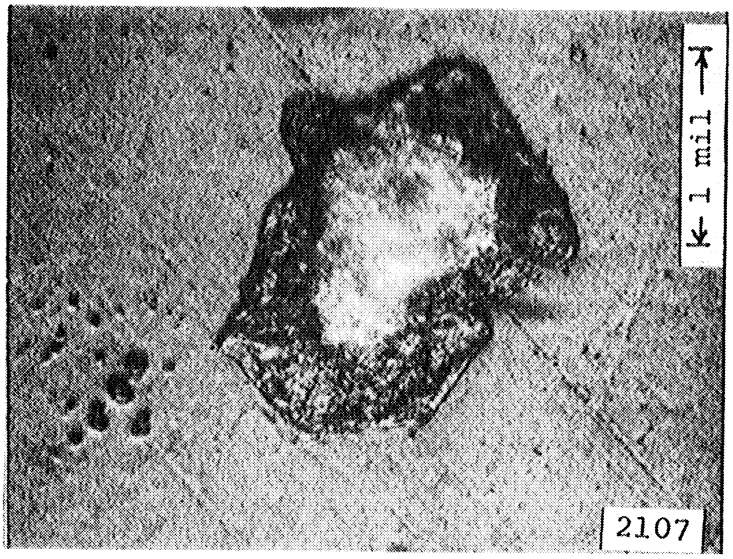

Fig. 116.--Photomicrograph (1000X) of a Plexiglas specimen showing damage after exposure to cavitation in water for 5 minutes, 27 seconds, frequency 20,564 cps, and amplitude approximately 2 mils.

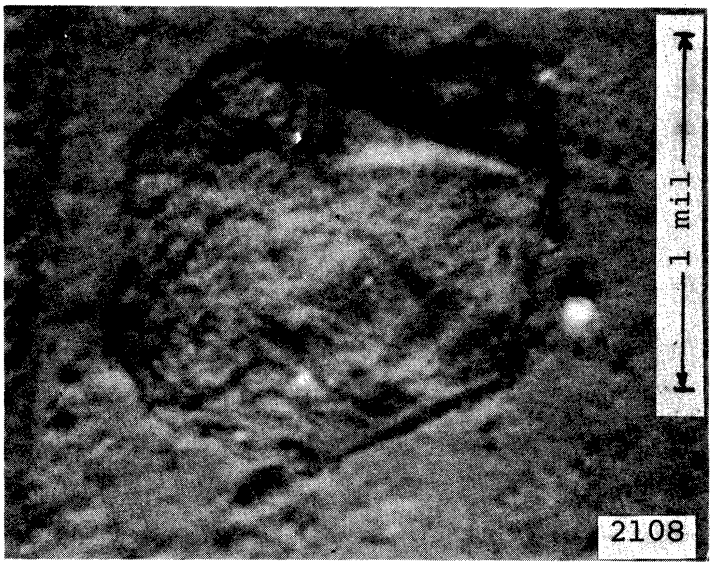

Fig. 117.--Photomicrograph (1800X) of a Plexiglas specimen showing damage after exposure to cavitation in water for 5 minutes, 27 seconds, frequency 20,564 cps, and amplitude approximately 2 mils.

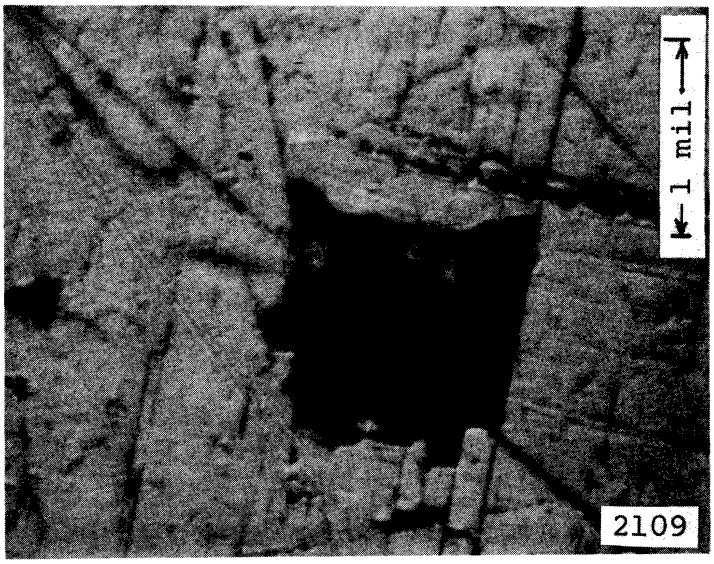

Fig. 118.--Photomicrograph (1000X) of a Plexiglas specimen showing damage after exposure to cavitation in water for 5 minutes, 27 seconds, frequency 20,564 cps, and amplitude approximately 2 mils.

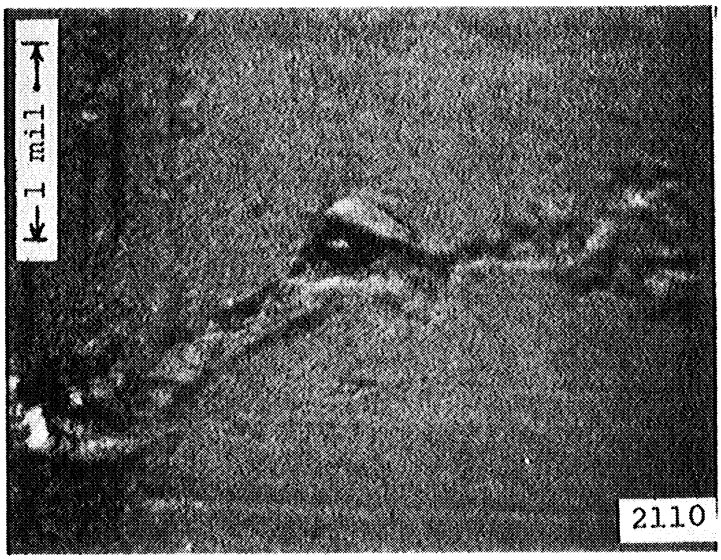

Fig. 119.--Photomicrograph (1000X) of a Plexiglas specimen showing a portion of center marking scribe after exposure to cavitation in water for 27 seconds, frequency 20,564 cps and amplitude approximately 2 mils.

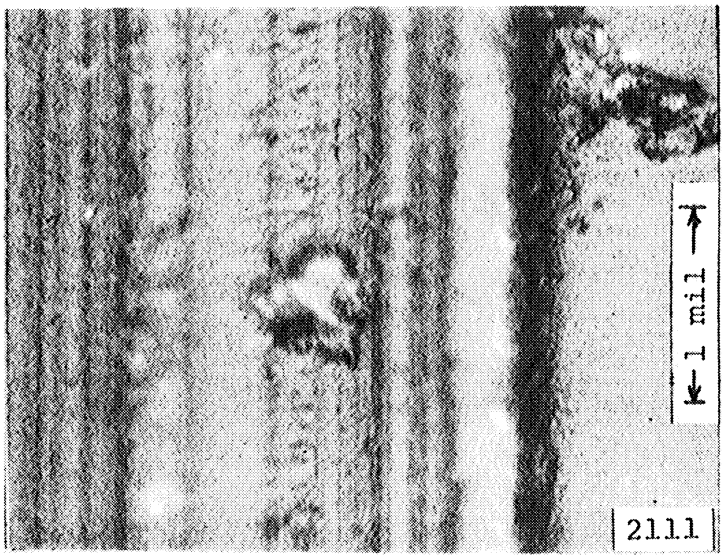

Fig. 120.--Photomicrograph (1000X) of a Plexiglas specimen showing a portion of center marking scribe after exposure to cavitation in water for 27 seconds, frequency 20,564 cps, and amplitude approximately 2 mils.

(1000X) show pits near the center-marking scribe that occurred after 27 seconds of exposure.

8. Damage Near Center Marking Scribe

As already mentioned, pitting damage is heaviest where the bubble population is most dense. It is interesting to note how the center-marking scribe affects the bubble fields and the resulting damage. Damage occurred in the scribe valley itself as was shown in the previous section for Plexiglas.

Figs. 121, 122, 123, and 124 (500X) show damage in the scribe valley for the following specimens: copper 900°F annealed; 60% c. w. copper (as rec'd); 75% c. w. nickel (as rec'd); and type 304 stainless steel. The pitting was in all cases similar and the shape of the pits (long and narrow) may be due in part to the pre-exposure damage in the valley caused by making the scribe mark. However, the pits are often not parallel to the scribe marks.

Fig. 125 shows the bubble field on the copper 900°F annealed specimen with the frequency set at 20,419 cps and the amplitude at approximately 2 mils. Fig. 126 is for a 60% c. w. copper specimen (as rec'd) for a frequency of 20,542 cps and an approximate 2 mil amplitude. The bubble field was more dense below and left of the scribe mark in Fig. 125 and below the scribe mark in Fig. 126. The respective sections from the composite photomicrograph assemblies (53X) about the marking scribe, which were taken from the center portion of the specimen where the contrast in bubble population density was the most

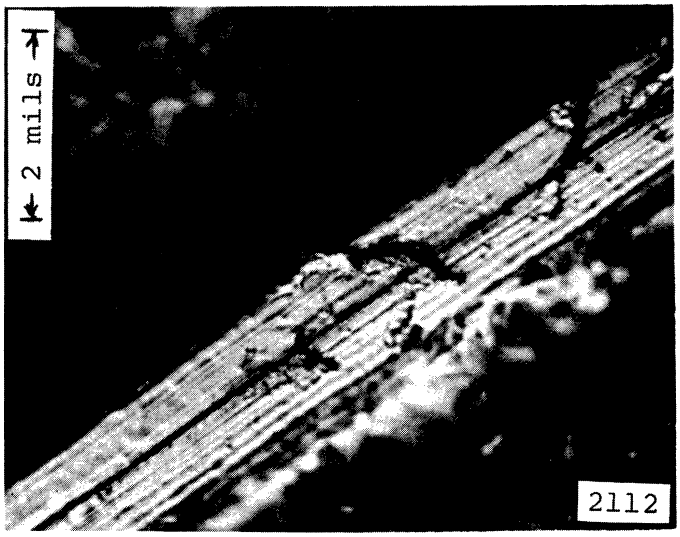

Fig. 121.--Photomicrograph (500X) of a copper 900°F annealed specimen showing a portion of center marking scribe after exposure to cavitation in water for 33 seconds, frequency 20,419 cps, and amplitude approximately 2 mils.

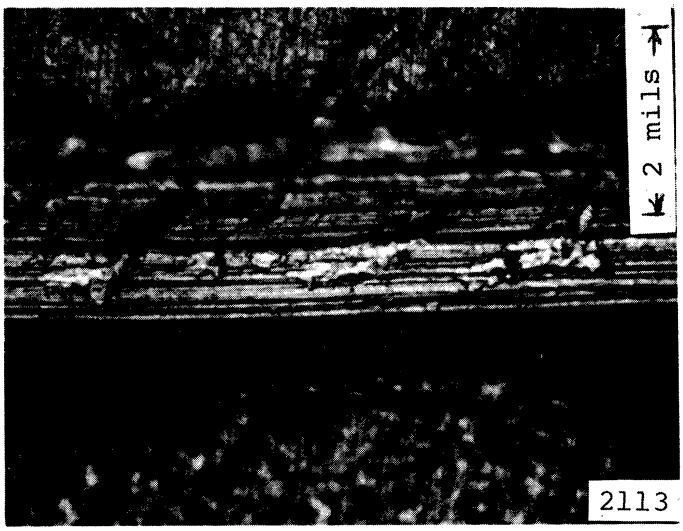

Fig. 122.--Photomicrograph (500X) of a 60% c.w. copper (as rec'd) specimen showing a portion of center marking scribe after exposure to cavitation in water for 32 seconds, frequency 20,542 cps, and amplitude approximately 2 mils.

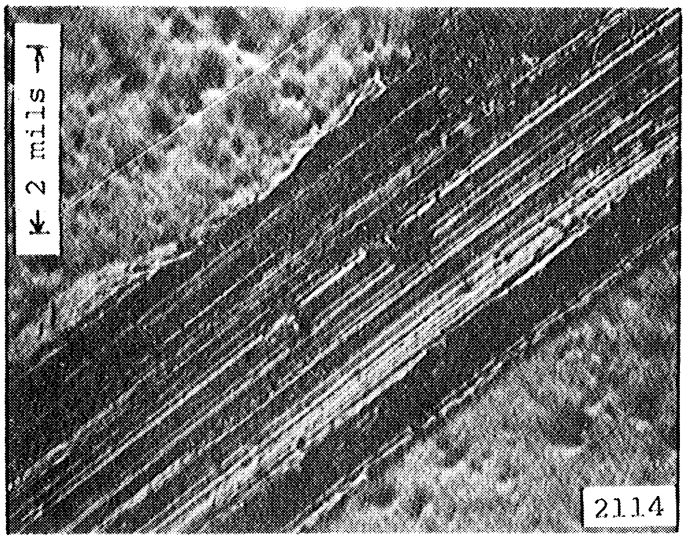

Fig. 123.--Photomicrograph (500X) of a 75% c. w. nickel (as rec'd) specimen showing a portion of center marking scribe after exposure to cavitation in water for 44 seconds, frequency 20,454 cps, and amplitude approximately 2 mils.

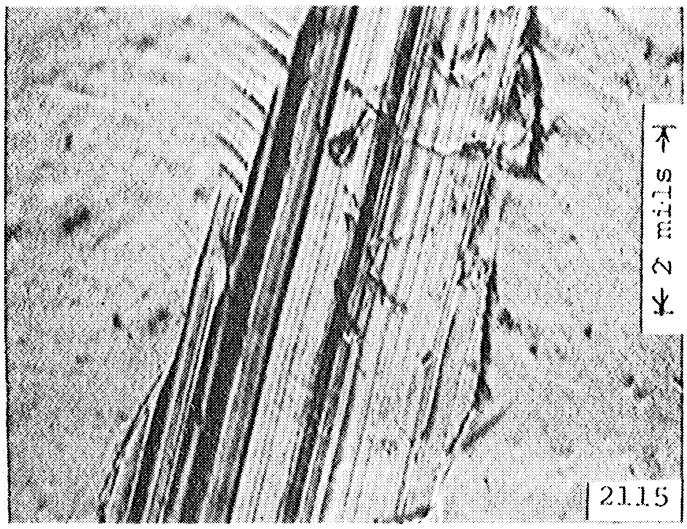

Fig. 124.--Photomicrograph (500X) of a type 304 stainless steel specimen showing a portion of center marking scribe after exposure to cavitation in water for 54 seconds, frequency 20,325 cps, and amplitude approximately 2 mils.

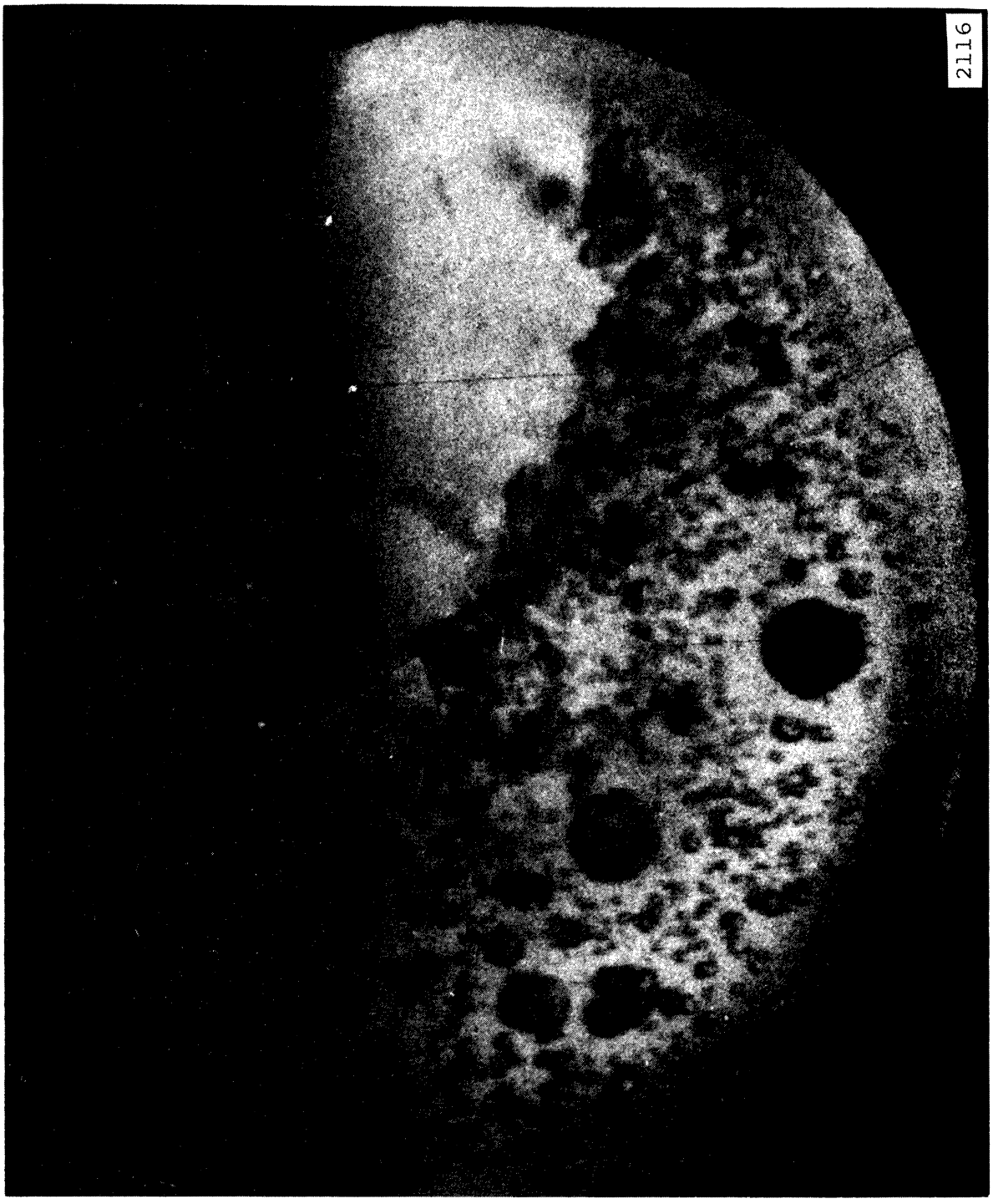

Fig. 125.--High speed photograph (14X) of a copper 900°F annealed specimen in water, frequency 20,419 cps, amplitude approximately 2 mils, exposure time per frame of 1.3 μ seconds, photographed at 20,430 fps.

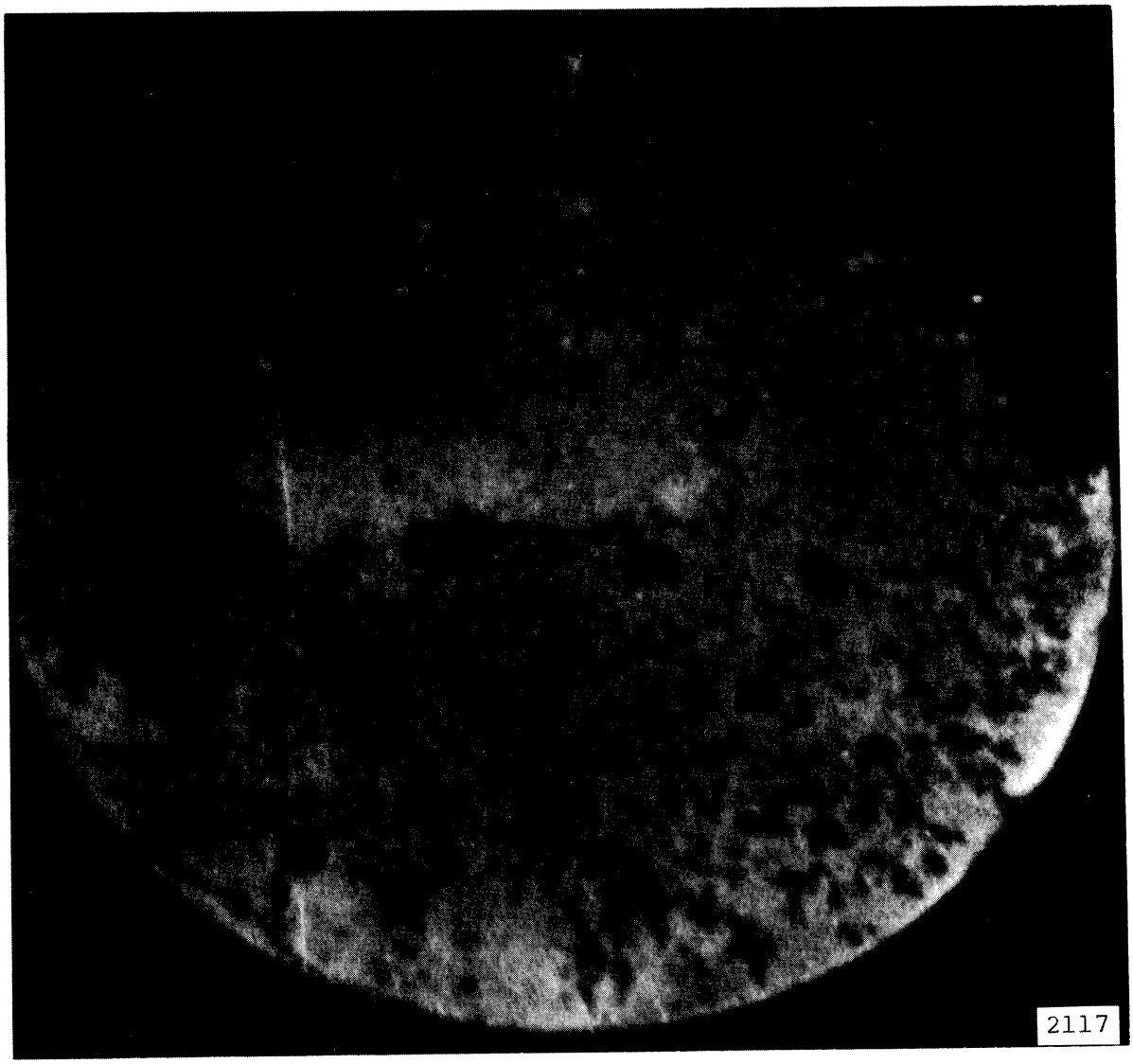

Fig. 126.--High speed photograph (14X) of a 60% c. w. copper (as rec'd) specimen in water, frequency 20,542 cps, amplitude approximately 2 mils, exposure time per frame of 1.3 μ seconds, photographed at 20,530 fps.

striking, are shown in Figs. 127-A and B. The sections correspond respectively to Figs. 125 and 126. Pitting damage is heavy both above and below the scribe marks, but is heaviest below it. The pitting is extremely heavy in the central area below the scribe in Fig. 127-A. This damage corresponds to the location of a heavy bubble field that persisted throughout the sequence and is typified by Fig. 125.

L. Rating of Specimens

The specimens have been compared according to weight loss, depth of damage, diameter and number of pits and the number of bubbles occurring during each experimental run.

MDPR, i.e., Mean Depth of Penetration Rate (mils or cm per unit time), has been used by this laboratory in the past for rating materials, and will be adopted here. MDPR is the weight loss per second divided by the product of face area of the specimen and density. In reality then, MDPR is a specific volume loss rate, or a depth of penetration rate, if the volume loss is considered as smeared uniformly over the cavitated area.

Table 4-a tabulates the present data for the very short runs in cm/sec and mils/hr, and this is then compared to Garcia's[7] data for longer runs which is in mils/hr. Note that with the exception of the Plexiglas and aluminum alloys the damage rates are of the same order of magnitude for the present very short tests and the much longer tests of Garcia.[7] It

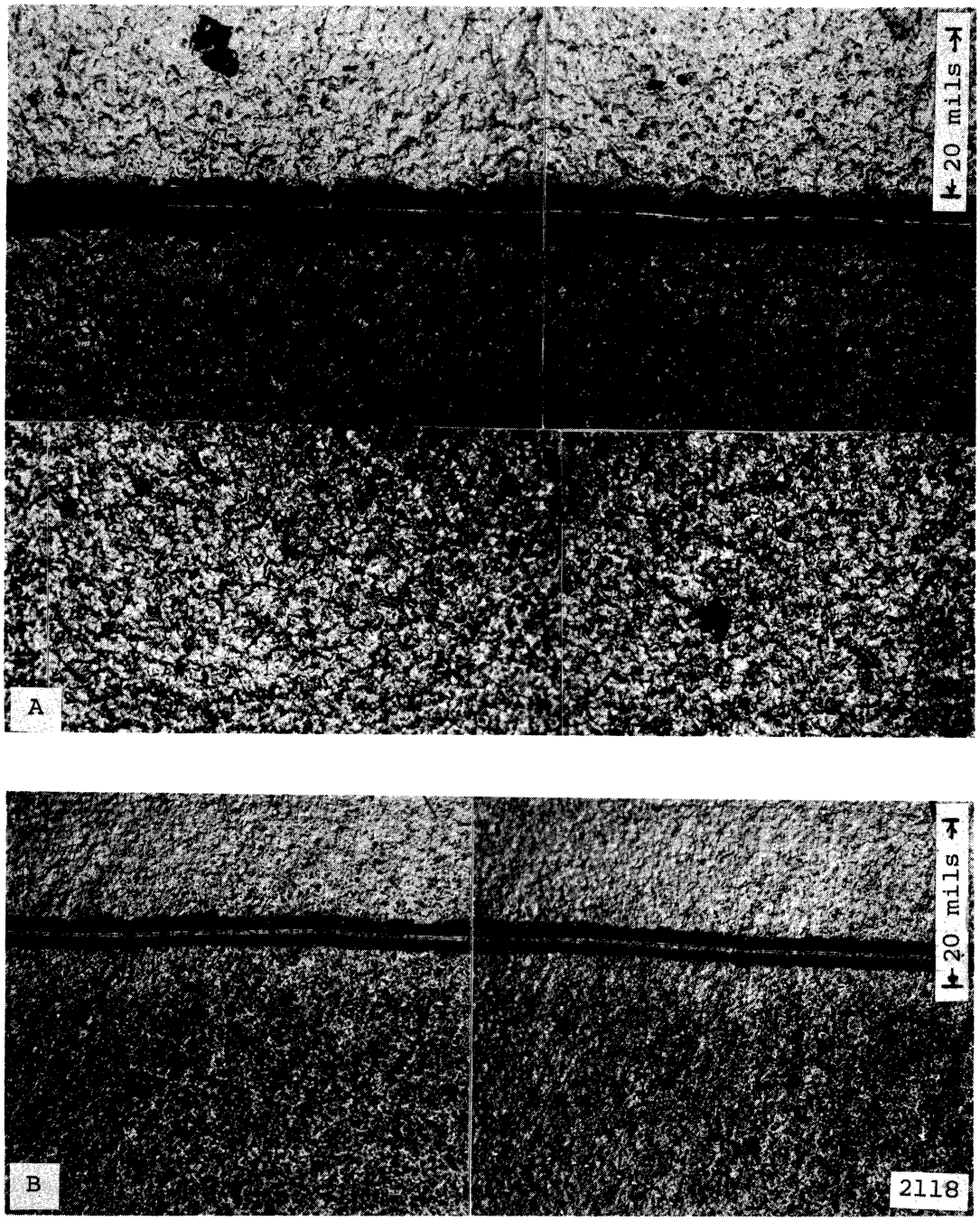

Fig. 127.--A and B. Sections from a composite photomicrograph assembly (53X); A of a copper 900°F ammealed specimen exposed to cavitation in water for 33 seconds, frequency 20,419 cps, and amplitude approximately 2 mils; and B of a 60% c. w. copper (as rec'd) specimen exposed to cavitation in water for 32 seconds, frequency 20,542 cps, and amplitude approximately 2 mils.

TABLE 4

RATING OF SPECIMENS

(a) MDPR	cm/sec x10^6	mils/hr	Garcia[7] Data mils/hr
304 Stainless Steel	.11	.15	.10
75% C. W. Nickel (As Rec'd)	.50	.71	.44
2024-T351 Aluminum	.67	.95	.57
Copper 900°F Annealed	.70	.99	1.02
60% C. W. Copper (As Rec'd)	1.20	1.70	.95
Plexiglas	9.0	12.8	1.39
6061-T651 Aluminum	11.0	15.6	.72
1100-0 Aluminum	18.5	26.3	2.70

(b) Normalized* MDPR	cm/sec x10^6	mils/hr	Garcia[7] Data mils/hr
304 Stainless Steel	.12	.17	.10
75% C. W. Nickel (As Rec'd)	.50	.71	.44
60% C. W. Copper (As Rec'd)	1.56	2.22	.95
Copper 900°F Annealed	1.72	2.44	1.02
2024-T351 Aluminum	1.91	2.73	.57
6061-T651 Aluminum	31.4	44.6	.72
Plexiglas	49.4	69.2	1.39
1100-0 Aluminum	53.7	75.2	2.70

*Normalization of approximate maximum bubble population of individual specimens to the approximate maximum bubble population of nickel.

TABLE 4--Continued

(c) Depth/Diameter		Robinson[10] Data
304 Stainless Steel	.0095	.027
75% C. W. Nickel (As Rec'd)	.0149	
Copper 900°F Annealed	.0182	
1100-0 Aluminum	.0198	
6061-T651 Aluminum	.0236	
60% C. W. Copper (As Rec'd)	.0257	
2024-T351 Aluminum	.0304	
Plexiglas*	.1462	
Columbium 1 Zirconium		.035
Tenelon (USS)		.022
Copper-Nickel (As Rec'd)		.039
Nickel (L. Ht. Trt.) (85-Ni)		.022

(d) Bubbles/Pit		Robinson & Hammitt Data[12,13]
Plexiglas	475×10^4	10^4 to 10^5
304 Stainless Steel	8.71×10^4	
75% C. W. Nickel (As Rec'd)	4.53×10^4	
60% C. W. Copper (As Rec'd)	2.65×10^4	
Copper 900°F Annealed	2.03×10^4	
2024-T351 Aluminum	1.75×10^4	
1100-0 Aluminum	$.68 \times 10^4$	
6065-T651 Aluminum	$.66 \times 10^4$	

*After second run.

is apparent then that the concept of the existence of an "incubation period" before volume loss occurs does not apply to these tests. The same conclusion was drawn in the venturi tests both from visual examination of the surface,[10,12,13,39] and tests using an irradiated specimen.[58] As in the present tests the early damage rate was markedly higher than that obtained later.

The rating of materials for resistance to cavitation damage by a factor that is dependent on the time-rate of volume loss without considering the possibly differing bubble populations to which the individual specimens are exposed, may be questionable. Also there is no assurance that the bubble pattern observed in this very initial portion of a test remains constant as the test continues. For gross damage, Plesset and Devine[34] showed a very substantial decrease in the bubble population as the exposure time progressed. In this investigation it was noticed that the bubble pattern changed very early in the test for type 1100-0 aluminum (Fig. 70), where apparently the threads of the specimen were too weak to maintain an adequate bond of the specimen to the horn. Perhaps a better rating method, using MDPR, for obtaining basic understanding of the phenomenon rather than actual standardized testing would be to normalize the approximate maximum bubble populations of the specimens to the specimen with the highest approximate maximum bubble population. For this investigation, this was the 75% c. w. nickel (as rec'd) specimen. With this technique,

the other specimens can be rated as if they too had faced the approximate maximum bubble population seen by the nickel specimen. Fig. 128[7] shows after many hours of exposure to cavitation in water at room temperature experimental evidence of full and partial damage patterns that probably relate to similar bubble field patterns.

This normalized MDPR rating is shown in Table 4-b, and again is presented with a comparison to Garcia's[7] data. The first four of the specimens in the column compare well to Garcia's data, as far as order, which they also did in the unnormalized data, but damage rate is somewhat greater than that observed by Garcia. The last three specimens, especially, show strikingly higher damage rates than those shown by Garcia. This not only completely refutes the idea that an incubation period is necessary for cavitation damage, as was mentioned earlier, but also shows that early damage is very heavy on the type 6061-T651 aluminum (medium hardness) and heavier yet on the soft Plexiglas and type 1100-0 aluminum. Perhaps this excessive "early damage" so changes the bubble pattern that the specimen sees substantially fewer bubbles as the test progresses, thus decreasing the MDPR.

The average depth to diameter ratio was calculated for the given materials from the data obtained from the Proficorder and the values are tabulated in Appendix "C." These ratios vary considerably for the different materials, while for the materials tested by Robinson[10] in a venturi they varied only

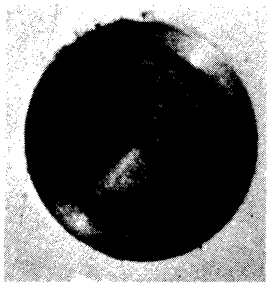

(1) T-222(P & W)
36 Hour Exposure

(2) T-111(P & W)
30 Hour Exposure

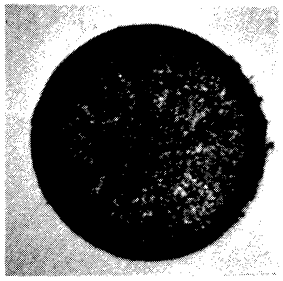

(3) Mo-1/2Ti(P & W)
36 Hour Exposure

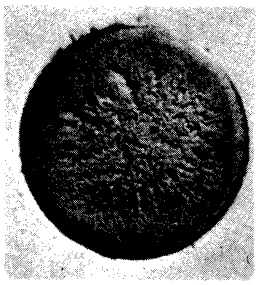

(4) 316 SS(U-M)
36 Hour Exposure

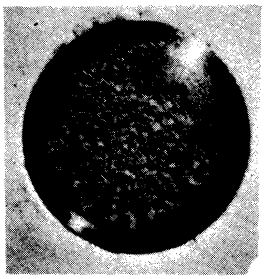

(5) 304 SS(U-M)
30 Hour Exposure

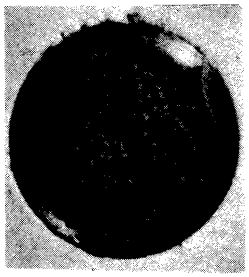

(6) Cb-1Zr(P & W)
32 Hour Exposure

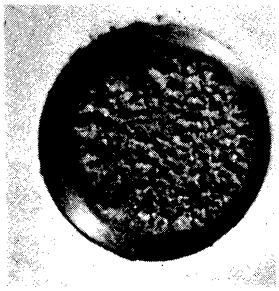

(7) Cb-1Zr(A)(P & W)
30 Hour Exposure

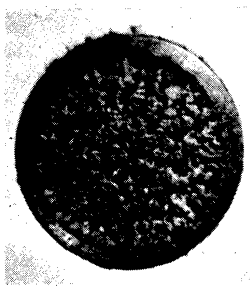

(8) Carbon Steel(U-M)
21 Hour Exposure

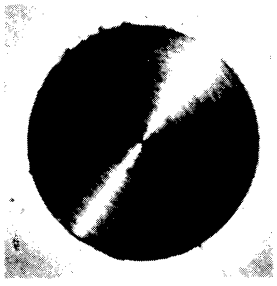

304 SS(U-M)
Before Exposure

2119

Fig. 128.--Still photographs[7] (2.5X) showing damaged specimens after exposure to cavitation in water at 70°F.

slightly. The only material tested in both investigations was type 304 stainless steel, but other materials from Robinson's work are also included, so that an overall comparison can be made. Typical ratios from Robinson's experiment are in the range of ~.022 to ~.039. Most of the ratios shown in Table 4-c are not very far from this range, with the strong exception of Plexiglas which is well above it. The relatively large depth of the Plexiglas pits suggests that it is not very resistant to the damaging mechanism, since, as previously mentioned, the diameter of the Plexiglas pits is also relatively very large.

Rating of the specimens by depth to diameter ratio gives the same rating as MDPR and normalized MDPR for type 304 stainless steel and 75% c. w. nickel (as rec'd), since they rank one and two respectively in all three ratings. Type 1100-0 aluminum shows a much higher ranking when considering depth to diameter ratio than for MDPR or normalized MDPR, but Plexiglas is bad on all three ratings.

Table 4-d rates the material in terms of bubbles per pit ratio. This ratio is of significance when with respect to the damage mechanism. As previously mentioned, Robinson[10] found there were approximately 10^4 to 10^5 bubbles observed adjacent to the exposed specimen surfaces for every pit that was later detected for tests in a cavitating venturi using mercury. Plesset[11] had previously reported approximately 10^4 bubbles per pit for a vibratory facility which is in approximate

agreement with the present data (Table 4-d), except for Plexiglas where the ratio is larger by a factor of about 10^2. This may indicate that Plexiglas is quite immune to relatively non-energetic bubbles, but highly susceptible to damage from more energetic collapses. The same indication was afforded by the venturi tests[10,12,13,39] where it was found that Plexiglas suffered relatively little damage in water tests compared with metallic materials, but very heavily in mercury tests, compared to the same materials. This anomalous behavior of soft resilient materials as some elastomerics with respect to cavitation damage has long been known.[59] The materials rank according to this parameter somewhat the same as when ranking with MDPR, normalized MDPR and depth to diameter ratio, except for types 6061-T651 and 2024-T351 aluminums which reverse rating positions, and Plexiglas which rates extremely well on bubbles/pit, as already mentioned. Plexiglas has a low number of detectable pits, but they are large and account for a high volume removal rate, i.e., low MDPR rating. Also when Plexiglas is exposed for a longer run, as in the case of the second exposure which was for 5 minutes, its entire surface becomes battered and large erosion areas become evident on the specimen surface.

In some cases it was extremely difficult to count bubbles and pits accurately. While the high speed photographs were clear, there were far too many bubbles on some for an accurate count. The specimens even for exposures as short as 15 seconds (type 6061-T651 aluminum) damaged so heavily that miltiple pitting occurred in some areas. A more accurate

bubbles/pit ratio could be obtained for cavitation exposures of several seconds, or less, and with a lower horn amplitude, so that the bubbles would not be raised to such a large diameter before their collapse, thus probably reducing both the size and the number of pits.

Over-all rating by MDPR (a), Normalized MDPR (b), Depth to Diameter Ratio(c), and Bubbles/Pit (d), neglecting the high rating of Plexiglas in (d), would show the stainless steel first, nickel second, the coppers third and fourth, followed by the three aluminums with type 2024-T351 the best of these. Plexiglas, despite its apparent resistance to pitting in the early portion of the test, would be rated among the poorest materials in terms of a, b, and c, while type 1100-0 aluminum is poor in a, b, and c, but somewhat better in d.

M. Correlation with Mechanical Properties

Table 2 lists twelve different mechanical properties[56,57] for the eight specimens. Nine of these mechanical properties were used when attempting correlations in this investigation.* An attempt was made to correlate the damage to the specimens as measured by four damage parameters, MDPR, depth to diameter ratio, bubbles/pit, and a volume/pit parameter that is explained later. Figs. 129 through 159 show plots of the various mechanical properties vs. the four damage parameters.

---

*True strain energy (a), % elongation and % reduction in area were included for convenience in Table 2, but they were not used for correlations.

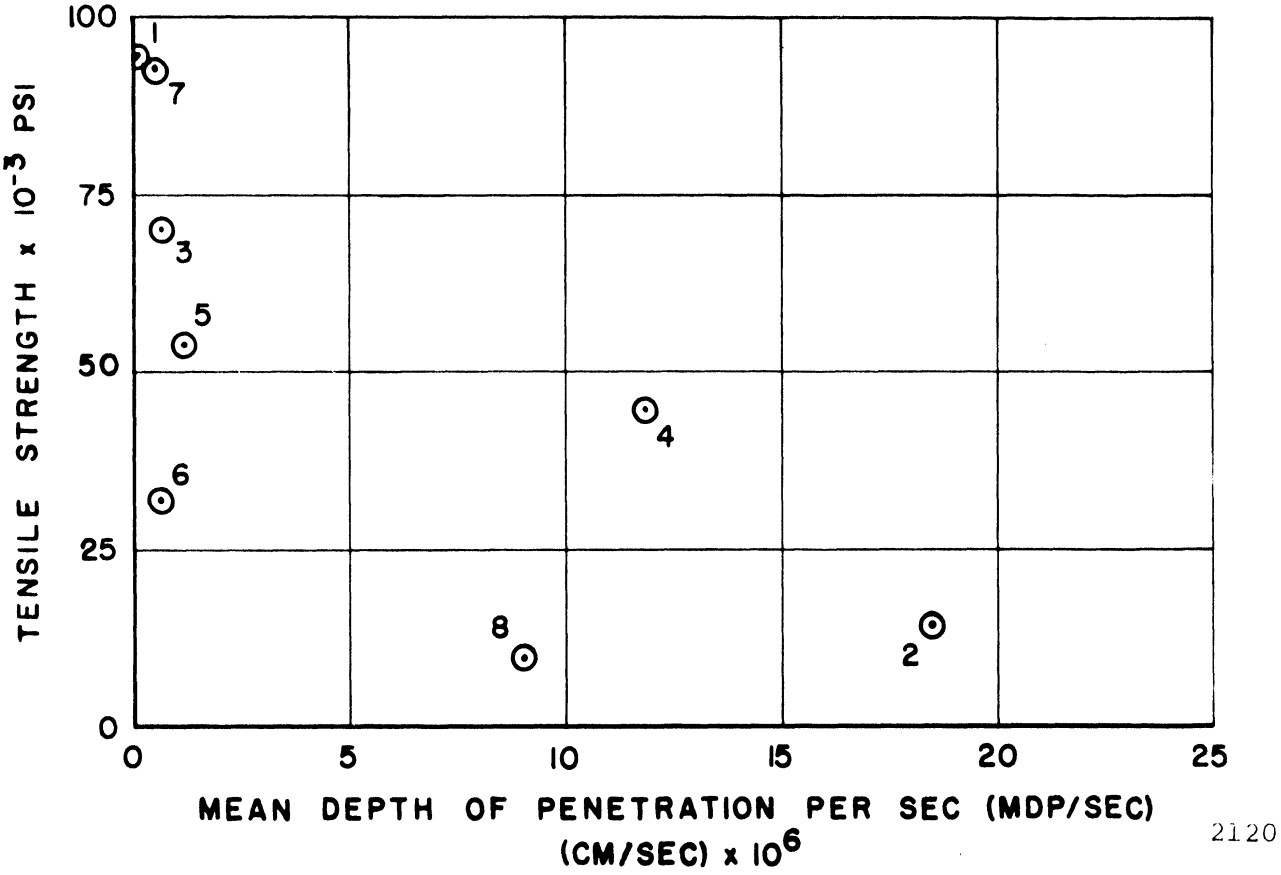

Fig. 129.--MDPR vs. tensile strength.

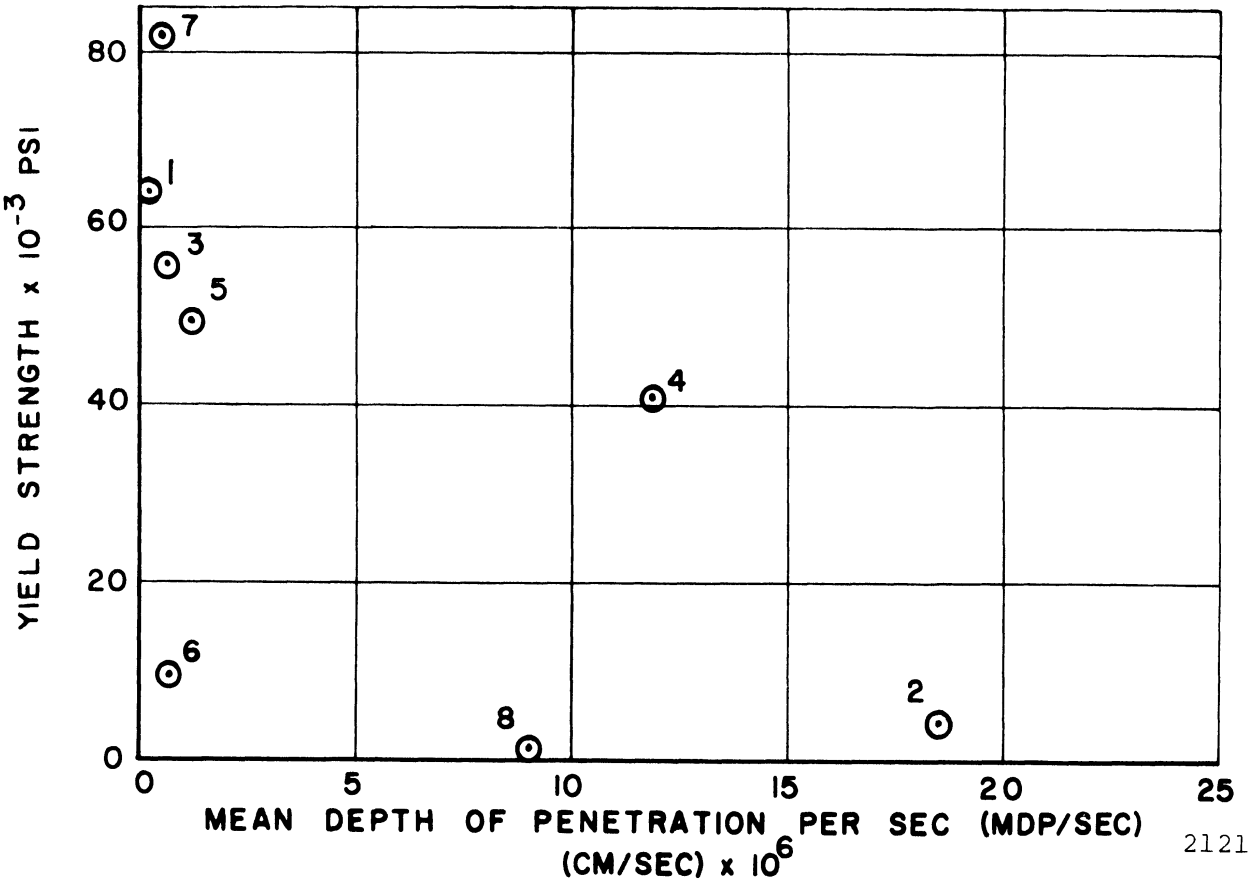

Fig. 130.--MDPR vs. yield strength.

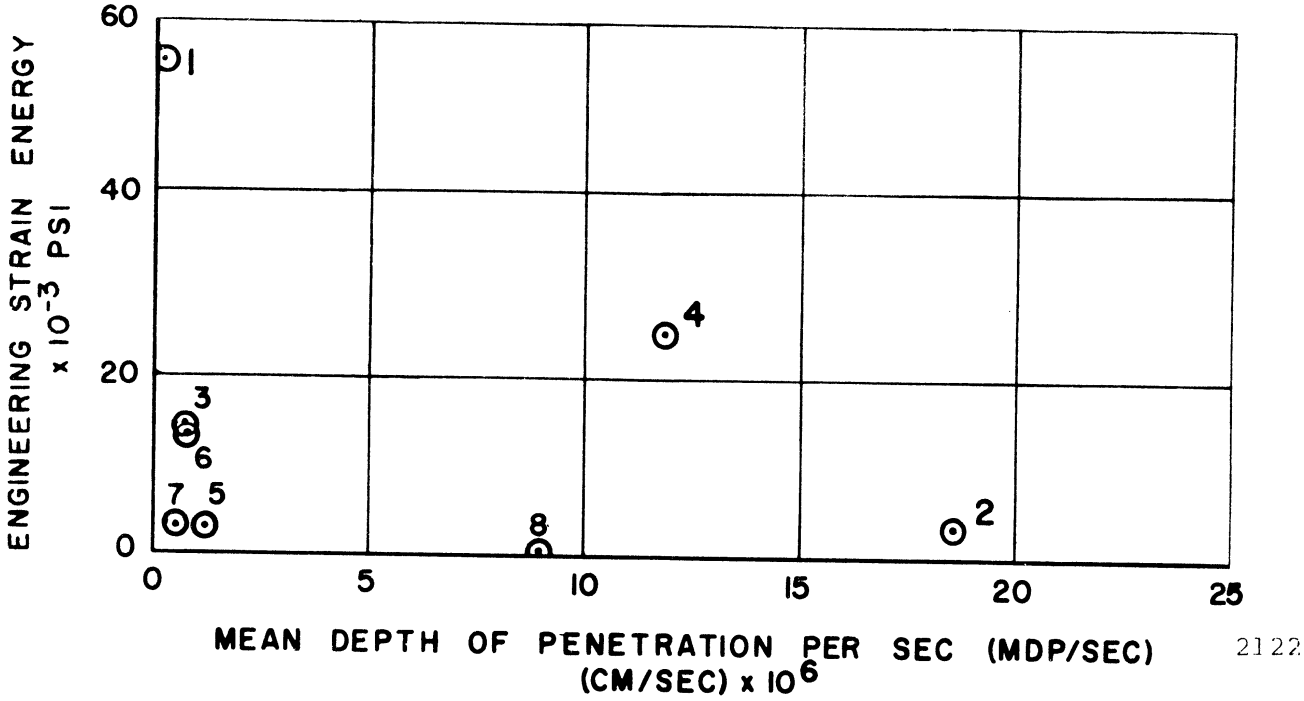

Fig. 131.--MDPR vs. engineering strain energy.

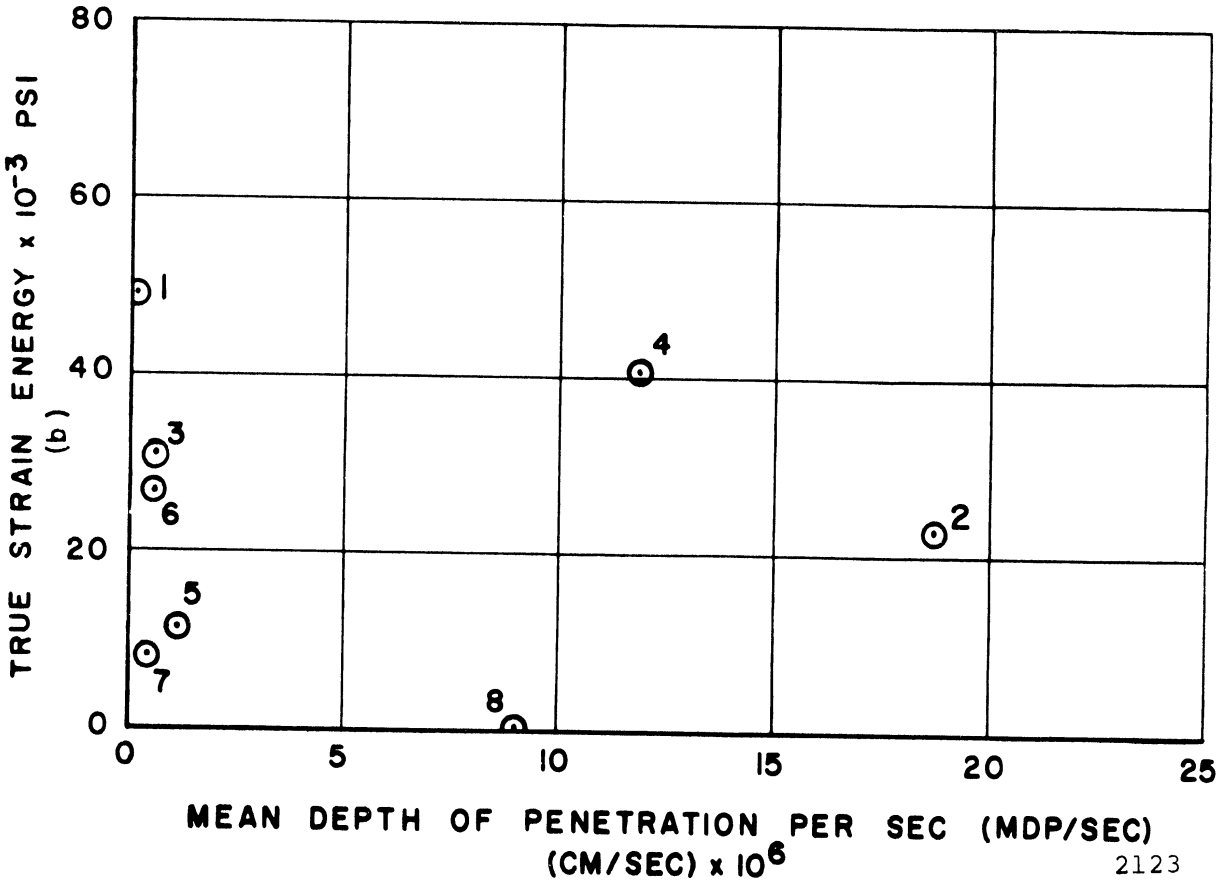

Fig. 132.--MDPR vs. true strain energy (b).

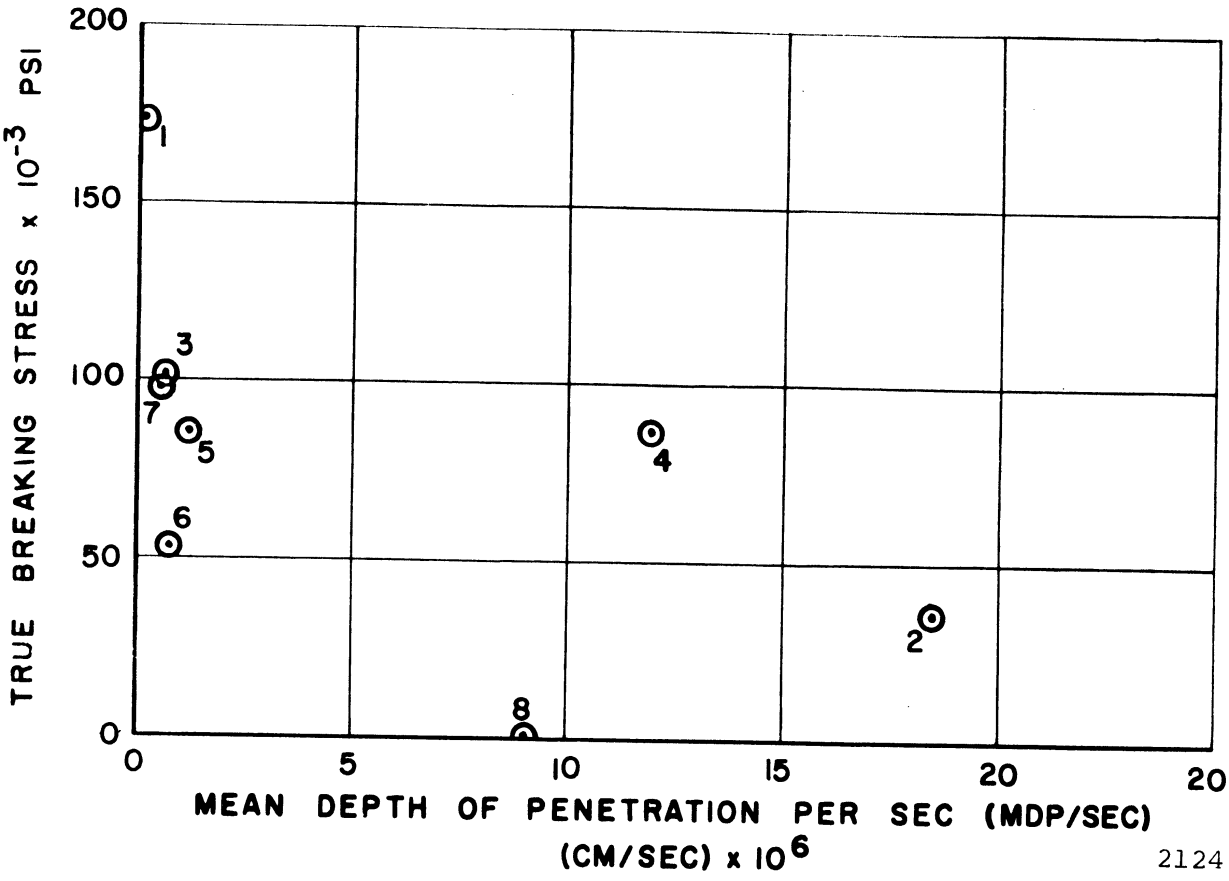

Fig. 133.--MDPR vs. true breaking stress.

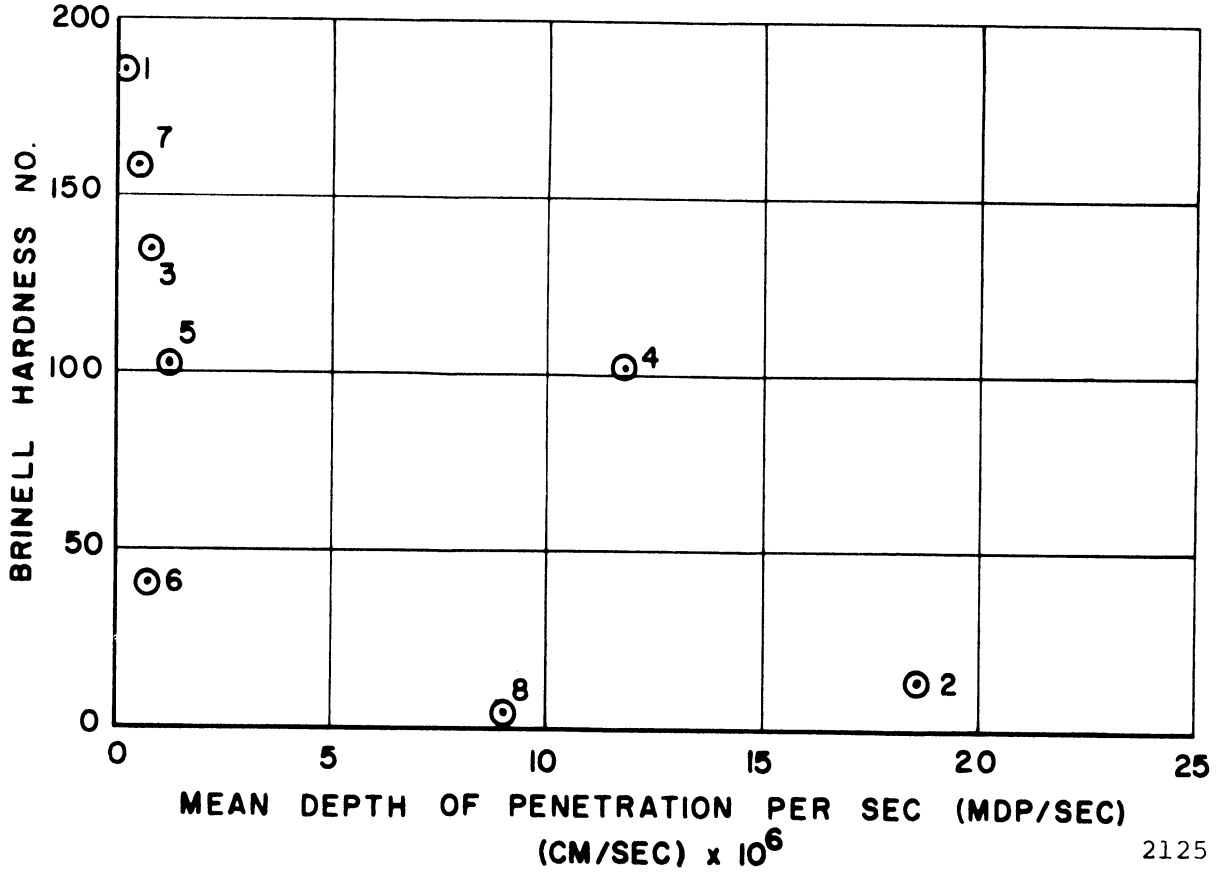

Fig. 134.--MDPR vs. Brinell hardness number.

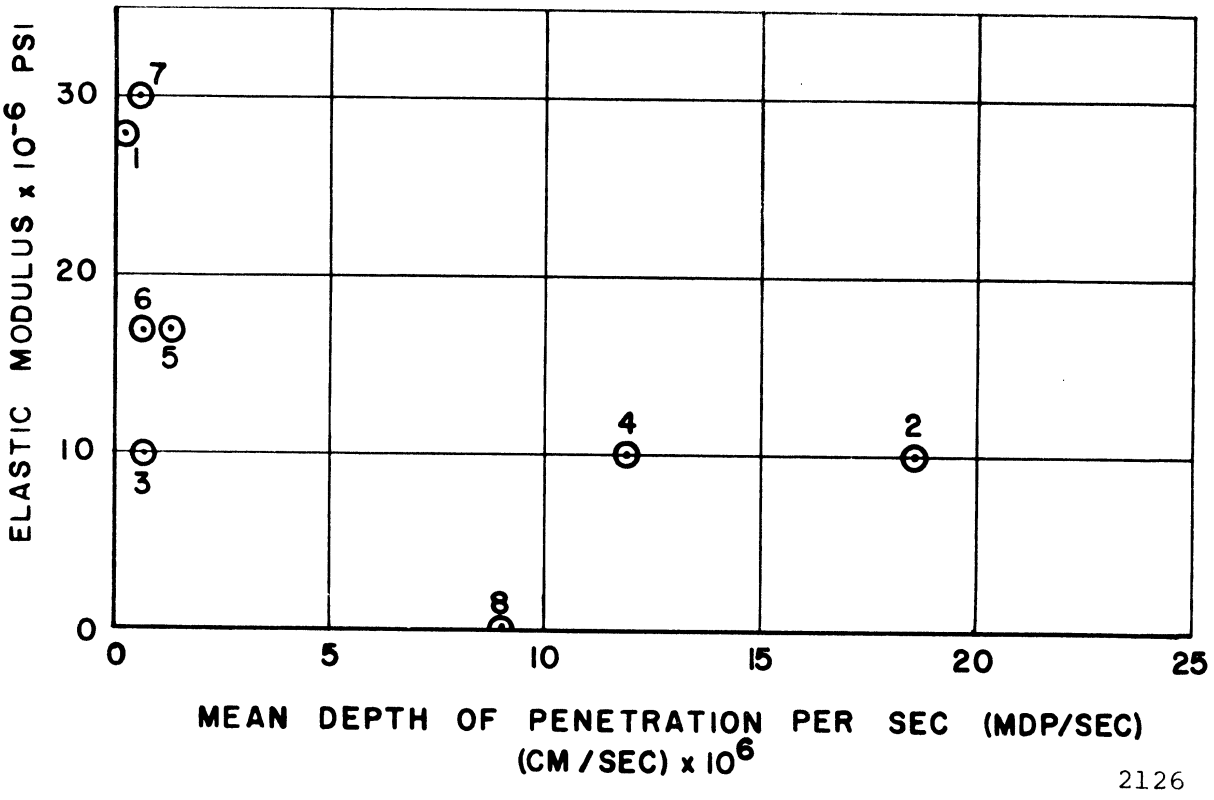

Fig. 135.--MDPR vs. elastic modulus.

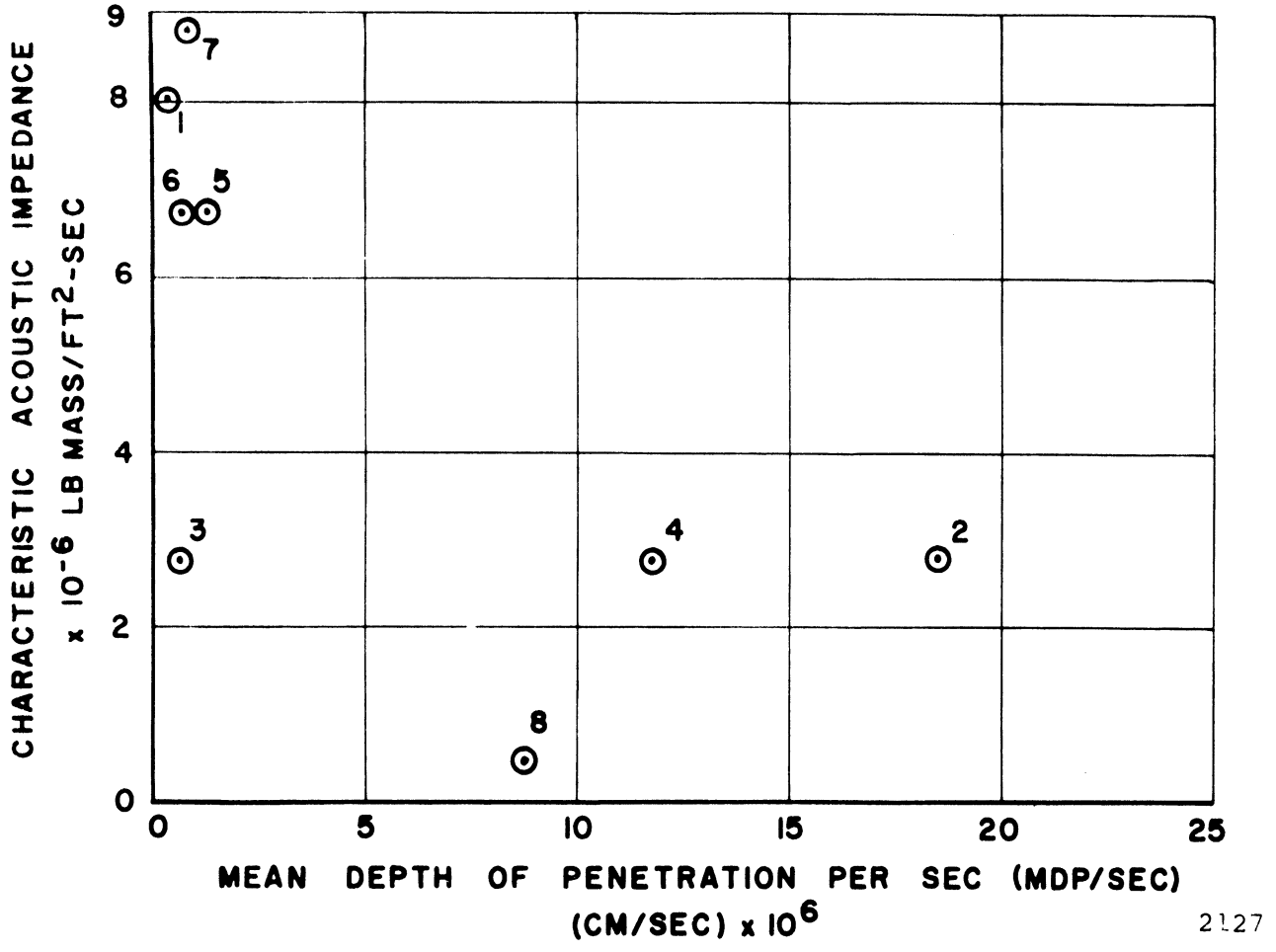

Fig. 136.--MDPR vs. characteristic acoustic impedance.

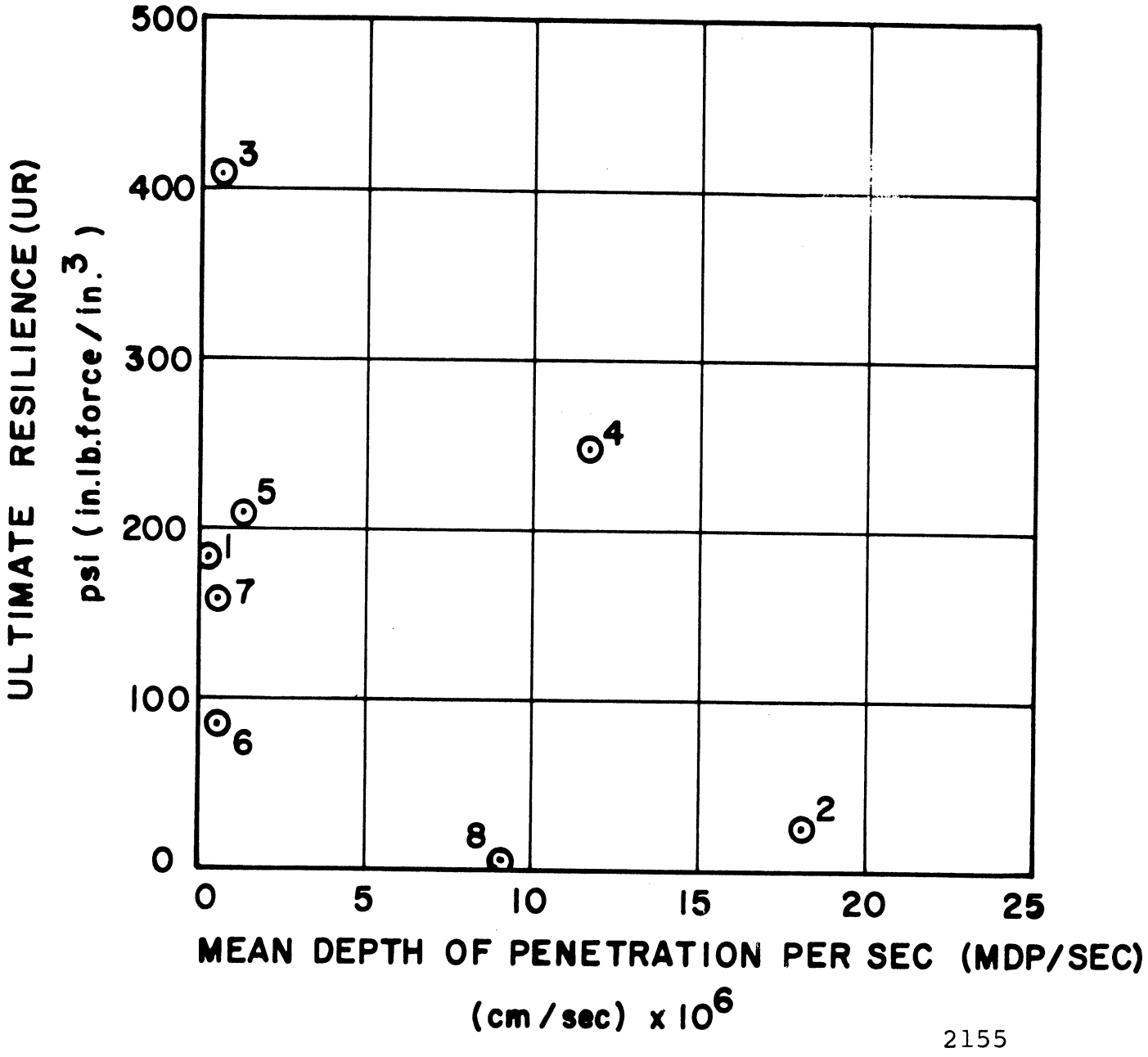

Fig. 137.--MDPR vs. ultimate resilience.

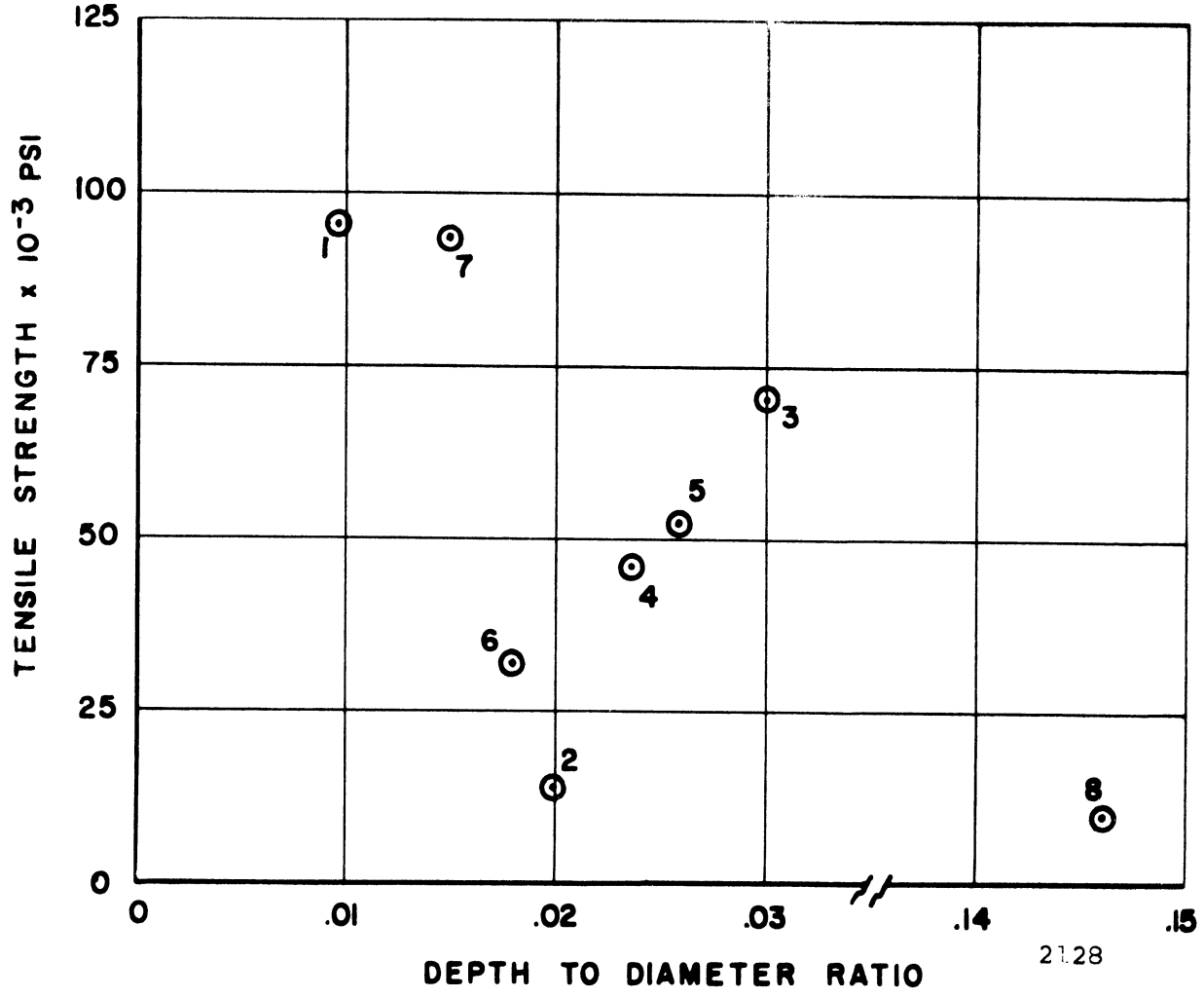

Fig. 138.--Depth to diameter ratio vs. tensile strength.

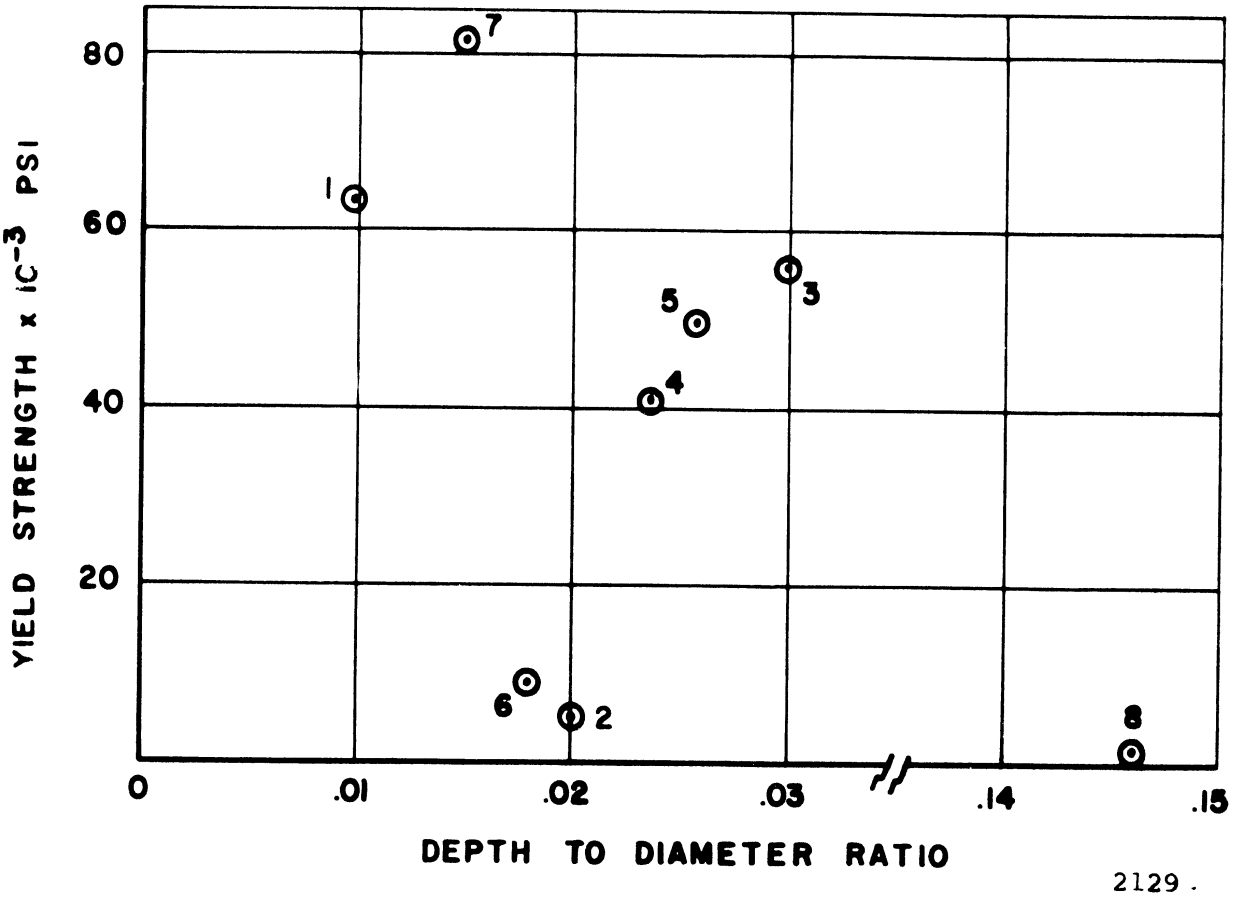

Fig. 139.--Depth to diameter ratio vs. yield strength.

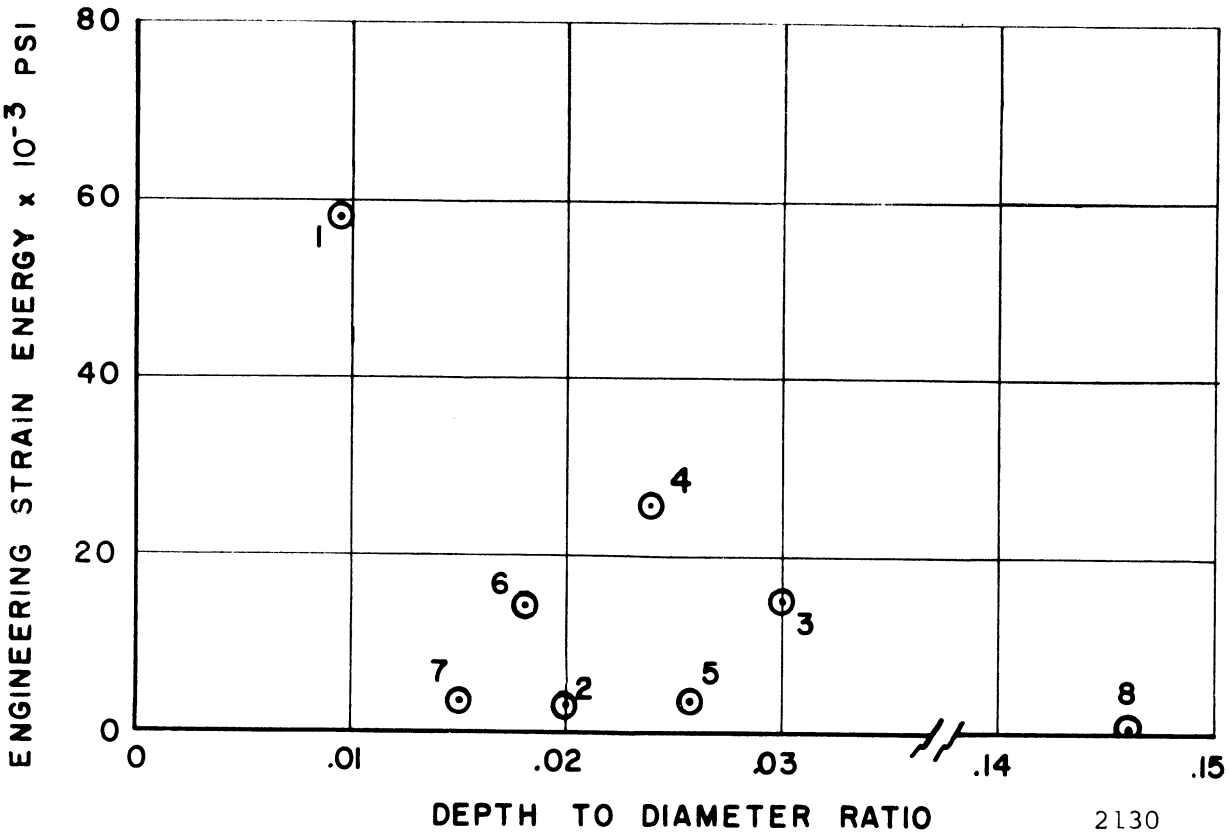

Fig. 140.--Depth to diameter ratio vs. engineering strain energy.

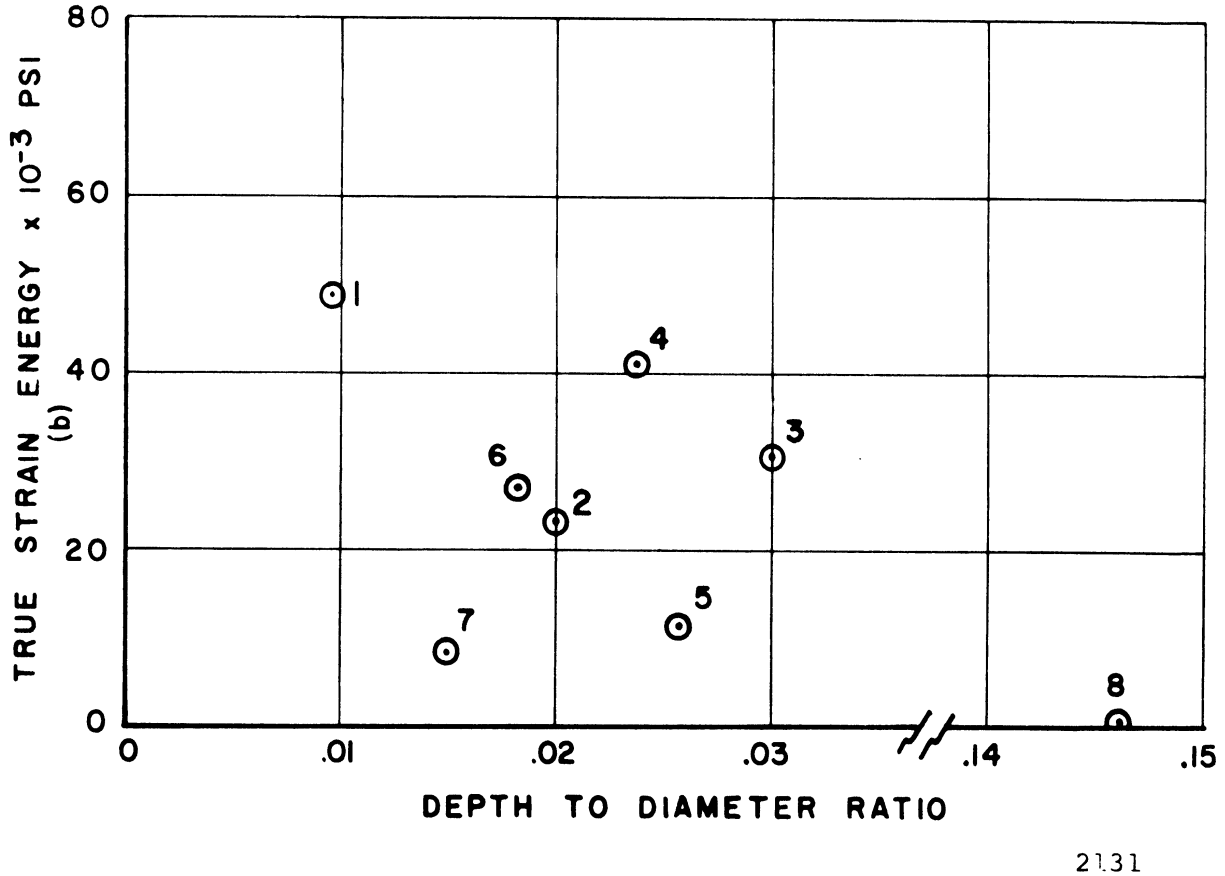

Fig. 141.--Depth to diameter ratio vs. true strain energy (b).

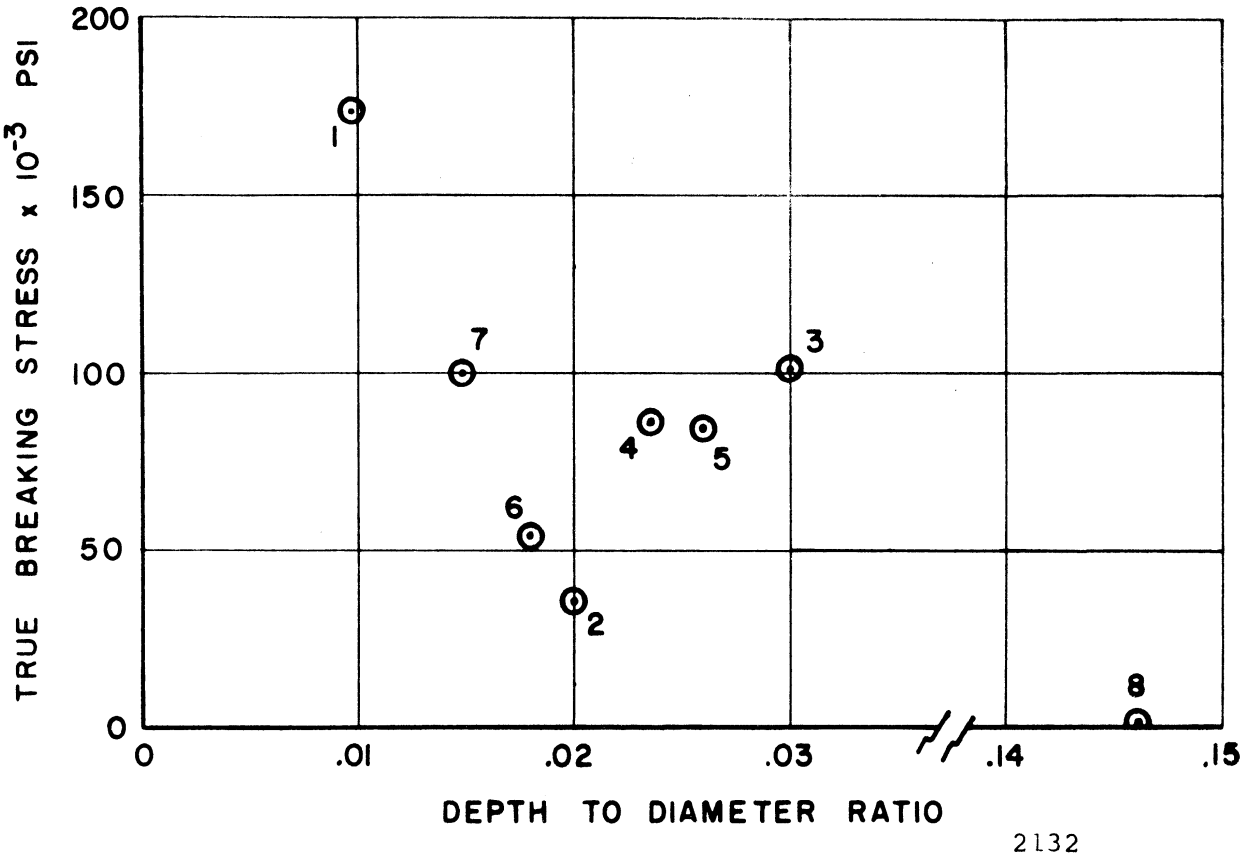

Fig. 142.--Depth to diameter ratio vs. true breaking stress.

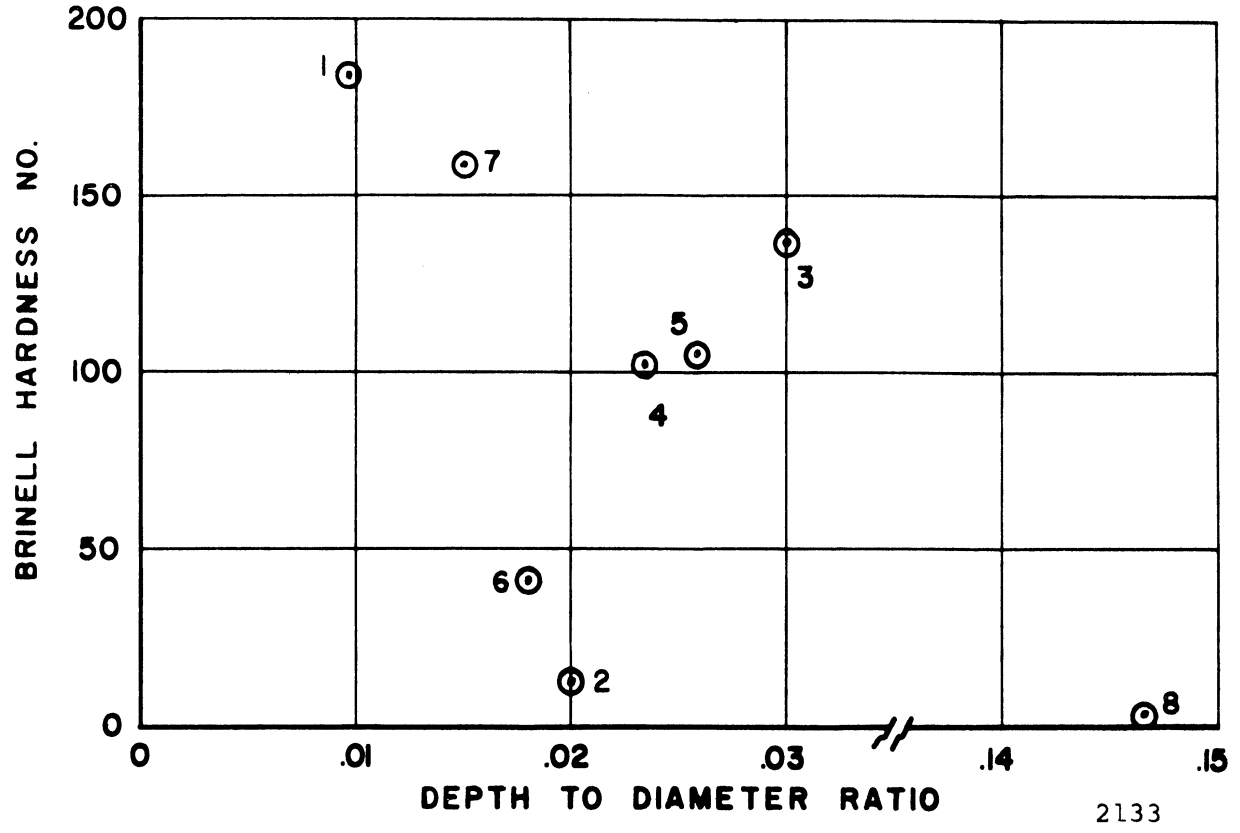

Fig. 143.--Depth to diameter ratio vs. Brinell hardness number.

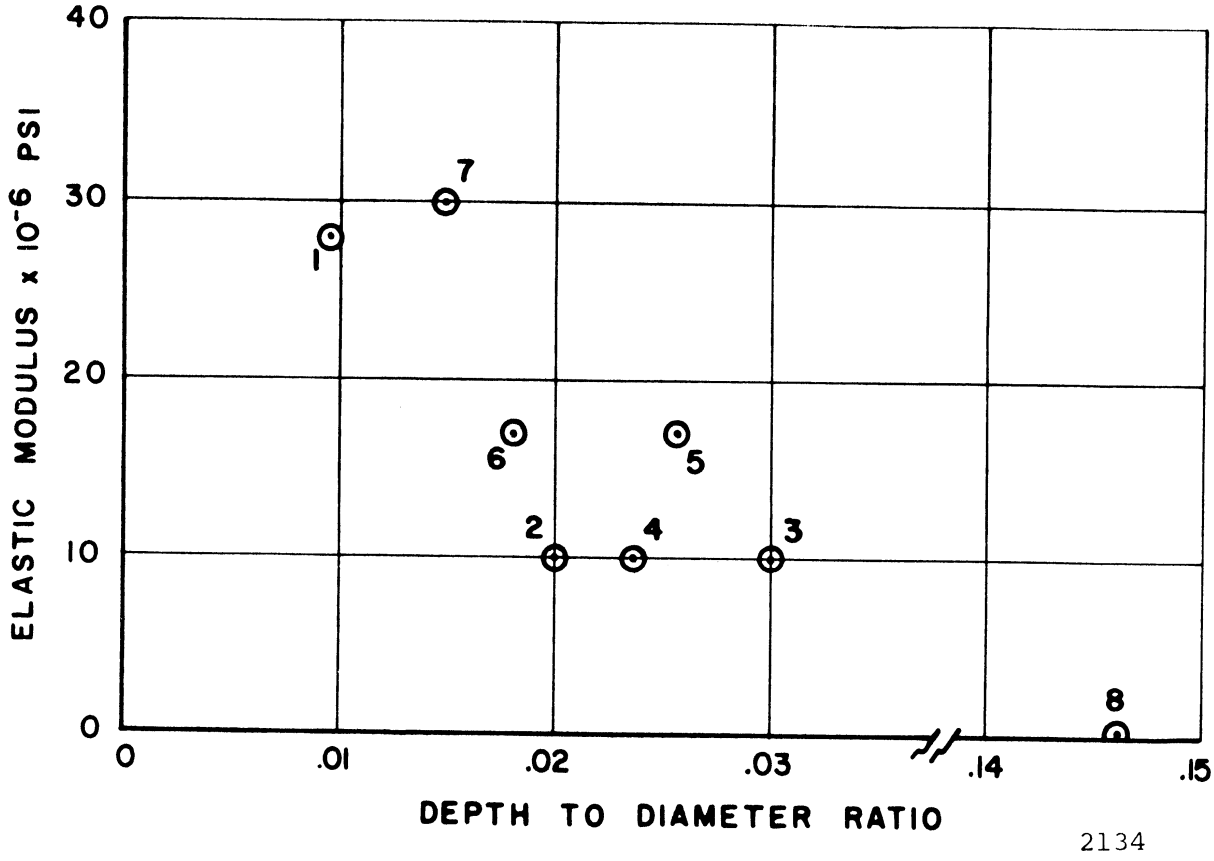

Fig. 144.--Depth to diameter ratio vs. elastic modulus.

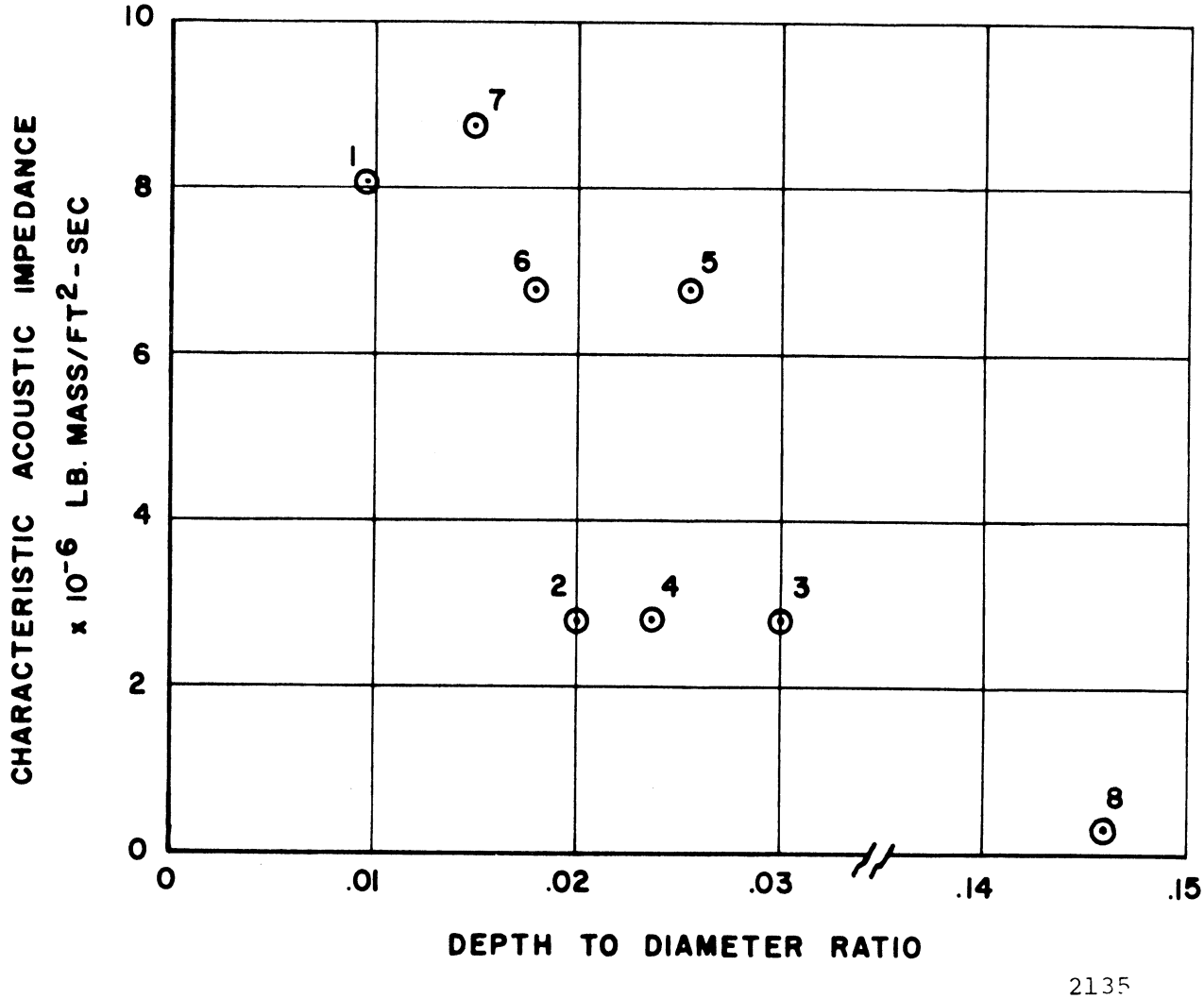

Fig. 145.--Depth to diameter ratio vs. characteristic acoustic impedance.

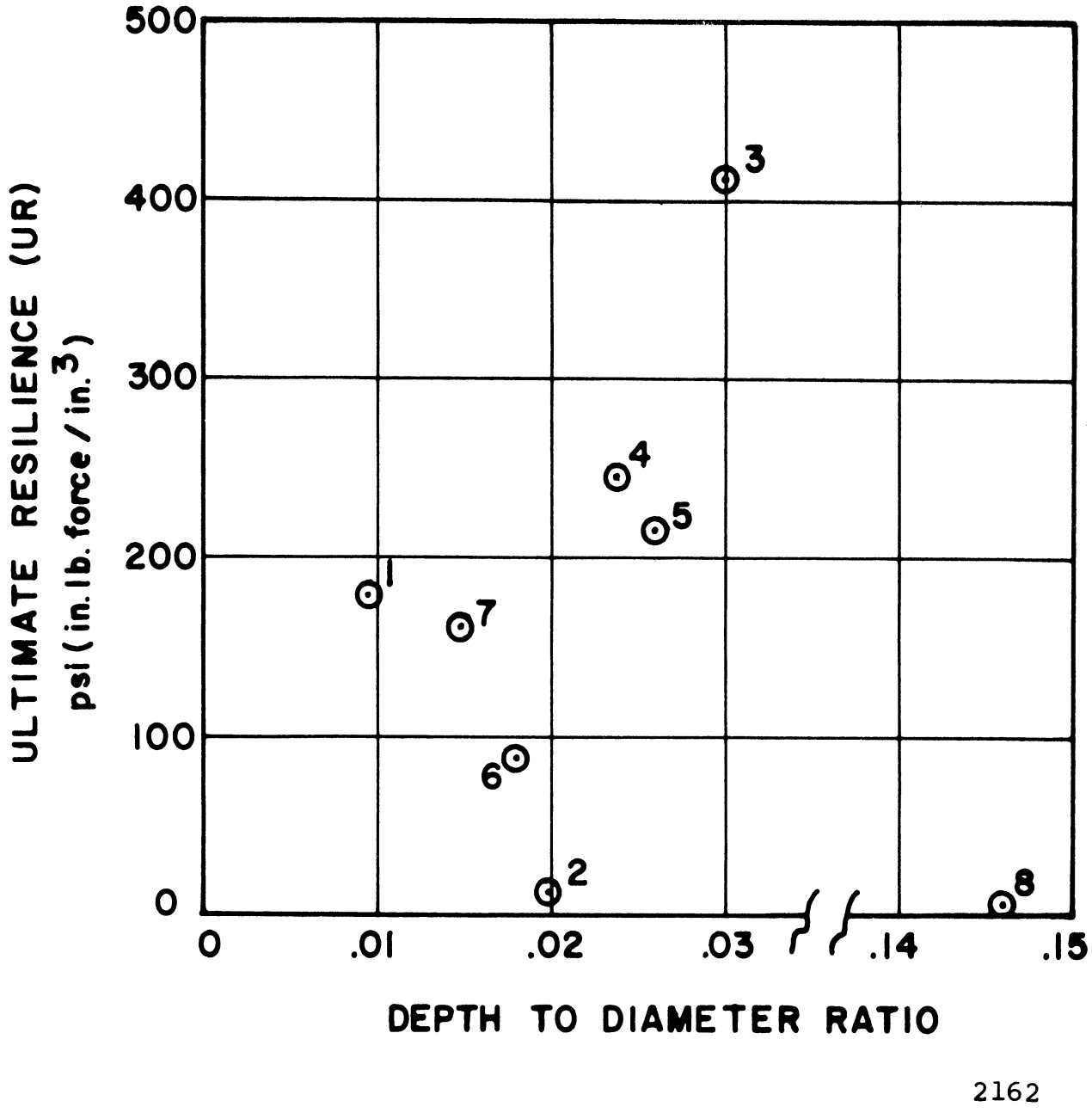

Fig. 146.--Depth to diameter ratio vs. ultimate resilience.

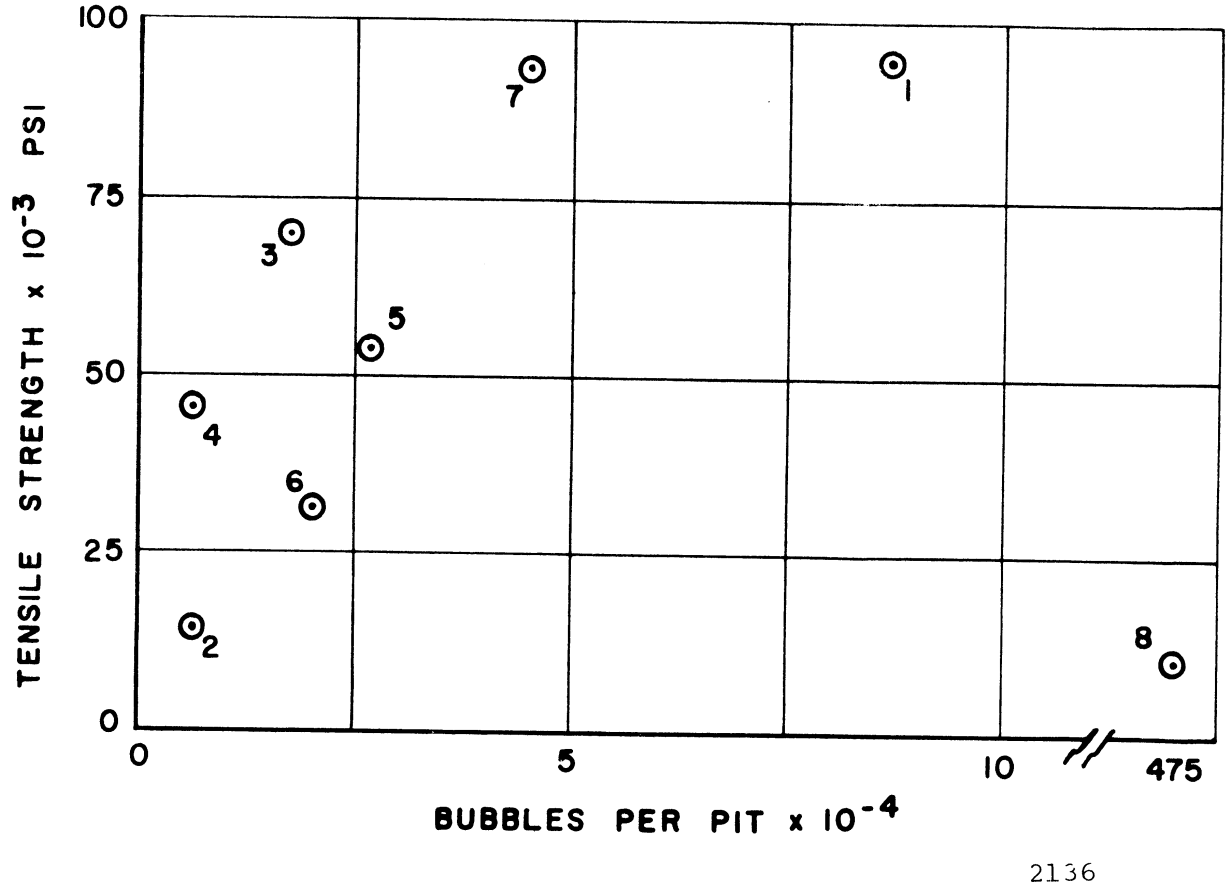

Fig. 147.--Bubbles per pit vs. tensile strength.

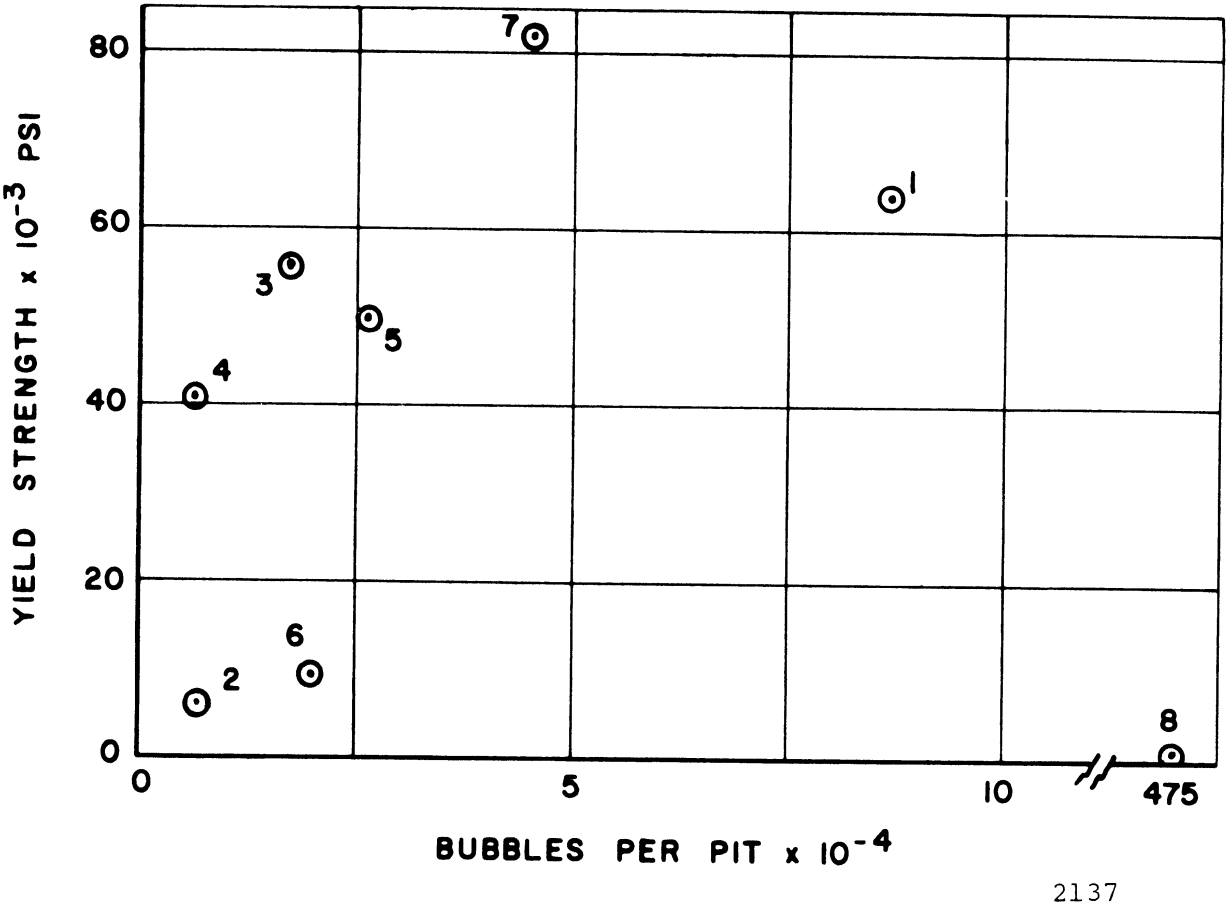

Fig. 148.--Bubbles per pit vs. yield strength.

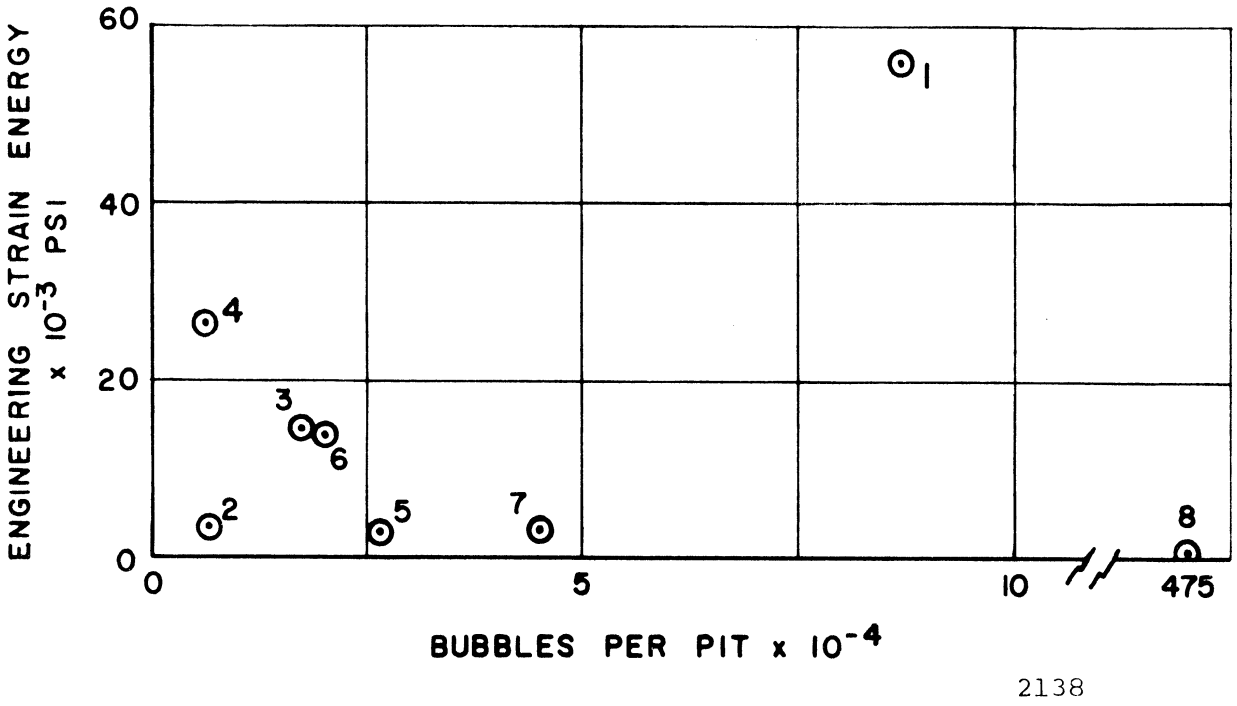

Fig. 149.--Bubbles per pit vs. engineering strain energy.

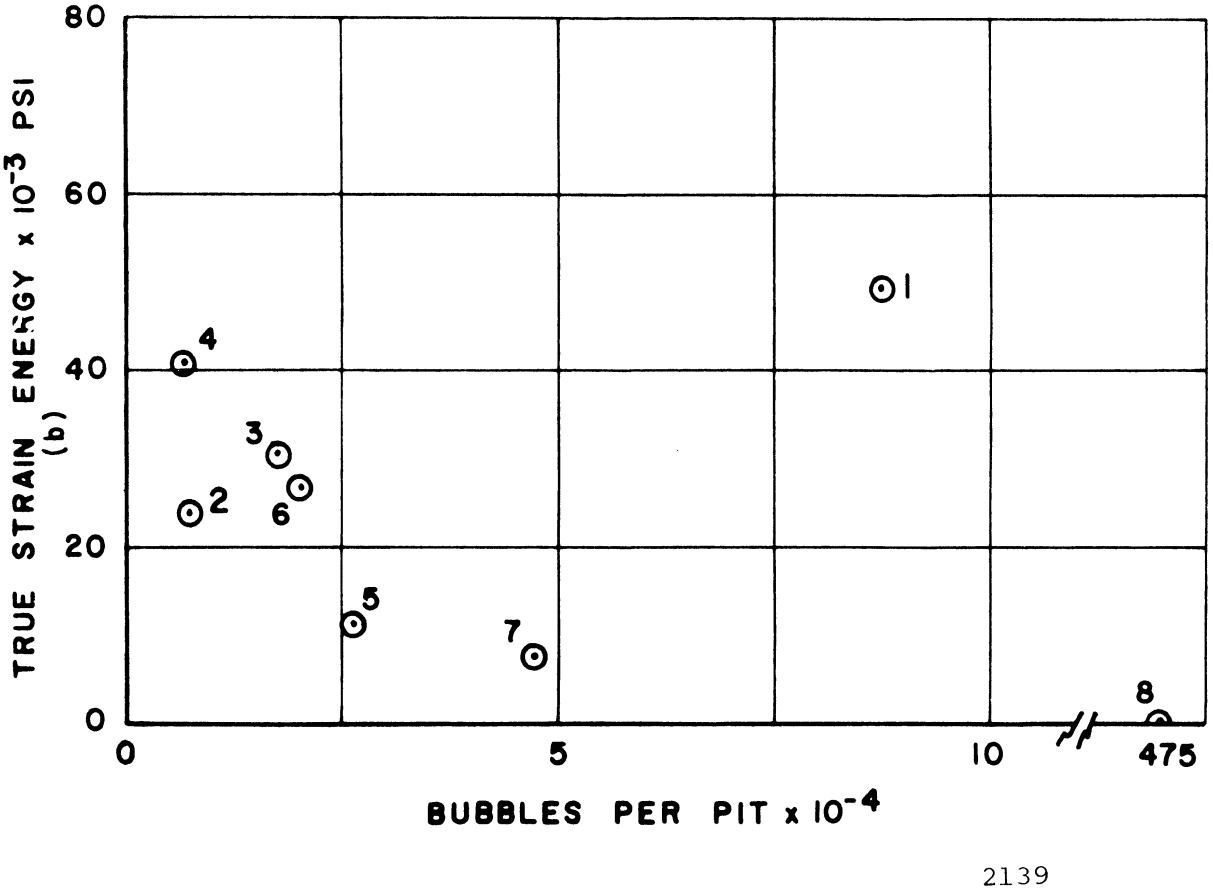

Fig. 150.--Bubbles per pit vs. true strain energy (b).

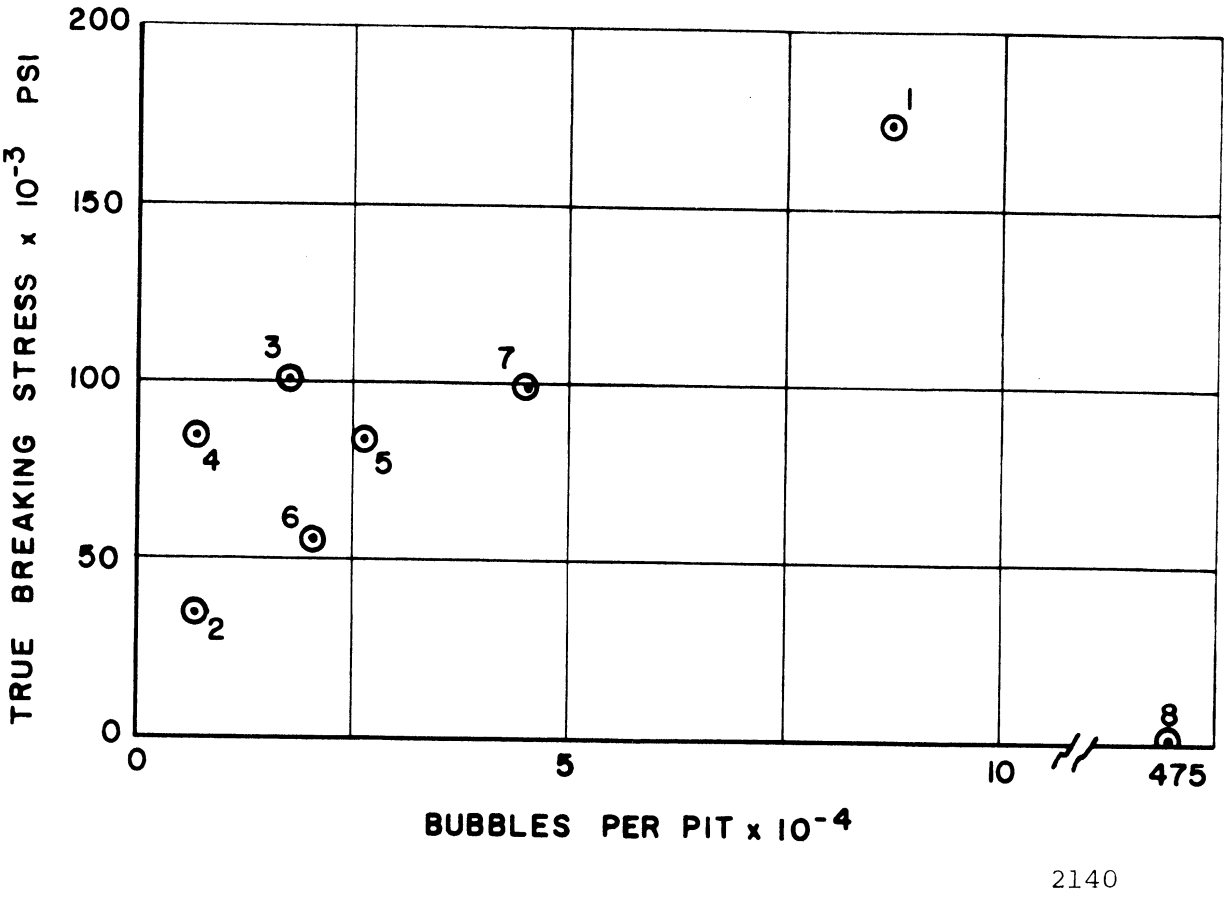

Fig. 151.--Bubbles per pit vs. true breaking stress.

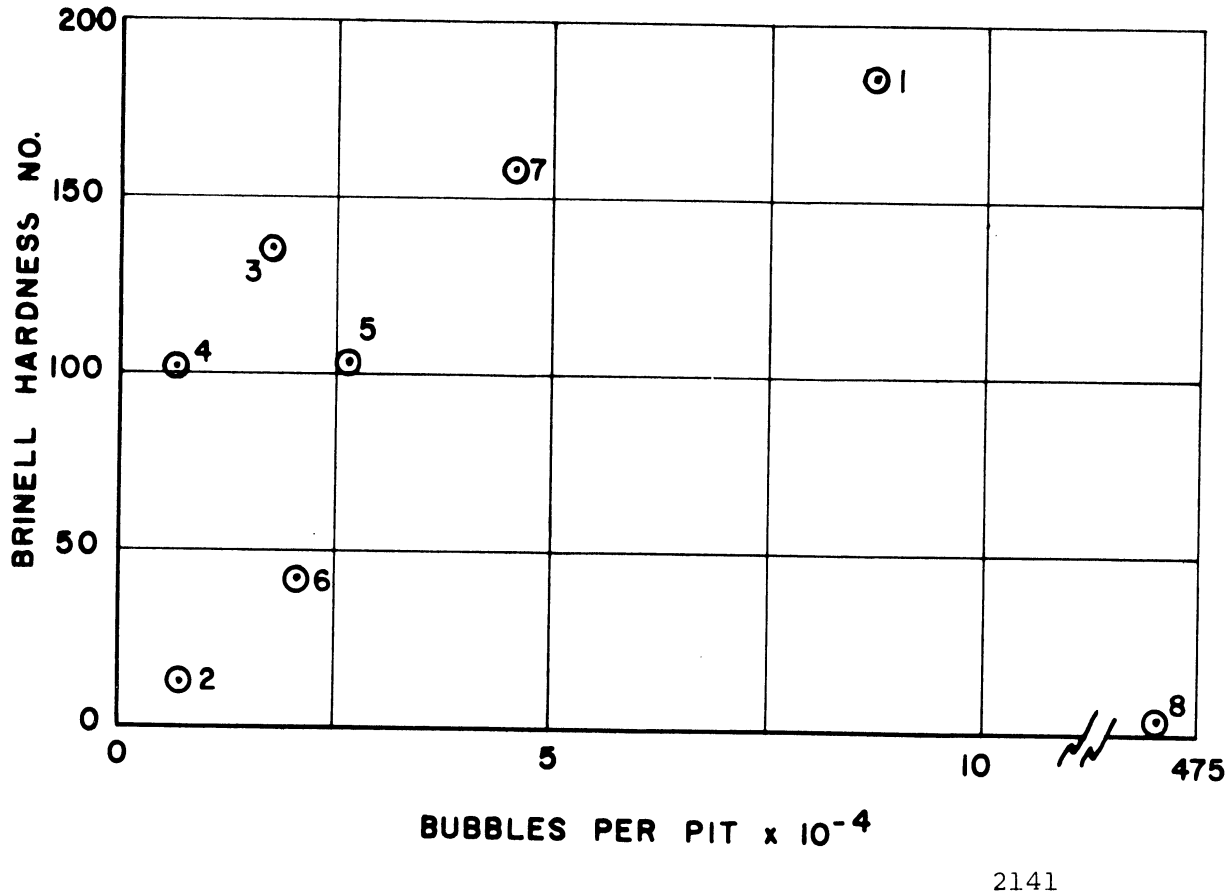

Fig. 152.--Bubbles per pit vs. Brinell hardness number.

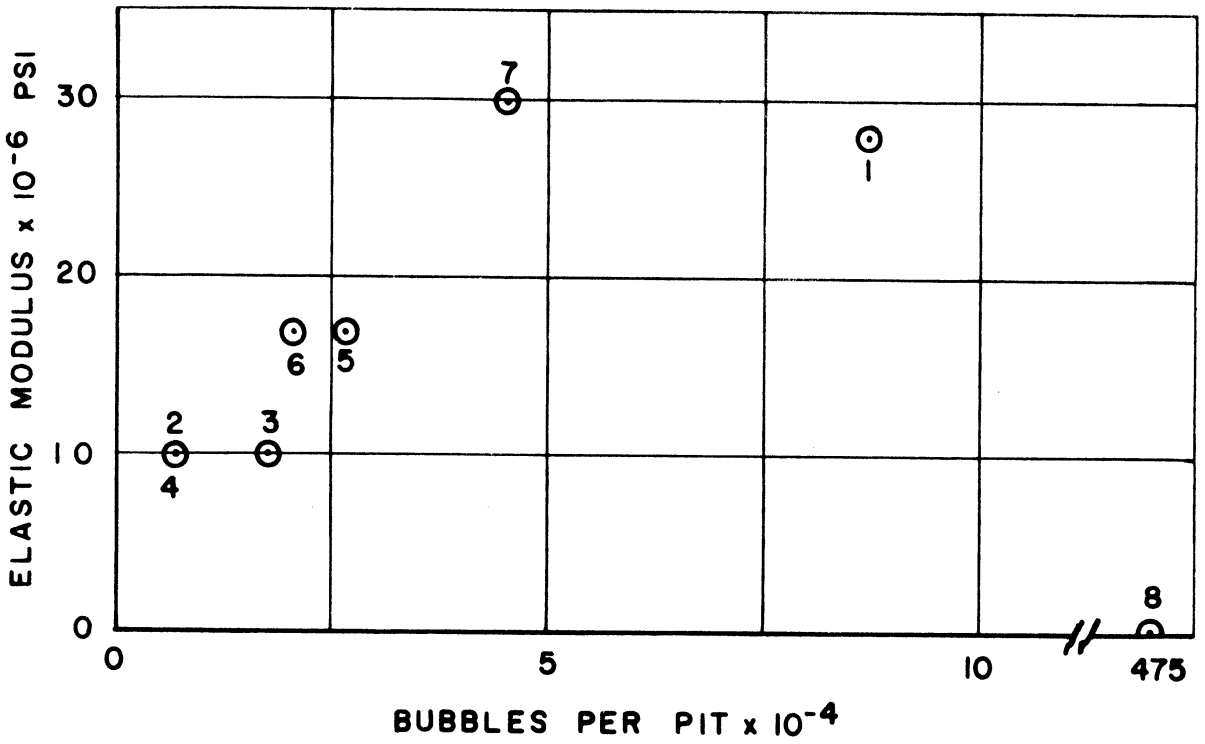

Fig. 153.--Bubbles per pit vs. elastic modulus.

2142

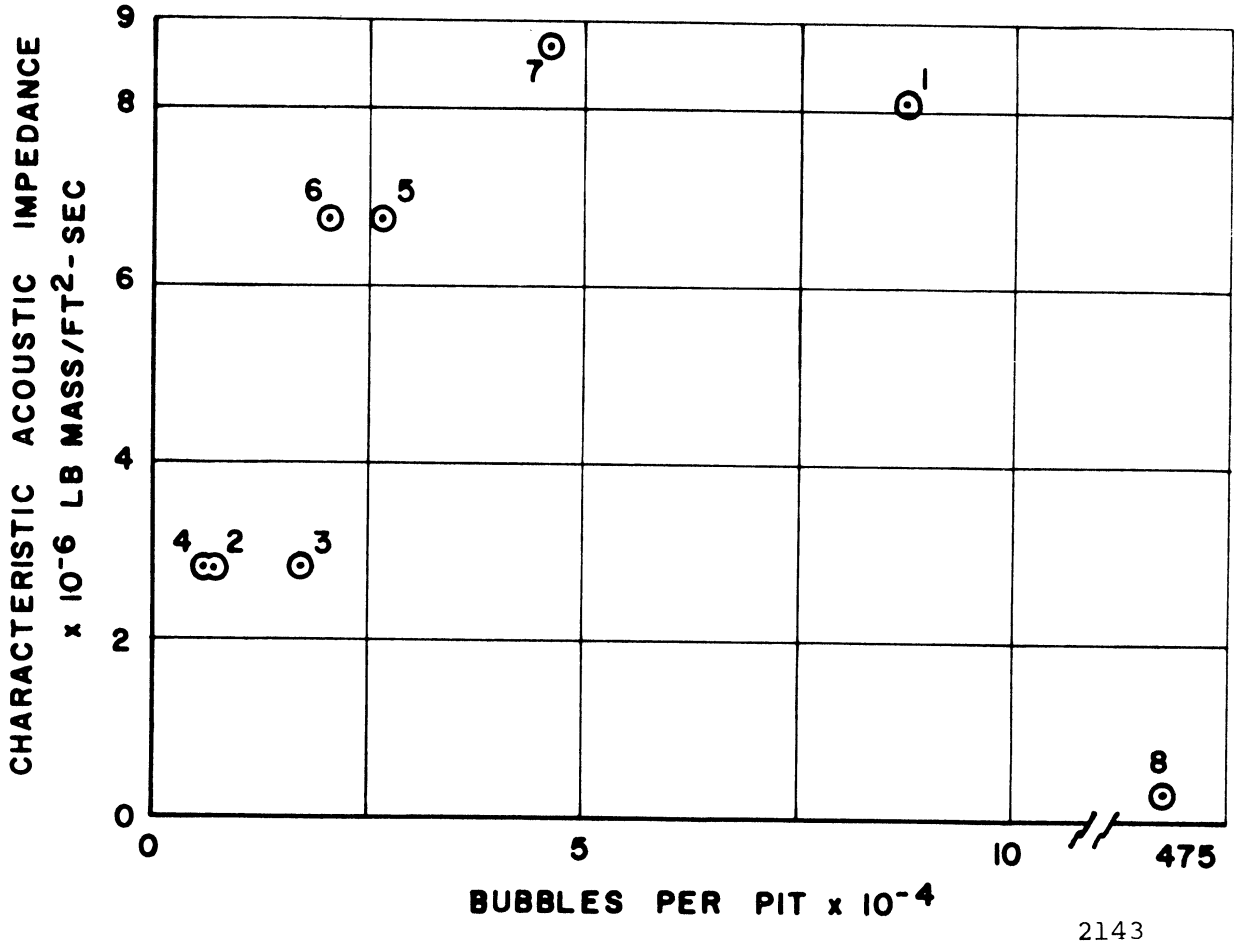

2143

Fig. 154.--Bubbles per pit vs. characteristic acoustic impedance.

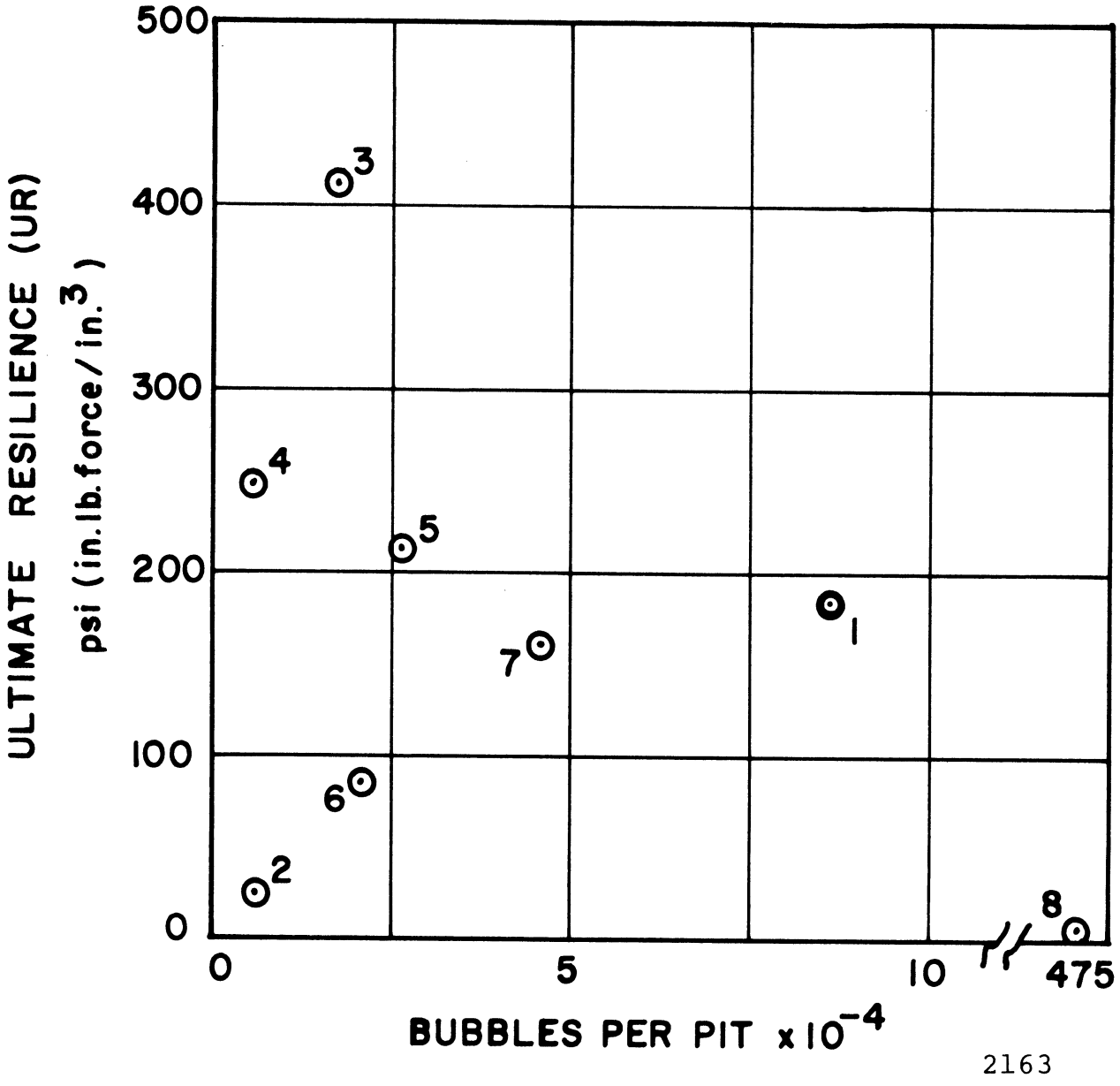

Fig. 155.--Bubbles per pit vs. ultimate resilience.

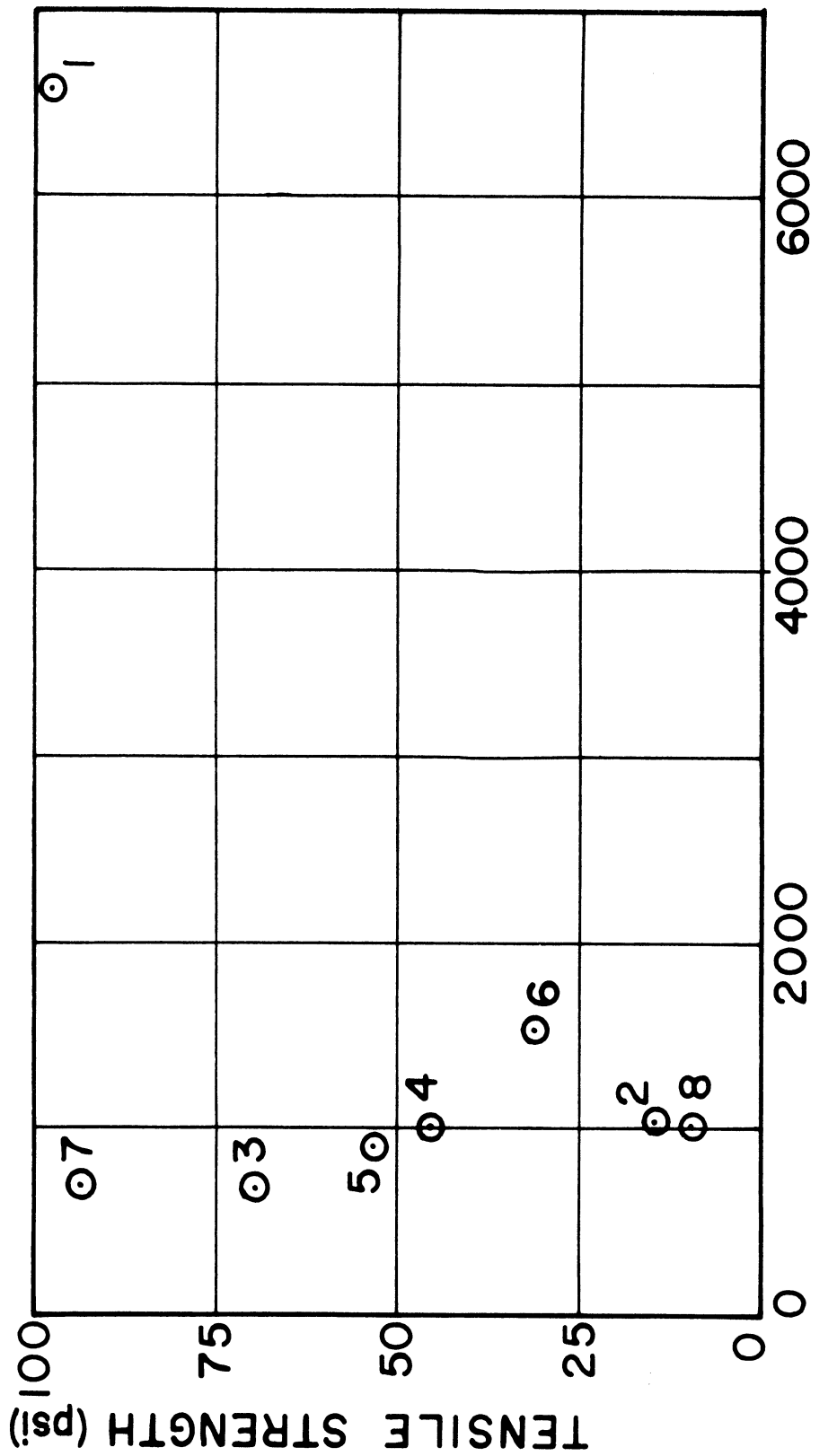

2144

Fig. 156.--Average pit diameter vs. tensile strength.

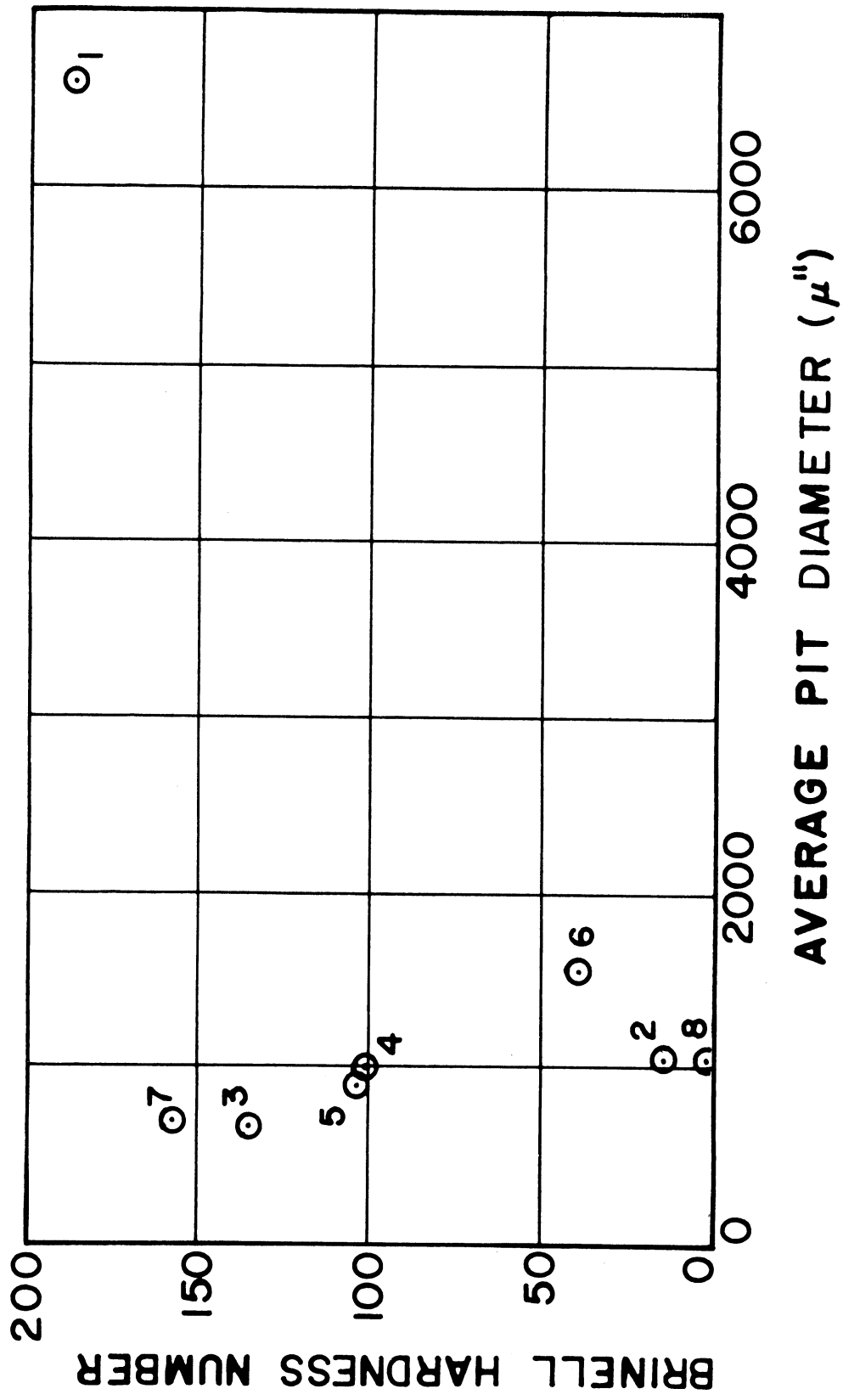

2145

Fig. 157.--Average pit diameter vs. Brinell hardness number.

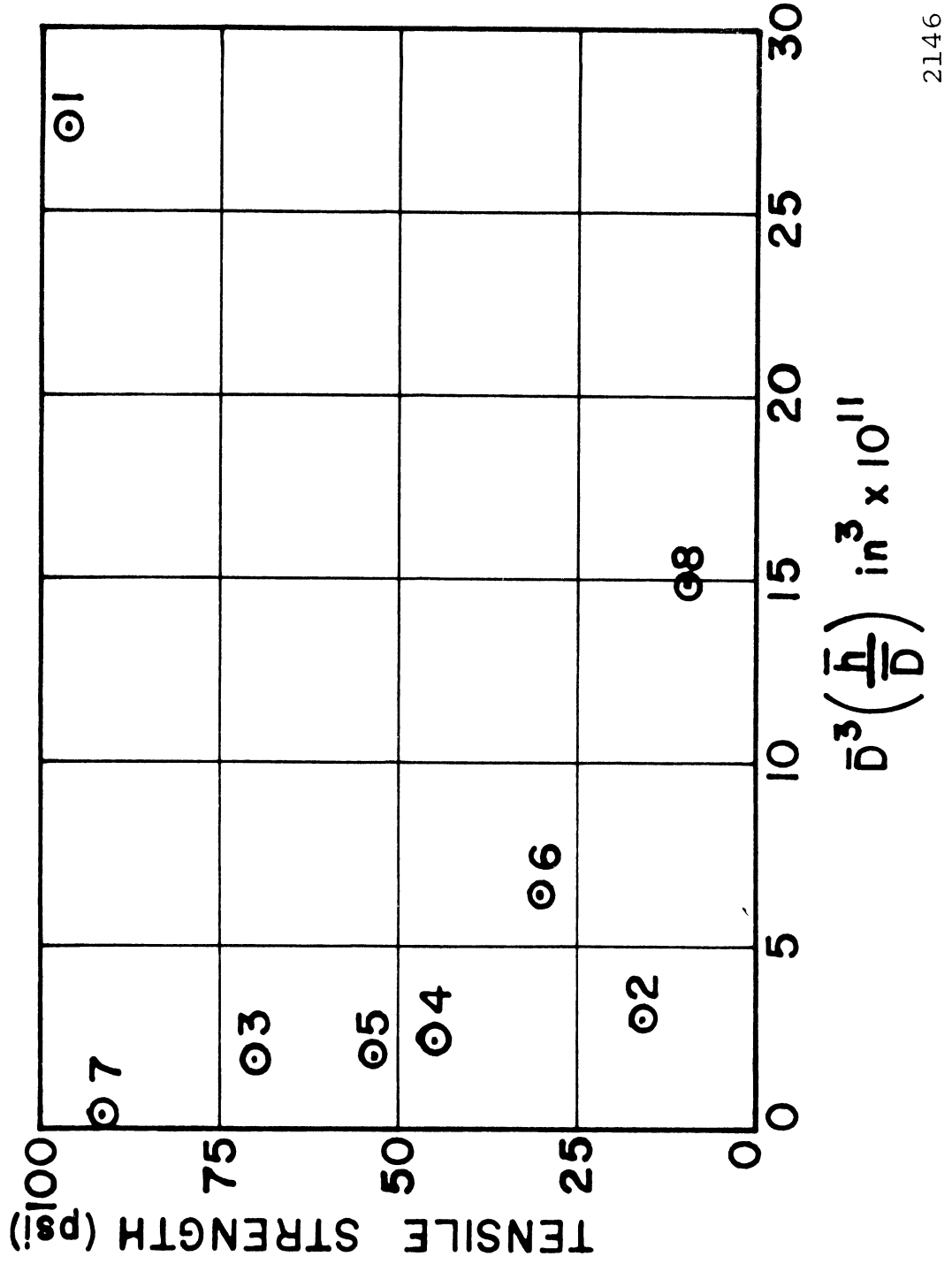

Fig. 158.--Average pit volume vs. tensile strength.

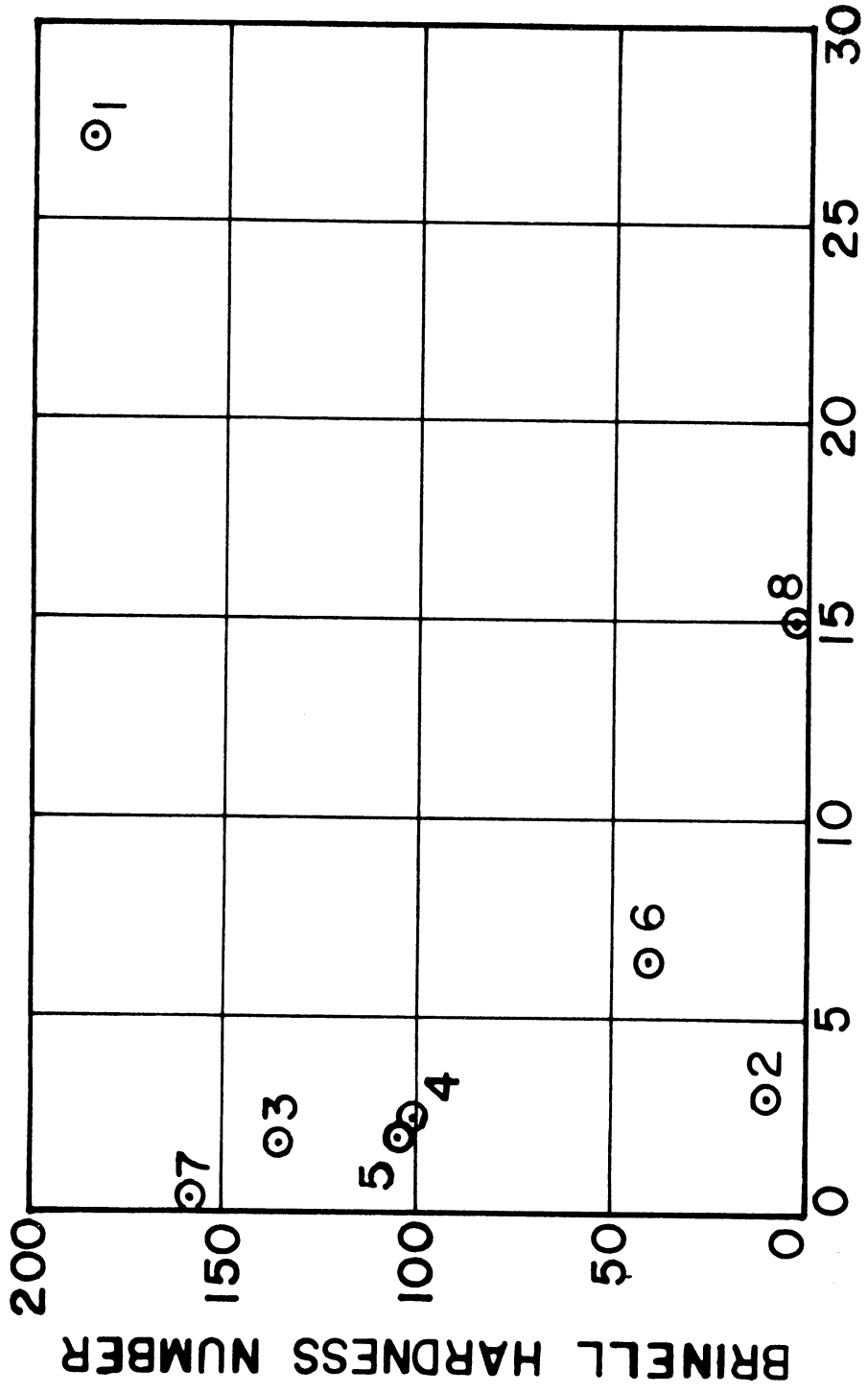

Fig. 159.--Average pit volume vs. Brinell hardness number.

The data points on the plots are numbered and correspond to specimen materials as follows:

1. Type 304 Stainless Steel
2. Type 1100-0 Aluminum
3. Type 2024-T351 Aluminum
4. Type 6061-T651 Aluminum
5. 60% C. W. Copper (As Rec'd)
6. Copper 900°F Annealed
7. 75% C. W. Nickel (As Rec'd)
8. Plexiglas

No good fit to the first three damage parameters listed above existed for any one of these mechanical properties. In general, correlation of bubbles/pit was the best if both stainless steel and Plexiglas were ignored. Ignoring stainless steel and Plexiglas, the number of bubbles to produce a pit increases (Fig. 147) with increasing tensile strength as would be expected, and the bubbles per pit decreases (Fig. 150) as the true strain energy increases which is not explainable. Considering stainless steel, but not Plexiglas, the bubbles per pit increase as true breaking stress increases (Fig. 151) as expected. Ignoring stainless steel and Plexiglas the bubbles per pit increase as the Brinell hardness, elastic modulus, and characteristic acoustic impedance increases (Figs. 152, 152, and 154 respectively).

The lack of any general and precise relationship between cavitation damage and the conventional mechanical

properties either singly or together, has been previously reported[7,8,9,10] by this laboratory, and it is felt that this is also the general consensus of researchers in this field. This is perhaps partially due to the fact that the surface loading which produces cavitation damage occurs in a highly transient manner, whereas the conventional mechanical properties are determined in a semi-static fashion. However, in a specific case it was demonstrated that a good correlation of cavitation damage with impact resistance, which itself involves failure under transient loading, also did not exist.[57]

While Plexiglas showed little pitting in times less than one minute, general heavy erosion occurred after five minutes, a type of failure that has not been noted on the metals.[7,8,9] This points out the fact that various types of materials fail in different ways, further indicating the unlikelihood of finding a precise, general correlation between cavitation damage and the conventional mechanical properties of materials, even assuming the use of a single test fluid and identical cavitation conditions.

Figs. 156 and 157 show plots of average pit diameters ($\bar{D}$) for the specimens vs. the tensile strength and the Brinell hardness respectively. Excepting type 304 stainless steel which is distant from any other points on both plots, but including Plexiglas, the trend is linear with a slight increase in $\bar{D}$ as the tensile strength decreases. $\bar{D}$ for stainless steel is approximately four times that of the others.

Figs. 158 and 159 show plots of average pit volume, $V \cong \bar{D}^3 \frac{(\bar{h})}{(\bar{D})}$ where $\bar{h}$ is the average pit depth, vs. the tensile strength and the Brinell hardness respectively. With the exception of stainless steel which is located far from the other data, but again including Plexiglas, there is a reasonably good trend showing a decrease in pit volume as both tensile strength and hardness increase.

N. Possible Damage Mechanisms

On the basis of the photographic studies that are included, it is felt that the normal collapse mode for a cavitation bubble is an asymmetrical collapse where perhaps through the action of an asymmetrical pressure distribution, the bubble involutes, the direction being dependent on perturbations of the bubble surface (doubtlessly greatly influenced by the form of the asymmetrical pressure distribution), forming a vortex or torus, and then producing a micro-jet.[16,17] This can be understood by examining Fig. 160 which is from an experiment by Ellis[30] where bubbles were formed by boiling water at a reduced pressure and subsequently collapsing them by admitting air at atmospheric pressure to the surface of the water. The photographs were made at 33,000 frames per second so that the entire sequence consumes approximately 1/2 millisecond. In frame no. 13 of the sequence, the bubble sides are collapsing so that a jet will be extruded through

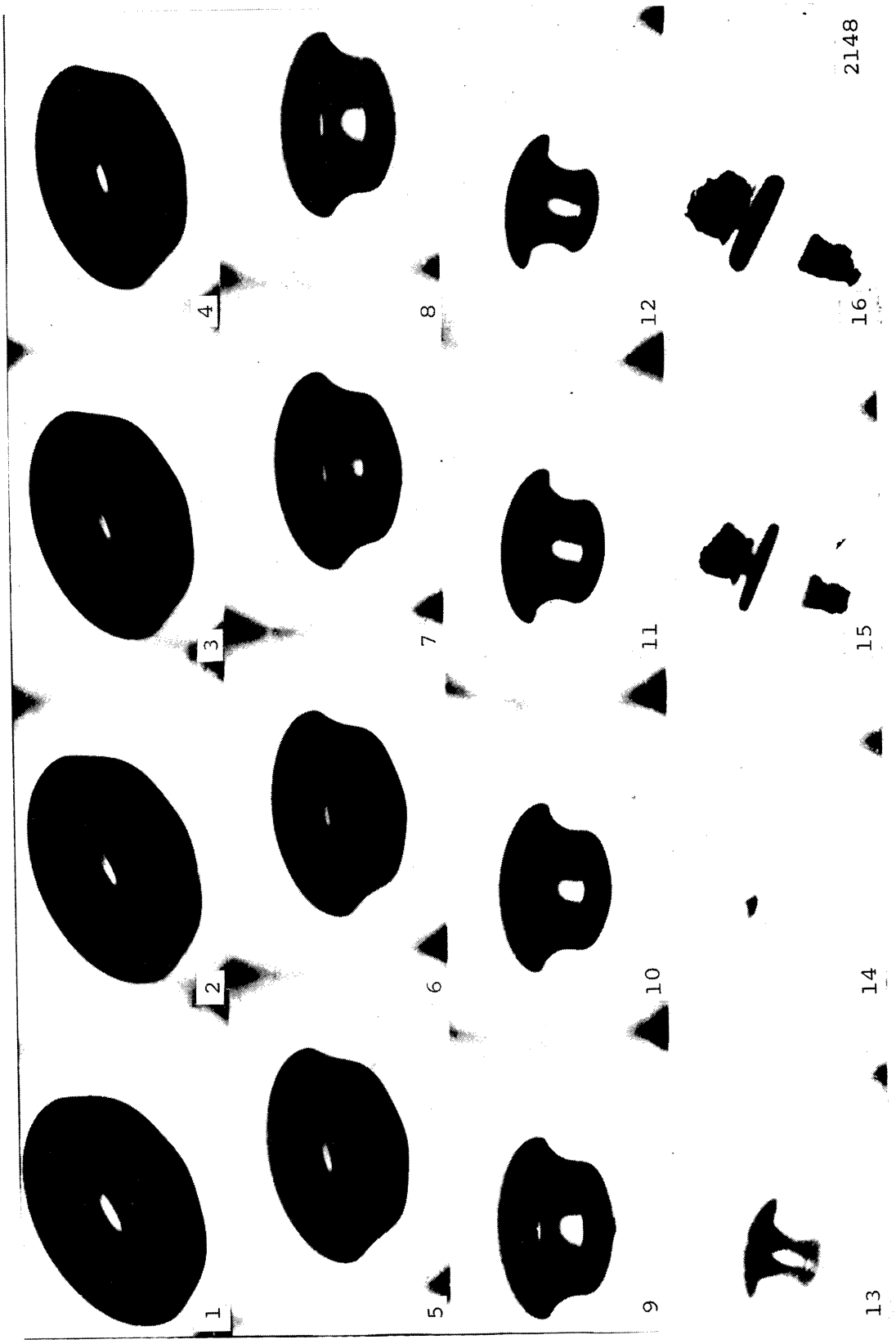

Fig. 160.--High speed photographs by Ellis[30] showing collapse sequence of bubbles formed by boiling water at reduced pressure, photographed at 33,000 fps.

the large flattened face. The jet appears at the final collapse in frame no. 14. In this frame, the torus and another separated section of the bubble on the opposite side of the torus from the jet are both barely visible. A rebound of this conglomeration occurs coincident with the arresting of the jet in the water. The energy for such a rebound can be stored in the vapor or gas within the "voids," in the elasticity of the water, and/or in the centrifugal field of the torus which is presumably a closed-end ring-vortex similar to a "smoke ring." The rebounding torus and the two additional separated sections of the bubble can be seen in frames no. 15 and 16. If the microjet had struck an adjacent surface rather than dissipating its energy in the water, presumably the familiar pit type of damage could have resulted.

A model is constructed, Fig. 161-A, which describes the collapse and rebound of a spherically symmetrical bubble in a fluid adjacent to or on a solid surface. When possible, high speed photographs of the bubbles in the various stages of collapse and rebound corresponding to the particular sequence in the model will be shown.

Through the apparent action of the acoustic pressure field, the once spherical bubbles assume a bar-bell type of appearance at the start of their collapse mode (Fig. 161-A-1). The ends of the bar-bell become unequal in volume in A-2. In A-3 the difference in diameters between the ends of the bar-bell is more pronounced and the bubble sides are

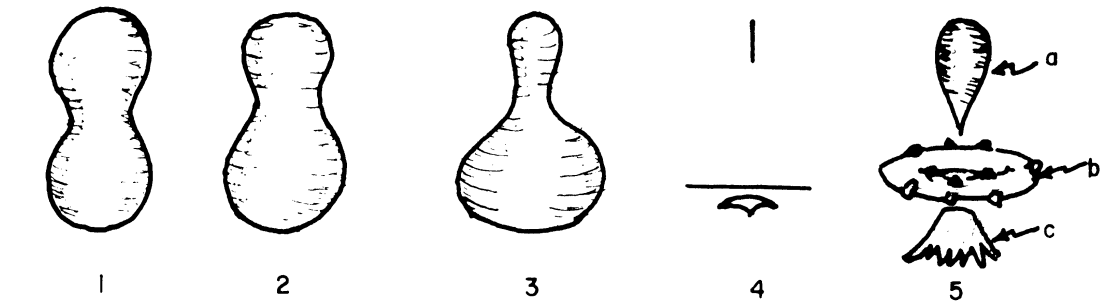

MODEL A

COLLAPSE & REBOUND OF A SPHERICALLY SYMMETRICAL BUBBLE IN A FLUID ADJACENT TO OR ON THE SURFACE

a. Pinched-off section
b. Torus
c. Jet

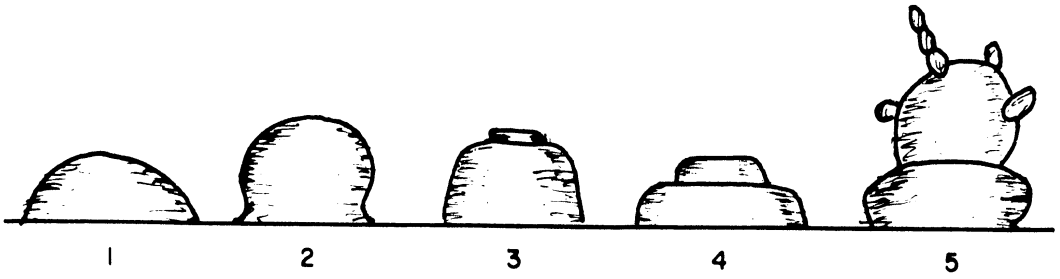

MODEL B

COLLAPSE & REBOUND OF A HEMISPHERICAL BUBBLE ON A FLAT SURFACE

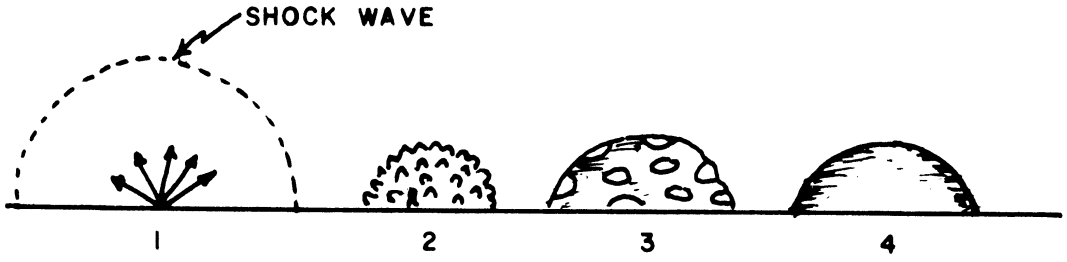

MODEL C

COLLAPSE OF A TRANSIENT BUBBLE AND REBOUND TO A HEMISPHERICAL BUBBLE

2149

Fig. 161.--A, B, and C.--Drawings of: A, Model for collapse and rebound of a spherically symmetrical bubble in a fluid adjacent to or on the surface; B, Model for collapse and rebound of a hemispherical bubble on a flat surface; C, Model for collapse of a bubble adjacent to a surface and subsequent rebound to form a hemispherical bubble.

collapsing. The involution into a torus is the next step as in A-4 where the jet has already been extruded. At this point, both the torus and the pinched-off section opposite the jet (formerly the smaller end of the bar-bell) are compressed to very small volumes. In A-5, the torus, the pinched-off section, and the bubble mass formed during the arresting of the jet in the water, all rebound.

Figs. 162, 163, 164, and 165 from this study show the bar-bell bubbles as in the model, Fig. 161-A-1 and 2. All four of these high speed photographs were from a run using a type 304 stainless steel specimen with the oscillator set at 20,300 cps and the camera operating at 26,000 frames per second. At this camera speed the exposure time per frame was 1 μ second. In Fig. 162 almost all of the transient bubbles are of the bar-bell type. Examples are Nos. 3, 4, 5, and 6 which are all indicated on the photograph, although close examination indicates many more of this type. Note that the major axis of the bar-bell almost always appears to be perpendicular to the specimen surface. This suggests that the existence of this type of bubble may indeed be due to the time-varying acoustic pressure and velocity induced by the vibration of the horn, since the major axis of the bar-bell is usually parallel to the direction of vibration. Figs. 163, 164 and 165 also show the acoustic bubbles in the bar-bell mode where typical examples are marked "X." Many additional similar configurations can be seen on close examination.

Fig. 162.--High speed photograph (15X) of a partially polished, partially abrased, type 304 stainless steel specimen in water, frequency 20,300 cps, amplitude approximately 2 mils, exposure time per frame of 1 μ second, photographed at 26,000 fps.

Fig. 163.--High speed photograph (15X) of a partially polished, partially abrased, type 304 stainless steel specimen in water, frequency 20,300 cps, amplitude approximately 2 mils, exposure time per frame of 1 μ second, photographed at 26,000 fps.

Fig. 164.--High speed photograph (15X) of a partially polished, partially abrased, type 304 stainless steel specimen in water, frequency 20,300 cps, amplitude approximately 2 mils, exposure time per frame of 1 μ second, photographed at 26,000 fps.

Fig. 165.--High speed photograph (15X) of a partially polished, partially abrased, type 304 stainless steel specimen in water, frequency 20,300 cps, amplitude approximately 2 mils, exposure time per frame of 1 μsecond, photographed at 26,000 fps.

The arrow and "X" in Fig. 163, e.g., indicates a bar-bell as in model A-2 with the larger diameter section of the bar-bell apparently resting on the specimen surface. Many other similar bubble configurations are evident in this figure also. One extremely interesting feature is that each bubble of the bar-bell when in the A-1 mode is approximately as large as the typical single transient bubble that is noted before the collapse sequence begins. The bar-bell-like bubble is then apparently at the point of maximum expansion.

The next part of the collapse model (A-3) where one end of the bar-bell becomes considerably larger than the other is typified by Fig. 166-A, where the smaller parts of the bubbles appear to be uniformly closer to the surface for all the bar-bell bubbles that can be seen. One typical configuration is marked by an arrow. This was from a run using a type 304 stainless steel specimen with the frequency set at 20,000 cps and the camera operating at 26,000 frames per second. In this case the resultant jet would apparently be directed normal to and away from the specimen surface. The bubble to the left in Fig. 167-D is similarly constructed, but in this case the jet would be directed toward the surface. Note the rings on the larger bubble of this bar-bell. Figs. 167-B through E were from a run using a type 304 stainless steel specimen tilted slightly towards the camera with the frequency set at 20,300 cps and the camera was operated at 26,000 frames per second. The non-symmetrical bar-bell-like bubbles (one end smaller) are also shown in Figs. 167-H, V and X.

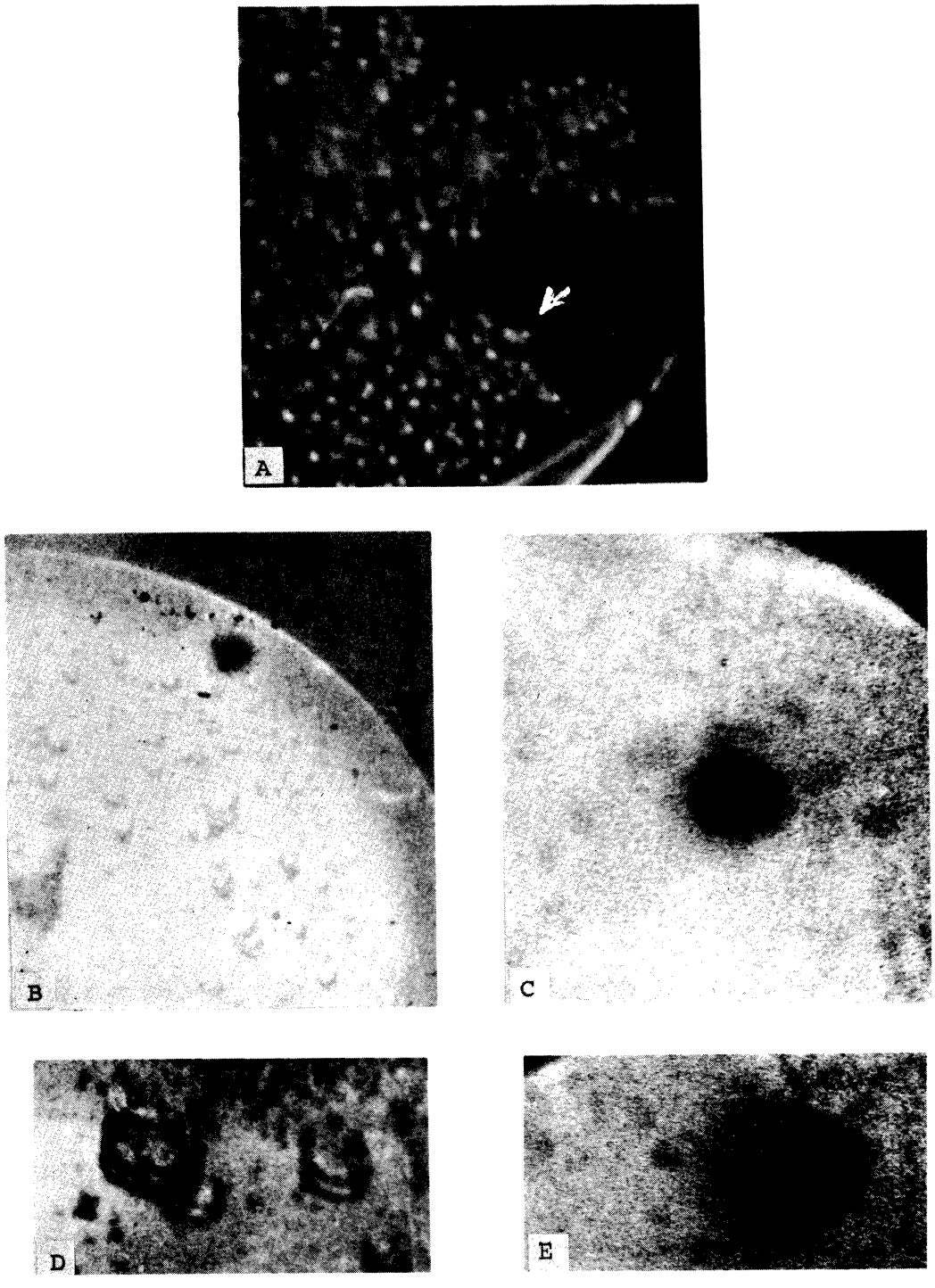

Fig. 166.--High speed photographs (14X), A through H, not in sequence, of: A, a type 304 stainless steel specimen in water, frequency 10,000 cps, exposure time per frame 1μ second, photographed at 26,000 fps; B, a type 2024-T351 aluminum specimen in water, frequency 20,195 cps, amplitude approximately 2 mils, exposure time per frame 1.3 μ seconds, photographed at 20,200 fps; C and E, a 75% c. w. nickel (as rec'd) specimen in water, frequency 20,454 cps, amplitude approximately 2 mils, exposure time per frame 1.3 μ seconds, photographed at 20,470 fps; D, F, G, and H, a type 304 stainless steel specimen in water, frequency 20,300 cps, amplitude approximately 2 mils, exposure time per frame of 1μ second, photographed at 26,000 fps.

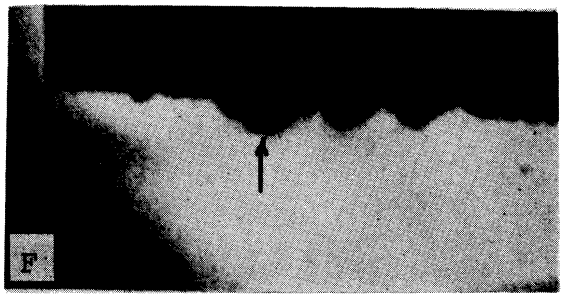

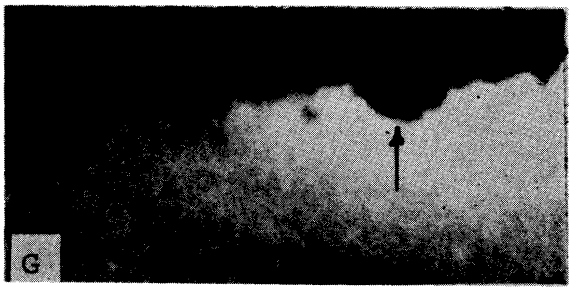

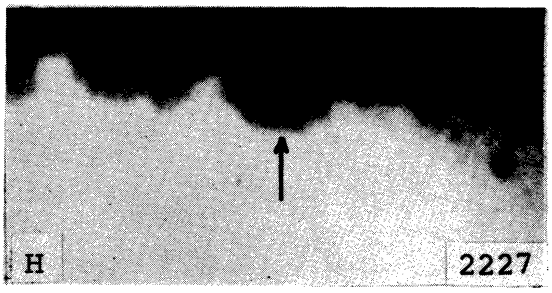

Fig. 166.--Continued

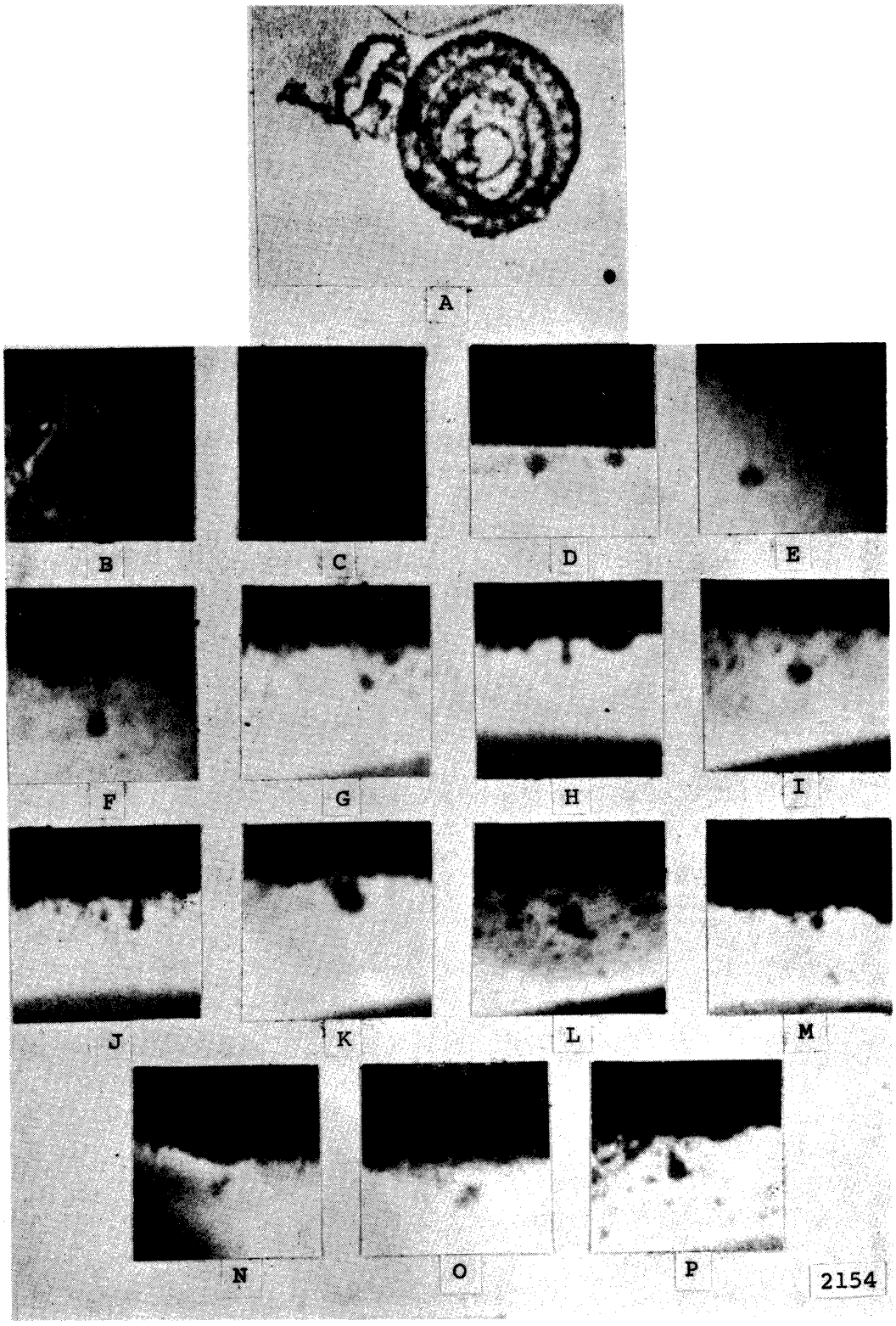

Fig. 167.--High speed photographic sections, A through X, not in sequence, of a type 304 stainless steel specimen in water, frequency 20,300 cps, amplitude approximately 2 mils: A, (30X) exposure time per frame 1.3 μ seconds, photographed at 20,800 fps; B through E, (15X), F through X, (11X), exposure time per frame 1 μ second, photographed at 26,000 fps.

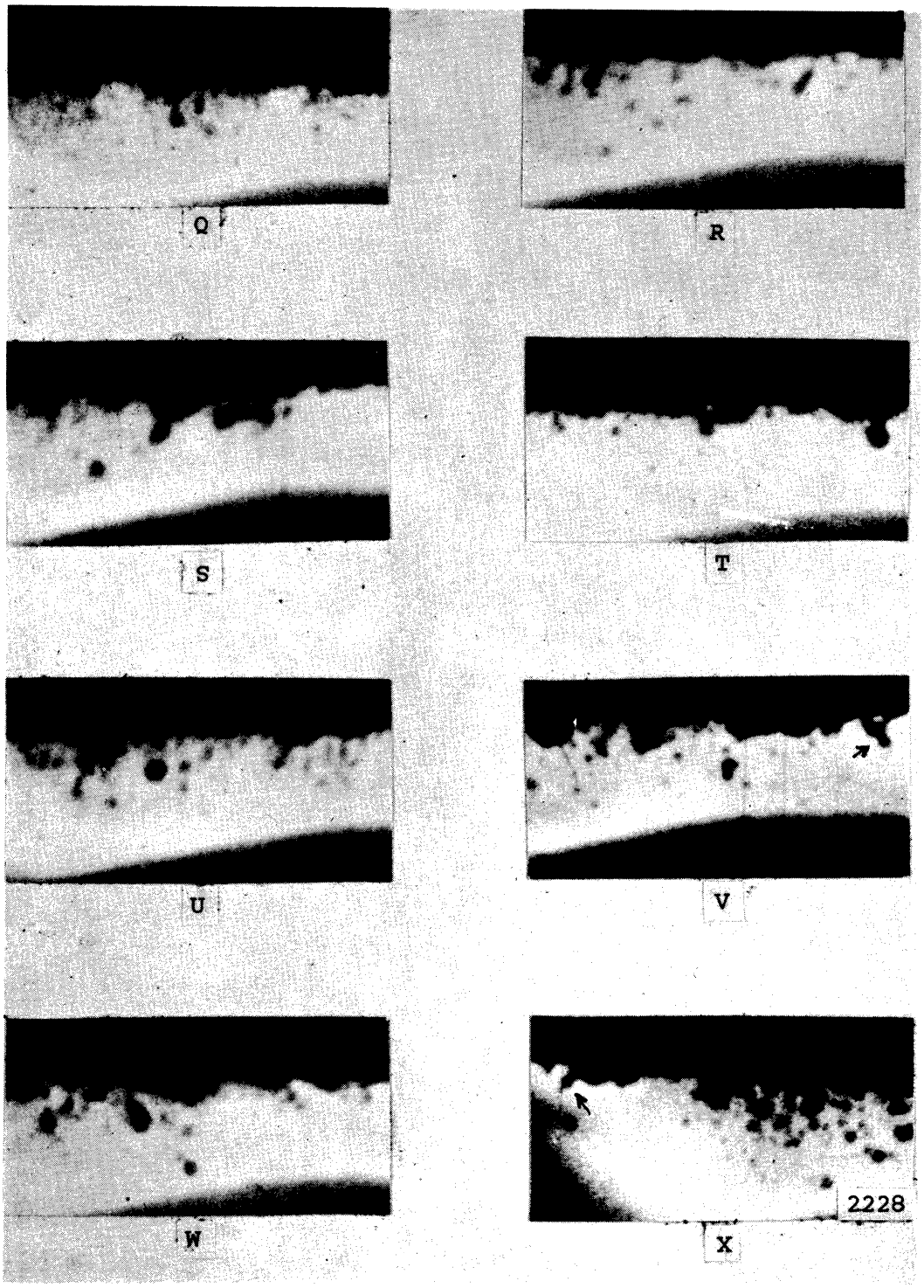

Fig. 167.--Continued

Figs. 167-F through X were from a similar run to that for Figs. 167-B through E, but they were profile shots. Fig. 167-H shows a bubble at the center of the specimen with the smaller top visible. It is situated next to a hemispherical bubble. Here again the jet would be directed toward the surface of the specimen. Figs. 167-V and X show the bar-bell bubble (both indicated by arrows), but it is situated away from the specimen surface and angled toward it. Interestingly enough, none have been noted at an angle when either section of the bar-bell is resting directly on the specimen surface.

No photographic image of the jet at its minimum diameter point as in A-4 of the model and as Fig. 160-14 from Ellis's[30] sequence, was found in the thousands of high speed photographs that were studied, but the peculiar and characteristic shape of the bubble just prior to jet formation and also a hint of the existence of the separated (pinched off) part of the bubble was noticed in a high speed photographic sequence made at 7,600 frames per second with exposures at 1 μsecond in this laboratory using a cavitating venturi and reported by Mitchell, Kling, and Hammitt.[61] Figs. 168-A through C show a bubble near a wedge: in A in an apparent toroidal collapse; in B the formation of the jet tip as in Fig. 160-14 is seen; in C the rebound occurs. This phase of the bubble collapse perhaps exists for only a fraction of a microsecond. Hence the lack of the obtaining of a photographic image in a random time-sampling such as used is not surprising.

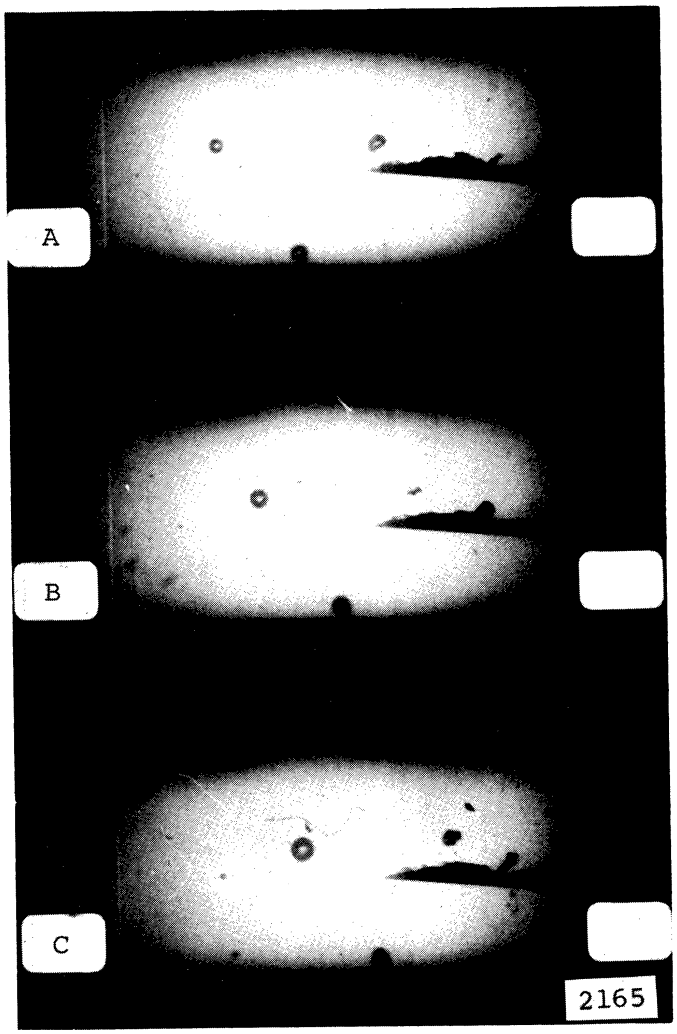

Fig. 168.--High speed photographic sequence[61] (2X), A through C, showing cavitation near a wedge in a venturi, exposure time per frame of 1 μsecond, photographed at 7,600 fps.

Numerous photographs of the rebounded sections of the bubble (A-5 of the model) exist. The best example of this is Fig. 167-A which is from a run using a type 304 stainless steel specimen with the frequency set at 20,300 cps and the camera operating at 20,800 frames per second. This is the same photograph as Fig. 35-K, Section D of this Chapter, but it is (30X) instead of (16X) so that the details of the apparent rebound can be studied. Smaller bubbles or at least hemispherical roughness appear to be attached to all sections of the torus. Their existence is not readily explained. The rebound of the conglomeration of bubbles caused by the jet impacting the surface or by its energy being dissipated in the water is also evident. The third, or pinched-off section (which would be at the lower right) does not appear in this photograph.

The micro-jet passing through the water must cause considerable local cavitation, which then presumably rebounds into the irregular mass that often appears as the jet is arrested. The diverging shape of this mass also suggests the form of a free jet in a quiescent fluid. Similar rebounds are shown in Figs. 167-B, C, E through G, I through U, and W. The toroidal shape is often evident and suggestions of jets are seen in many cases. N and O show rebounds of the pinched-off section of the bubble and the volume around the arrested jet, but the torus cannot be seen. All three segments can be seen in P on the large bubble below the specimen surface.

In the background the smaller bubbles have a similar appearance. In fact, in a number of photographs where hundreds of bubbles are seen off of the surface, the toroidal rebound shapes are the only ones that are present. Unfortunately these shapes are so faint on the original photographs that they cannot be reproduced satisfactorily for inclusion. The bubble in W, which is furthest from the surface, shows the rebound of the pinched-off small section of the bubble and the fanned-out jet conglomeration. The torus is not visible. A pinched-off top that rebounded is also evident in Fig. 49-B (indicated by arrow).

A second series of drawings shown in Fig. 161-B suggests a model for the incomplete collapse and subsequent rebound from this incomplete collapse of a hemispherical bubble resting on the surface. These large bubbles have often been mentioned in cavitation literature and it has been generally noted that they do not collapse.[28] In this investigation it has been noted that they may exist from 3 to 50 or more acoustic cycles, but eventually disappear, probably after a final collapse. B-1 shows the hemisphere on the surface. B-2 shows a shape similar to a helmet (this shape is often noted in cavitating venturi tests during the collapse sequence[20,21,22]); in B-3 the bubble assumes a more cylindrical shape with a small button on the top. These parts of the sequence are identical with those shown by Shutler and Mesler[23] for the collapse sequence of a single, spark-induced bubble. Apparently because

of proximity to the surface or because the bubble's required collapse time is too long, the jet does not develop sufficiently to complete the collapse through the torus, but apparently scatters back through the torus forming a large bubble that is seated on the rebounded torus. Instabilities during the rebound or collapse could probably cause the protuberances so often seen on bubbles after an apparent rebound. The weak jet hitting the surface could also be deflected in such a manner that it could cause additional local secondary cavitation which could appear as strings of bubbles attached or adjacent to the rebounded bubble. Engel[62] has concluded that for a rain drop striking a hard surface radial flow velocities up to eight times that of the impinging velocity could occur, since the pressure in the impact area approximates the "water hammer" pressure rather than conventional stagnation pressure. Thus even for a relatively weak jet the resultant scattered or deflected jets could obtain sufficiently high velocities to cause secondary cavitation.

There are many high speed photographs showing hemispheres as in Fig. 161-B-1 (Figs. 44-B and 47-B for example). The helmet-like bubble of B-2 is also visible in many photographs as typified by Fig. 53-B (as indicated by an arrow). The bubble off the surface shown in Fig. 45-H also shows this peculiar shape.

B-3 of the model is typified by the bubble at the right in Fig. 51-B. Apparently this is precisely at the time before

collapse. The corrugation seen in this photograph and the similar ones on the bar-bell bubble in Fig. 167-D are interesting, but unexplainable at the present.

B-4, believed to occur at the instant when the weak jet has been arrested at the surface and the bubble is rebounding is typified by Figs. 166-F, G, and H, which were from a run using a type 304 stainless steel specimen tilted slightly toward the camera with the frequency at 20,300 cps and the camera operated at 26,000 frames per second.

The full rebound as in B-5 causes shapes as shown in Figs. 162 and 166-D. Bubble No. 2 in Fig. 162 is typical of the larger rebounding types. An unusual bubble, No. 1,Fig. 162, appears to include "strings" due to symmetrically diverted jets, which were made visible by secondary cavitation.

These bubbles often persist for many cycles as previously mentioned, but sometimes collapse completely or disintegrate during rebound, so that they have disappeared from subsequent photographs.

A third model is suggested, Fig. 161-C, in an effort to explain the rapid growth of newly rebounding bubbles and to possibly explain the actual damaging mechanism. C-1 shows the hemispherically-symmetrical scattering of the micro-jet from a spherical bubble collapse, which may occur through an ideal combination of circumstances involving energy of the jet, proximity of the surface, condition of the surface, etc. (e.g. a previous pit may provide suitable guidance). These

scattered jets, which as mentioned previously may possess velocities considerably in excess of the original impinging jet and could cause localized secondary cavitation as they pass through the liquid. The collapse and rebound of the bubbles in the wake of the scattered jets could cause the localized overpressure or shock that is usually evident during and after bubble rebound. The high pressure region that exists around the rebounding bubbles could persist until the scattered jets are arrested and the collapses and rebounds from the secondary cavitation ceases. The rebounding conglomeration probably includes the torus and the pinched off section of the collapsing bubble, both of which could have been shattered by the scattered jets.

This mass, as in C-2, takes on a spiny appearance. As previously discussed, it reflects little light in the type of photography such as has been used which is dependent on reflected light for film exposure. Thus the rebounding bubbles appear very dark on the photographic print ("charcoal smudges"). In C-3 the bubble rebounds to its full size, but the surface is very rough. In C-4, after fully rebounding or possibly after oscillating in the acoustic field, the bubble is smooth and lustrous.

Fig. 166-B is from an experimental run using a type 2024-T351 aluminum specimen with the horn frequency at 20,195 cps and the camera set at 20,200 frames per second. Figs. 166-C and E are from a different photographic run made using

a 75% c. w. nickel (as rec'd) specimen with a horn frequency of 20,454 cps and the camera set at 20,470 frames per second. It is postulated that Figs. 166-B and C correspond to C-2 of the model, possibly as the hemispherically-symmetrical scattered jet or less likely, debris from the specimen surface are causing secondary cavitation. Fig. 166-E probably corresponds to C-3 as the rebound is further developed. The examples of the smooth hemisphere as in C-4 have been previously given.

The author feels intuitively that the only damaging types of collapses are from spherical bubbles on the surface or immediately adjacent to it and that the predominant damaging mechanism in the vibratory horn cavitation regime is the micro-jet from the toroidal collapse. According to the present photographic study it appears to be the only prevalent collapse mode. The pressure pulses arising from collapse and rebound of the bubble sections remaining after a toroidal collapse are very likely too weak to be damaging. A portion of the collapse energy is used in forming the jet and imparting vorticity to the torus, assuming the normal dissipative processes applicable to "real" fluids. The energy of the jet itself is then dissipated on the specimen surface or in the water. In an ordinary rebound from a spherical collapse as in the model shown in Fig. 161-A, the bubble apparently rebounds into three fragments: the torus, the section of the bubble

opposite to the jet which is pinched off, and the accumulation of secondary cavitation around the jet. These non-spherical fragments are probably highly unstable and quickly disappear during the next positive pressure cycle. This has been confirmed by the previously mentioned instability (i.e., impermanence) of the tear-dropped shaped bubble which is apparently the rebounded-pinched off section.

Since the bar-bell bubble on the surface is noted always with its major axis normal to the surface, those micro-jets that are directed to the surface should impinge normally and the crater of the pits should have a symmetrically raised rim. Only symmetrical rims exist, although the rim is very small. This normal impingement could also explain the consistent symmetry of the rapid expanding rebounding bubbles that probably originate from a spherically-symmetric collapsing bubble (model 161-C).

Typically, two to five rebounded bubbles of the type described in the model shown in Fig. 161-C have been observed in each cycle. Assuming an average number of 3.5 rebounds per cycle and a 30 second run at 20,000 cps for illustrative purposes, the specimen would be exposed to 2×10^6 such collapses. For such an exposure less than 100,000 pits have been detected, even for one of the softest materials used, type 1100-0 aluminum. However, few rebounds are as massive as those typified by Figs. 166-B, C, and E. These occur roughly twice an experimental run which usually includes a sequence of 117

photographic frames. Then there would be approximately 10,000 such events for a 30 second run, which is considerably less than the number of pits observed in soft material during such a run. Thus, if the rebounding bubbles indeed cause most of the damage, both the massive and the smaller ones must be involved.

CHAPTER V

CONCLUSIONS

Some of the more important conclusions are summarized below.

A. Cavitation Bubble Fields

High speed photographic techniques were developed to photograph an ultrasonically-induced cavitation field using profile and reflective lighting. Exploration of various parts of the acoustic cycle was done photographically by advancing the camera speed at a known rate slightly greater than the horn frequency.

A comprehensive high-speed photographic study of the bubbles that make up the ultrasonically-induced cavitation bubble field has been made at four different frequencies.

Photographic proof of Noltingk and Neppiras's[41,42] theories that most bubbles in a cavitation field are expanded and collapsed in one acoustic cycle was obtained. The existence of resonant bubbles was not clearly established, possibly because the available nuclei in the water that was being used were less than that diameter required for resonance at the various frequencies. The existence for more than one cycle of bubbles larger than the resonant size was noted.

The transient cavitation bubble is approximately spherical except during its collapse. Larger bubbles, which appear to result from a violent expansion (or rebound) after the collapse of a spherical bubble often have surface protuberances. These bubbles may persist for many cycles.

A spectrum of cavitation bubble field sizes exists with the predominant size being the smallest which could be observed. It is believed that the shock rings sometimes noticeable around rebounding bubbles greatly inhibit the population of transient bubbles in the vicinity of this overpressure.

The bubble population varies throughout the acoustic cycle. There are portions of the cycle where the only detectable bubbles are very large. These are believed to be rebounding from collapses.

B. Possible Collapse Modes

Three models were hypothesized and high speed photographs presented as partial substantiation of their existence. These models are:

1) The collapse of a spherically-symmetrical bubble adjacent to or on the specimen surface. The bubble assumes a bar-bell shape, and then completes a toroidal collapse forming a high-speed central jet. A rebound results in three distinct sections, the torus, the arrested jet, and the pinched-off small

section of the bar-bell bubble. The arrested jet section is believed to be made visible by the local secondary cavitation which it generates.

2) The asymmetrical collapse of a hemispherically-shaped bubble on the specimen surface. A central jet develops, but may not reach its fully mature velocity because of proximity to the surface or because its collapse time is too long to be completed before the start of the negative pressure portion of the cycle. In many cases portions of the jet appear to scatter back through the torus. The mass rebounds into one large, often grotesquely-shaped bubble, which has the appearance of a large spherical bubble attached to the rebounded torus. Strings of bubbles on, or adjacent to the rebounded bubble mass are believed due to secondary cavitation caused by the scattered jets.

3) The collapse of a bubble adjacent to the specimen surface and subsequent rebound to form a hemispherical bubble. Due to optimum and highly selective conditions the jet from a toroidal collapse strikes the specimen surface so that the impinging jet is scattered in a hemispherically-symmetrical manner, resulting in substantial secondary cavitation. Collapse of the secondary cavitation causes a shock which causes noticeable circular areas which are free of bubbles surrounding the rebounding bubbles. The collapse

axis always appears normal to the surface for surface bubbles and may be in either direction.

If the normal collapse mode in ultrasonically-induced cavitation is toroidal, as this study appears to show, then those investigations which have assumed the symmetrical Rayleigh[18] type collapse model incur an error both in collapse time and predicted pressure pulse from the collapse and rebound.

For the toroidal-type collapse, a portion of the collapse energy is consumed in extruding the jet and imparting vorticity to the torus. The energy of the jet is dissipated in the water or by impacting the surface. The non-spherical rebounding sections appear to be highly unstable in that they do not persist generally for more than one cycle. The damage capability from the rebound of such a non-symmetrical mass appears to be small.

C. Cavitation Damage

The author believes that the only important damaging mechanism is the high speed micro-jet that evolves from the toroidal collapse of a bubble that is adjacent to, or on, the specimen surface. The jets from the asymmetrical collapse of the hemispherically-shaped bubbles are not believed to be damaging in these tests since there does not appear to be time or space for the jet to develop to its full velocity. The possibility exists that the massive rebounds themselves occur coincidental with the type of micro-jet impingement that could result in damage.

The rims of the damage pits are small but symmetrical, suggesting that impingement is normal to the specimen surface. The pits resemble those incurred in cavitating venturi tests.[10]

Individual pits appear to be, due to their symmetry, the result of a single impact. This is most noticeable on soft foils.

A pit size spectrum has been measured for all of the eight specimens tested. These spectra are quite similar, showing an increasing number of pits as the pit diameter decreases. Most of the bubbles had diameters < 0.02 cm, while most of the pits had diameters < 0.0002 cm. This 100:1 ratio between bubble and pit diameter again suggests that damage is due to an impinging micro-jet rather than to a spherical shock front originating at a distance from the surface of the order of the maximum bubble radius.

The existence of an edge ring vortex, around the specimen which was detected photographically, may explain the lack of damage on the edge annulus which is so often noticed on exposed specimens.

Visible indications of cavitation damage were noticed after approximately five seconds of exposure on all specimens. Pit damage ranged up to approximately 100,000 pits for maximum exposures of 60 seconds and significant weight losses occurred, proving that no significant incubation period exists for the formation of pits or the accruing of a measurable weight loss.

D. Rating of Specimens

The specimens were rated according to decreasing MDPR (Mean Depth of Penetration Rate), depth to diameter ratio, and reciprocal bubbles/pit. In general, the rankings were similar to those obtained in other vibratory[7] and cavitating venturi tests[10] in this laboratory, but in a direct comparison to the vibratory tests[7] where materials from the same bar or strip stock were used for both investigations, it was found that the "early damage" rates measured in this investigation were strikingly higher for some of the specimens than those obtained for the longer period.

Comparing bubble patterns for all specimens, it was found that some specimens see far more bubbles during a given test period than others. These differences may be due to differences in acoustic impedance ratios between specimen and cavitating fluid. Hence any rating of materials should ideally take into account the differing bubble populations.

There are approximately 10^4 to 10^5 bubbles growing and collapsing adjacent to a specimen required to cause a pit, showing that damage is indeed a highly selective occurrence. Plexiglas required approximately 5×10^6 bubbles to cause one pit in a 30 second run, but the pits were very much larger than those occurring in the metallic specimens. However, extremely heavy damage occurred after an additional five minute run, showing general failure, and also emphasizing

that different materials fail under cavitation attack in different modes.

E. Correlation to Mechanical Properties

An attempt was made to correlate MDPR, depth to diameter ratio and bubbles/pit to nine different mechanical properties.[56,57] No real fit existed, but bubbles/pit showed the best fit if both stainless steel and Plexiglas were ignored.

F. General Conclusion

The use of the vibratory facility to rate materials for cavitation resistance faces limitations in that the rating of materials is strongly dependent on the bubble population, and any changes that occur in this population due to surface damage brought on by multiple pitting damage, etc., must be considered when ranking materials for resistance to cavitation.

It is of paramount importance that a tight mechanical bond between specimen and horn be established and maintained throughout the test period since this greatly affects the bubble pattern and population.

While minor frequency differences ($\sim$2%) used for different specimens do not make important bubble population changes, careful attention should be given to amplitude settings where it is more difficult to attain relative precision, and where the effect of small changes may be greater.

The same physical positioning, far from bounding surfaces, should be used for testing all specimens so as to avoid any change in overall flow patterns.

By exercising great care and the use of a high-precision balance it is possible to rank specimens for resistance to cavitation damage for exposure times less than one minute. It is also possible to correct these ratings for differences in bubble population if high-speed photographic equipment is available.

APPENDIX "A"

DETAILED RESULTS OF PIT COUNTING

The pits have been classified as follows:

		Pit Diameter in Cm.
VVL	(Very, very large)	VVL $>$ 0.0120
VL	(Very large)	0.0120 $>$ VL $>$ 0.0034
L	(Large)	0.0034 $>$ L $>$ 0.0010
S	(Small)	0.0010 $>$ S

Extimates of the S pits were obtained by selecting areas of approximately uniform pit density, then multiplying the pit density by the area. The respective sketches show the various areas. The diameters are in cm. The O.D. of the specimen is 1.39 cm.

1) Type 304 Stainless Steel (First Run)

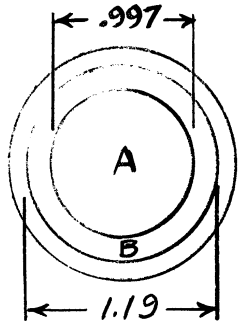

Area	Pits/cm^2	Pits
A	40,000	31,200
B	88,000	30,800

Pit Size Distribution	
VVL	= 1
VL	= 3
L	= 15
S	$\tilde{=}$ 62,000
Total	$\tilde{=}$ 62,000

2) Type 1100-0 Aluminum

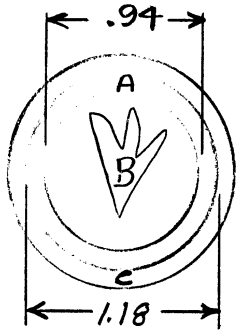

Area	Pits/cm^2	Pits
A	120,000	38,400
B	79,000	3,950
C	50,000	29,450

Pit Size Distribution

VVL = 3
VL = 3
L = 75
S $\cong$ 71,800

Total $\cong$ 71,900

3) Type 2024-T351 Aluminum

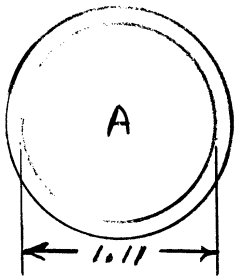

Area	Pits/cm^2	Pits
A	127,500	122,800

Pit Size Distribution

VVL = 4
VL = 22
L = 50
S $\cong$ 122,800

Total $\cong$ 122,900

4) Type 6061-T651 Aluminum

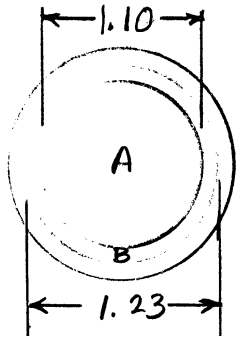

Area	Pits/cm^2	Pits
A	79,000	75,050
B	55,000	13,350

Pit Size Distribution

VVL = 1
VL = 9
L = 50
S $\cong$ 88,400

Total $\cong$ 88,500

5) 60% C.W. Copper (As Rec'd)

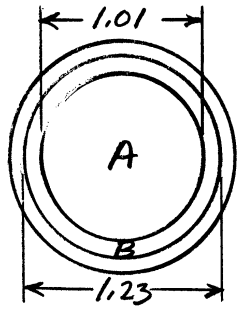

Area	Pits/cm^2	Pits
A	104,000	83,200
B	84,000	18,600

Pit Size Distribution

VVL = 3
VL = 7
L = 38
S $\cong$ 101,800
Total $\cong$ 101,900

6) Copper 900°F Annealed

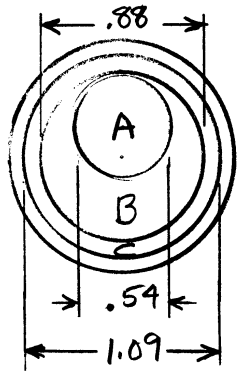

Area	Pits/cm^2	Pits
A	45,200	10,400
B	95,000	51,400
C	51,500	9,800

Pit Size Distribution

VVL = 4
VL = 7
L = 31
S $\cong$ 71,600
Total $\cong$ 71,700

7) 75% C.W. Nickel (As Rec'd)

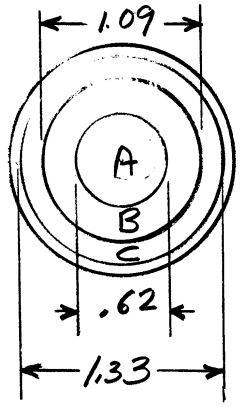

Area	Pits/cm^2	Pits
A	50,000	23,800
B	120,000	65,200
C	60,000	18,000

Pit Size Distribution

VVL = 3
VL = 4
L = 52
S $\cong$ 107,000
Total $\cong$ 107,100

8) Plexiglas

Pit Size Distribution

VVL = 0
VL = 3
L = 50
S = 60
Total = 113

9) Type 304 Stainless Steel (Second Run)

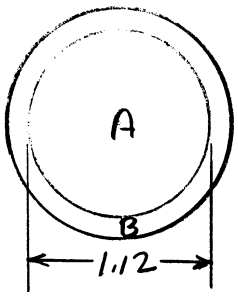

Area	Pits/cm^2	Pits
A	65,000	63,100
B	23,000	22,700

Pit Size Distribution

VVL = 0
VL = 16
L = 22
S $\cong$ 85,800

Total $\cong$ 85,800

APPENDIX "B"

NUMBER OF PITS IN SELECTED SIZE RANGES:
DATA FROM PHOTOMICROGRAPHS (500X)
IN AN AREA OF 0.000252 SQ. IN.

Diameter in cm X 10^4	0 to 2	2 to 4	4 to 6	6 to 8	8 to 10	>10
Material						
304 Stainless Steel	306	194	71	15	9	6
1100-0 Aluminum	445	149	53	15	8	7
204-T351 Aluminum	476	223	115	75	33	21
6061-T651 Aluminum	388	126	91	32	25	9
60% C.W. Copper (As Rec'd)	710	290	121	68	32	12
Copper 900°F Annealed	3124	192	120	62	20	17
75% C.W. Nickel (As Rec'd)	520	141	59	32	18	9

APPENDIX "C"

DEPTH TO DIAMETER RATIOS

1) Type 304 Stainless Steel (First Run)

Proficorder Trace	Depth (μ")	Diameter(")	Depth/Diameter
(#1)	10	0.0010	0.01000
	10	.0010	.01000
	7.5	.0010	.00750
	5	.0006	.00833
	7	.0007	.01000
	10	.0010	.01000
	10	.0015	.00666
	4	.0003	.00133
	10	.0015	.00666
	4	.0006	.00666
	5	.0007	.00714
	10	.0005	.02000
	5	.0005	.01000
	3	.0003	.01000
(#2)	12	.0010	.01200
	5	.0005	.01000
	7	.0007	.01000
	5	.0006	.00833
	4	.0008	.00500
	4	.0006	.00666
	5	.0005	.01000
	2	.0005	.00400
	5	.0007	.00714
	7	.0005	.01400
	5	.0007	.00714
	5	.0006	.00833
	8	.0008	.01000
	7	.0005	.01400
	7	.0005	.00714
	7	.0005	.01400

1) Type 304 Stainless Steel (First Run) continued

Proficorder Trace (#3)	Depth (μ")	Diameter(")	Depth/Diameter
	5	0.0004	0.01250
	6	.0003	.02000
	4	.0007	.00571
	10	.0010	.01000
	5	.0005	.01000
	10	.0012	.00833
	8	.0007	.01142
	2	.0003	.00666
	10	.0005	.02000
	7	.0008	.0875
	5	.0005	.01000
	3	.0002	.01500
	5	.0006	.00833
	3	.0003	.01000
	10	.0010	.01000

$\overline{\text{Depth}} = 6.2765\,\mu$"

$\overline{\text{Diameter}} = 0.00659$"

$\overline{\text{Depth}}/\overline{\text{Diameter}} = 0.009516$

Average (Depth/Diameter) = 0.009717

2) Type 1100-0 Aluminum

Proficorder Trace	Depth (μ")	Diameter (")	Depth/Diameter
(#1)	20	0.0013	0.01538
	20	.0009	.0222
	20	.0015	.01333
	25	.0017	.01470
	10	.0008	.01250
	20	.0008	.02500
	28	.0008	.03500
	10	.0009	.01111
	25	.0012	.02083
	18	.0009	.02000
	10	.0007	.01428
	22	.0009	.02444
	22	.0007	.03142
	30	.0010	.03000
	35	.0015	.02333
	32	.0013	.02461
	52	.0020	.02600
(#2)	8	.0006	.01333
	10	.0010	.01000
	10	.0008	.01250
	7	.0010	.00700
	10	.0007	.01428
	12	.0008	.01500
	10	.0009	.01111
	14	.0008	.01750
	9	.0006	.01500
(#3)	20	.0015	.01333
	30	.0014	.02142
	20	.0020	.01000
	38	.0018	.02111
	20	.0013	.01538
	30	.0011	.02727
	16	.0010	.01600
	6	.0004	.01500
	12	.0012	.01000
	11	.0005	.02200
	18	.0011	.01636
	18	.0009	.02000
	24	.0010	.02400
	22	.0007	.03142

2) Type 1100-0 Aluminum (continued)

Proficorder Trace	Depth (μ")	Diameter (")	Depth/Diameter
(#3)	42	0.0013	0.03230
	32	.0007	.04571
	28	.0007	.04000

$\overline{\text{Depth}}$ = 21.720 μ"

$\overline{\text{Diameter}}$ = 0.0010395"

$\overline{\text{Depth}}/\overline{\text{Diameter}}$ = 0.019820

Average (Depth/Diameter) = 0.020027

3) Type 2024-T351 Aluminum

Proficorder Trace	Depth (μ")	Diameter (")	Depth/Diameter
(#1)	35	0.0010	0.03400
	35	.0010	.03500
	30	.0007	.04285
	22	.0007	.03142
	20	.0003	.06666
	45	.0012	.03750
	12	.0007	.01714
	17	.0006	.02833
	38	.0013	.02923
	26	.0007	.03714
	20	.0008	.02500
	20	.0007	.02857
	23	.0008	.02875
	20	.0007	.02857
	12	.0006	.02000
(#2)	20	.0008	.02500
	12	.0003	.04000
	18	.0011	.01636
	33	.0011	.03000
	50	.0018	.02777
	33	.0015	.02200
	30	.0012	.02500
	23	.0010	.02300
	12	.0008	.01500
(#3)	21	.0007	.03000
	20	.0006	.03333
	26	.0007	.03714
	14	.0003	.04666
	58	.0009	.06444
	25	.0006	.04166
	22	.0007	.03142
	30	.0010	.03000

3) Type 2024-T351 Aluminum (continued)

Proficorder Trace	Depth (μ")	Diameter (")	Depth/Diameter
(#3)	20	.0006	.03333
	25	.0009	.02777
	15	.0006	.02500

$\overline{\text{Depth}} = 25.200\,\mu$"

$\overline{\text{Diameter}} = 0.000829$"

$\overline{\text{Depth}}/\overline{\text{Diameter}} = 0.030410$

Average (Depth/Diameter) = 0.031887

4) Type 6061-T651 Aluminum

Proficorder Trace	Depth (μ")	Diameter (")	Depth/Diameter
(#1)	35	0.0008	0.04375
	30	.0008	.03750
	28	.0008	.03500
	23	.0012	.01916
	31	.0010	.03100
	40	.0015	.02666
	20	.0015	.01333
	20	.0010	.02000
	15	.0010	.01500
	30	.0010	.03000
	30	.0010	.03000
	15	.0010	.01500
(#2)	25	.0012	.02083
	45	.0011	.04090
	40	.0010	.04000
	12	.0007	.01714
	30	.0010	.03000
	15	.0010	.01500
	45	.0013	.03461
	35	.0010	.03500
	17	.0011	.01545
	15	.0010	.01500
	15	.0010	.01500
	30	.0013	.02307
	25	.0020	.01250
	20	.0011	.01818
	20	.0010	.02000
	18	.0007	.02571
	18	.0010	.01800
(#3)	15	.0008	.01875
	25	.0015	.01666
	21	.0008	.02625
	19	.0010	.01900
	11	.0010	.01100
	10	.0008	.01250
	30	.0010	.03000
	20	.0017	.01176
	18	.0004	.04500
	15	.0008	.01875
	10	.0007	.01428

4) Type 6061-T651 Aluminum (continued)

Proficorder Trace	Depth (μ")	Diameter(")	Depth/Diameter
(#3)	20	0.0007	.02857
	30	.0008	.03750
	38	.0015	.02533
	25	.0010	.02500
	30	.0005	.06000
	20	.0004	.05000

$\overline{\text{Depth}}$ = 23.891 μ"

$\overline{\text{Diameter}}$ = 0.001011"

$\overline{\text{Depth}}/\overline{\text{Diameter}}$ = 0.0236357

Average (Depth/Diameter) = 0.025285

5) 60% C. W. Copper (As Rec'd)

Proficorder Trace	Depth (μ")	Diameter (")	Depth/Diameter
(#1)	15	0.0006	0.02500
	25	.0008	.03125
	30	.0011	.02727
	27	.0007	.03857
	30	.0008	.03750
	18	.0008	.02250
	22	.0018	.01222
	19	.0008	.02375
	22	.0010	.02200
	30	.0011	.02727
	20	.0008	.02500
	18	.0010	.01800
	26	.0009	.02888
	32	.0012	.02666
	14	.0007	.02000
	12	.0006	.02000
	27	.0017	.01588
	20	.0013	.01538
	16	.0010	.01600
	20	.0012	.01666
	21	.0009	.02333
	25	.0011	.02272
	18	.0007	.02571
(#2)	25	.0012	.02083
	19	.0009	.02111
	30	.0008	.03750
	20	.0006	.03333
	30	.0008	.03750
	27	.0009	.03000
	45	.0012	.03750
	32	.0014	.02285
	30	.0008	.03750
	22	.0008	.02750
	31	.0008	.03875
	22	.0010	.02200
	21	.0007	.03000
	19	.0010	.01900
	34	.0012	.02833
	14	.0008	.01750
	31	.0012	.02583
	8	.0003	.02666
	10	.0009	.01111
	16	.0007	.02285

5) 60% C.W. Copper (As Rec'd) continued

Proficorder Trace	Depth (μ")	Diameter(")	Depth/Diameter
(#3)	15	0.0006	0.02500
	32	.0009	.03555
	25	.0007	.03571
	18	.0004	.04500
	23	.0008	.02875
	31	.0008	.03875
	29	.0011	.02636
	27	.0005	.05600
	12	.0004	.03000
	16	.0007	.02285
	32	.0008	.04000
	30	.0012	.02500
	26	.0010	.02600
	22	.0008	.02750
	13	.0006	.02166
	30	.0012	.02500
	28	.0010	.01555
	16	.0008	.02000
	13	.0007	.01857
	20	.0012	.01666
	18	.0006	.03000

$\overline{\text{Depth}} = 22.953\mu"$

$\overline{\text{Diameter}} = 0.000910"$

$\overline{\text{Depth}}/\overline{\text{Diameter}} = 0.025681$

Average (Depth/Diameter) = 0.026548

6) Copper 900°F Annealed

Proficorder Trace	Depth (μ")	Diameter (")	Depth/Diameter
(#1)	60	0.00200	0.03000
	20	.00150	.01333
	20	.00050	.00400
	25	.00150	.01666
	20	.00090	.02500
	40	.00150	.02666
	25	.00150	.01666
	30	.00150	.02000
	25	.00110	.02272
	25	.00110	.02272
	30	.00175	.01750
	25	.00100	.02500
(#2)	50	.00300	.01666
	30	.00150	.02000
	25	.00170	.01470
	20	.00160	.01250
	15	.00110	.01363
	30	.00200	.01500
	15	.00150	.01000
	25	.00225	.01111
	35	.00250	.01400
	25	.00250	.01000
	20	.00170	.01176
	25	.00150	.01666
	40	.00200	.02000
	25	.00150	.01666
	40	.00150	.02666
	35	.00150	.02333
	30	.00100	.03000
	20	.00120	.01666
(#3)	40	.00220	.01818
	30	.00150	.02000
	30	.00170	.01764
	15	.00100	.01500
	33	.00170	.01941
	35	.00150	.02333
	20	.00100	.02000
	17	.00080	.02125

6) Copper 900°F Annealed (continued)

Proficorder Trace	Depth (μ")	Diameter (")	Depth/Diameter
	17	.00100	.01700
	30	.00120	.02500
	30	.00150	.02000

$\overline{\text{Depth}} = 27.634\mu$"

$\overline{\text{Diameter}} = 0.001521$ "

$\overline{\text{Depth}}/\overline{\text{Diameter}} = 0.018235$

Average (Depth/Diameter) = 0.018448

7) 75% C.W. Nickel (As Rec'd)

Proficorder Trace	Depth (μ")	Diameter (")	Depth/Diameter
(#1)	8	0.0005	0.01600
	7	.0004	.01750
	7	.0004	.01750
	5	.0003	.01400
	8	.0004	.02000
	5	.0006	.00833
	4	.0005	.00800
	8	.0006	.01333
	8	.0008	.01000
	8	.0007	.01142
	10	.0006	.01666
	13	.0010	.01300
	11	.0007	.01571
	7	.0008	.00875
	8	.0005	.01600
	15	.0008	.01875
	7	.0008	.00875
	20	.0008	.02500
	10	.0008	.01250
	12	.0008	.01500
	10	.0007	.01428
	10	.0010	.01000
	20	.0010	.02000
	10	.0004	.02500
	8	.0005	.01600
(#2)	18	.0011	.01636
	11	.0007	.01571
	10	.0005	.02000
	8	.0005	.01600
	10	.0007	.01428
	12	.0010	.01200
	10	.0008	.01250
	16	.0007	.02285
	5	.0003	.01666
	10	.0007	.01428
	20	.0011	.01818
	9	.0006	.01500

7) 75% C.W. Nickel (As Rec'd) continued

Proficorder Trace	Depth (μ")	Diameter (")	Depth/Diameter
(#3)	8	0.0008	0.01000
	6	.0003	.02000
	10	.0005	.02000
	8	.0005	.01600
	10	.0007	.01428
	18	.0008	.02250
	10	.0006	.01666
	12	.0010	.01200
	9	.0005	.01800
	12	.0010	.01200
	11	.0007	.01571
	6	.0006	.01000
	10	.0008	.01250
	10	.0010	.01000
	8	.0007	.01142
	11	.0008	.01375
	10	.0009	.01111
	10	.0009	.01111
	16	.0010	.01600
	9	.0004	.02250
	16	.0008	.02000
	10	.0010	.01000
	13	.0003	.04333
	7	.0005	.01400

$\overline{\text{Depth}} = 10.295\ \mu$"

$\overline{\text{Diameter}} = 0.000692$"

$\overline{\text{Depth}}/\overline{\text{Diameter}} = 0.014881$

Average (Depth/Diameter) = 0.015543

8) Plexiglas (Second Run)

Proficorder Trace	Depth (μ")	Diameter (")	Depth/Diameter
(#1)	80	0.00100	0.09000
	75	.00080	.09375
	75	.00050	.15000
	100	.00100	.10000
	75	.00075	.10000
	175	.00150	.11666
	175	.00100	.17500
	50	.00075	.06666
(#2)	150	.00100	.15000
	300	.00150	.20000
	200	.00125	.16000
	185	.00150	.12333
	150	.00100	.15000
	200	.00100	.20000
	175	.00100	.17500
(#3)	90	.00075	.12000
	150	.00100	.15000
	75	.00100	.07500
	140	.00080	.17500
	250	.00125	.20000
	150	.00110	.13636
	100	.00075	.13333
	225	.00125	.18000
	225	.00110	.20454
	175	.00100	.17500
	100	.00075	.13333

$\overline{\text{Depth}} = 147.884\ \mu$"

$\overline{\text{Diameter}} = 0.001012$"

$\overline{\text{Depth}}/\overline{\text{Diameter}} = 0.14620$

Average (Depth/Diameter) = 0.143190

SUMMATION FOR ALL EIGHT SPECIMENS

Specimen	$\overline{\text{Depth}}$ μ"	$\overline{\text{Diameter}}$ in.	$\overline{\text{Depth}}/\overline{\text{Diameter}}$	Average (Depth/Diameter)
Type 304 Stainless Steel	6.2765	0.006590	0.009516	0.009717
Type 1100-0 Aluminum	21.720	0.001040	0.019820	0.020027
Type 2024-T351 Aluminum	25.200	0.000829	0.030410	0.031887
Type 6061-T651 Aluminum	23.891	0.001011	0.023636	0.025285
60% C.W. Copper (As Rec'd)	22.953	0.000910	0.025681	0.026548
Copper 900°F Annealed	27.634	0.001522	0.018235	0.018448
75% C.W. Nickel (As Rec'd)	10.295	0.000692	0.014881	0.015543
Plexiglas	147.884	0.001012	0.14620	0.143190

APPENDIX "D"

CHARACTERISTIC ACOUSTIC IMPEDANCES OF THE SPECIMENS VS. APPROXIMATE MAXIMUM BUBBLE POPULATION

In Chapter IV, Section H, the approximate maximum bubble population of seven of the eight specimens (type 1100-0 aluminum was excluded because of a poor specimen to horn bond) was discussed and also tabulated in Table 1. All of the specimens were exposed to cavitation at frequencies within a range of 2% and with the applied amplitude of the horn at approximately 2 mils.

When this approximate maximum population was plotted vs. the characteristic acoustic impedances of the individual specimens (which can be considered as equivalent to the acoustic impedance ratio between specimen and horn or specimen and fluid, since the same fluid and horn were used in all cases), an interesting linearity developed (Fig. 169), excepting the copper 900°F annealed specimen, with the bubble population increasing for the higher acoustic impedances, i.e., for the denser materials.

As mentioned in Chapter IV, Section H, the actual amplitudes of the various specimens were measured and were found to be the same (within 10%, which is the precision of

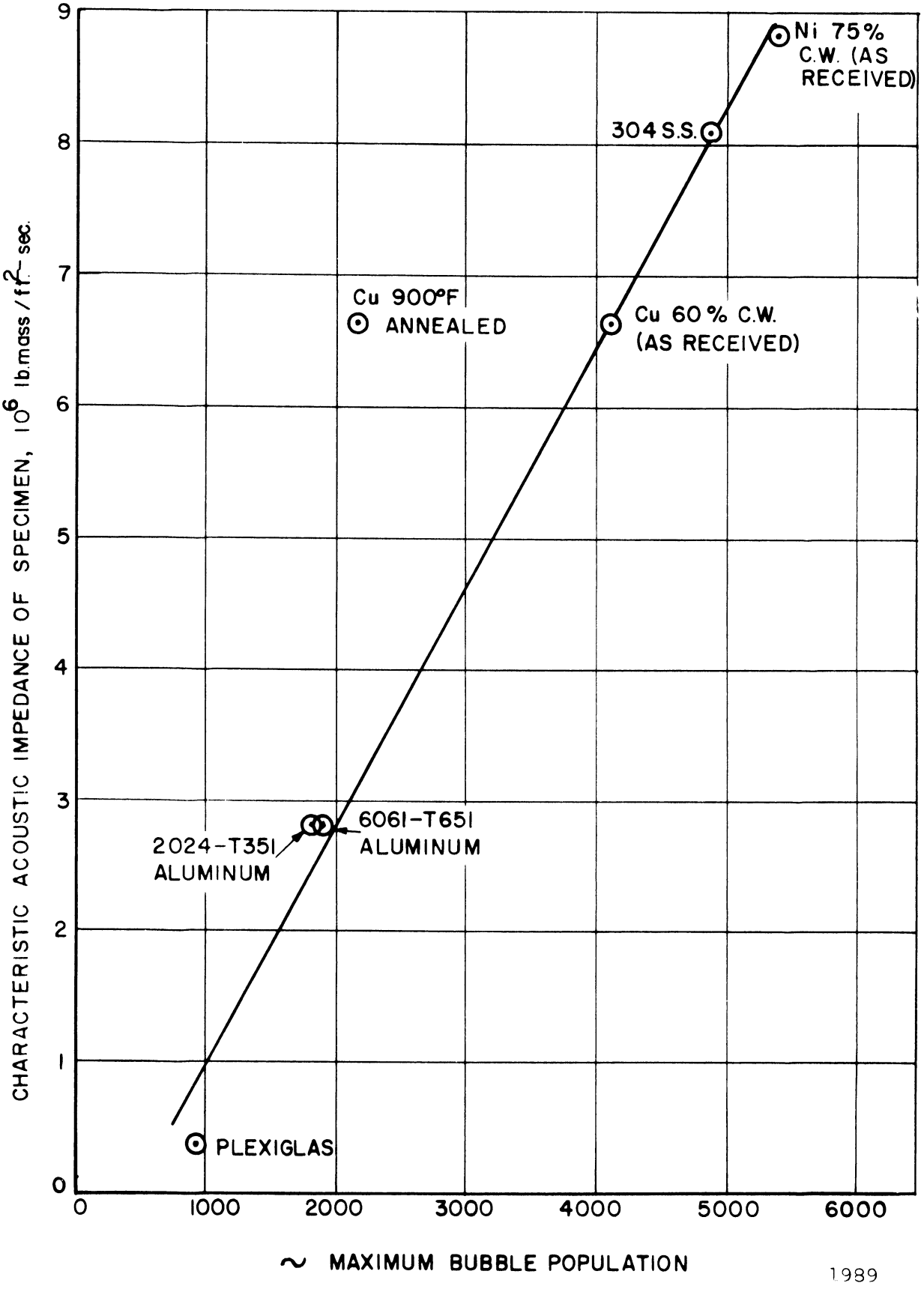

Fig. 169.--Approximate maximum bubble population vs. characteristic acoustic impedance of the specimens.

the measuring system) with the exception of Plexiglas which was approximately 20% less. The reduced Plexiglas specimen amplitude was apparently due to a poor mechanical specimen to horn bond. That the specimens should have the same amplitude where a good bond existed would be expected since the height of the specimens is very much less than the vibration wave length in the material. Thus it is too short to develop a standing wave system of its own, and hence must vibrate essentially with the same amplitude as the horn. Hence the explanation for reduced bubble population with lower specimen acoustic impedance ratio is not to be found in possible reduced specimen amplitude, other than the effects of a poor mechanical bond. This effect was operative in the case of the Plexiglas and may also have been important with the aluminums, although no amplitude difference with the aluminums could be detected within the precision of the measurements.

An explanation for the scatter of bubble population for the heavier specimens may be that the application of 2 mils amplitude to the horn was not done with great precision since at the time of this particular experiment precise amplitude measurements were not available and the attainment of a full bubble cloud on each specimen was the primary requirement. Since the acoustic pressure varies as the square of both the amplitude and the frequency, slight changes in either of these could affect the population. The correlation among the heavier materials with acoustic impedance ratio could then be only

coincidental, and the drastically reduced populations with Plexiglas and the aluminums could be the result only of poor mechanical bonds. However, the overall correlation between acoustic impedance and bubble population is impressive and may well be significant. Since frequency varied only by a maximum of 2% and the horn amplitude could have varied perhaps by 20%, it is felt that the latter parameter was the main contributer to variations in the approximate maximum bubble population.

The specimen to water acoustic impedance ratio may also be important. In this connection it should be realized that the ratio of interest is between the specimen and a vaporous mixture rather than to liquid. Since the sonic velocity in such mixtures is very low as compared to either liquids or metals, the match may be extremely poor with any specimen material so that the effect of differences between specimens may be significant.

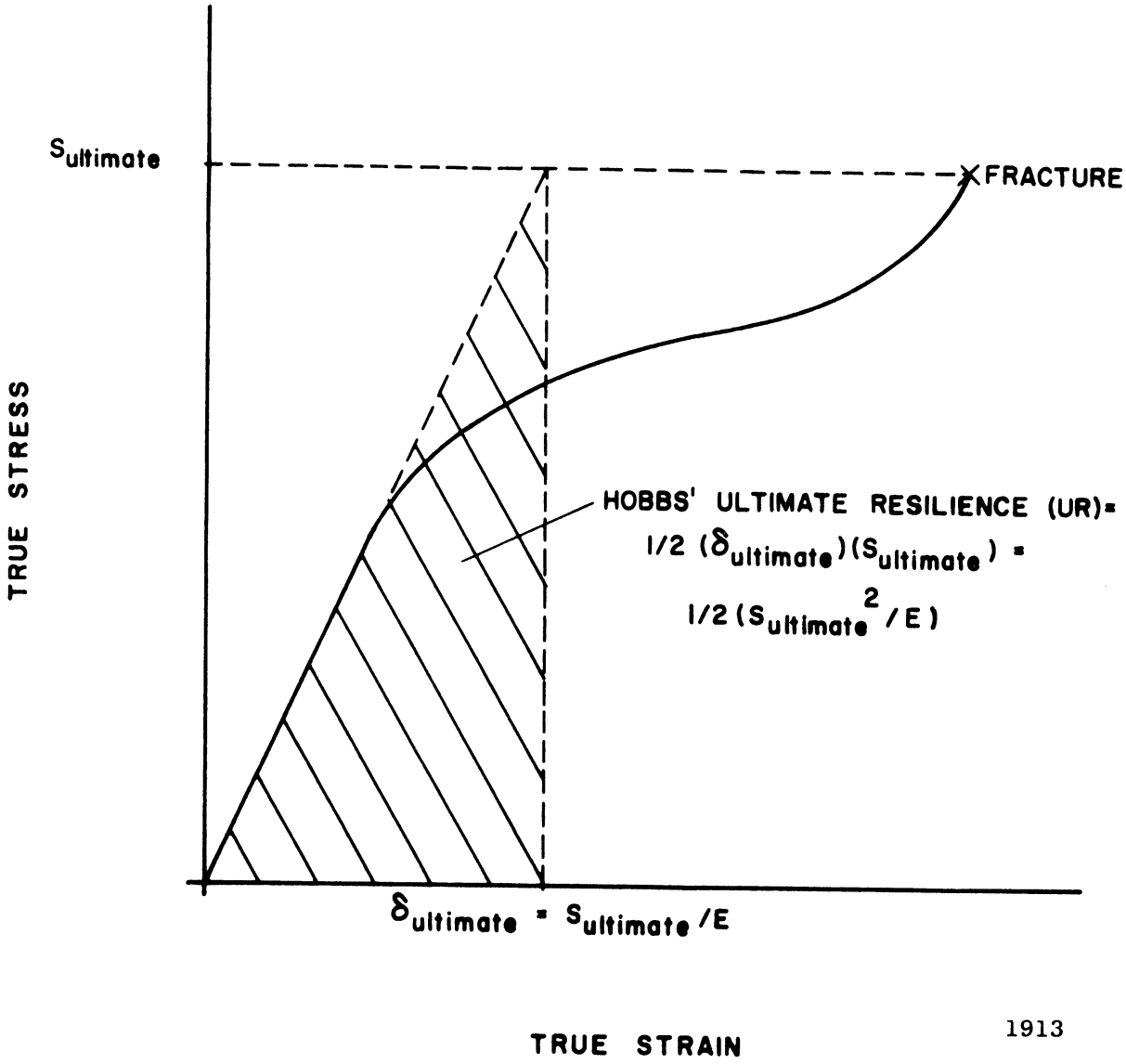
$S_{ultimate}$
FRACTURE
TRUE STRESS
HOBBS' ULTIMATE RESILIENCE (UR)=
1/2 ($\delta_{ultimate}$)($S_{ultimate}$) =
1/2 ($S_{ultimate}^2$ / E)
$\delta_{ultimate} = S_{ultimate}$ /E
TRUE STRAIN
1913

APPENDIX "E"

REFERENCES

1. Wheeler, W. H., "Indentation of Metals by Cavitation," J. of Basic Eng., Trans. of the ASME, Mar., 1960, pp. 184-194.

2. Kerr, S. L., "Determination of Relative Resistance to Cavitation Erosion by Vibratory Method," Trans. of the ASME, Vol. 59, July, 1937, pp. 373-397.

3. Rheingans, W. J., "Accelerated Cavitation Research," Trans. of the ASME, Vol. 72, No. 5, July, 1950, pp. 705-719.

4. Plesset, M. S. and Ellis, A. T., "On the Mechanism of Cavitation Damage," Trans. of the ASME, Vol. 77, No. 7, Oct. 1955, pp. 1055-1064.

5. Thiruvengadam, A. and Preiser, H. S., "On Testing Materials for Cavitation Damage Resistance," Hydronautics, Inc., Technical Report 233-3, Dec. 1963.

6. Kerr, S. L., and Leith, W. C., "A Review of Cavitation Damage by the Vibratory Method at the Dominion Engineering Works LTd," Paper presented at the ASME meeting in Nov. 1955, Milwaukee, Wisconsin.

7. Garcia, R., "Comprehensive Cavitation Damage Data for Water and Various Liquid Metals Including Correlations with Materials and Fluid Properties," PHD Thesis (to be published) Department of Nuclear Engineering, Laboratory for Fluid Flow and Heat Transport Phenomena, University of Michigan, 1966.

8. Garcia, R., Nystrom, R. E., and Hammitt, F. G., "Technical Report No. 3, Ultrasonic-Induced Cavitation Studies in Mercury and Water," Department of Nuclear Engineering, Laboratory for Fluid Flow and Heat Transport Phenomena, University of Michigan, Report No. 05031-3T, May, 1966.

9. Garcia, R., Hammitt, F. G., and Nystrom, R. E., "Comprehensive Cavitation Damage Data for Water and Various Liquid Metals Including Correlations with Materials and Fluid Properties," Department of Nuclear Engineering, Laboratory for Fluid Flow and Heat Transport Phenomena, University of Michigan, Report No. 05031-4-T, May, 1966.

10. Robinson, M. J., "On the Detailed Flow Structure and the Corresponding Damage to Test Specimens in a Cavitating Venturi," PhD Thesis, Department of Nuclear Engineering, Laboratory for Fluid Flow and Heat Transport Phenomena, University of Michigan, 1965.

11. Plesset, M. S., "Shock Waves from Cavitation Collapse," Paper presented at Royal Society Discussion, Deformation of Solids Due to Liquid Impact, London, May 27, 1965 (to be published in Proc. Roy. Soc.).

12. Robinson, M. J. and Hammitt, F. G., "Cavitation Damage Characteristics in Water and Mercury from Studies in a Cavitating Venturi," Department of Nuclear Engineering, Laboratory for Fluid Flow and Heat Transport Phenomena, University of Michigan, Report No. 03434-17-T, Aug., 1965.

13. Robinson, M. J. and Hammitt, F. G., "Detailed Damage Characteristics in a Cavitating Venturi," Department of Nuclear Engineering, Laboratory for Fluid Flow and Heat Transport Phenomena, University of Michigan, Report No. 03434-30-I, June, 1966.

14. Engel, O. G., "Pits in Metals Caused by Collision with Liquid Drops and Soft Metal Spheres," J. of Res. of Nat. Bur. of Stand., Vol 62, No. 6, Res. Paper No. 2958, June, 1959, pp. 229-246.

15. DeCorso, S. M., "Erosion Tests of Steam Turbine Blade Materials," ASTM Proceedings, American Soc. for Testing Materials, Vol 64, pp. 782-796.

16. Kornfield, M and Suvorov, L., "On the Destructive Action of Cavitation," J. of Applied Physics 15, No. 6 (1944), pp. 495-496.

17. Naudé, C. G., and Ellis, A. T., "On the Mechanism of Cavitation Damage by Non-Hemispherical Cavities Collapsing in Contact with Solid Boundaries," ASME Trans., Ser. D, 83, 1961, pp. 648-656.

18. Lord Rayleigh, "On the Pressure Developed in a Liquid During the Collapse of a Spherical Cavity," Phil. Mag. 34, (1917), pp. 94-98.

19. Harrison, M., "An Experimental Study of Single Bubble Cavitation Noise," J. of Acoust. Soc. Amer., Vol. 24, No. 6, Nov. 1952, pp. 776-782.

20. Ivany, R. D., "Collapse of a Cavitation Bubble in Viscous, Compressible Liquid-Numerical and Experimental Analyses," PhD Thesis, Department of Nuclear Engineering, Laboratory for Fluid Flow and Heat Transport Phenomena, University of Michigan, 1965.

21. Ivany, R. D. and Hammitt, F. G., "Cavitation Bubble Collapse in Viscous, Compressible Liquids-Numerical Analyses," Department of Nuclear Engineering, Laboratory for Fluid Flow and Heat Transport Phenomena, University of Michigan, Report No. 03424-24-I, April, 1965.

22. Ivany, R. D., Hammitt, F. G. and Mitchell, T. M., "Cavitation Bubble Collapse Observations in a Venturi," to be published in the J. of Basic Eng., Trans. of the ASME.

23. Shutler, N. D. and Mesler, R. B., "A Photographic Study of the Dynamics and Damage Capabilities of Bubbles Collapsing Near Solid Boundaries," Dept. of Chem. and Petrol. Eng., University of Kansas, 1964.

24. Benjamin, T. B. and Ellis, A. T., "The Collapse of Cavitation Bubbles and the Pressures Thereby Produced Against Solid Boundaries," Paper presented at Royal Society Discussion, Deformation of Solids Due to Liquid Impact, London, May 27, 1965 (to be published in Proc. Roy. Soc.).

25. Florschuetz, L. W. and Chao, B. T., "On the Mechanics of Vapor Bubble Collapse," J. of Basic Eng., Trans. of the ASME, 1964.

26. Hickling, R. and Plesset, M., "The Collapse of a Spherical Cavity in a Compressible Liquid," Div. of Eng. and Applied Science, Cal. Inst. of Tech., Report No. 85-24, Mar. 1963.

27. Schmid, J., "Cinematographic Investigation of Single Bubble Cavitation," Acoustica, Vol. 9, 1959, pg. 321.

28. Willard, G. W., "Ultrasonically Induced Cavitation in Water: A Step-by-Step Process," J. of Acoust. Soc. Amer., Vol. 25, No. 4, July, 1953, pp. 669-686.

29. Ellis, A. T., "Production of Accelerated Cavitation Damage by an Acoustic Field in a Cylindrical Cavity," J. of Acoust. Soc. Amer., Vol. 27, No. 5, Sept. 1955, pp. 913-921.

30. Ellis, A. T., "Techniques for Pressure Pulse Measurement and High Speed Photography in Ultrasonic Cavitation," Calif. Inst. of Tech., Report No. 21-20, July 1955.

31. Leith, W. C. and Thompson, A. L., "Some Corrosion Effects in Accelerated Cavitation Damage," ASME Trans., Ser. D, 82, 1960, pp. 795-807.

32. Rosenberg, L. D. and Eknadiosyants, O. K., "Kinetics of Ultrasonic Fog Formation," Akusticheskii Zhurnal, Vol. 6, July 1960, pp. 370-373.

33. Numachi, F., "An Experimental Study of Accelerated Cavitation Induced by Ultrasonics," J. of Basic Eng., Trans. of the ASME, Dec. 1965, pp. 967-976.

34. Plesset, M. S., and Devine, R. E., "Effect of Exposure Time on Cavitation Damage," (to be published), Engineering Science Dept., Calif. Inst. of Tech.

35. Saneyoshi, J. and Okushima, M., "Observation of Ultrasonic Cavitation," Proc. 3-rd Intern. Congr. Acoustic., Stuttgart, 1, Amsterdam-London-N. Y.-Princeton, p. 333, (1959).

36. Jackson, F. J. and Nyborg, W. L., "Microscopic Eddying Near a Vibrating Ultrasonic Tool Tip," J. of Applied Physics 30, 1959, p. 949.

37. Jackson, F. J., and Nyborg, W. L., "Sonically-Induced Microstreaming Near a Plane Boundary. I. The Sonic Generator and Associated Acoustic Field," J. of Acoust. Soc. Amer., Vol 32, No. 10, Oct. 1960, pp. 1243-1250.

38. Jackson, F. J., "Sonically Induced Microstreaming Near a Plane Boundary. II. Acoustic Streaming," J. of Acoust. Soc. Amer., Vol 32, No. 11, Nov., 1960, pp. 1387-1395.

39. Hammitt, F. G., "Observations of Cavitation Damage in a Flowing System," J. of Basic Eng., Trans. of the ASME, Vol. 85, Sept. 1963, pp. 347-359.

40. Knapp, R. T., "Accelerated Field Tests of Cavitation Intensity," ASME Trans., Ser. D, 80, 1958, pp. 1315-1324.

41. Noltingk, B. E., and Neppiras, E. A., "Cavitation Produced by Ultrasonics," Proc. Phy. Soc., (London), Vol. B63, 1950, pp. 674-685.

42. Neppiras, E. A., and Noltingk, B. E., "Cavitation Produced by Ultrasonics: Theoretical Condition for the Onset of Cavitation," Proc. Phy. Soc., (London), Vol. B64, 1951, pp. 1032-1038.

43. Robinson, L. E., Holmes, B. A., and Leith, W. C., "Progress Report on Standardization of the Vibratory Cavitation Test," Trans. of the ASME, Jan. 1958, pp. 103-107.

44. Flynn, H. G., Section 9. "Physical Acoustics, Vol. 1, Part B," Edited by W. P. Mason, Academic Press, 1964.

45. Minnaert, M., "On Musical Air Bubbles and the Sounds of Running Water," Phil. Mag., Vol. 16, 1933, pp. 235-248.

46. Sirotyuk, M. G., "Behavior of Cavitation Bubbles at Large Ultrasonic Intensities," Akusticheskii Zhurnal, Vol. 7, No. 4, Oct., 1961, pp. 499-501.

47. Strasberg, M., "Onset of Ultrasonic Cavitation in Tap Water," J. of Acoust. Soc. Amer., Vol 31, No. 2, Feb. 1959, pp. 163-176.

48. Fox, F. E. and Herzfeld, K. F., Gas Bubbles with Organic Skin as Cavitation Nuclei," J. of Acoust. Soc. Amer., Vol. 26, No. 6, 1954, p. 984.

49. Bernd, L. H., "Study of the Surface Films of Gas Nuclei (As Related to Cavitation and Tensile Strength in Water)," Report TIS64GL143, Advanced Technology Lab., General Electric Co., Sept. 1964.

50. Sette, D. and Wanderlingh, F., "Nucleation by Cosmic Rays in Ultrasonic Cavitation," Phys. Rev., Vol. 125, No. 2, Jan., 1962, pp. 409-417.

51. Harvey, E. N., McElroy, W. D., and Whitely, A. H., "On Cavity Formation in Water," J. of Appld. Phys., Vol 18, 1947, pp. 162-172.

52. Knapp, R. T., "Cavitation and Nuclei," J. of Basic Eng., Trans. of the ASME, Aug. 1958, pp. 1315-1324.

53. Hsieh, D. Y., and Plesset, M. S., "Theory of Rectified Diffusion of Mass into Gas Bubbles," J. of Acoust. Soc. Amer., Vol 33, 1961, pp. 206-214.

54. Blitz, J., "Elements of Acoustics," Washington Butterworths, 1964, p. 22.

55. Rattray, M., "Perturbation Effects in Bubble Dynamics," PhD Thesis CIT, 1951.

56. Harrison, C. A., Robinson, M. J., Siebert, C. A., Hammitt, F. G., and Lawrance, J., "Complete Mechanical Properties Specifications for Materials as Used in Venturi Cavitation Damage Tests," Department of Nuclear Engineering, Laboratory for Fluid Flow and Heat Transport Phenomena, University of Michigan, Report No. 03424-29-I, Aug., 1965.

57. Hobbs, J. M., "Experience with a 20 Kilocycle Cavitation-Erosion Test," Paper No. 120, ASTM Symposium on Erosion by Cavitation or Impingement, June 28, 1966.

58. Walsh, W. J., and Hammitt, F. G., "Cavitation and Erosion Damage Measurements with Radio-Isotopes," Nucl. Sci. and Engr., Vol 14, No. 3, Nov., 1962, pp. 217-223.

59. Lichtman, J. Z., "Cavitation and Erosion Performance and Related Properties of Elastomeric Coatings," Paper No. 123, 69th Annual Meeting, ASTM, June, 1966.

60. Discussion by R. Garcia and F. G. Hammitt, Department of Nuclear Engineering, Laboratory for Fluid Flow and Heat Transport Phenomena, University of Michigan, Paper 120, ASTM Symposium on Erosion by Cavitation or Impingement, June 28, 1966, entitled "Experience with a 20 Kilocycle Cavitation-Erosion Test," J. M. Hobbs.

61. Mitchell, T. M., Kling, C. L., Hammitt, F. G., "Bubble Collapse Behavior Around a Sharp Wedge in a Diffuser," Department of Nuclear Engineering, Laboratory for Fluid Flow and Heat Transport Phenomena, University of Michigan, Report No. 07738-T-1, July, 1966.

62. Engel, O. H., "Waterdrop Collisions with Solid Surfaces," J. of Res. of Nat. Bur. of Stand., Vol 54, No. 5, May, 1955.